ADVANCES IN TERAHERTZ DETECTION AND IMAGING

EDITED BY: Lianhe Li, Yingxin Wang, Xinke Wang and Meng Chen
PUBLISHED IN: Frontiers in Physics

frontiers Research Topics

ISSN 1664-8714
ISBN 978-2-88976-020-6
DOI 10.3389/978-2-88976-020-6

About Frontiers

Frontiers is more than just an open-access publisher of scholarly articles: it is a pioneering approach to the world of academia, radically improving the way scholarly research is managed. The grand vision of Frontiers is a world where all people have an equal opportunity to seek, share and generate knowledge. Frontiers provides immediate and permanent online open access to all its publications, but this alone is not enough to realize our grand goals.

Frontiers Journal Series

The Frontiers Journal Series is a multi-tier and interdisciplinary set of open-access, online journals, promising a paradigm shift from the current review, selection and dissemination processes in academic publishing. All Frontiers journals are driven by researchers for researchers; therefore, they constitute a service to the scholarly community. At the same time, the Frontiers Journal Series operates on a revolutionary invention, the tiered publishing system, initially addressing specific communities of scholars, and gradually climbing up to broader public understanding, thus serving the interests of the lay society, too.

Dedication to Quality

Each Frontiers article is a landmark of the highest quality, thanks to genuinely collaborative interactions between authors and review editors, who include some of the world's best academicians. Research must be certified by peers before entering a stream of knowledge that may eventually reach the public - and shape society; therefore, Frontiers only applies the most rigorous and unbiased reviews.
Frontiers revolutionizes research publishing by freely delivering the most outstanding research, evaluated with no bias from both the academic and social point of view. By applying the most advanced information technologies, Frontiers is catapulting scholarly publishing into a new generation.

What are Frontiers Research Topics?

Frontiers Research Topics are very popular trademarks of the Frontiers Journals Series: they are collections of at least ten articles, all centered on a particular subject. With their unique mix of varied contributions from Original Research to Review Articles, Frontiers Research Topics unify the most influential researchers, the latest key findings and historical advances in a hot research area! Find out more on how to host your own Frontiers Research Topic or contribute to one as an author by contacting the Frontiers Editorial Office: frontiersin.org/about/contact

ADVANCES IN TERAHERTZ DETECTION AND IMAGING

Topic Editors:
Lianhe Li, University of Leeds, United Kingdom
Yingxin Wang, Tsinghua University, China
Xinke Wang, Capital Normal University, China
Meng Chen, Tsinghua University, China

Citation: Li, L., Wang, Y., Wang, X., Chen, M., eds. (2022). Advances in Terahertz Detection and Imaging. Lausanne: Frontiers Media SA. doi: 10.3389/978-2-88976-020-6

Table of Contents

frontiers in Physics

EDITORIAL
published: 07 February 2022
doi: 10.3389/fphy.2022.855623

Editorial: Advances in Terahertz Detection and Imaging

Meng Chen[1], *Yingxin Wang*[1]*, *Xinke Wang*[2] *and Lianhe Li*[3]

[1]National Engineering Laboratory for Dangerous Articles and Explosives Detection Technologies, Department of Engineering Physics, Tsinghua University, Beijing, China, [2]Department of Physics, Beijing Key Lab for Metamaterials and Devices, Capital Normal University, Beijing, China, [3]School of Electronic and Electrical Engineering, University of Leeds, Leeds, United Kingdom

Keywords: terahertz detection, terahertz imaging, functional devices, terahertz technology, terahertz applications

Editorial on the Research Topic

Advances in Terahertz Detection and Imaging

Terahertz waves have many unique properties and show great potential for both fundamental scientific research and applications in various fields, such as astronomy, communication, biomedicine, and security inspection [1–3]. Terahertz detection is a process of converting terahertz signal into a measurable electrical signal. It can be used to obtain the amplitude, phase, spectroscopic, temporal, or polarization information of the THz signal, which may reveal rich physical phenomena about the interaction of terahertz waves with matter. Effective detection of terahertz signal is crucial for realizing real-world applications of terahertz technology, especially for the passive techniques [4]. Terahertz waves show good capability of penetration through objects which are usually opaque to infrared and visible light, and their appropriate wavelengths may yield a higher spatial resolution than microwave. Many organic substances exhibit fingerprint absorption spectra in this frequency range, enabling identification of different materials. Therefore, imaging with terahertz waves allows one to see through an object with millimeter- or submillimeter-scale resolution and even spatially resolve its chemical composition [5, 6]. Nowadays, terahertz detection and imaging are two fundamental and hot topics in the area of terahertz science and technology, and a series of significant advances have emerged in recent years.

Limited by the cut-off frequency of conventional electronic devices and the relatively large bandgap of conventional photonic devices, detection of terahertz waves at room temperature (RT) is still a challenge. For terahertz detection, the underlying mechanisms can be generally classified into three categories: thermal effect, electronic effect and photonic effect. Thermal detectors, relying on the temperature change of the photoactive materials induced by the incident radiation, have a broadband photoresponse (theoretically covering the entire terahertz range). Bolometers are the most widely used thermal detectors and their focal-plane arrays have been commercially available. At cryogenic temperatures, bolometers show very high sensitivities, with noise-equivalent power (NEP) levels on the order of $\mathrm{fW}/\sqrt{\mathrm{Hz}}$ or below, and have been successfully applied to astronomical observation and personnel screening [4, 7]. Thermal response is usually slow (of about milliseconds). However, the hot-carrier assisted photothermoelectric effect occurring in graphene is an exception, which is capable of reaching the picosecond level [8]. Electronic detectors, relying on the interaction of terahertz waves with the collective motion of electrons or induces an electron transition (across a potential barrier) [9], have a fast response but low-frequency operation (typically below 1 THz). Photonic detectors, relying on the generation of electron-hole pairs in narrow bandgap semiconductors upon terahertz photoexcitation, usually require cryogenic cooling to reduce the background thermal noise. Nevertheless, after years of development, exciting progress has been achieved in terahertz detection techniques [9, 10]. Benefiting from novel photoactive materials, optimized device structure design and refined fabrication process, terahertz detector performances,

OPEN ACCESS

Edited and reviewed by:
Lorenzo Pavesi,
University of Trento, Italy

Correspondence:
Yingxin Wang
wangyingxin@tsinghua.edu.cn

Specialty section:
This article was submitted to Optics and Photonics, a section of the journal Frontiers in Physics

Received: *15 January 2022*
Accepted: *19 January 2022*
Published: *07 February 2022*

Citation:
Chen M, Wang Y, Wang X and Li L (2022) Editorial: Advances in Terahertz Detection and Imaging. Front. Phys. 10:855623. doi: 10.3389/fphy.2022.855623

in term of sensitivity, speed, bandwidth, working temperature and integrability, have been remarkably improved.

Since the first demonstration of terahertz transmission imaging based on a time-domain spectroscopy (TDS) system [11], different modalities have been proposed to achieve better imaging performance or to provide new physical information for understanding of light-matter interactions at terahertz frequencies. The spatial resolution of conventional terahertz imaging is on the order of terahertz wavelength, limited by diffraction. Using near-field technique [12] or sub-diffraction optics [13], imaging with subwavelength resolution becomes viable. From pixel-by-pixel scanning to real-time 2D imaging, faster image acquisition can be realized with the advent of focal plane array detectors [14, 15] and computational imaging based on a single-pixel detector [16, 17]. Broadband pulses, frequency-tunable continuous-wave sources or frequency combs enables spectroscopic or hyperspectral imaging, which is appealing for acquiring both the structure and composition information of the object from multiple spectral bands [5, 18, 19]. When combining the techniques of interferometeric, holographic or self-mixing, phase images can be measured or reconstructed to reveal the terahertz wave front and the object depth information quantitatively [20–23]. In addition, imaging systems for radar, personnel screening and non-destructive evaluation applications have been well established and some even become commercially available.

Through this Research Topic, we aim to present the research advances in terms of new mechanisms, technical improvements, functional devices, and signal processing methods developed for terahertz detection and imaging. The first sub-topical area of this topic is terahertz detection, which serves as a basis of terahertz science and technology. Terahertz quantum-well photodetectors (QWP) have high sensitivity and fast response. In the article by Shao et al. the authors describes QWP theory and review the research progress for imaging and communication applications. In the work by Bai et al. QWP is integrated with a light-emitting diode to upconvert terahertz radiation into near infrared emission for broadband upconversion terahertz detection and pixelless imaging. Hou et al. present theoretical studies on the neon glow discharge characteristics and the interaction between the discharge plasma with terahertz waves so as to develop low cost, RT operation and user-friendly detectors. Photoactive materials are vital for RT terahertz bolometers. Jiang et al. report that the Nb_5N_6 thin film coupled with a radio frequency choke-enhanced dipole antenna enables a $pW/\sqrt{Hz}$ level NEP and a response time below 10 μs. Photoconductive antennas (PCAs) are widely used detectors in TDS systems. By fabricating a PCA array with a special substrate micromachining process to eliminate the reverse current between adjacent antenna, Shi et al. report an enhanced synthesis efficiency. Layered MoS2 crystals are promising materials for novel optoelectronic devices. Using optical pump-terahertz probe technique—a powerful tool for investigating the ultrafast process in semiconductors, Yang et al. present a study on their photo-generated carrier dynamics.

As for terahertz imaging, Zhang et al. report the non-contact and non-invasive characterization of Chinese lacquerware by terahertz reflection imaging. The layer structures of a lacquer-covered ornamental wood panel are clearly resolved by the time-of-flight of terahertz pulses. Wang et al. report the spatiotemporal distribution measurement of terahertz wave generated from two-color-induced plasma by focal plane imaging, allowing one to fully understand the characteristics of terahertz emission from plasma. To improve the terahertz image quality for nondestructive testing of composite materials, Li et al. propose an image enhancement method based on wavelet unsharp masking and guided filtering. Experimental results show that different types of defects can be accurately identified using this method. For self-mixing imaging by quantum cascade laser (QCL), interferometric signal extraction and analysis plays a key role. Ge et al. present a theoretical model to study the self-mixing interference in complex coupled distributed feedback THz QCLs, which is valuable for further development of terahertz self-mixing imaging technique.

In detection and imaging systems, functional devices play an important role in manipulating terahertz waves. Liu et al. report a flexible broadband terahertz modulator based on a strain-sensitive MXene film. Under a stretching force, the device can efficiently change terahertz transmission amplitude. Furthermore, a sensitive terahertz intensity change measurement is desirable for a sensor. Wang et al. design a composite device consisting of a carbon nanotube metasurface and a microfluidic channel to monitor the refractive index of the analyte with a high sensitivity for biological and chemical sensing applications. Besides amplitude modulation, polarization control also deserves special attention. Wang et al. propose an electronically tunable graphene composite metasurface to actively control the terahertz wave polarization state. By changing the chemical potential of graphene, they achieved the interconversion among linear, circular and elliptical polarizations of the THz signal. Wang et al. investigates the focusing and dispersive properties of circularly polarized terahertz vortex beams, which is promising for the applications in terahertz imaging and microscopy.

AUTHOR CONTRIBUTIONS

All authors listed have made a substantial, direct, and intellectual contribution to the work and approved it for publication.

REFERENCES

1. Tonouchi M. Cutting-Edge Terahertz Technology. *Nat Photon* (2007) 1: 97–105. doi:10.1038/nphoton.2007.3
2. Dhillon SS, Vitiello MS, Linfield EH, Davies AG, Hoffmann MC, Booske J, et al. The 2017 Terahertz Science and Technology Roadmap. *J Phys D Appl Phys* (2017) 50:043001. doi:10.1088/1361-6463/50/4/043001
3. Lu X, Venkatesh S, Saeidi H. A Review on Applications of Integrated Terahertz Systems. *China Commun* (2021) 18:175–201. doi:10.23919/JCC.2021.05.011

4. Grossman E, Dietlein C, Ala-Laurinaho J, Leivo M, Gronberg L, Gronholm M, et al. Passive Terahertz Camera for Standoff Security Screening. *Appl Opt* (2010) 49:E106–20. doi:10.1364/AO.49.00E106
5. Kawase K, Ogawa Y, Watanabe Y, Inoue H. Non-Destructive Terahertz Imaging of Illicit Drugs Using Spectral Fingerprints. *Opt Express* (2003) 11: 2549–54. doi:10.1364/OE.11.002549
6. Mittleman DM. Twenty Years of Terahertz Imaging [Invited]. *Opt Express* (2018) 26:9417–31. doi:10.1364/OE.26.009417
7. Siegel PH. THz Instruments for Space. *IEEE Trans Antennas Propagat* (2007) 55:2957–65. doi:10.1109/TAP.2007.908557
8. Cai X, Sushkov AB, Suess RJ, Jadidi MM, Jenkins GS, Nyakiti LO, et al. Sensitive Room-Temperature Terahertz Detection via the Photothermoelectric Effect in Graphene. *Nat Nanotech* (2014) 9:814–9. doi:10.1038/NNANO.2014.182
9. Lewis RA. A Review of Terahertz Detectors. *J Phys D Appl Phys* (2019) 52: 433001. doi:10.1088/1361-6463/ab31d5
10. Rogalski A, Sizov F. Terahertz Detectors and Focal Plane Arrays. *Opto-electron Rev* (2011) 19:346–404. doi:10.2478/s11772-011-0033-3
11. Hu BB, Nuss MC. Imaging with Terahertz Waves. *Opt Lett* (1995) 20:1716–8. doi:10.1364/OL.20.001716
12. Cocker TL, Jelic V, Hillenbrand R, Hegmann FA. Nanoscale Terahertz Scanning Probe Microscopy. *Nat Photon* (2021) 15:558–69. doi:10.1038/s41566-021-00835-6
13. Zhao F, Li Z, Dai X, Liao X, Li S, Cao J, et al. Broadband Achromatic Sub-Diffraction Focusing by an Amplitude-Modulated Terahertz Metalens. *Adv Opt Mater.* (2020) 8:2000842. doi:10.1002/adom.202000842
14. Lee AW, Hu Q. Real-Time, Continuous-Wave Terahertz Imaging by Use of a Microbolometer Focal-Plane Array. *Opt Lett* (2005) 30:2563–5. doi:10.1364/OL.30.002563
15. Guerboukha H, Nallappan K, Skorobogatiy M. Toward Real-Time Terahertz Imaging. *Adv Opt Photon* (2018) 10:843–938. doi:10.1364/AOP.10.000843
16. Chan WL, Charan K, Takhar D, Kelly KF, Baraniuk RG, Mittleman DM. A Single-Pixel Terahertz Imaging System Based on Compressed Sensing. *Appl Phys Lett* (2008) 93:121105. doi:10.1063/1.2989126
17. Stantchev RI, Yu X, Blu T, Pickwell-MacPherson E. Real-Time Terahertz Imaging with a Single-Pixel Detector. *Nat Commun* (2020) 11:1–8. doi:10.1038/s41467-020-16370-x
18. Bandyopadhyay A, Sengupta A. A Review of the Concept, Applications and Implementation Issues of Terahertz Spectral Imaging Technique. *IETE Tech Rev* (2021) 38:1–19. doi:10.1080/02564602.2020.1865844
19. Sterczewski LA, Westberg J, Yang Y, Burghoff D, Reno J, Hu Q, et al. Terahertz Hyperspectral Imaging with Dual Chip-Scale Combs. *Optica* (2019) 6:766–71. doi:10.1364/OPTICA.6.000766
20. Wang Y, Zhao Z, Chen Z, Zhang L, Kang K, Deng J. Continuous-Wave Terahertz Phase Imaging Using a Far-Infrared Laser Interferometer. *Appl Opt* (2011) 50:6452–60. doi:10.1364/AO.50.006452
21. Petrov NV, Kulya MS, Tsypkin AN, Bespalov VG, Gorodetsky A. Application of Terahertz Pulse Time-Domain Holography for Phase Imaging. *IEEE Trans Thz Sci Technol* (2016) 6:464–72. doi:10.1109/TTHZ.2016.2530938
22. Wang X, Xiong W, Sun W, Zhang Y. Coaxial Waveguide Mode Reconstruction and Analysis with THz Digital Holography. *Opt Express* (2012) 20:7706–15. doi:10.1364/OE.20.007706
23. Dean P, Valavanis A, Keeley J, Bertling K, Leng Lim Y, Alhathlool R, et al. Coherent Three-Dimensional Terahertz Imaging through Self-Mixing in a Quantum cascade Laser. *Appl Phys Lett* (2013) 103:181112. doi:10.1063/1.4827886

Conflict of Interest: The authors declare that the research was conducted in the absence of any commercial or financial relationships that could be construed as a potential conflict of interest.

Publisher's Note: All claims expressed in this article are solely those of the authors and do not necessarily represent those of their affiliated organizations, or those of the publisher, the editors and the reviewers. Any product that may be evaluated in this article, or claim that may be made by its manufacturer, is not guaranteed or endorsed by the publisher.

frontiers in Physics

ORIGINAL RESEARCH
published: 28 May 2021
doi: 10.3389/fphy.2021.670972

Flexible Broadband Terahertz Modulation Based on Strain-Sensitive MXene Material

Yangqi Liu, Xiang Li, Tingting Yang, Jingyu Liu, Bin Liu, Jingling Shen, Bo Zhang and Fuhe Wang**

Key Laboratory of Terahertz Optoelectronics, Ministry of Education, Advanced Innovation Center for Imaging Technology, Beijing Key Laboratory for Terahertz Spectroscopy and Imaging, Beijing Key Laboratory of Metamaterials and Devices, Department of Physics, Capital Normal University, Beijing, China

A flexible broadband terahertz modulator based on a strain-sensitive MXene material is reported. MXene is shown to have high terahertz wave absorption through experimental testing of various substrate samples. Results show that the THz signal transmission increases with increasing stretching degree, which differs obviously from transmission through pure PVAc substrates. Analysis of the terahertz time-domain spectrum and electrical characterization indicate that the sample's conductivity decreases with increasing stretching degree. The trend and magnitude of the electrical conductivity results are also very similar to those from the time-domain spectrum. MXene is shown to be a simple, efficient terahertz broadband spectrum modulator with transmittance that can be affected by applying external forces.

Keywords: terahertz modulation, MXene, strain-sensitive, flexible, broadband

OPEN ACCESS

Edited by:
Yingxin Wang,
Tsinghua University, China

Reviewed by:
Zhen Tian,
Tianjin University, China
Faustino Wahaia,
Pontificia Universidad Católica de chile, Chile
Qiwu Shi,
Sichuan University, China

****Correspondence:***
Bo Zhang
bzhang@cnu.edu.cn
Fuhe Wang
wfh-phy@cnu.edu.cn

Specialty section:
This article was submitted to Optics and Photonics, a section of the journal Frontiers in Physics

Received: *22 February 2021*
Accepted: *12 May 2021*
Published: *28 May 2021*

Citation:
Liu Y, Li X, Yang T, Liu J, Liu B, Shen J, Zhang B and Wang F (2021) Flexible Broadband Terahertz Modulation Based on Strain-Sensitive MXene Material. Front. Phys. 9:670972. doi: 10.3389/fphy.2021.670972

INTRODUCTION

As a unique radiation wave type, terahertz waves have had a profound impact on fields including molecular biology, medical imaging, security detection and future communication systems [1–5]. The terahertz wave modulator is the core component of terahertz wireless communications, high-speed data transmission and high-resolution imaging systems. This modulator has characteristics that include low energy requirements, low transients, broadband performance, high coherence and strong perspective properties. In recent years, increasing numbers of different terahertz modulator types have been proposed. The functions of terahertz devices (including modulators [6–11], filters [12], polarizers [13, 14] and metamaterials [15–19]) are critical to the acceleration of spectral, imaging and communications applications using terahertz technology. In recent years, various methods for fabrication of high-efficiency THz modulators have been proposed, including fabrication of an in-band transition using graphene-induced perturbation, phase changes using vanadium dioxide (VO_2), formation of composite metamaterials using split ring resonators and silicon light excitation. Although considerable efforts have been made to design and optimize the THz wave dynamic tuning materials, these efforts have been hindered by the low tuning efficiency of these materials. Therefore, the efforts to develop new terahertz modulation materials with high efficiency are of major significance. In recent years, flexible optoelectronic devices have attracted widespread attention because they can operate under various mechanical deformation conditions to meet the requirements of wearable or flexible applications [20–24]. For example, in 2018, Zhang et al. reported an engineering three-dimensional integrated framework for grinding stretchable electronic products by combining material design with advanced micromachining strategies [20]. At the same

time, some research on flexible terahertz devices was proposed [25–27], but most of the research focused on the integration of device units with flexible substrates. For example, Suzuki et al. designed terahertz metal cells that contained carbon nanotubes (CNTs) to form a flexible terahertz scanner and demonstrated the potential of this scanner in imaging of three-dimensional curvature objects [26]. Cong et al. fabricated a THz metamaterial quarter-wave plate composed of a metal wire grid layer and an isotropic polyimide layer that can be bent to cover a detector and used to explore the chirality of biomacromolecules [27]. However, these functions are essentially dependent on the nature of the device unit and must be performed using metamaterials with complex structures. In 2020, Shi et al. developed a flexible terahertz modulation method based on conductive polymer composites composed of thermoplastic polyurethane (TPU) and conductive Ni particles. This flexible layer exhibits the resistivity change of six to seven orders under tensile strain, which can be used to control the THz transmission with a giant modulation depth as high as 96%. Starting from the structural role of metamaterials, THz radiation can be modulated flexibly using the properties of materials [28]. Therefore, flexible material modulators with simple structures and obvious effects are desirable.

Mxenes represent a new family of two-dimensional transition metal carbides and nitrides with the general formula $M_{n+1}X_nT_x$ [where M is an early transition metal (Sc, Ti, Zr, Hf, V, Nb, T a, Cr, Mo, etc.), X is carbon or nitrogen, and T_x represents surface terminations, (e.g. hydroxyl, oxygen, or fluorine terminations)] [38, 39]. Mxenes have attracted major interest because of their interesting and diverse mechanical, structural, physical and chemical properties. Most importantly, MXenes exhibit ultra-high conductivity (1500 S/cm) on hydrophilic surfaces [29]. Because of this unique characteristic, MXenes have attracted extensive attention in fields such as energy storage [30–32], selective ion screening [33, 34], intelligent materials [35], electromagnetic interference shielding [36], and lasers [37]. Current research indicates that MXenes show excellent responses to electromagnetic waves. Jhon reported that Ti_3C_2 has high absorption and extinction coefficients in the terahertz range based on a first principles study [38]. This type of material with its strong absorption properties has drawn our interest strongly and we have previously fabricated a flexible broadband terahertz modulator based on a strain-sensitive MXene material.

In this work, the terahertz signal absorption of an MXene [$Ti_3C_2T_x$(T_x = −OH, −O)]/PVAc(latex) sample is obviously reduced under the application of external tension, and the terahertz wave is thus modulated effectively to a large extent. During the material stretching process, the conductivity of the sample decreases as the degree of stretching increases, which results in increased THz wave transmission. The THz modulator introduced in this paper has advantages that include a simple structure, simple implementation and an obvious effect.

EXPEROMENTAL DETAILS

The substrate was fixed on a clean quartz wafer, then a thin MXene dispersion layer was spin coated on a clean emulsion substrate (1.5 cm × 3 cm × 0.2 mm), and sintered at 100°C for 15 min. Subsequently, silver parallel electrodes(1 cm long × 0.5 cm wide × 200 nm thick, with a distance between the electrodes of 5 mm) are deposited on the MXene layer by thermal evaporation in a vacuum chamber. Finally, a silver glue layer is coated onto the silver electrode and sintered at 100°C for 15 min.The sample is then removed from the quartz sheet and fixed onto a stretchable sample holder.

By performing scanning electron microscopy (SEM) surface morphology tests, we obtained the surface morphologies of the samples in the relaxed and flat state and the tensile state. The SEM surface topography of the MXene[$Ti_3C_2T_x$(T_x = −OH, −O)]/PVAc(latex) sample are shown in **Figures 1B,C**. **Figure 1C** shows the morphology of the surface and section of MXene sample in the non-tensile state (the small picture in the upper right corner is a sectional view). **Figure 1C** shows the surface morphology of mxene under tension. As shown in **Figures 1B,C**, when the magnification is 35,000 times, we can see that the surface under tension is less wrinkled and much smoother than that in the relaxed state.

A GaAs photoconductive antenna was used to generate terahertz pulses with bandwidths in the 0.2–1.2 THz range. To detect the transmitted terahertz signals, a ZnTe crystal was used with an electro-optical sampling technique. The electro-optic effect is basically a nonlinear coupling effect between a low-frequency electric field (the terahertz pulse) and an optical pulse in the sensor crystal (ZnTe). The modulation of the polarization ellipticity of an optical probe beam that passes through the ZnTe crystal caused by modulation of the ZnTe crystal's birefringence by a terahertz pulse is analyzed to gain information on both the amplitude and the phase of the terahertz wave. The tensile sample holder with the sample is placed into a THz time-domain spectroscopy (THz-TDS) system and the terahertz light spot is aimed at the titanium carbide part of the holder between the electrodes, as shown in **Figure 1A**. By adjusting the knob on the left side of the sample holder to adjust the stretching degree of the sample, the terahertz time-domain spectra of terahertz transmission characteristics of different stretched samples are obtained. The corresponding frequency spectrum can be obtained by applying a Fourier transform, and the conductivities of the samples with different tensile degrees can be calculated using the method described in **Formula 2**. The reference value is taken from the tensile data of an uncoated titanium carbide substrate.

The procedure is described as follows. First, connect the two ends of the sample via the electrodes to the source meter, and take the relaxed and flat state of the sample as the initial state; stretch the sample by a stretching amount of 5.7%, which acts as the change unit, and apply voltagesranging from 1V to −1V; collect the current information at 10 points, obtain the current-voltage (I-V) diagram for different stretching degrees, and then calculate the resistance value and conductivity of the sample.

RESULTS AND DISCUSSION

The terahertz time domain spectra of PVAc samples with and without MXene coatings are shown in **Figure 2A**. The sample

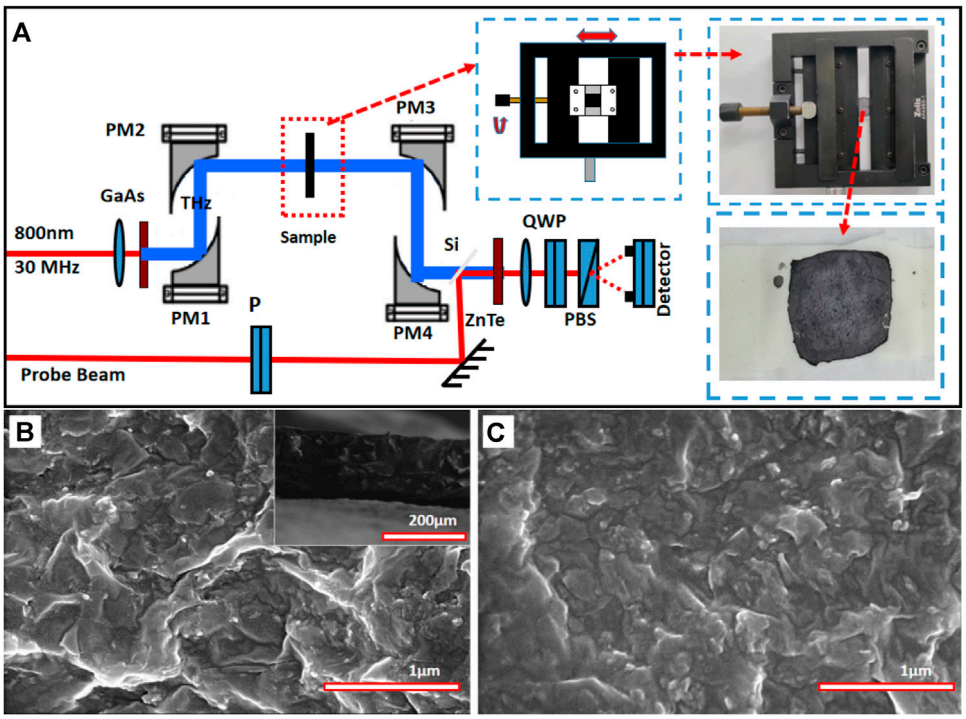

FIGURE 1 | (A) Schematic of the experimental setup. **(B)** Surface morphology of the sample without tension. **(C)** Surface morphology of the sample under tension.

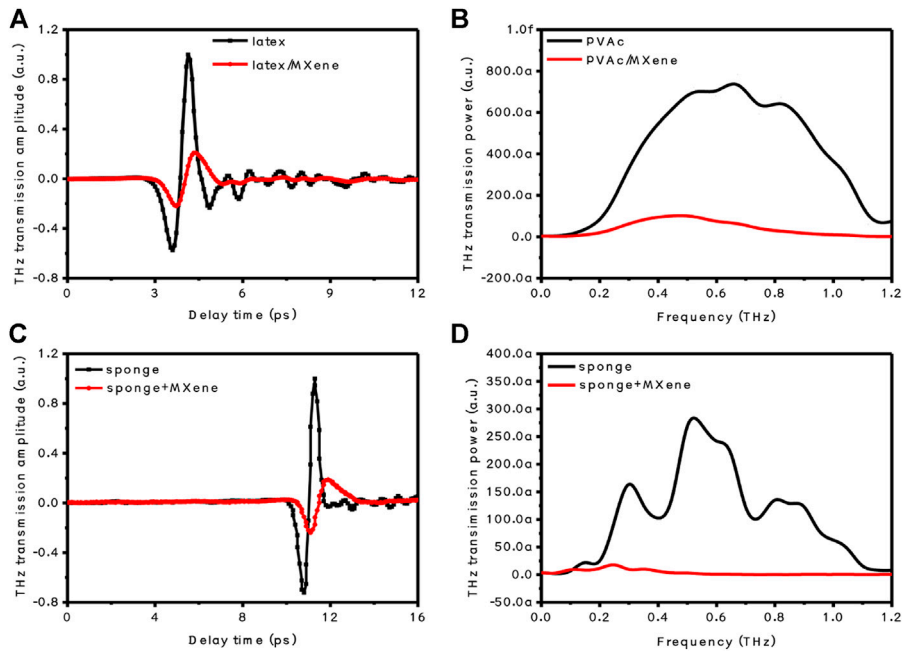

FIGURE 2 | (A) Terahertz time-domain spectra of samples with and without MXene coating on PVAc substrates. **(B)** Terahertz frequency-domain spectra of samples with and without MXene coating on PVAc substrates. **(C)** Terahertz time-domain spectra of samples with and without MXene coating on sponge substrates. **(D)** Terahertz frequency-domain spectra of samples with and without MXene coating on sponge substrate.

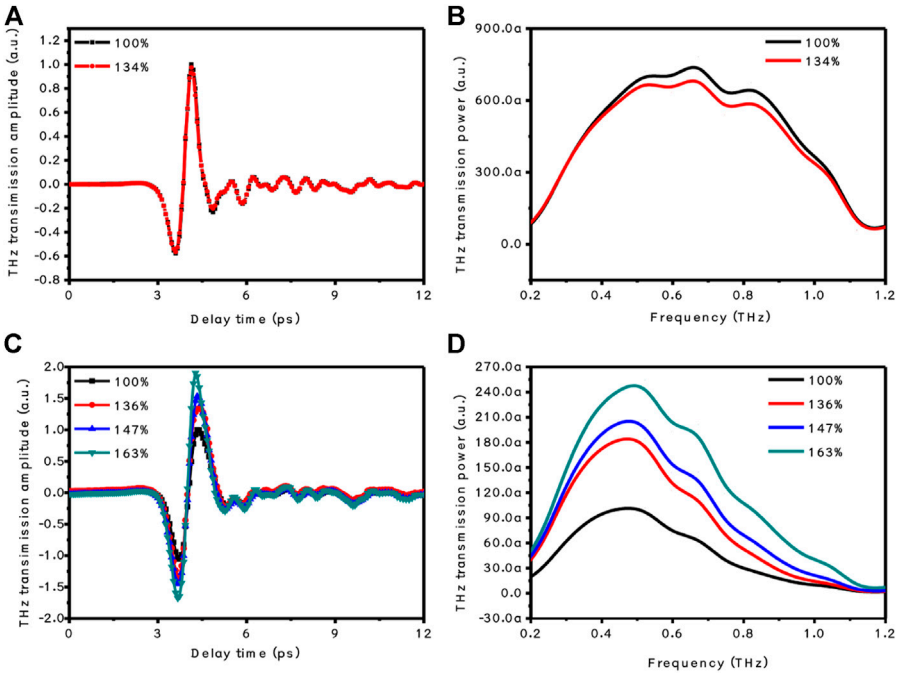

FIGURE 3 | (A) Terahertz time-domain spectra of samples without MXene coating on a PVAc substrate under tensile and non-tensile conditions. **(B)** Terahertz time-domain spectra of samples coated with MXene on PVAc substrate under different tensile degrees. **(C)** Terahertz frequency-domain spectra of samples without MXene coating on PVAc substrate under tensile and non-tensile conditions. **(D)** Terahertz frequency-domain spectra of samples coated with MXene on PVAc substrate under different tensile degrees.

that was coated with MXene reduced the transmission peak of the THz wave by approximately 80%. As shown in **Figure 2B**, the transmission frequency spectrum of the terahertz wave shows a major transmission difference before and after spin coating of the MXene material. This shows that the MXene has a very high absorbing capacity. At the same time, a sponge material was also used as a sample substrate in an additional experiment, with results as shown in **Figures 2C,D**. The results obtained are similar to those for the PVAc substrate.

The tensile results for the PVAc substrate are shown in **Figure 3A**. These results show that the substrate self-stretching has little effect on the THz transmission. **Figure 3B** shows the terahertz transmission power spectrum of the PVAc under tension. When the substrate is stretched, the THz signal decreases slightly. The time-domain spectra of the MXene/PVAc(latex) structure are studied under different tensile degrees, with results as shown in **Figure 3C**. All the tensile percentages in this paper are calculated by the ratio of the length after stretching to the original length. When the degree of stretching is 136%, the transmission amplitude of the time-domain spectrum increases by more than 42%. When the tensile strength is 147%, the transmission amplitude then increases by more than 63%. When the tensile strength reaches 163%, the transmission amplitude then increases by more than 98%. **Figure 3D** shows the terahertz transmission power spectrum of the MXene/PVAc(latex) structure under different degrees of stretching. When the tensile strength increases, the transmission of the THz intensity also increases obviously. When the tensile strength reaches 163%, the modulation of the transmission strength is approximately 281%.

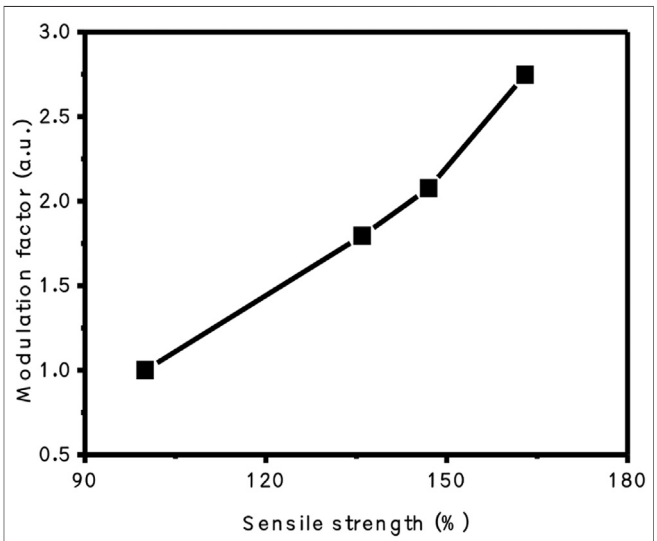

FIGURE 4 | Modulation factor (MF) of samples versus different tensile strengths.

To evaluate the modulation performance of the sample, the modulation factor (*MF*) is introduced and is defined as the change in the integrated terahertz power emission caused by the light excitation intensity:

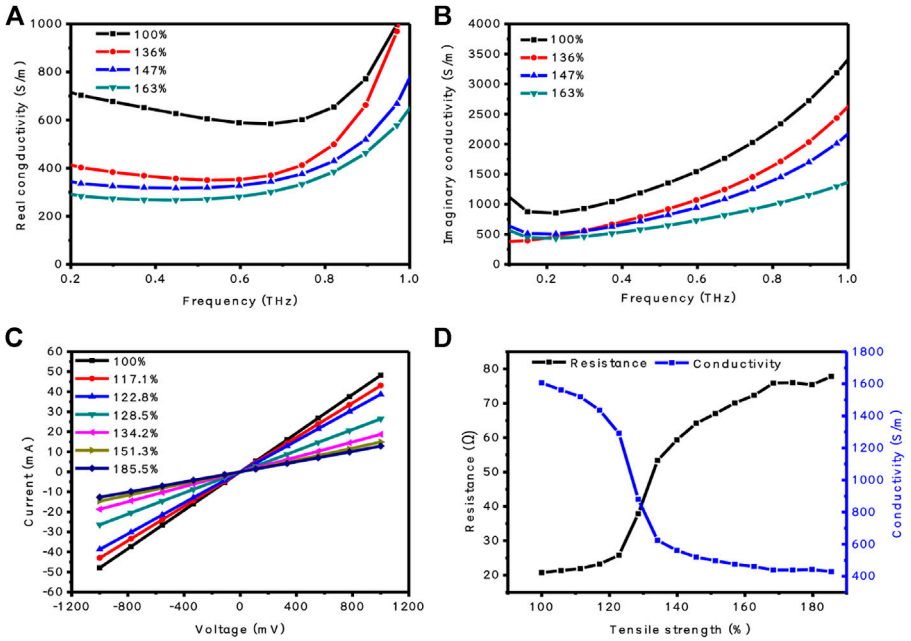

FIGURE 5 | (A) Change in the real part of the conductivity of samples at different tensile degrees. **(B)** Change in the imaginary part of the conductivity of samples excited by different tensile degrees. **(C)** I-V diagram for electrical characterization of samples at different tensile degrees. **(D)** Relationship between the resistance and conductivity of the sample with respect to the tensile degree during electrical characterization.

$$MF = \frac{\int P_{\mathrm{lax}}(\omega)\mathrm{d}\omega - P_{\mathrm{stretch}}(\omega)\mathrm{d}\omega}{\int P_{lax}(\omega)\mathrm{d}\omega}. \quad (1)$$

$P_{\mathrm{lax}}(\omega)\mathrm{d}\omega$ and $P_{\mathrm{stretch}}(\omega)\mathrm{d}\omega$ are the powers of the terahertz signal in the relaxed state and the stretched state, respectively. **Figure 4** shows the dependence of the MF on the tensile strength. When the tensile strength was 136%, MF increased by 1.96. When the tensile strength reaches 147%, MF increases to 2.12. When the tensile strength reaches 163%, MF increases to 2.81. The change range of MF also increases with the increase of tensile strength. Due to the limitation of material properties, the limit of tensile strength is about 170%. If the tensile degree exceeds this limit, the damage to the substrate cannot be recovered.

To explain the modulation mechanism in further depth, the variations in the conductivity of the samples with the tensile degree have been calculated. From these calculations, we can extract the transient frequency-dependent complex conductivity from the time-domain data of the transmitted THz pulses, denoted by $E_{\mathrm{strentch}}(\omega)$ and $E_{\mathrm{non\text{-}strentch}}(\omega)$. The transmission ratio $T(\omega)$ of the Fourier transform of these two wave forms is related to the complex conductivity as follows [39]:

$$T_{(\omega)} = \frac{\tilde{E}_{\mathrm{stretch}}(\omega)}{\tilde{E}_{\mathrm{non-stretch}}(\omega)} = \frac{n+1}{n+1+Z_0 d\tilde{\sigma}(\omega)}, \quad (2)$$

Where $Z_0 = 377\ \Omega$ is the impedance of free space, $n = 1.5$ is the refractive index of the non-stretch PVAc substrate within the THz range, and d is the thickness of the MXene coating, which is estimated to be 150 μm from the results in **Figure 1B**. **Figures 5A,B** show the real part $\sigma_{\mathrm{r}}(\omega)$ and the imaginary part $\sigma_{\mathrm{i}}(\omega)$ of the conductivity of Mxene coating under different tensile degrees, respectively. Because the THz signal is strongly attenuated by the modulators, the calculation results in the higher and lower frequency ranges are not reliable, and thus we have only presented data measured between 0.1 and 1.0 THz in **Figures 5A,B**. To make the TDS calculations more scientifically accurate, the electrical experiment was performed as a reference group, with results as shown in **Figure 5C**. The relationship between the resistance and the degree of stretching is derived from the *I-V* diagram using the relationship among the current, the voltage and the resistance. The black curve in **Figure 5D** shows the variation in the resistance of the sample with the degree of drawing, while the blue curve shows the variation in the conductivity of the sample with the degree of drawing. The figure shows that the sample's resistance increases as the tensile strength increases and the sample's conductivity decreases as the tensile strength increases. The increase of the tensile strength from 100 to 136% is also shown to have a significant effect on the modulation of the tensile strength; at 147 and 163%, the stretching degree has little effect on the modulation. This is consistent with the peak modulation and the *MF* of the terahertz radiation time-domain spectrum.

CONCLUSION

A flexible broadband terahertz modulator based on a strain-sensitive MXene/PVAc(latex) material is reported. It is found that the MXene can absorb nearly 80% of the THz waves through testing of sponge and latex substrate-based samples. The results obtained show that the transmission rate of the THz signal increases with increases in the

degree of stretching. When the stretching degree reaches 136, 147 and 163%, the terahertz time-domain spectrum signals are modulated by 42, 67 and 98%, respectively. The maximum modulation of the terahertz projection power spectrum reaches 281%. Through an analysis based on THz TDS and comparison of the electrical properties of the samples, it is concluded that the conductivity of each sample decreases with increasing tensile strength. In addition, the trends for both properties are the same and the order of magnitude remains consistent. The results show that MXene is a type of terahertz modulator that can modulate the terahertz transmission signal intensity of a sample effectively by stretching that sample with a strong force to change the conductivity of the sample.

DATA AVAILABILITY STATEMENT

The raw data supporting the conclusion of this article will be made available by the authors, without undue reservation.

AUTHOR CONTRIBUTIONS

YL: Conceptualization, Methodology, Validation, Investigation, Writing-Original Draft; XL: Investigation; TY: Investigation; JL: Investigation; BL: Investigation; JS: Conceptualization, Funding acquisition; BZ: Supervision, Conceptualization, Writing-Reviewing and Editing, Funding acquisition; FW: Supervision, Conceptualization.

FUNDING

This research was supported by the National Natural Science Foundation of China (Grant No. 61505125), the Nature Science Foundation of Beijing (Grant No. 4202013), Youth Innovative Research Team of Capital Normal University and High-level Teachers in Beijing Municipal Universities in the Period of 13th Five–year Plan.

REFERENCES

1. Ferguson B, and Zhang X-C (2002). Materials for Terahertz Science and Technology. *Nat Mater* 1(1):26–33. doi:10.1038/nmat708
2. Tonouchi M (2007). Cutting-edge Terahertz Technology. *Nat Photon* 1(2): 97–105. doi:10.1038/nphoton.2007.3
3. Padilla WJ, Cich MJ, Azad AK, Averitt RD, Taylor AJ, and Chen HT (2009). A Metamaterial Solid-State Terahertz Phase Modulator. *Nat Photon* 3(3):148. doi:10.1038/nphoton.2009.3
4. Chen H-T, Padilla WJ, Zide JMO, Gossard AC, Taylor AJ, and Averitt RD (2006). Active Terahertz Metamaterial Devices. *Nature* 444(7119):597–600. doi:10.1038/nature05343
5. Hendry E, Garcia-Vidal FJ, Martin-Moreno L, Rivas JG, Bonn M, Hibbins AP, et al. (2008). Optical Control over Surface-Plasmon-Polariton-Assisted THz Transmission through a Slit Aperture. *Phys Rev Lett* 100(12):123901. doi:10.1103/PhysRevLett.100.123901
6. Chen S, Fan F, Miao Y, He X, Zhang K, and Chang S (2016). Ultrasensitive Terahertz Modulation by Silicon-Grown MoS2nanosheets. *Nanoscale* 8(8): 4713–9. doi:10.1039/c5nr08101g
7. Wen Q-Y, Tian W, Mao Q, Chen Z, Liu W-W, Yang Q-H, et al. (2014). Graphene Based All-Optical Spatial Terahertz Modulator. *Sci Rep* 4:7409. doi:10.1038/srep07409
8. Mittendorff M, Li S, and Murphy TE. Graphene-based Waveguide-Integrated Terahertz Modulator. *ACS Photon* (2017). 4(2):316–21. doi:10.1021/acsphotonics.6b00751
9. Lai W, Huang P, Pelaz B, Pino Pd., and Zhang Q. Enhanced All-Optical Modulation of Terahertz Waves on the Basis of Manganese Ferrite Nanoparticles. *J Phys Chem C* (2017). 121(39):21634–40. doi:10.1021/acs.jpcc.7b07756
10. Weis P, Garcia-Pomar JL, Höh M, Reinhard B, Brodyanski A, and Rahm M (2012). Spectrally Wide-Band Terahertz Wave Modulator Based on Optically Tuned Graphene. *ACS Nano* 6(10):9118–24. doi:10.1021/nn303392s
11. Liang GZ, Hu XN, Yu XH, Shen YD, Li LH, Davies AG, et al. (2015). Integrated Terahertz Graphene Modulator with 100% Modulation Depth. *ACS Photon* 2(11):1559–66. doi:10.1021/acsphotonics.5b00317
12. Lu M, Li W, and Brown ER (2011). Second-order Bandpass Terahertz Filter Achieved by Multilayer Complementary Metamaterial Structures. *Opt Lett* 36(7):1071. doi:10.1364/OL.36.001071
13. Harrison H, Lancaster AJI, Konoplev V, Doucas G, Aryshev A, Shevelev M, et al. (2017). The Design of a Non-destructive Single-Shot Longitudinal Bunch Profile Monitor Using Smith-purcell Radiation. *Rev Sci Instrum* 89:035116. doi:10.18429/JACoW-IPAC2017-MOPAB128
14. Ren L, Pint CL, Booshehri LG, Rice WD, Wang X, Hilton DJ, et al. (2009). Carbon Nanotube Terahertz Polarizer. *Nano Lett* 9(7):2610–3. doi:10.1021/nl900815s
15. He X, Zhang Q, Lu G, Ying G, Wu F, and Jiang J (2016). Tunable Ultrasensitive Terahertz Sensor Based on Complementary Graphene Metamaterials. *RSC Adv* 6(57):52212–8. doi:10.1007/s12200-016-0563-x10.1039/c5ra21974d
16. Grady NK, Heyes JE, Chowdhury DR, Zeng Y, Reiten MT, Azad AK, et al. (2013). Terahertz Metamaterials for Linear Polarization Conversion and Anomalous Refraction. *Science* 340(6138):1304–7. doi:10.1126/science.1235399
17. Xiao S, Wang T, Jiang X, Yan X, Cheng L, Wang B, et al. (2017). Strong Interaction Between Graphene Layer and Fano Resonance in Terahertz Metamaterials. *J Phys D: Appl Phys* 50(9):195101. doi:10.1088/1361-6463/aa69b1
18. Ji H, Zhang B, Wang W, Lv L, and Shen J (2018). Ultraviolet Light-Induced Terahertz Modulation of an Indium Oxide Film. *Opt Express* 26(6):7204. doi:10.1364/oe.26.007204
19. Hong JT, Park J-Y, Lee S, and Ahn YH (2016). UV-induced Terahertz Wave Modulation in Free-Standing ZnO Nanowire Films. *Opt Mater Express* 6(12): 3751. doi:10.1364/OME.6.003751
20. Huang Z, Hao Y, Li Y, Hu H, Wang C, Nomoto A, et al. (2018). Three-dimensional Integrated Stretchable Electronics. *Nat Electron* 1(8):473–80. doi:10.1038/s41928-018-0116-y
21. Mohammed MG, and Kramer R (2017). All-Printed Flexible and Stretchable Electronics. *Adv Mater* 29(19):1604965. doi:10.1002/adma.201604965
22. Yang W, Feng Y, Si Q, Yan Q, Long P, Dong L, et al. (2019). Efficient Cycling Utilization of Solar-thermal Energy for Thermochromic Displays with Controllable Heat Output. *J Mater Chem A* 7(1):97–106. doi:10.1039/C8TA05333B
23. Zhu B, Gong S, and Cheng W (2019). Softening Gold for Elastronics. *Chem Soc Rev* 48(6):1668–711. doi:10.1039/c8cs00609a
24. Wang Y, Gong S, Wang SJ, Yang X, Ling Y, Yap LW, et al. (2018). Standing Enokitake-like Nanowire Films for Highly Stretchable Elastronics. *ACS Nano* 12(10):9742–9. doi:10.1021/acsnano.8b05019
25. Xiao D, Zhu M, Sun L, Zhao C, Wang Y, Tong Teo EH, et al. (2019). Flexible Ultra-wideband Terahertz Absorber Based on Vertically Aligned Carbon Nanotubes. *ACS Appl Mater Inter* 11(46):43671–80. doi:10.1021/acsami.9b14428
26. Suzuki D, Oda S, and Kawano Y (2016). A Flexible and Wearable Terahertz Scanner. *Nat Photon* 10(12):809–13. doi:10.1038/nphoton.2016.209
27. Cong L, Xu N, Gu J, Singh R, Han J, and Zhang W (2014). Highly Flexible Broadband Terahertz Metamaterial Quarter-Wave Plate. *Laser Photon Rev* 8(4):626–32. doi:10.1002/lpor.201300205
28. Shi Q, Tian K, Zhu H, Li Z-R, Zhu L-G, Deng H, et al. (2020). Flexible and Giant Terahertz Modulation Based on Ultra-strain-sensitive Conductive Polymer Composites. *ACS Appl Mater Inter* 12(8):9790–6. doi:10.1021/acsami.9b21890

29. Xia Y, Mathis TS, Zhao M-Q, Anasori B, Dang A, Zhou Z, et al. (2018). Thickness-independent Capacitance of Vertically Aligned Liquid-Crystalline MXenes. *Nature* 557(7705):409–12. doi:10.1038/s41586-018-0109-z
30. Lukatskaya MR, Kota S, Lin Z, Zhao M-Q, Shpigel N, Levi MD, et al. (2017). Ultra-high-rate Pseudocapacitive Energy Storage in Two-Dimensional Transition Metal Carbides. *Nat Energ* 2(8):17105. doi:10.1038/nenergy.2017.105
31. Yan J, Ren CE, Maleski K, Hatter CB, Anasori B, Urbankowski P, et al. (2017). Flexible MXene/Graphene Films for Ultrafast Supercapacitors with Outstanding Volumetric Capacitance. *Adv Funct Mater* 27(30):1701264. doi:10.1002/adfm.201701264
32. Zhao M-Q, Torelli M, Ren CE, Ghidiu M, Ling Z, Anasori B, et al. (2016). 2D Titanium Carbide and Transition Metal Oxides Hybrid Electrodes for Li-Ion Storage. *Nano Energy* 30:603–13. doi:10.1016/j.nanoen.2016.10.062
33. Xu Z, Liu G, Ye H, Jin W, and Cui Z (2018). Two-dimensional MXene Incorporated Chitosan Mixed-Matrix Membranes for Efficient Solvent Dehydration. *J Membr Sci* 563:625–32. doi:10.1016/j.memsci.2018.05.044
34. Ren CE, Hatzell KB, Alhabeb M, Ling Z, Mahmoud KA, and Gogotsi Y (2015). Charge- and Size-Selective Ion Sieving through Ti3C2Tx MXene Membranes. *J Phys Chem Lett* 6(20):4026–31. doi:10.1021/acs.jpclett.5b01895
35. Muckley ES, Naguib M, Wang H-W, Vlcek L, Osti NC, Sacci RL, et al. (2017). Multimodality of Structural, Electrical, and Gravimetric Responses of Intercalated MXenes to Water. *ACS Nano* 11(11):11118–26. doi:10.1021/acsnano.7b05264
36. Choi G, Shahzad F, Bahk Y-M, Jhon YM, Park H, Alhabeb M, et al. (2018). Enhanced Terahertz Shielding of MXenes with Nano-Metamaterials. *Adv Opt Mater* 6(5):1701076. doi:10.1002/adom.201701076
37. Jhon YI, Koo J, Anasori B, Seo M, Lee JH, Gogotsi Y, et al. (2017). Metallic MXene Saturable Absorber for Femtosecond Mode-Locked Lasers. *Adv Mater* 29(40):1702496. doi:10.1002/adma.201702496
38. Jhon YI, Seo M, and Jhon YM (2018). First-principles Study of a MXene Terahertz Detector. *Nanoscale* 10(1):69–75. doi:10.1039/C7NR05351G
39. He T, Zhang B, Wang G-c., Zang M-d., Hou Y-b., and Shen J-l. (2016). High Efficiency THz-Wave Modulators Based on Conjugated Polymer-Based Organic Films. *J Phys D: Appl Phys* 49(7):075111. doi:10.1088/0022-3727/49/7/075111

Conflict of Interest: The authors declare that the research was conducted in the absence of any commercial or financial relationships that could be construed as a potential conflict of interest.

frontiers in Physics

ORIGINAL RESEARCH
published: 31 August 2021
doi: 10.3389/fphy.2021.736831

Longitudinal Component Properties of Circularly Polarized Terahertz Vortex Beams

Miao Wang, Xinke Wang, Peng Han, Wenfeng Sun, Shengfei Feng, Jiasheng Ye and Yan Zhang*

Department of Physics, Beijing Key Lab for Metamaterials and Devices, Capital Normal University, Beijing, China

A circularly polarized vortex beam possesses similar focusing properties as a radially polarized beam. This type of beam is highly valuable for developing optical manufacturing technology, microscopy, and particle manipulation. In this work, a left-hand circularly polarized terahertz (THz) vortex beam (CPTVB) is generated by utilizing a THz quarter wave plate and a spiral phase plate. Focusing properties of its longitudinal component E_z are detailedly discussed on the simulation and experiment. With reducing the F-number of the THz beam and comparing with a transverse component E_x of a general circularly polarized THz beam, the simulation results show that the focal spot size and intensity of its E_z component can reach 87 and 50% of E_x under a same focusing condition. In addition, the experimental results still demonstrate that the left-hand CPTVB can always maintain fine E_z focusing properties in a broad bandwidth, which manifest the feasibility of this class of THz beams.

Keywords: terahertz, circularly polarized vortex beam, longitudinal component, focusing properties, dispersive characteristics

OPEN ACCESS

Edited by:
Yiqi Zhang,
Xi'an Jiaotong University, China

Reviewed by:
Dong Mao,
Northwestern Polytechnical University, China
Tongyi Zhang,
Xian Institute of Optics and Precision Mechanics (CAS), China
Zuanming Jin,
University of Shanghai for Science and Technology, China

****Correspondence:***
Xinke Wang
wxk82721@cnu.edu.cn

Specialty section:
This article was submitted to Optics and Photonics, a section of the journal Frontiers in Physics

Received: *05 July 2021*
Accepted: *18 August 2021*
Published: *31 August 2021*

Citation:
Wang M, Wang X, Han P, Sun W, Feng S, Ye J and Zhang Y (2021) Longitudinal Component Properties of Circularly Polarized Terahertz Vortex Beams. Front. Phys. 9:736831. doi: 10.3389/fphy.2021.736831

INTRODUCTION

As the maturation of terahertz (THz) technology, this kinds of far-infrared sensing and imaging methods have gradually presented powerful application values in many research and industrial fields [1, 2]. Recently, investigations and applications of THz special beams have obviously become a hot spot and attracted growing attention. Taking advantages of their distinctive diffraction characteristics, all kinds of special beams have been successfully applied in THz imaging [3], THz communications [4], electron acceleration [5], and so on. In 2006, Zhan Q. W. theoretically proposed that the longitudinal electric field component of a circularly polarized vortex beam is analogous to that of a radially polarized beam, which possesses a sharper focal spot [6]. In 2016, our report experimentally verified the properties of this kind of optical beam in the THz waveband and pointed out its application prospects in THz microscopy and particle acceleration [7]. In 2017, Minasyan A. et. al designed a space-variant birefringent slab to achieve a circularly polarized THz vortex beam (CPTVB) [8]. In 2019, Sirenko A. A. et. al demonstrated that modified broadband circularly polarized THz vortices can be utilized as a spectroscopic probe of magnetism [9]. In 2021, Sobhani H. theoretically discussed the creation of a THz pulse carrying orbital angular momentum *via* beating twisted laser pulses in the plasma [10]. Apparently, the generation methods and characteristics of CPTVBs have gained more and more attention. Compared to a radially polarized THz beam, a CPTVB can be more easily produced and modulated by using a THz quarter wave plate (TQWP) and a spiral phase plate (SPP). Therefore, a further study on longitudinal component features of a CPTVB is valuable for improving the performances of current THz systems.

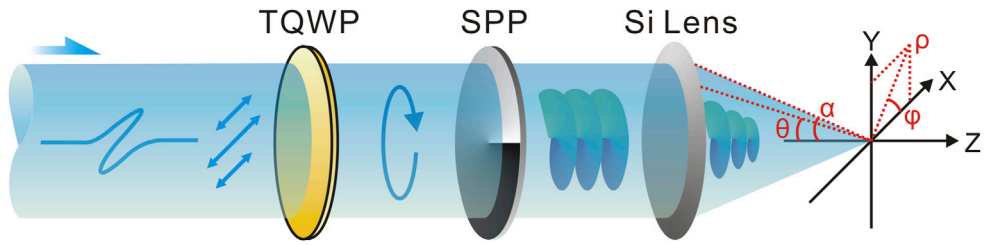

FIGURE 1 | Schematic diagram of a circularly polarized THz vortex beam (CPTVB). TQWP: THz quarter wave plate; SPP: spiral phase plate.

In this paper, we compared focusing properties of the longitudinal component of a CPTVB and the transverse component of a general circularly polarized THz beam on the simulation and experiment. Under different focusing conditions, evolutions of their focal spots are presented and analyzed. Besides, the dispersive characteristics of the longitudinal component of a CPTVB produced by using a TQWP and a SPP are also observed and discussed.

SIMULATION

Firstly, we present and analyze the field distributions of CPTVBs on the simulation. **Figure 1** gives the schematic diagram of a CPTVB generated by a TQWP and a SPP. The incident THz wave with a x-linear polarization illuminates a TQWP to possess a circular polarization. Then, the circularly polarized THz beam carries a spiral wave front after passing through a SPP. To generate a strong longitudinal electric field component, a high resistivity silicon (Si) lens is adopted to focus the THz beam. Here, a modified Richards-Wolf integration algorithm is utilized to simulate vector THz field components [11]. In the high-aperture aplanatic focusing system, the focal spot is located at a sufficient distance away from the aperture. Then, vector components of a THz vortex beam in a homogeneous dielectric medium near the focus can be written as

$$E(\rho,\varphi,z) = -jkf\int_0^{\alpha} Q(\rho,\varphi,\theta)q(\theta)d\theta, \tag{1}$$

where (ρ,φ,z) is the cylindrical coordinate on an observation plane, $k = 2\pi/\lambda$ is the wave number in the vacuum, λ is the wavelength of the incident THz beam, f is the focal length of the Si lens, θ is the angle between the converging THz beam and the z axis, α is the maximum value of θ. $q(\theta)$can be described as $q(\theta) = \sqrt{\cos\theta}\sin\theta\exp(jkz\cos\theta)$, which is related to the pupil apodization function of the focusing system. The expression of $Q(\rho,\varphi,\theta)$ depends on the incident THz polarization. When the incident THz field possesses a circular polarization, $Q(\rho,\varphi,\theta)$ can be written as

$$Q(\rho,\varphi,\theta) = \frac{1}{\sqrt{2}}j^m\exp(jm\varphi) \times \begin{bmatrix} J_m(t) + \frac{1}{2}\left[J_m(t) + B_m^{EE}(t,\varphi)\right](\cos\theta - 1) \\ \mathrm{sgn}(p)j\left\{J_m(t) + \frac{1}{2}\left[J_m(t) - B_m^{EE}(t,\varphi)\right](\cos\theta - 1)\right\} \\ -B_m^{E}(t,\varphi)\sin\theta \end{bmatrix} \tag{2}$$

where m is the topological charge of the SPP, sgn (p) is the sign of the input polarization, $J_m(t)$ is the Bessel function of the first kind and $t = k\rho\sin\theta$. In addition,

$$B_m^{EE}(t,\varphi) = -\exp(\mathrm{sgn}(p)j2\varphi)J_{m+\mathrm{sgn}(p)2}(t), \tag{3}$$

$$B_m^{E}(t,\varphi) = \mathrm{sgn}(p)jexp(\mathrm{sgn}(p)j\varphi)J_{m+\mathrm{sgn}(p)1}(t). \tag{4}$$

In the initial simulation, these parameters are set as $\lambda = 400\mu m$ (corresponding to 0.75 THz), $f = 20$ mm, $\alpha = 26.56^{\circ}$, $\mathrm{sgn}(p) = 1$ (corresponding to a left-hand circular polarization). By using **Eqs. 1–4**, the polarization components E_x and E_z of a left-hand CPTVB with $m = 0$ are simulated and presented on the focal plane, as shown in **Figures 2A,B** and **Figures 2E,F**. **Figures 2A,B** give the amplitude and phase distributions of E_x. **Figures 2E,F** show the amplitude and phase patterns of E_z. When $m = 0$, the CPTVB is just a general circularly polarized THz beam. Therefore, E_x shows a typical focal spot and its phase nearly exhibits a flat plane near the focal spot. Meanwhile, the E_z component presents a vortex pattern, including a doughnut-shaped amplitude and a spiral phase in a clockwise direction. These phenomena can be easily explained. With a circular polarization, longitudinal components E_z can be simultaneously generated on both X-Z and Y-Z planes and a $\pi/2$ phase difference exists between them, so the interference between them results in the E_z morphology of the CPTVB with $m = 0$. When the topological charge of the SPP is set as $m = -1$, a spiral phase modulation is introduced into the THz beam. In this case, the E_x and E_z components are simulated and presented in **Figures 2C,D** and **Figures 2G,H**. It can be seen that E_x shows a ring-shaped amplitude and a spiral phase in a counterclockwise direction, as shown in **Figures 2C,D**. In **Figures 2G,H** the E_z amplitude exhibits a main focal spot as well as some weak annular side-lobes and the E_z phase is composed of a series of concentric rings. On the interfaces between adjacent ring-shaped phases, there are always a π phase jump. To understand the features of the E_z component, a normalized left-hand circularly polarized THz beam can be expressed as [6].

$$\mathbf{E}_{LHC} = \exp(j\varphi)\left(\mathbf{e}_r + j\mathbf{e}_\varphi\right)/\sqrt{2}, \tag{5}$$

where $\mathbf{e}_r$ and $\mathbf{e}_\varphi$ are the unit vectors on radial and azimuthal directions. When a spiral phase modulation with $m = -1$ is loaded on the THz beam, the original spiral phase term $\exp(j\varphi)$ is eliminated and the THz field can be expressed as

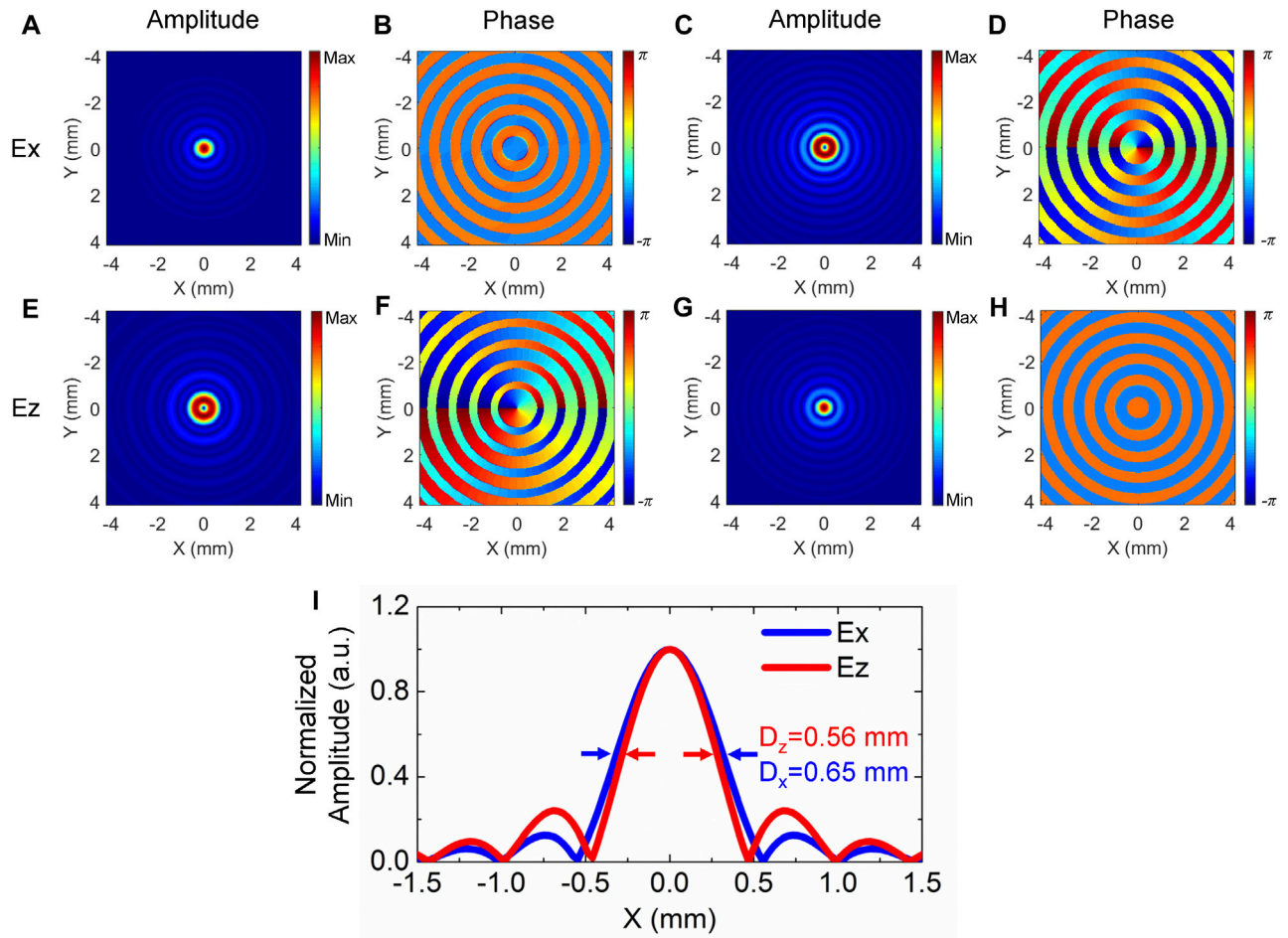

FIGURE 2 | (A,E) Amplitude and **(B,F)** phase patterns of E_x and E_z for a left-hand CPTVB with $m = 0$. **(C,G)** Amplitude and **(D,H)** phase distributions of E_x and E_z for a left-hand CPTVB with $m = -1$. **(I)** Normalized amplitude profile curves of E_x with $m = 0$ and E_z with $m = -1$. These curves are extracted from **(A)** and **(G)**, respectively.

$$\mathbf{E} = \left(\mathbf{e}_r + j\mathbf{e}_\varphi\right)/\sqrt{2}. \tag{6}$$

Then, the THz beam can be considered as a linear superposition of the $\mathbf{e}_r$ and $\mathbf{e}_\varphi$ components. When the THz beam is focused, the $\mathbf{e}_\varphi$ component cannot induce a longitudinal electric field component, so the formation of E_z completely arises from the contribution of the $\mathbf{e}_r$ component [12]. Therefore, the E_z distribution features of the left-hand CPTVB with $m = -1$ are very similar to the longitudinal component of a radially polarized THz beam. These simulation results are very consistent with our previous report [7].

In addition, it should be noted that a right-hand circularly polarized THz beam can be also used to generate a sharp real focus of E_z in a similar manner. When a spiral phase modulation with $m = 1$ is loaded on a THz beam with a right-hand circular polarization, the constructive interference of E_z is fulfilled on the optical axis and a focal spot of E_z is formed. However, E_z suffers from destructive interference when a spiral phase modulation with $m = -1$ is loaded on a right-hand circularly polarized THz beam. In that case, the E_z component will present a vortex pattern with a topological charge of −2. The related discussions have been reported in our previous work [7].

The most important property of a converging radially polarized beam is that the focal spot size of its E_z component is smaller than that of the E_x component of a general focused beam with a same F-number, which is very valuable for optical microscopy [13] and particle acceleration [5]. Herein, we compare the focal spot sizes of E_z with $m = -1$ and E_x with $m = 0$ for left-hand CPTVBs. The amplitude profiles of E_z with $m = -1$ and E_x with $m = 0$ are separately extracted along the x axis from **Figures 2A,G**. Their normalized curves are plotted and compared, as shown in **Figure 2I**. The full width half maximum (FWHM) D_z and D_x of E_z and E_x are marked by red and blue arrows, which are 0.56 and 0.65 mm, respectively. It clearly manifests that a CPTVB can be utilized to form a smaller focal spot.

To further analyze E_z properties of a CPTVB, the focal length f is varied from 10 to 80 mm and other parameters are fixed in the simulation. The amplitude patterns of E_x with $m = 0$ and E_z with $m = -1$ of left-hand CPTVBs are simulated and their amplitude profiles are extracted along the x axis. **Figures 3A,B** exhibit the

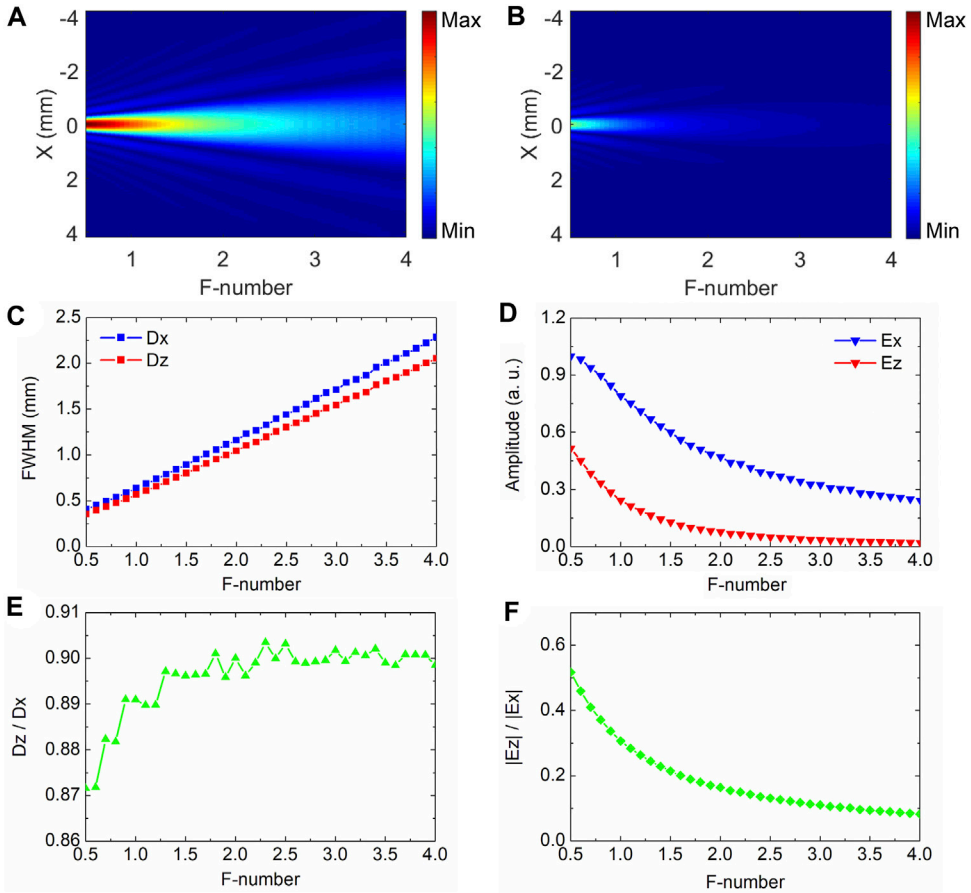

FIGURE 3 | Variations of amplitude profiles with different F-numbers for **(A)** E_x with $m = 0$ and **(B)** E_z with $m = -1$ of left-hand CPTVBs. **(C)** and **(E)** give the variation tendencies of the FWHMs D_x and D_z of E_x and E_z and their ratio D_z/D_x with varying the F-number. **(D)** and **(F)** exhibit the evolution trends of E_x and E_z amplitude peaks and their ratio $|E_z|/|E_x|$ with adjusting the F-number.

amplitude profile distributions of E_x and E_z along different F-numbers. Obviously, their common points are that the focal spot sizes of E_x and E_z monotonically enlarge and their intensities progressively attenuate with increasing the F-number. To more intuitively observe the variation tendencies of their focal spots, the FWHMs D_x and D_z of E_x and E_z are extracted and plotted in **Figure 3C**. D_x and D_z vary from 0.40 mm and 0.35 mm to 2.28 mm and 2.05 mm with adjusting the F-number from 0.5 to 4. Meanwhile, it is apparent that D_z is always smaller than D_x with different F-numbers. In addition, the ratio of D_z to D_x is also calculated and exhibited in **Figure 3E**, which alters from 0.87 to 0.90 with changing the F-number from 0.5 to 4. It can be found that the ratio almost remains unchanged with decreasing the F-number from 4 to 1.5 and it sharply reduces when the F-number is less than 1.5. Besides, intensities of E_x and E_z with different F-numbers are also compared and analyzed. **Figure 3D** gives the variations of the E_x and E_z amplitude peaks at $x = 0$ with changing the F-number. It should be noted that both E_x and E_z amplitudes are normalized to the E_x amplitude peak. It can be observed that both E_x and E_z amplitudes monotonically enhance with decreasing the F-number and the evolution trend of E_z is more pronounced when the F-number is less than 1.5. The ratio $|E_z|/|E_x|$ of the E_x and E_z amplitudes is also calculated and shown in **Figure 3F**, which shows that the proportion of E_z is more and more significant with reducing the F-number and can approach 50% with the F-number of 0.5. According to these simulation results, it indicates that a focusing condition with a smaller F-number is essential for acquiring a E_z focal spot with a smaller size and a higher intensity.

EXPERIMENT

On the experiment, CPTVBs are also achieved and analyzed. A THz focal-plane imaging system is applied to characterize the features of CPTVBs, as shown in **Figure 4**. A Spectra-Physics femtosecond laser amplifier (800 nm central wavelength, 35 fs pulse duration, 1 W average power, and 1 kHz repetition ratio) is used as the light source. The laser pulse is divided into the pump and probe beams by a half wave plate (HWP) and a polarization beam splitter (PBS) for exciting and detecting the THz wave. After passing through a motorized linear stage, the pump beam with a 990 mW average power is expanded by a concave lens L1 with a 50 mm focal length and is guided to illuminate a <110>

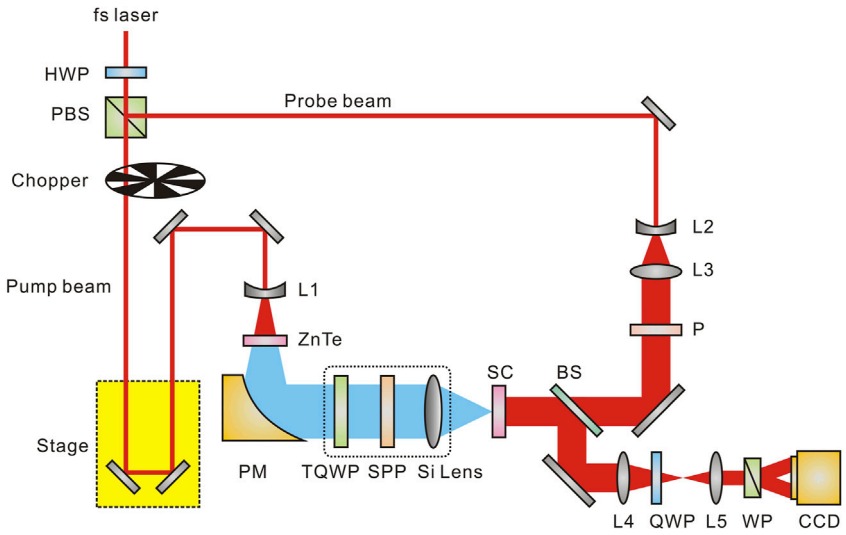

FIGURE 4 | Schematic diagram of a THz focal-plane imaging system.

ZnTe crystal with a 2 mm thickness. Then, the THz radiation with a linear polarization is generated by the optical rectification effect [14]. An axis-off parabolic mirror (PM) with a 100 mm focal length is utilized to collimate the THz beam. Herein, the diameter of the THz beam is approximately 20 mm. After successively transmitting through a TQWP, a SPP and a Si lens, a converging left-hand CPTVB is formed and is incident into the sensor crystal (SC). On the path of the probe beam, the laser pulse with a 10 mW average power is sequentially expanded and collimated by concave and convex lenses (L2 and L3) with focal lengths of 50 and 150 mm. The diameter of the probe beam roughly reaches 30 mm. A polarizer (P) is used to ensure the probe polarization and the probe beam is reflected onto the SC. In the SC, the two-dimensional THz information is modulated on the probe polarization by the linear electro-optic effect [15]. The probe beam carrying the THz information is reflected by the SC and a 50/50 non-polarizing beam splitter in sequence and is guided into the imaging module of the system, which is constituted of a lens group (L4 and L5), a quarter wave plate (QWP), a Wollaston prism (WP), and a CCD camera with a 4 Hz frame rate. The imaging module is applied to capture the image of the probe beam on the SC. A mechanical chopper is mounted in the pump beam to modulate the output frequency of the THz pulse and is synchronously controlled with the CCD camera. Dynamics subtraction and balanced electro-optic detection methods are adopted to remove the background intensity of the probe beam [16, 17] and a two-dimensional THz image is accurately extracted. By continuously adjusting the time delay between the pump and probe beams, a series of THz temporal images are measured and the Fourier transformation is operated on each pixel to acquire the THz spectral information. To suppress the background noise of the system, 25 frames are averaged at each temporal scan point. In this system, the effective imaging area is 12 mm × 12 mm and the size of a pixel is 57 μm.

To characterize the different polarization components of the THz beam, the SCs with various crystalline orientations are carefully selected. In the measurement, the probe polarization is always fixed as the horizontal direction. A <110> ZnTe with a 1 mm thickness is chosen to measure the transverse electric field E_x of the THz beam. To maximize the detection efficiency, the angle between the <001> direction of the crystal and the probe polarization is set as 0°. A <100> ZnTe with a 1 mm thickness is selected to acquire the longitudinal electric field E_z of the THz beam. The <010> direction of the crystal is tuned to 45° with respect to the probe polarization to optimize the detection efficiency [7].

To achieve a left-hand circularly polarized THz beam, a quartz TQWP (TYDEX Company, Russia) with a 400 μm central wavelength is applied. A Teflon SPP with a topological charge of −1 and a 400 μm central wavelength is used to impart a spiral phase modulation on the THz beam. Three Si lenses with focal lengths of 20 mm, 30 mm, 50 mm are separately picked up to produce the converging CPTVBs for comparing the features of E_z with different focusing conditions. On the focal plane, the E_x and E_z components of the left-hand CPTVBs are measured and analyzed by using the imaging system.

Figure 5 exhibits the comparison of the E_x and E_z components under different focusing conditions. **Figures 5A,D,G** give the amplitude distributions of the focal spots with f = 20 mm, 30 mm, 50 mm at 0.75 THz for E_x with m = 0 of left-hand CPTVBs. **Figures 5B,E,H** show the amplitude patterns of E_z with three different focal lengths at 0.75 THz on the focal plane for left-hand CPTVBs with m = −1. Obviously, the focal spot sizes of E_x and E_z are gradually magnified with increasing f. For clarity, their corresponding amplitude profile curves are extracted along the x axis. The normalized curves of E_x and E_z with f = 20 mm, 30 mm, 50 mm are plotted and compared, as shown in **Figures 5C,F,I**. When the focal length of the Si lens is 20 mm, the FWHMs D_x and D_z of E_x and E_z are 0.87 and 0.61 mm, respectively. When f is adjusted as 30 mm,

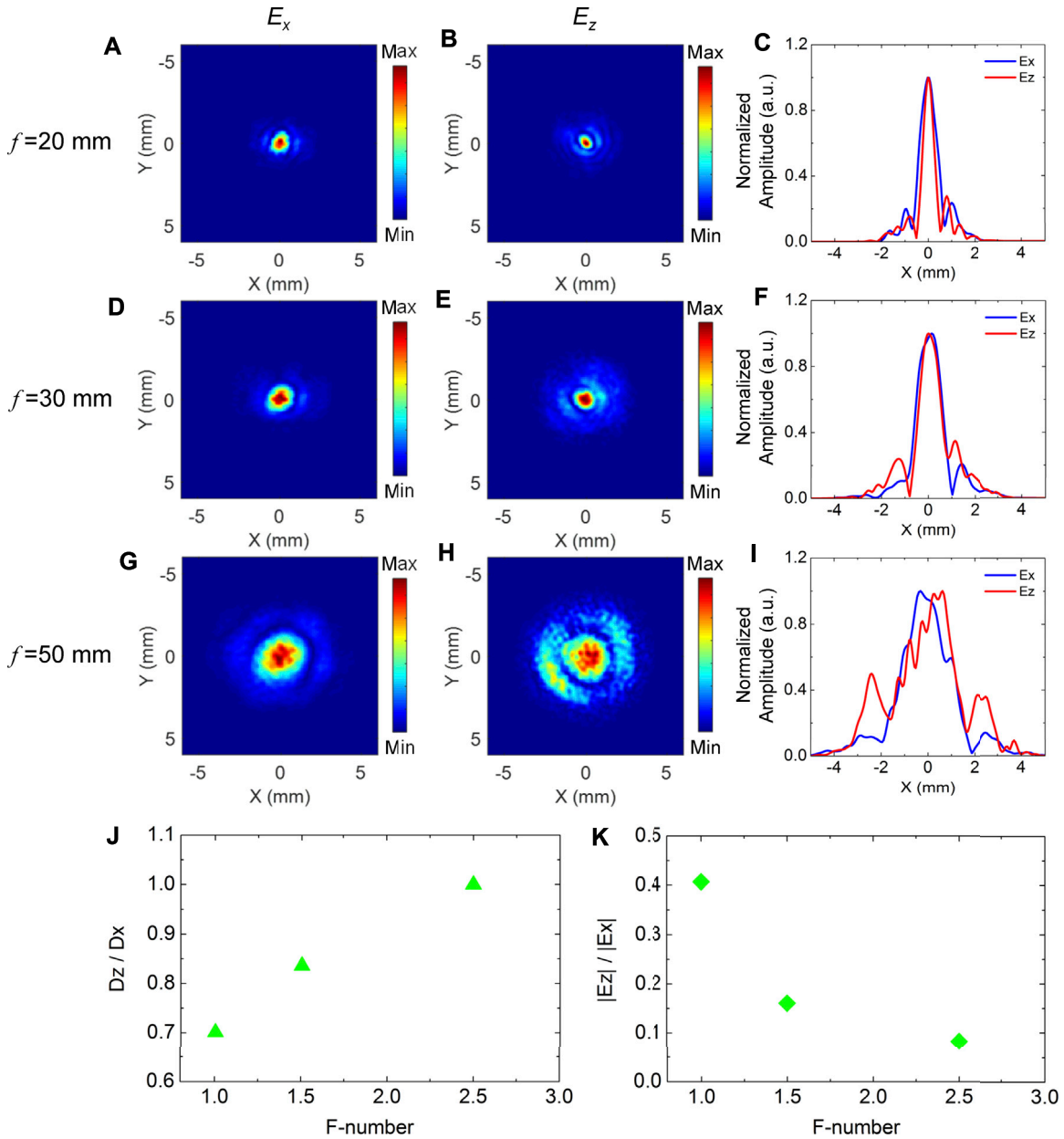

FIGURE 5 | Comparison of the transverse and longitudinal components under different focusing conditions. **(A)**, **(D)**, **(G)** and **(B)**, **(E)**, **(H)** separately present the amplitude distributions of the focal spots with focal lengths of 20 mm, 30 mm, 50 mm at 0.75 THz for E_x with $m = 0$ and E_z with $m = -1$ of left-hand CPTVBs. **(C)**, **(F)**, **(I)** give their corresponding normalized amplitude profile curves along the x axis **(J)** and **(K)** show the ratios of D_z/D_x and $|E_z|/|E_x|$ with varying the F-number, respectively.

D_x and D_z are 1.22 and 1.02 mm. When f is varied as 50 mm, both D_x and D_z are almost equal to 2.32 mm. Simultaneously, the side-lobes of E_z becomes more striking. Experimental results are mainly consistent with the simulation. When a CPTVB is more tightly focused, the E_z component with a smaller focal spot is formed. In addition, the focal spot size of E_z is always less than that of E_x. Some slight deviations between the experimental and simulation results are mainly attributed to the integral effect of the 1 mm-thick SCs [18] and other measurement errors. Besides, the ratios of D_z/D_x and $|E_z|/|E_x|$ are also calculated and exhibited in **Figures 5J,K**, which presents similar tendencies as the simulation results.

Moreover, the dispersive characteristics of the focal spots with different focal lengths are also checked for E_z with $m = -1$ of left-hand CPTVBs. From the measurement results of E_z, each spectral amplitude profile curves are extracted along the x axis. **Figures 6A–C** present the amplitude profile distributions of E_z with f = 20 mm, 30 mm, and 50 mm along different frequencies. In **Figures 6A,B**, it can be seen that E_z always possesses a clear real focus from 0.5 THz to 1.0 THz. With f =

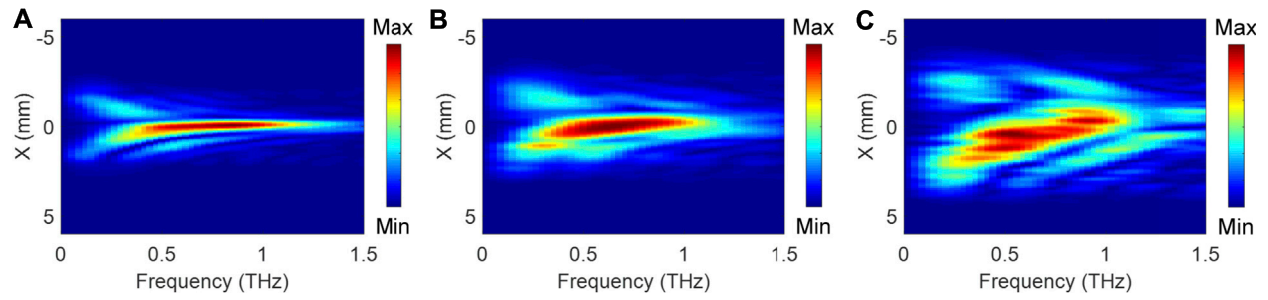

FIGURE 6 | Dispersive characteristics of the focal spots with f = 20 mm **(A)**, 30 mm **(B)**, and 50 mm **(C)** for the E_z components with m = −1 of left-hand CPTVBs.

50 mm, the focal spot gets blurred at frequencies away from 0.75 THz due to the weaker E_z component, as shown in **Figure 6C**. It manifests that a CPTVB can generate a fine converging E_z component with a broad bandwidth, although the modulation effects of the TQWP and SPP are the most perfect at the central wavelength.

CONCLUSION

In conclusion, the focusing properties of the E_z component are analyzed in detail for a converging CPTVB. The simulation and experimental results show that a CPTVB can form a real E_z focus when its topological charge is carefully adjusted. With reducing the F-number, the E_z component can get a sharper focal spot and a higher intensity. Particularly, the focal spot size of E_z is always less than that of the E_x component of a general circularly polarized THz beam with the same F-number. In addition, E_z can remain a fine focusing effect in a broad bandwidth for a CPTVB generated by a TQWP and a SPP. This work provides an effective avenue to produce a longitudinal THz polarization component with a smaller size and a stronger intensity. It can be expected that this class of CPTVBs will exhibit important application values for improving current THz inspection systems.

DATA AVAILABILITY STATEMENT

The original contributions presented in the study are included in the article/Supplementary Material, further inquiries can be directed to the corresponding author.

AUTHOR CONTRIBUTIONS

MW performed the research and wrote the paper. XW and YZ proposed the concept. PH, WS, SF, and JY supervised the project. All authors discussed the results and co-wrote the article.

FUNDING

This research was supported by the National Natural Science Foundation of China (61735002, 11774243, 11774246, and 11404224), Youth Innovative Research Team of Capital Normal University (008/20530290053, 008/19530050146, 008/18530500155), Connotative Development Foundation for Distinguished Young Talents in Capital Normal University (2055105), and Capacity Building for Sci-Tech Innovation-Fundamental Scientific Research Funds (008/20530290072, 008/19530050180, 025185305000/142).

REFERENCES

1. Tonouchi M. Cutting-Edge Terahertz Technology. *Nat Photon* (2007) 1: 97–105. doi:10.1038/nphoton.2007.3
2. Guerboukha H, Nallappan K, and Skorobogatiy M. Toward Real-Time Terahertz Imaging. *Adv Opt Photon* (2018) 10:843–938. doi:10.1364/AOP.10.000843
3. Bitman A, Moshe I, and Zalevsky Z. Improving Depth-Of Field in Broadband THz Beams Using Nondiffractive Bessel Beams. *Opt Lett* (2012) 37:4164–6. doi:10.1364/OL.37.004164
4. Hui X, Zheng S, Chen Y, Hu Y, Jin X, Chi H, et al. Multiplexed Millimeter Wave Communication with Dual Orbital Angular Momentum (OAM) Mode Antennas. *Sci Rep* (2015) 5:10148. doi:10.1038/srep10148
5. Nanni EA, Huang WR, Hong K-H, Ravi K, Fallahi A, Moriena G, et al. Terahertz-Driven Linear Electron Acceleration. *Nat Commun* (2015) 6:8486. doi:10.1038/ncomms9486
6. Zhan Q. Properties of Circularly Polarized Vortex Beams. *Opt Lett* (2006) 31: 867–9. doi:10.1364/OL.31.000867
7. Wang X, Shi J, Sun W, Feng S, Han P, Ye J, et al. Longitudinal Field Characterization of Converging Terahertz Vortices with Linear and Circular Polarizations. *Opt Express* (2016) 24:7178–90. doi:10.1364/OE.24.007178
8. Minasyan A, Trovato C, Degert J, Freysz E, Brasselet E, and Abraham E. Geometric Phase Shaping of Terahertz Vortex Beams. *Opt Lett* (2017) 42:41–4. doi:10.1364/OL.42.000041
9. Sirenko AA, Marsik P, Bernhard C, Stanislavchuk TN, Kiryukhin V, and Cheong S-W. Terahertz Vortex Beam as a Spectroscopic Probe of Magnetic Excitations. *Phys Rev Lett* (2019) 122:237401. doi:10.1103/PhysRevLett.122.237401
10. Sobhani H. Creation of Tunable Longitudinally Polarized Terahertz Pulse Carrying Orbital Angular Momentum. *Phys Lett A* (2021) 387:127011. doi:10.1016/j.physleta.2020.127011
11. Khonina SN, Kazanskiy NL, and Volotovsky SG. Vortex Phase Transmission Function as a Factor to Reduce the Focal Spot of High-Aperture Focusing System. *J Mod Opt* (2011) 58:748–60. doi:10.1080/09500340.2011.568710
12. Youngworth KS, and Brown TG. Focusing of High Numerical Aperture Cylindrical-Vector Beams. *Opt Express* (2000) 7:77–87. doi:10.1364/OE.7.000077

13. Huse N, Schönle A, and Hell SW. Z-Polarized Confocal Microscopy. *J Biomed Opt* (2001) 6:480–4. doi:10.1117/1.1417974
14. Löffler T, Hahn T, Thomson M, Jacob F, and Roskos HG. Large-Area Electro-Optic ZnTe Terahertz Emitters. *Opt Express* (2005) 13:5353–62. doi:10.1364/OPEX.13.005353
15. Wu Q, Litz M, and Zhang XC. Broadband Detection Capability of ZnTe Electro-Optic Field Detectorsfield Detectors. *Appl Phys Lett* (1996) 68:2924–6. doi:10.1063/1.116356
16. Jiang Z, Xu XG, and Zhang X-C. Improvement of Terahertz Imaging with a Dynamic Subtraction Technique. *Appl Opt* (2000) 39:2982–7. doi:10.1364/AO.39.002982
17. Wang X, Cui Y, Sun W, Ye J, and Zhang Y. Terahertz Real-Time Imaging with Balanced Electro-Optic Detection. *Opt Commun* (2010) 283:4626–32. doi:10.1016/j.optcom.2010.07.010
18. Wang S, Zhao F, Wang X, Qu S, and Zhang Y. Comprehensive Imaging of Terahertz Surface Plasmon Polaritons. *Opt Express* (2014) 22:16916–24. doi:10.1364/OE.22.016916

Conflict of Interest: The authors declare that the research was conducted in the absence of any commercial or financial relationships that could be construed as a potential conflict of interest.

Publisher's Note: All claims expressed in this article are solely those of the authors and do not necessarily represent those of their affiliated organizations, or those of the publisher, the editors and the reviewers. Any product that may be evaluated in this article, or claim that may be made by its manufacturer, is not guaranteed or endorsed by the publisher.

frontiers in Physics

TECHNOLOGY AND CODE
published: 03 September 2021
doi: 10.3389/fphy.2021.751205

Characterizing the Layer Structures of the Lacquerware From the Palace Museum by Terahertz Imaging in Reflection Geometry

Hongfei Zhang[1], *Yuanmeng Zhao*[1]*, *Chenyu Li*[2] *and Cunlin Zhang*[1]*

[1]Key Laboratory of Terahertz Optoelectronics, Ministry of Education, and Beijing Advanced Innovation Center for Imaging Technology, Department of Physics, Capital Normal University, Beijing, China, [2]Conservation Department, The Palace Museum, Beijing, China

Chinese lacquerware is an important invention of arts and crafts in China. In this study, Chinese lacquerware is characterized using terahertz reflectometric imaging. The lacquerware studied herein comprises an ornamental wood panel covered by multiple layers of lacquers to portray motifs. For characterizing lacquerware, a terahertz time-domain spectroscopic reflectometric imaging system is proposed. The role of the proposed terahertz imaging system in highlighting the interface between layers during stratigraphic buildup in reflection geometry is proved. The proposed system provides a universal method for assessing the structural information of lacquered objects in a contactless and non-invasive manner; moreover, it provides two-dimensional images, subsurface three-dimensional images, and stratigraphic images (b-scans) in a contactless and non-invasive manner. Using the proposed system, we examine the buried layers of the lacquerware, including faults in the wooden layer and damages in the lacquerware. Research shows the promising prospects of terahertz time-domain spectroscopic reflectometric imaging as a non-destructive detection technique suited to lacquerware.

Keywords: lacquerware, terahertz imaging, time-of-flight, b-scan, C-scan

OPEN ACCESS

Edited by:
Meng Chen,
Tsinghua University, Beijing, China

Reviewed by:
Xudong Liu,
Shenzhen University, Shenzhen, China
Jiaguo Liu,
Beijing Institute of Environmental Features, Beijing, China

***Correspondence:**
Yuanmeng Zhao
zhao.yuanmeng@cnu.edu.cn
Cunlin Zhang
cunlin_zhang@cnu.edu.cn

Specialty section:
This article was submitted to Optics and Photonics, a section of the journal Frontiers in Physics

Received: *31 July 2021*
Accepted: *23 August 2021*
Published: *03 September 2021*

Citation:
Zhang H, Zhao Y, Li C and Zhang C (2021) Characterizing the Layer Structures of the Lacquerware From the Palace Museum by Terahertz Imaging in Reflection Geometry. Front. Phys. 9:751205. doi: 10.3389/fphy.2021.751205

INTRODUCTION

Chinese lacquerware is an important invention of arts and crafts in China. It is used to create beautiful colored patterns on the surface of utensils. Traditional Chinese lacquerware, as ornamental artifacts, comprise several composite layers of lacquer and rank among the most important forms of expression in Chinese art. Generally, raw lacquer is applied onto utensil surfaces. Raw lacquer is obtained from lacquer trees and primarily comprises urushiol, laccase, gum, and water. By using raw lacquer as paint, the Chinese formulated different colors of paint gloriously. Moreover, lacquer has special functions such as moisture resistance, high temperature resistance, and corrosion resistance. Since the Neolithic Age, the Chinese have recognized the performance of lacquer and used it to paint utensils. During the Shang and Zhou Dynasties and the Ming and Qing Dynasties, the Chinese lacquerware technique witnessed continuous development and achieved a very high level. Deeply appreciated by people worldwide, Chinese lacquerware has had a great impact on worldwide arts and crafts. Scientific analysis of lacquer provides information on the constituent layer compositions and conditions and allows conservators to propose appropriate conservation measures. Standard approaches for visualizing the internal structure of artifacts include infrared reflectography and X-ray radiography technologies, often in conjunction with microscopic analysis of the cross-sections

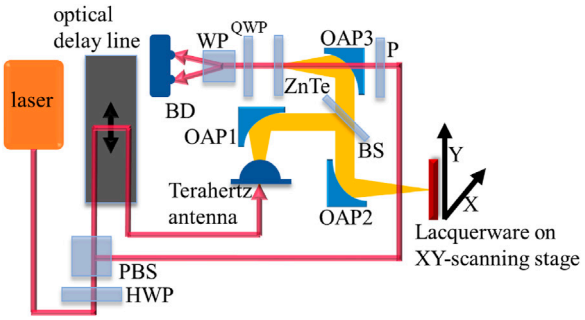

FIGURE 1 | Schematic of the experimental setup of the proposed THz-TDSRI system. HWP: Half-wave plate. PBS: Polarizing beam splitter. BS: THz beam splitter. P: Polarizer. QWP: Quarter-wave plate. WP: Wollaston prism. BD: Balance detector. OAP1, OAP2, OAP3: Off-axis parabolic mirror.

of the samples [1, 2]. However, current methods are still underdeveloped and fail at generating the three-dimensional view without damaging the lacquerware. Combining these methods with terahertz (THz) imaging can provide a universal method to enrich information about Chinese lacquerware.

THz radiation (1 THz = 10^{12} Hz) includes the frequencies in the range of 0.1–10 THz (wavelength: 0.3–3 mm). The terahertz time-domain spectroscopic reflectometric imaging (THz-TDSRI) system proposed in this study can depict 2D images as well as subsurface 3D images due to its ability to highlight the interface between layers for the stratigraphic buildup. This system provides stratigraphic images in a contactless and non-invasive manner; however, cross-sectioned samples could destroy the sample. Furthermore, as THz radiation is nonionizing because of its low photon energy (4.1 meV at 1 THz) and requires very low power levels (~1 μW), internal structure visualization can be accomplished without damaging the artifacts. As such, the THz-TDSRI system can be employed to acquire the structural information of lacquered artifacts.

In *Terahertz Time-Domain Spectroscopic Reflectometric Imaging System*, we describe the proposed THz-TDSRI system. In *Imaging of Chinese Lacquerware*, the THz-TDSRI system is used to examine the hidden layers in lacquerware, such as cracks in the wooden layer, without damaging the lacquer layers. Finally, we conclude that the THz-TDSRI system is an important and promising non-destructive inspection method for lacquerware examination.

TERAHERTZ TIME-DOMAIN SPECTROSCOPIC REFLECTOMETRIC IMAGING SYSTEM

THz time-domain spectroscopic reflectometric (or THz pulsed) imaging is a non-invasive and coherent imaging technique that is used to obtain the inherent 3D information. As for imaging, the most advantageous trait of THz radiation is its capability of penetrating visually opaque and nonconducting materials.

To measure the outer layer of the lacquerware, a terahertz time-domain spectroscopic reflectometric imaging (THz-TDSRI) system is established in this study. This system comprises a femtosecond laser, a scanning optical delay line, a THz antenna, a THz detector, and an XY-scanning stage. A sketch map of the device in normal incidence reflection geometry is illustrated in **Figure 1**. Laser average power, pulse width, and repetition frequency in optical pulses are 100 mW, 100 fs, and 79 MHz, respectively. Using a half-wave plate and a polarization beam splitter, the optical pulses are divided into generation and detection beams; the ratio of generation beams to detection beams is set to 9:1 by rotating the half-wave plate. A beam with 90% power is passed through the scanning optical delay line, and the THz antenna is irradiated to produce THz waves. The THz beam is reflected by an off-axis parabolic mirror 1 (OAP1) to obtain a parallel beam. The parallel THz beam is then incident on the THz beam splitter; half of the THz energy is reflected. The reflected THz waves are focused on the lacquerware by OAP2 and reflected multiple times by the lacquerware. The reflected beam is focused on ZnTe by OAP2 and OAP3. Simultaneously, another beam with 90% power is irradiated on ZnTe as the probe beam. The probe beam is passed through a polarizer before irradiating ZnTe to ensure that it is linearly polarized. Then, the detection light probe beam is irradiated on the balance detector through a quarter-wave plate and a Wollaston prism to detect THz waves. The lacquerware is placed in the XY-scanning stage. The THz beam is used to perform raster scanning on the lacquerware in the X and Y spatial dimensions. A time-domain pulse is documented at every spatial coordinate for image formation. 2D and 3D THz tomography plots are acquired by scanning the lacquerware in the *X* and *Y* directions.

The C-scan method is employed for scanning. First, a THz wave is focused on a point in the lacquerware; then, the XY-scanning is stopped and spectral scanning is started. After the optical delay line completes the spectral scan of the point, the *X*-axis of the XY-scanning stage moves to the next point to perform the spectral scan again. This process is repeated until the *X*-axis spectral scanning is completed. At this time, the *X*-axis returns to the origin and the *Y*-axis moves to the next point. The same operation is repeated until the entire lacquerware is scanned [3].

Terahertz time-domain systems (THz-TDS) can emit and detect very short electromagnetic pulses (with duration below picosecond) in the THz frequency range. This THz-TDSRI system can be operated in the frequency range of 0.1–2.6 THz. THz radiation reflected by the gold mirror is shown in **Figure 2**.

In the proposed system, the temporal spacing between reflections is directly proportional to the optical thickness of the layers, implying that the time scale affords information concerning penetrated depth in the reflected signals, thereby enabling 3D time-of-flight (TOF) imaging [4, 5]. Time-domain images are reconstructed based on the measured data following the aforementioned pulse delay for the reference pulse. The principle is shown in **Figure 3**.

E_0 is the incident THz radiation. E_{r1} is the THz radiation reflected from the upper surface of the lacquer. This THz pulse appears at 15 ps E_{r2} is the THz radiation reflected by the interface between the lacquer and the wood. This THz pulse appears at 35 ps The time difference between these 2 THz pulses is 20 ps(Δt = 20 ps). Therefore, the thickness of the lacquer layer can be estimated using the expression, $d = \Delta t \cdot c/2n$, where c is the speed of light and n denotes the refractive index of lacquer. As for

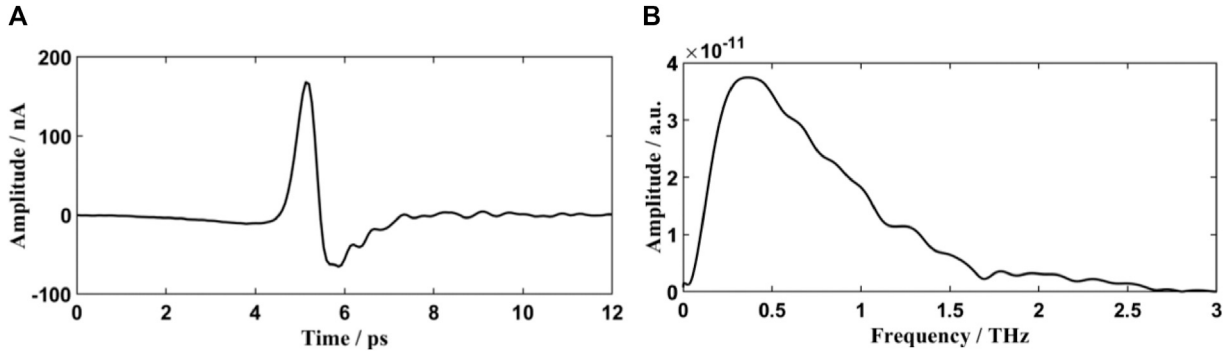

FIGURE 2 | (A) Time-domain spectrum of THz radiation reflected by a gold mirror; here, the time-domain width is 12 ps **(B)** Frequency-domain spectrum of THz radiation reflected by a gold mirror.

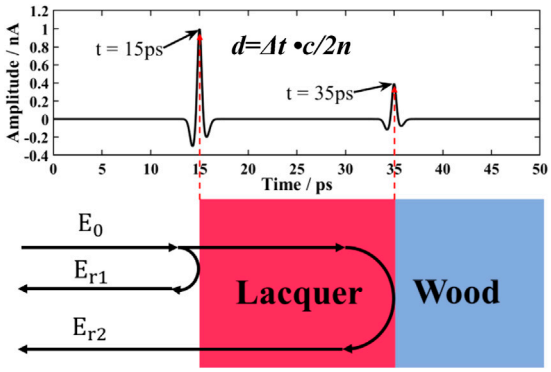

FIGURE 3 | Principle of THz-TDSRI system.

FIGURE 4 | Visible-light picture of the lacquerware replica; red lines mark the scanned area.

the spectral bandwidth of the THz pulse, its depth resolution is approximately half of the coherence length of the THz radiation. The coherence length of the radiation is based on $LC = cn/\Delta\omega$, where $\Delta\omega$ is the spectral bandwidth and cn denotes the speed of light within the intervening medium [6, 7].

IMAGING OF CHINESE LACQUERWARE

The studied lacquerware was procured from the Palace Museum, Beijing (**Figure 4**). The lacquerware is an ornamental object comprising a wood panel covered by multiple layers of lacquer to portray motifs, with its wood panel covered with thick glossy black lacquer. The pattern was portrayed by a layer of red-colored lacquer and a layer of gold-like yellow-colored lacquer.

The electric field value calculated at every spatial coordinate (x, y) across the scanned area was applied in lacquerware bidimensional visualization. The XY scan step was 0.25 mm, subject to the restriction of THz radiation wavelength. C-scan allowed us to obtain the time-domain intensity value of each point in space. The spectrum value was obtained via fast Fourier transform. A code was used to produce the frequency-and time-domain parametric THz images (**Figure 5**). THz reflection images were obtained by assigning intensity values to each pixel, thus, yielding various shades of gray within the black-white range in proportion to the parameter values.

The grayscale intensity images demonstrated a favorable THz optical contrast of the materials. The background is black lacquer, and the glittering patterns and gray is red lacquer.

In contrast to the time-domain parametric image, the frequency-domain image can be used to display images at a specific frequency. Different frequencies can provide us different information. To avoid the effect of THz waves reflected by the wood on the frequency spectrum, the reflected THz pulse of the lacquer was extracted, and the time-domain spectrum was normalized. The spectrogram of a specific frequency range was made. To improve the contrast, composite false-color rendering was applied while creating the reflected composite THz frequency-domain images [8] (**Figure 6**).

The different images correspond to different frequency ranges. The red lacquer was highlighted at frequencies of 0.16113–0.45410 THz. The yellow lacquer was highlighted at frequencies of 1.112,790–1.42090 THz and 1.81640–2.10940 THz. To improve the visual effect, these images were converted to RGB channels, and composite reflected THz composite images for RGB false-color were rendered (**Figure 6D**). RGB false-color rendering enabled the differentiation of multiple materials and textures on the

FIGURE 5 | (A) THz time-domain parametric image (maximum of temporal amplitude). **(B)** THz frequency-domain image (integral of the spectral amplitude over the 0–2.6-THz frequency range). Both panels are normalized, so they can share a color bar. There is a problem that needs to be explained: although the XY scan step length is 0.25 mm, but its horizontal resolution is 1 mm. This is because the size of the THz wave focus is limited by the wavelength and spectral width. We are currently working to improve the horizontal resolution.

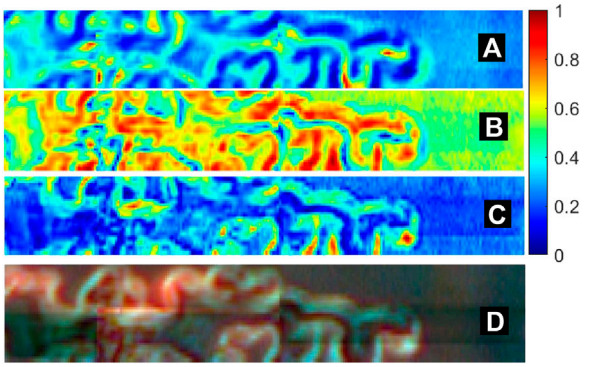

FIGURE 6 | THz reflection frequency spectrum composite image. **(A)** The image is recorded in the 0.16113–0.45410 THz range. **(B)** The image is recorded in the 1.112,790–1.42090 THz range. **(C)** The image is recorded in the 1.81640–2.10940 THz range. **(D)** The image is synthesized via false RGB. (a) Image of the red channel, (b) image of the green channel, and (c) image of the blue channel. The panels arebeen normalized to share a color bar.

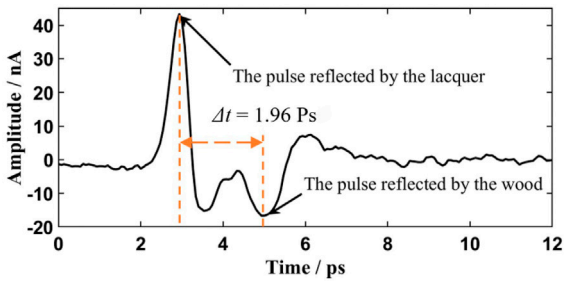

FIGURE 7 | A time-domain spectrum of one point.

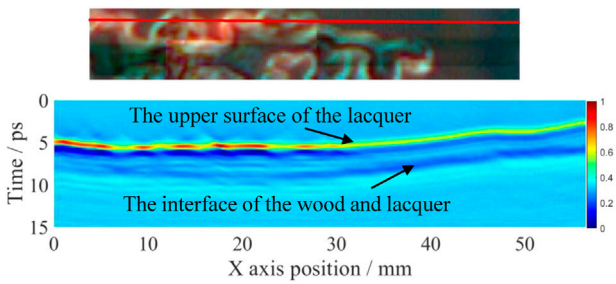

FIGURE 8 | B-scan image. The figure has been normalized.

lacquerware surface. The improvement in the recorded pattern is especially evident, in which the texture is much clearer due to the difference in the RGB colors.

The comparison between **Figure 6** and **Figure 4** shows that the yellow part is stronger in the mid-frequency (1.112,790–1.42090 THz) and high-frequency (1.81640–2.10940 THz) range. Because gold powder has been added to the yellow part. The red part is stronger in the low frequency (0.16113–0.45410 THz) range.

TERAHERTZ REFLECTION SLICE IMAGES

Figure 7 shows the time-domain spectrum of a point. This point is at x = 55 mm and y = 3 mm. It can be found that this point is a point in the upper right corner of the red box, compared with **Figure 4**. We can clearly see two reflected THz pulses. The first is the THz pulse reflected by the lacquer, and the second is the THz pulse reflected by the wood. The time difference between the appearance of these two peaks is 1.96 ps, Δt = 1.96 ps Phase analysis revealed that the THz pulse reflected by lacquer and the THz pulse reflected by wood have a phase difference of 180°; therefore, the THz pulse reflected by wood shows a negative amplitude. All time-domain spectra are similar to this one, but they have different amplitudes and Δt.

B-scans show the TOF in the electric field in the vertical axis and (x) transceiver linear position in the horizontal axis [9, 10]. In the lacquerware sample, depth difference was observed between the upper surface of the lacquer and the interface of the wood and

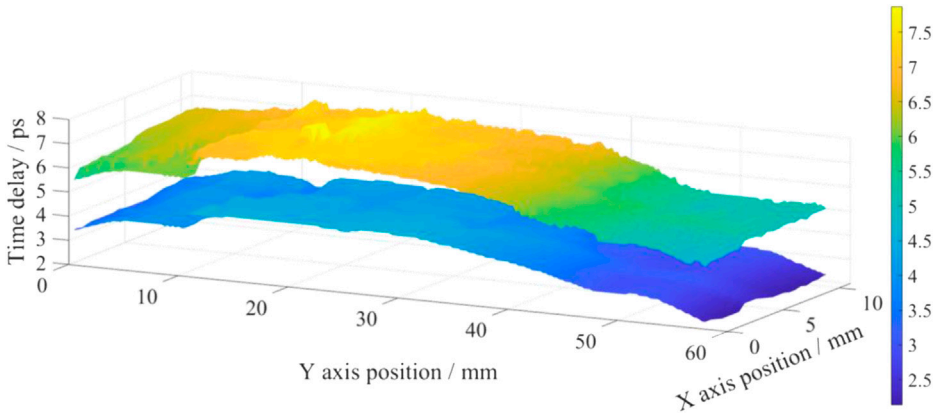

FIGURE 9 | Time-of-flight image.

lacquer [11, 12]. **Figure 8** shows the b-scan image of the red dashed scan line from a THz time-domain parametric graph. In the picture, we can clearly see the two surfaces (the upper surface of the lacquer and the interface of the wood and lacquer).

TIME-OF-FLIGHT IMAGE

TOF imaging is used to study the relationship between layers [13]. By using ultrashort THz pulses in high-resolution TOF THz tomography, the tomographic spectrum can be acquired by detecting the pulses reflected from each layer [14]. **Figure 9** presents the THz TOF images of the scanned areas. We analyzed all time-domain spectra. The time of each reflection peak in each time-domain spectrum has been extracted. To improve the visual effect, the figure is displayed in pseudo-color. The time of the first reflection peak in each time-domain spectrum forms the lower surface. The time of the second reflection peak in each time-domain spectrum forms the upper surface.

Figure 9 shows the layers for the area shown in **Figure 4**. The figure clearly shows two layers: the upper layer is the interface of lacquer and wood, and the lower layer is the upper surface of the lacquer. **Figure 9** shows that both reflection layers have a fault (*Y*-axis position near 10 mm) and that the faults on the wood layer are slightly greater compared with those on the lacquer layer. In this study, a sample of black lacquer with a thickness of 0.5 mm and a diameter of 10 mm has been produced, in order to evaluate the thickness of lacquer layer. By analyzing the frequency domain spectra in the air and reflected by the sample, it is found that the refractive index (n) is 1.83, which is obtained by integration in the frequency range of 0.1–2.6 THz. After calculation, the average thickness of the lacquer layer is 159.318 μm and the average fault of the wood layer and lacquer layer was found to be 65.42 and 46.38 μm, respectively. This proves that the lacquer repaired the fault of the wood to a certain extent. Comparing with **Figure 4**, it can be concluded that the wood layer and the lacquer layer are slightly convex at the edge of the lacquerware and the trend is the same in both layers. The probability of visualizing the wooden support's inner structure enables relevant integrity detection.

CONCLUSION

In this study, we demonstrated that the THz-TDSRI system proposed herein can highlight the interface between layers for the stratigraphic buildup and can be employed as a universal method to obtain the structural information (2D images, subsurface 3D images, and stratigraphic images (b-scans)) of lacquerware in a contactless and non-invasive manner. Using the proposed THz-TDSRI system, we examined the buried layers involving wood layer faults in the lacquerware without damaging the artifact. A traditional Chinese lacquerware artifact was studied using reflectometric THz imaging, which proves that THz-TDSRI has great potential in lacquerware inspection.

DATA AVAILABILITY STATEMENT

The original contributions presented in the study are included in the article/Supplementary Material, further inquiries can be directed to the corresponding authors.

AUTHOR CONTRIBUTIONS

HZ: conceptualization, methodology, validation, investigation, writing-original draft. YZ: supervision, conceptualization, writing-reviewing, and editing. CL: sample selection and acquisition. CZ: conceptualization and funding acquisition.

ACKNOWLEDGMENTS

The authors would like to thank Beijing Broad Hengtong S&T Development Co, Ltd., for having provided the femtosecond laser in this study. Thanks for the support of Capital Normal University Development Funds by Category-Physics Department-Practice base Projects for Degree Study Program (No. 008–2155089).

REFERENCES

1. Fabien D, and Christophe B. Impact damages detection on composite materials by THz imaging [J]. *Case Stud Non-destructive Test Eval* (2016) 6:53–62.
2. Niijima S, Shoyama M, Murakami K, and Kawase K. Evaluation of the sintering properties of pottery bodies using terahertz time-domain spectroscopy. *J Asian Ceram Societies* (2018) 6(1):37–42. doi:10.1080/21870764.2018.1439610
3. Iskandarani MZ. Abnormalities in Ultrasonic (C-Scan) Images of Composite Structures: Impact Damaged versus Hole Damaged. *J Comp Sci* (2019) 15(7):972–82. doi:10.3844/jcssp.2019.972.982
4. Eom KH, Peltek SE, Popik VM, Jeong YU, and Park GS. *Irradiative damage characterization of a lysozyme during high-power THz ablation using MALDI-TOF mass spectrometry: Proceedings of the Infrared, Millimeter, and Terahertz Waves (IRMMW-THz), 2012 37th International Conference on IEEE* (2012). [C]. Wollongong.
5. Dandolo CLK, Gomezsepulveda AM, Hernandezserrano AI, and Castrocamus E. Examination of Painting on Metal Support by Terahertz Time-Domain Imaging [J]. *J Infrared Millimeter Terahertz Waves* (2017) 38(10):1–10. doi:10.1007/s10762-017-0409-7
6. Walker GC, Bowen JW, Labaune J, Jackson J-B, Hadjiloucas S, Roberts J, et al. Terahertz deconvolution. *Opt Express* (2012) 20(25):27230–41. doi:10.1364/oe.20.027230
7. Schwerdtfeger M, Castro-camus E, Krügener K, Viöl W, and Koch M. Beating the wavelength limit: three-dimensional imaging of buried subwavelength fractures in sculpture and construction materials by terahertz time-domain reflection spectroscopy. *Appl Opt* (2013) 52(3):375–80. doi:10.1364/AO.52.000375
8. Lu WL, Lou SQ, Wang X, Shen Y, and Sheng XZ. False-color terahertz imaging system based on terahertz time domain spectrocsopy [J]. *Acta Physica Sinica* (2015) 64(11):0. doi:10.7498/aps.64.114206
9. Sim YC, Ahn K-M, Park JY, Park C-S, and Son J-H. Temperature-Dependent Terahertz Imaging of Excised Oral Malignant Melanoma. *IEEE Trans Thz Sci Technol* (2013) 3(4):368–73. doi:10.1109/tthz.2013.2267415
10. Dandolo CLK, Fukunaga K, Kohzuma Y, Kiriyama K, and Jepsen PU. Inspection of Asian Lacquer Substructures by Terahertz Time-Domain Imaging (THz-TDI)[J]. *J Infrared Millimeter Terahertz Waves* 38(4):1–10.
11. Bardon T, May RK, Jackson JB, Beentjes GL, De Bruin G, Taday PF, et al. Contrast in Terahertz Images of Archival Documents—Part I: Influence of the Optical Parameters from the Ink and Support [J]. *J Infrared Millimeter Terahertz Waves* 38(4):443–66.
12. Oh SJ, Kim S-H, Jeong K, Park Y, Huh Y-M, Son J-H, et al. Measurement depth enhancement in terahertz imaging of biological tissues. *Opt Express* (2013) 21(18):21299. doi:10.1364/oe.21.021299
13. Spranger H, and Beckmann J. *THz – ToF Optical Layer Analysis (OLA) to determine optical properties of dielectric materials: proceedings of the Review of Progress in Quantitative Nondestructive Evaluation* (2017). [C].
14. Xin G, Yoshikazu U, Xiangrong Z, Takeshi H, and Takahiko A. A Fast and Fully Automatic Method for Cerebrovascular Segmentation on Time-of-Flight (TOF) MRA Image [J]. *J Digital Imaging* (2010).

Conflict of Interest: The authors declare that the research was conducted in the absence of any commercial or financial relationships that could be construed as a potential conflict of interest.

Publisher's Note: All claims expressed in this article are solely those of the authors and do not necessarily represent those of their affiliated organizations or those of the publisher, the editors, and the reviewers. Any product that may be evaluated in this article, or claim that may be made by its manufacturer, is not guaranteed or endorsed by the publisher.

frontiers in Physics

ORIGINAL RESEARCH
published: 06 September 2021
doi: 10.3389/fphy.2021.751026

Active Control of the THz Wave Polarization State by an Electronically Controlled Graphene Composite Metasurface

Guocui Wang[1,2], *Bin Hu*[1]*, *Muhammad Ismail Khan*[1] *and Yan Zhang*[2]

[1]School of Optics and Photonics, Beijing Engineering Research Center for Mixed Reality and Advanced Display, Beijing Institute of Technology, Beijing, China, [2]Department of Physics, Beijing Key Lab for Metamaterials and Devices, Key Laboratory for Terahertz Optoelectronics, Ministry of Education, Beijing Advanced Innovation Center for Imaging Theory and Technology, Capital Normal University, Beijing, China

Active control of terahertz (THz) wave polarization state is of great significance for sensitive detection, imaging and communication. Here, a tunable THz quarter wave plate is designed by electronically controlling a composite metasurface consisting of the gold cross antennas and a monolayer graphene. The graphene composite metasurface acts as a quarter-wave plate when the chemical potential of graphene is 0 eV, by which the polarization state of the incident THz wave is converted from linear polarization to circular polarization. After the chemical potential of graphene is increased gradually, and to 0.5 eV, the transmitted polarization state of the THz wave is changed from right circular polarization to right elliptical polarization, and to linear polarization. Furthermore, the polarization state of the THz wave is able to be changed from left circular polarization to left elliptical polarization, and to linear polarization if the device is clockwise rotated by 90°. Therefore, the polarization state of THz wave could be actively controlled by the proposed tunable THz quarter wave plate. Our work will offer a new avenue for tunable THz polarization modulation devices.

Keywords: THz, polarization, tunable, graphene, metasurface

OPEN ACCESS

Edited by:
Meng Chen,
Tsinghua University, China

Reviewed by:
Lei Hou,
Xi'an University of Technology, China
Xinlong Xu,
Northwest University, China

***Correspondence:**
Bin Hu
hubin@bit.edu.cn

Specialty section:
This article was submitted to Optics and Photonics, a section of the journal Frontiers in Physics

Received: *31 July 2021*
Accepted: *24 August 2021*
Published: *06 September 2021*

Citation:
Wang G, Hu B, Khan MI and Zhang Y (2021) Active Control of the THz Wave Polarization State by an Electronically Controlled Graphene Composite Metasurface. Front. Phys. 9:751026. doi: 10.3389/fphy.2021.751026

INTRODUCTION

Recently, tunable metasurfaces have attracted enormous research interests as a means to control the polarization state of THz wave. In the conventional optical devices, polarization control of electromagnetic wave is mainly achieved using birefringent materials. However, these materials are not suitable in the THz band because of the inherent disadvantages including bulky size, and narrow band of operating frequency. The most important issue is that the THz wave interacts weakly with these materials in nature.

Metasurface is a sub-wavelength artificial structure with extraordinary properties that nature materials do not have [1]. The electromagnetic wave properties including amplitude, phase, frequency and polarization can be controlled completely based on the structure of a metasurface, because any permittivity and permeability can be achieved after the modulation of metasurface devices. Therefore, more and more people have been committed to design metasurface structures, and proposed various functional devices including the anomalous reflection or refraction devices [2, 3], the holographic devices [4–6], the metasurface lenses [7–9], and the polarization-control devices [10–17], which mainly include the

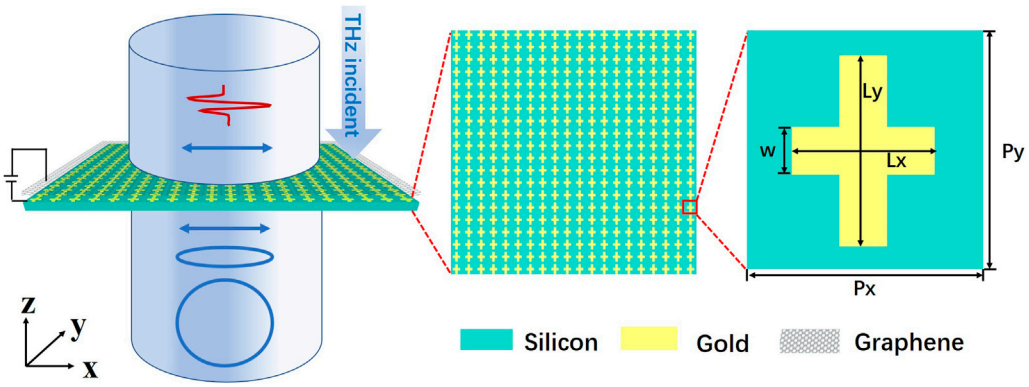

FIGURE 1 | (A) Diagram of the working principle of the tunable TQWP; **(B)** Schematic of the metasurface consisting of the gold anisotropy cross arrays; **(C)** Schematic of one unit cell among the gold gross arrays.

half-wave plate [10, 11], the quarter-wave plate [12–16], and the retarders [17]. These devices have the advantages of ultrathin thickness, high degree of design freedom and compactness, which will promote the miniaturization of the system. For example, Wang et al. designed an ultrathin THz quarter-wave plate using Babinet-inverted metasurface [14]. However, all the devices mentioned above are static, which hinders their convenience in the realistic application. Activating the functionalities of these devices will no doubt expand the application and improve the functional value, which is necessary to integrate tunable materials including the semiconductor [18, 19], the phase change material [20, 21], and graphene [22, 23], and externally control the functionalities by light [24], temperature [25], and an applied gate voltage [26]. More recently, a few THz polarization devices have been proposed [27–29]. Zhao et al. proposed a tunable transmission THz waveplate based on the electrically driving metasurface [28]. Luo et al. designed a dynamically reversible and strong circular dichroism based on Babinet-invertible chiral metasurface [29]. However, polarization devices whose function is tunable in the THz band is still vary lacking.

In this paper, we design a tunable THz quarte-wave plate (TQWP) by integrating a monolayer graphene with a metasurface consisting of the anisotropic gold cross arrays for actively and completely controlling the THz polarization state. The resonance characteristics of the cross will be modulated when the Fermi energy of the graphene is changed by an external voltage [30, 31]. A polarization state conversion from right circular polarization undergoes right elliptical polarization, and to linear polarization of 45° is achieved by changing the chemical potential of graphene from 0 to 0.5 eV, in which the device is irradiated normally by a linear polarized THz plane wave with a polarization angle of 45° to the x-axis. We further achieved the THz polarization conversion from left circular polarization state undergoes left elliptical polarization state, and to linear polarized of 135° only making the device clockwise rotate by 90°.

DESIGN OF STRUCTURE

The tunable TQWP is designed as shown in **Figure 1A**. The device is irradiated normally by a linear polarized THz plane wave. After modulated by this device, the THz polarization state is transformed to a circular state at first. Then, the polarization state of THz is changed from circular polarization goes through elliptical polarization and eventually returns to linear polarization with a changed gate voltage that increases the Fermi energy of the graphene. The tunable TQWP is consisting of three parts, including the monolayer graphene, the metasurface, and the silicon. The metasurface is composed of the anisotropic gold cross arrays, as shown in **Figure 1B**, and the unit cell of the metasurface is depicted in **Figure 1C**. The period of the unit cell is 100 μm. The arm lengths of the cross are $Lx = 66$ μm and $Ly = 86$ μm, respectively. The arm width is $w = 9$ μm. The Finite-Difference Time-Domain (FDTD) method of simulation software (FDTD Solutions, Lumerical Inc.) is used as the simulation tool to calculate the electromagnetic field of the THz wave. In the simulations, the graphene layer is modeled as a two-dimensional (2D) graphene sheet, whose Fermi energy is tuned by changing the graphene chemical potential. The silicon with a refractive index of 3.4 is used as a substrate of the device.

RESULTS AND DISCUSSION

Numerical simulations are then carried out to confirm the functions of the designed graphene composite metasurface. Graphene is a great popular functional material in tunable metasurface because the electronic characteristics are controlled by external stimuli. In the THz region, graphene is well described by the Drude-like surface conductivity as [32].

$$\sigma_{graphene}(\omega, \mu_c, \Gamma, T) = -j\frac{e^2 k_B T}{\pi\hbar^2(\omega - j2\Gamma)}\left(\frac{\mu_c}{k_B T} + 2In\left(e^{-\mu_c/k_B T} + 1\right)\right) \quad (1)$$

where e, k_B and $\hbar$ are universal constants representing the electron charge, Boltzmann's and Plank's constant, ω is the working radian frequency, T is the room temperature, Γ ($\Gamma = \hbar/2\tau$, where τ is the electron-photon relaxation time) is the scattering rate, and μ_c is the chemical potential of the

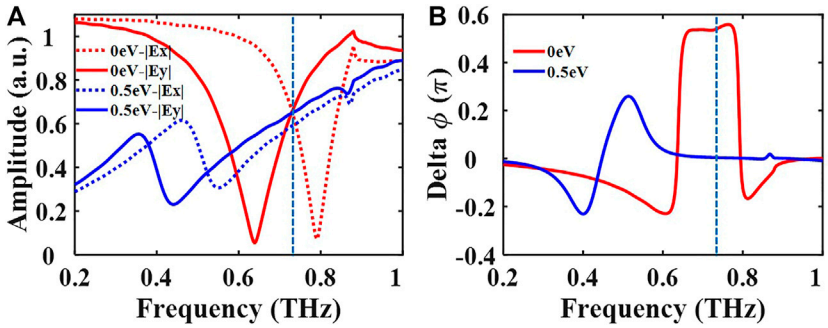

FIGURE 2 | (A) Variations of the transmission amplitude components $|E_y|$ (solid line) and $|E_x|$ (dashed line) when the chemical potential of graphene was increased from 0 to 0.5 eV, respectively; **(B)** Phase differences between $\varnothing_y$ and $\varnothing_x$ when the chemical potential of graphene was increased from 0 to 0.5 eV, respectively.

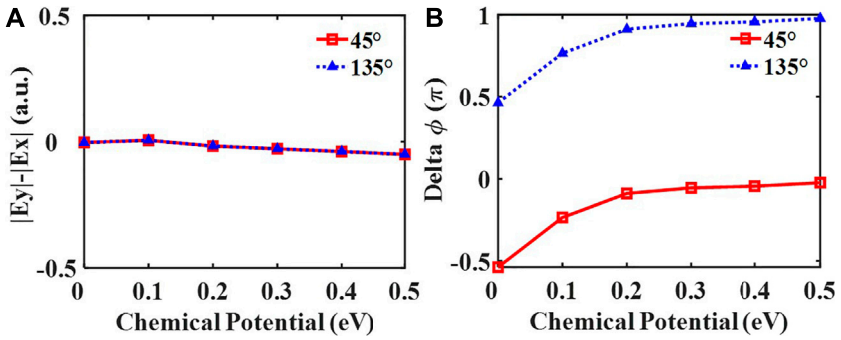

FIGURE 3 | (A) The amplitude difference ($|E_y| - |E_x|$) between the transmission components E_y and E_x for THz at frequency of 0.73 THz with incident polarize angle of 45° (square dotted line) and 135° (triangle dotted line) when the chemical potential of graphene was increased form 0–0.5 eV, respectively. **(B)** The phase difference ($\varnothing_y - \varnothing_x$) between the transmission components E_y and E_x for THz at frequency of 0.73 THz with incident polarize angle of 45° (square dotted line) and 135° (triangle dotted line) when the chemical potential of graphene was increased form 0–0.5 eV, respectively.

graphene. Therefore, the conductivity of graphene can be controlled by changing the chemical potential in the simulation, and the resonance characters affected by conductivity of the composite metasurface are controlled. In our simulation, the transmission characters were obtained for different graphene chemical potential changed from 0.1 to 0.5 eV by a step of 0.1 eV.

Red lines in **Figures 2A,B** show the simulated transmission amplitude components $|E_y|$ (solid line) and $|E_x|$ (dashed line) and the difference between phase components $\varnothing_y$ and $\varnothing_x$ along the two arms of the cross in the metasurface before the chemical potential of the graphene is changed ($E_F = 0$ eV), respectively. It is found that there are two resonant dips in the transmission amplitude components alone the two arms of the cross, respectively. If we set our sights at frequency of the 0.73 THz, we can observe that both the transmission amplitudes of the two arms are 0.67, and the phase delay is 90°, which demonstrates that a function of a quarter wave plate is obtained. When the chemical potential of the graphene is increased to 0.5 eV, the transmission amplitude components and the difference between phase components are illustrated by the blue lines in **Figures 2A,B**, respectively. Both resonant dips of the transmission amplitude corresponding to the two arms are red-shifted. The transmission amplitudes of the two arms are about 0.60 except for some negligible differences between the two components at the frequency of 0.73 THz, but the phase delay is reduced to 0°, which means that the polarization of the transmission THz wave is back to the linear polarization state.

In order to show the variation process of the transmitted THz polarization state along with the change of the graphene chemical potential, we calculated the difference between the transmission amplitude components, $|E_y| - |E_x|$, and the difference between the phase components, $\varnothing_y - \varnothing_x$, of the cross, respectively, at the frequency of 0.73 THz, when the graphene chemical potential is changed from 0 to 0.5 eV by a step of 0.1 eV. As shown by the red lines in **Figures 3A,B**, the difference between the two transmission amplitude components is almost zero, and the phase difference between the two transmission components is gradually changed from $-\pi/2$ to $0\,\pi$ at the incident polarization with the polarize angle of 45°, which indicates that the polarization state of THz wave changes from the right circular polarization to the right elliptical polarization, and back to the

Incident Polarization (\°)	Chemical Potential (\eV)	Number	s0	s1	s2	s3	Poincare Sphere
45°	0	1	0.86	0.00	-0.10	-0.86	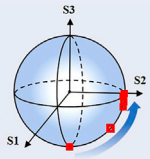
	0.1	2	0.69	0.01	0.51	-0.46	
	0.2	3	0.76	0.02	0.73	-0.21	
	0.3	4	0.71	0.03	0.70	-0.12	
	0.4	5	0.60	0.04	0.59	-0.08	
	0.5	6	0.52	0.05	0.51	-0.03	
135°	0	7	0.86	0.00	0.10	0.86	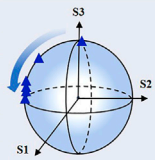
	0.1	8	0.70	0.01	-0.51	0.46	
	0.2	9	0.76	0.02	-0.73	0.21	
	0.3	10	0.71	0.03	-0.70	0.12	
	0.4	11	0.60	0.04	-0.60	0.08	
	0.5	12	0.52	0.05	-0.51	0.03	

FIGURE 4 | (Left column) The Stokes Parameters of the devices for the different graphene chemical potential with the THz incidence polarize angle 45°and 135°, respectively. **(Right column)** The Poincare Sphere is used to presents the polarization state of the device for different chemical potential of graphene.

linear polarization with the polarize angle of 45°. As shown by the blue lines in the **Figures 3A,B**, the difference between two transmission amplitude components is almost zero, and the phase difference between the two transmission components is gradually changed from $\pi/2$ to π only by rotating the sample of 90° clockwise, taking the z-axis as the center axis. In this situation, the polarization of the THz wave changes from the left circular polarization to the left elliptical polarization, and to the linear polarization with the polarize angle of 135°.

The polarization information of the transmitted wave can be represented by the Stokes parameters $[S_0, S_1, S_2, S_3]$, in which $S_0 = |E_x|^2 + |E_y|^2$, $S_1 = |E_x|^2 - |E_y|^2$, $S_2 = |E_x|*|E_y|*\sin(\Delta\varnothing)$, and $S_2 = |E_x|*|E_y|*\cos(\Delta\varnothing)$ [28]. From the simulated amplitude and phase of the both E_x and E_y components, we calculated the Stokes parameters of the designed metasurface for different graphene chemical potentials, as shown in **Figure 4** (Left column). The Poincare sphere is a way that can intuitively represents the polarization state of light, in which the north point represents the left circular polarization state, the south point represents the right circular polarization state, the equator line represents linear polarization state, the northern hemisphere represents the left elliptical polarization state, and the southern hemisphere represents the right elliptical polarization state, respectively. Therefore, the Stokes parameters calculated above is then represented by the Poincare sphere in **Figure 4** (Right column). It is easily to find that the polarization state of THz incident with polarize angle of 45° is modulated from the right circular polarization to the right elliptical polarization, and to the linear polarization when the chemical potential is changed from 0 to 0.5 eV. Furthermore, the polarization state of THz incident with polarize angle of 135° is modulated from the left circular polarization to the left elliptical polarization, and to the linear polarization. Therefore, the polarization of the THz wave can be controlled flexibly and completely by the tunable TQWP designed in this letter.

To further understand the physics underlying inside of the proposed tunable metasurface, in **Figures 5A,B**, we stimulated the energy distribution on the gold cross for different graphene chemical potentials of 0 and 0.5 eV, respectively. As shown in **Figure 5A**, the THz energy is uniformly distributing on the two arms of the whole cross, respectively, the energy distribution on the arm along with the *x*-axis is stronger than that on the arm along with the y-axis, with energy intensity of 7×10^{-1} when chemical potential of graphene is 0 eV. However, the THz energy is mainly distributing the end of arms of the cross, when the chemical potential of graphene is increased to 0.5 eV, as shown in **Figure 5B**. Furthermore, the energy intensity is reduced to 5.7×10^{-2} which is much smaller than that energy intensity of 7×10^{-1}. The above results indicating that interaction between the THz wave and the gold antenna will be gradually suppressed when the chemical potential of graphene is increasing, which results in reduction of the difference between phase components. Therefore, the polarization state of THz is actively controlled by the designed metasurface alone with the variation of the graphene chemical potential.

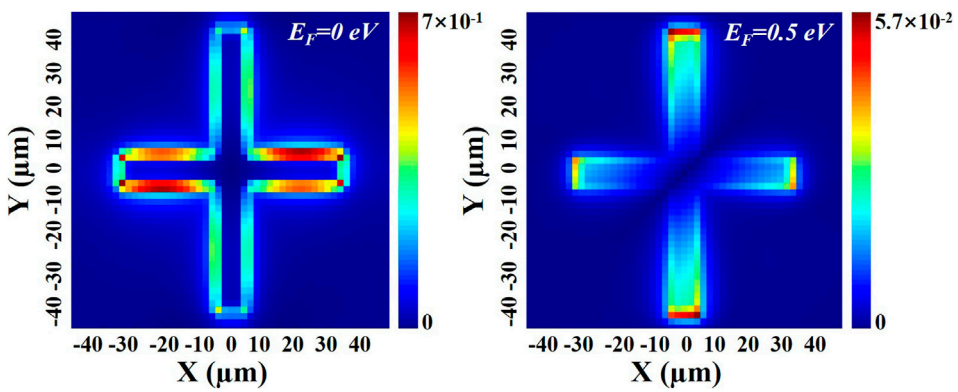

FIGURE 5 | (A,B) The THz energy distribution on the gold cross for graphene chemical potentials of 0 and 0.5 eV, respectively.

CONCLUSION

In summary, we have demonstrated a tunable TQWP which is realized by integrating the monolayer graphene with a metallic metasurface. This composite device acts as a TQWP at the frequency of 0.73 THz before the chemical potential of graphene is changed, by which the polarization state of THz with incident polarize angle of 45° to *x*-axis is converted from linear polarization to circular polarization. When the chemical potential of the graphene is increased from 0 to 0.5 eV, the polarization state of the THz wave is converted from the right circular polarization to the right elliptical polarization, and to the linear polarization state of 45°. And we further achieved the polarization conversion from the left circular polarization state to the left elliptical polarization, and to the linear polarization state of 135° by rotating the devise clockwise, taking the z-axis as the center axis. A total polarization state conversion is achieved by our composite metasurface. We hope our work can further enriches the THz polarization devices, and provide a new route for designing the tunable polarization devices.

DATA AVAILABILITY STATEMENT

The original contributions presented in the study are included in the article/Supplementary Material, further inquiries can be directed to the corresponding author.

AUTHOR CONTRIBUTIONS

GW, BH and YZ concived the ideas, BH and YZ improved the ideas, GW conducted the design, mumerical simulations. GW prepared the manuscript. BH and MK supervised the project. All the authors discussed and analyzed the results.

FUNDING

National Natural Science Foundation of China (62050410347, 61875010).

REFERENCES

1. Khorasaninejad M, and Capasso F. Metalenses: Versatile Multifunctional Photonic Components. *Science* (2017) 358(6367):eaam8100. doi:10.1126/science.aam8100
2. Li Z, Palacios E, Butun S, and Aydin K. Visible-Frequency Metasurfaces for Broadband Anomalous Reflection and High-Efficiency Spectrum Splitting. *Nano Lett* (2015) 15(3):1615–21. doi:10.1021/nl5041572
3. Li Y, Zhang J, Zhang Y, Chen H, and Fan Y. Wideband, Co-polarization Anomalous Reflection Metasurface Based on Low-Q Resonators. *Appl Phys A* (2016) 122(9):851. doi:10.1007/s00339-016-0374-3
4. Pfeiffer C, and Grbic A. Controlling Vector Bessel Beams with Metasurfaces[J]. *Phys Rev Appl* (2014) 2(4):044012. doi:10.1103/physrevapplied.2.044012
5. He J, Wang X, Hu D, Ye J, Feng S, Kan Q, et al. Generation and Evolution of the Terahertz Vortex Beam. *Opt Express* (2013) 21(17):20230–9. doi:10.1364/oe.21.020230
6. Guo J-Y, Wang X-K, He J-W, Zhao H, Feng S-F, Han P, et al. Generation of Radial Polarized Lorentz Beam with Single Layer Metasurface. *Adv Opt Mater* (2018) 6(1):1700925. doi:10.1002/adom.201700925
7. Jiang X-Y, Ye J-S, He J-W, Wang X-K, Hu D, Feng S-F, et al. An Ultrathin Terahertz Lens with Axial Long Focal Depth Based on Metasurfaces. *Opt Express* (2013) 21(24):30030–8. doi:10.1364/oe.21.030030
8. Wang B, Wu X, and Zhang Y. Multiple-Wavelength Focusing and Demultiplexing Plasmonic Lens Based on Asymmetric Nanoslit Arrays. *Plasmonics* (2013) 8(4):1535–41. doi:10.1007/s11468-013-9569-z
9. Ho JS, Qiu B, Tanabe Y, Yeh AJ, Fan S, and Poon ASY. Planar Immersion Lens with Metasurfaces. *Phys Rev B* (2015) 91(12):125145. doi:10.1103/physrevb.91.125145
10. Roberts A, and Lin L. Plasmonic Quarter-Wave Plate. *Opt Lett* (2012) 37(11):1820–2. doi:10.1364/ol.37.001820
11. Pors A, Nielsen MG, and Bozhevolnyi SI. Broadband Plasmonic Half-Wave Plates in Reflection. *Opt Lett* (2013) 38(4):513–5. doi:10.1364/ol.38.000513
12. Zhao Y, and Alù A. Tailoring the Dispersion of Plasmonic Nanorods to Realize Broadband Optical Meta-Waveplates. *Nano Lett* (2013) 13(3):1086–91. doi:10.1021/nl304392b
13. Jiang ZH, Lin L, Ma D, Yun S, Werner DH, Liu Z, et al. Broadband and Wide Field-Of-View Plasmonic Metasurface-Enabled Waveplates. *Sci Rep* (2014) 4:7511. doi:10.1038/srep07511
14. Wang D, Gu Y, Gong Y, Qiu C-W, and Hong M. An Ultrathin Terahertz Quarter-Wave Plate Using Planar Babinet-Inverted Metasurface. *Opt Express* (2015) 23(9):11114–22. doi:10.1364/oe.23.011114
15. Li Z, Liu W, Cheng H, Chen S, and Tian J. Realizing Broadband and Invertible Linear-To-Circular Polarization Converter with Ultrathin Single-Layer Metasurface. *Sci Rep* (2015) 5:18106. doi:10.1038/srep18106
16. Jiang Y, Wang L, Wang J, Akwuruoha CN, and Cao W. Ultra-Wideband High-Efficiency Reflective Linear-To-Circular Polarization Converter Based on Metasurface at Terahertz Frequencies. *Opt Express* (2017) 25(22):27616–23. doi:10.1364/oe.25.027616
17. Pors A, Nielsen MG, Valle GD, Willatzen M, Albrektsen O, and Bozhevolnyi SI. Plasmonic Metamaterial Wave Retarders in Reflection by Orthogonally Oriented Detuned Electrical Dipoles. *Opt Lett* (2011) 36(9):1626–8. doi:10.1364/ol.36.001626
18. Sarma R, Campione S, Goldflam M, Shank J, Noh J, Le LT, et al. A Metasurface Optical Modulator Using Voltage-Controlled Population of Quantum Well States. *Appl Phys Lett* (2018) 113(20):201101. doi:10.1063/1.5055013
19. Zhang Y, Zhao Y, Liang S, Zhang B, Wang L, Zhou T, et al. Large Phase Modulation of THz Wave via an Enhanced Resonant Active HEMT Metasurface. *J Nanophotonics* (2018) 8(1):153–70. doi:10.1515/nanoph-2018-0116
20. He J, Xie Z, Sun W, Wang X, Ji Y, Wang S, et al. Terahertz Tunable Metasurface Lens Based on Vanadium Dioxide Phase Transition. *Plasmonics* (2016) 11(5):1285–90. doi:10.1007/s11468-015-0173-2
21. Liu X, Wang Q, Zhang X, Li H, Xu Q, Xu Y, et al. Thermally Dependent Dynamic Meta-Holography Using a Vanadium Dioxide Integrated Metasurface. *Adv Opt Mater* (2019) 7(12):1900175. doi:10.1002/adom.201900175
22. Fang Z, Wang Y, Schlather AE, Liu Z, Ajayan PM, de Abajo FJ, et al. Active Tunable Absorption Enhancement with Graphene Nanodisk Arrays. *Nano Lett* (2014) 14(1):299–304. doi:10.1021/nl404042h
23. Dai S, Ma Q, Liu MK, Andersen T, Fei Z, Goldflam MD, et al. Graphene on Hexagonal boron Nitride as a Tunable Hyperbolic Metamaterial. *Nat Nanotech* (2015) 10:682–6. doi:10.1038/nnano.2015.131
24. Guo J, Wang T, Zhao H, Wang X, Feng S, Han P, et al. Reconfigurable Terahertz Metasurface Pure Phase Holograms. *Adv Opt Mater* (2019) 7(10):1801696. doi:10.1002/adom.201801696
25. Wang T, He J, Guo J, Wang X, Feng S, Kuhl F, et al. Thermally Switchable Terahertz Wavefront Metasurface Modulators Based on the Insulator-To-Metal Transition of Vanadium Dioxide. *Opt Express* (2019) 27(15):20347. doi:10.1364/oe.27.020347
26. Huang Y-W, Lee HWH, Sokhoyan R, Pala RA, Thyagarajan K, Han S, et al. Gate-Tunable Conducting Oxide Metasurfaces. *Nano Lett* (2016) 16(9):5319–25. doi:10.1021/acs.nanolett.6b00555
27. Wang D, Zhang L, Gu Y, Mehmood MQ, Gong Y, Srivastava A, et al. Switchable Ultrathin Quarter-Wave Plate in Terahertz Using Active Phase-Change Metasurface. *Sci Rep* (2015) 5:15020. doi:10.1038/srep15020

28. Zhao X, Schalch J, Zhang J, Seren HR, Duan G, Averitt RD, et al. Electromechanically Tunable Metasurface Transmission Waveplate at Terahertz Frequencies. *Optica* (2018) 5(3):303–10. doi:10.1364/optica.5.000303
29. Luo X, Hu F, and Li G. Dynamically Reversible and strong Circular Dichroism Based on Babinet-Invertible Chiral Metasurfaces. *Opt Lett* (2021) 46(6): 1309–12. doi:10.1364/ol.421016
30. Liu W, Hu B, Huang Z, Guan H, Li H, Wang X, et al. Graphene-enabled Electrically Controlled Terahertz Meta-Lens. *Photon Res* (2018) 6(7):703–8. doi:10.1364/prj.6.000703
31. Huang J, Guan H, Hu B, Wang G, Liu W, Wang Z, et al. Enhanced Terahertz Focusing for a Graphene-Enabled Active Metalens. *Opt Express* (2020) 28(23): 35179–91. doi:10.1364/oe.409746
32. Zhang Y, Feng Y, Zhu B, Zhao J, and Jiang T. Graphene Based Tunable Metamaterial Absorber and Polarization Modulation in Terahertz Frequency. *Opt Express* (2014) 22(19):22743–52. doi:10.1364/oe.22.022743

Conflict of Interest: The authors declare that the research was conducted in the absence of any commercial or financial relationships that could be construed as a potential conflict of interest.

frontiers in Physics

ORIGINAL RESEARCH
published: 08 September 2021
doi: 10.3389/fphy.2021.751128

A High Performance Terahertz Photoconductive Antenna Array Detector With High Synthesis Efficiency

Wei Shi, Zhiquan Wang, Lei Hou, Haiqing Wang, Meilin Wu and Chaofan Li*

The Key Laboratory of Ultrafast Photoelectric Technology and Terahertz Science in Shaanxi, Xi'an University of Technology, Xi'an, China

A 2 × 2 terahertz photoconductive antenna (PCA) array detector with high efficiency synthesis characteristic that improves the signal-to-noise ratio (SNR) of the detected signals has been reported in this paper. By processing the substrate material through a special micromachining process, the current signal generated by the adjacent antenna elements as opposed to that generated by the antenna gap is eliminated. Experiments show that the amplitude of the current signal output by the PCA array detector is consistent with the amplitude of the synchronous superposition of the current signals output by antenna elements, and the synthesis efficiency of the device achieves 93.7%. At the same time, the antenna array detector has low current noise, and its highest SNR is 62 dB under the excitation of different light energy, which is related to the number of antenna array elements.

Keywords: terahertz wave, antenna array, signal-to-noise ratio, synthesis, reverse current

OPEN ACCESS

Edited by:
Yingxin Wang,
Tsinghua University, China

Reviewed by:
Shengjiang Chang,
Nankai University, China
Jian Chen,
Nanjing University, China

****Correspondence:***
Wei Shi
swshi@mail.xaut.edu.cn

Specialty section:
This article was submitted to Optics and Photonics, a section of the journal Frontiers in Physics

Received: *31 July 2021*
Accepted: *25 August 2021*
Published: *08 September 2021*

Citation:
Shi W, Wang Z, Hou L, Wang H, Wu M and Li C (2021) A High Performance Terahertz Photoconductive Antenna Array Detector With High Synthesis Efficiency. Front. Phys. 9:751128. doi: 10.3389/fphy.2021.751128

INTRODUCTION

There are mainly two ways to detect terahertz (THz) time-domain waveforms: electro-optic (EO) crystal and photoconductive antenna. The principle of the former is based on the Pockels effect of crystals [1, 2]. A thinner EO crystal can provide a wider spectrum, but at the same time it leads to a decrease in detection sensitivity [3]. Compared with the photoconductive antennas, the EO detection requires more optical elements, higher cost and larger system size. THz waves detection by PCAs is the inverse process of the THz waves generation by PCAs. The performances of large spectral width, small size and ease of use make photoconductive antennas attractive for commercialization. In addition, pasting a silicon lens on the back of antennas will improve the detector's ability to collect THz waves and obtain a higher SNR [4]. Although a single THz PCA has been widely used in THz time-domain spectroscopy systems, it still has shortcomings in detecting weak terahertz signals and improving the SNR. In theory, connecting multiple PCAs in parallel to form a PCA array detector can make use of the THz electric field as much as possible to improve the SNR and detection sensitivity of the PCA array detector. Although the PCA array detector with hundreds to thousands antenna elements have been proposed and developed [5, 6], the synthesis efficiency of PCA array was not discussed in detail in the previous work, which is important to improve the detection efficiency. When the PCA array is used as a detector, it faces the same problem when it is used as an emitter. That is, the photo-generated carriers generated in the substrate materials between adjacent antennas move directionally under the action of the terahertz electric field, forming a current opposite to the current generated in the antenna gap, the reverse current will reduce the generation efficiency of THz

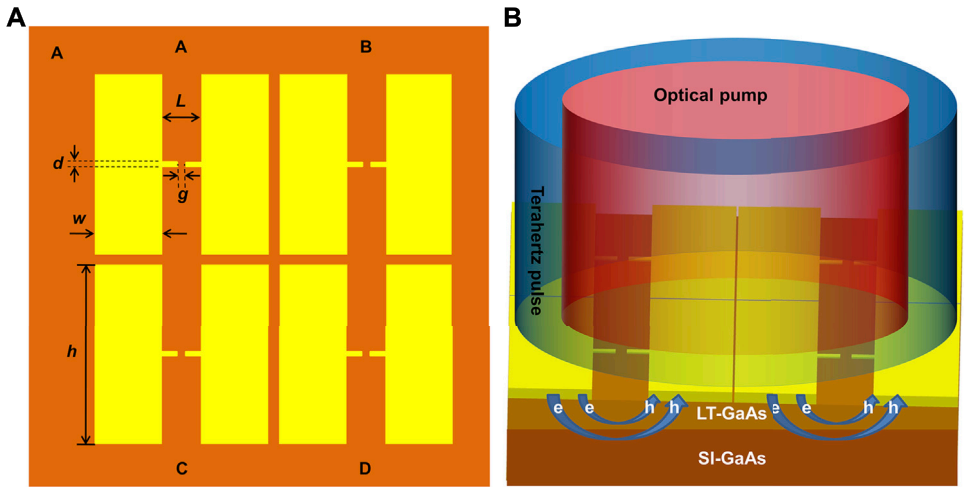

FIGURE 1 | Construction and use of 2 × 2 photoconductive antenna array: **(A)** Design structure of 2 × 2 photoconductive antenna array. **(B)** Schematic diagram of irradiation by laser and terahertz wave.

waves. The same phenomena will also reduce the synthesis efficiency of the PCA array detector [7]. At present, techniques to avoid the reverse current between adjacent antenna elements include employing shielding substrate between adjacent elements or using a micro-lenses array to split and focus the probe beams on the gaps [8, 9]. However, electrons transition from the valence band to the conduction band with the excitation of laser, the electrons generated in the antenna gap still can move to other antenna gaps due to the diffusion motion and the drift motion in response to the THz electric field. Therefore, these solutions cannot fundamentally solve the problem of reverse current between antenna elements.

In this work, a THz PCA array detector that eliminates the reverse current between the adjacent antenna elements is designed and fabricated, and its outstanding synthesis efficiency and signal-to-noise ratio have been demonstrated by comparing with a single antenna element.

ANTENNA DESIGN AND EXPERIMENTAL SETUP

Antenna Design

The structure diagram of the 2 × 2 PCA array detector is shown in **Figure 1A**. Its substrate is low-temperature-grown GaAs (LT-GaAs) with a thickness of 1 μm grown on (100) semi-insulating (SI)-GaAs at 250°C using MBE system. AuGeNiAu electrodes were deposited on the substrate by e-beam evaporation, and was metalized by rapid annealing to form an ohmic contact. The antenna element has a dipole length (L) of 250 μm, a dipole gap (g) of 50 μm, a dipole antenna width (d) of 30 μm, an electrode width (w) of 370 μm, and an electrode length (h) of 990 μm. The activation area of antenna element is 0.03 mm × 0.05 mm and the distance between adjacent antenna elements is about 10 μm. The pickup circuit designed in the experiment can not only output the synthetic signal of a PCA array detector, but also each signal of each antenna element by connecting different output ports.

Experimental Setup

In this paper, a THz time-domain spectroscopy system is used for measure the performance of the THz PCA array detector. A Ti: sapphire laser (Spectra-physics, MaiTai XF–1) with a center wavelength of 800 nm, a pulse width of 70 fs, and a repetition frequency of 80 MHz is used to excite the detector and the emitting antenna. The LT-GaAs PCA emitter with a gap of 150 μm was excited by a pump beam with the power of 200 mW and the voltage applied to the emitter was 300 V. The polarization direction of the THz electric field was parallel to the electrode gaps of the PCA array detector. The THz wave was focused on the PCA array detector through an off-axis parabolic mirror, and the diameter of focused THz beam measured by the knife edge method is 2.09 mm. The probe beam was focused to a spot with the diameter of 3 mm on the PCA array detector. The THz pulse and the laser pulse illuminate the PCA array detector vertically on the same side, as shown in **Figure 1B**. The output signal was recorded by a lock-in amplifier (SR830).

RESULTS

In order to explain that photo-generated carriers move freely throughout the semiconductor, an unmicromachined antenna array, which is similar to the interdigitated PCA detectors, was used for the verification experiment, we focused the laser with a power of 800 mW laser on the gap of one antenna element, and the diameter of the focus is 93 μm, the dark state resistance of the antenna was reduced from 1.1 GΩ to several MΩ. The resistance of other antenna elements in the unlit area was reduced by two orders of magnitude. In addition, the resistance between adjacent antenna elements was also reduced by two orders of magnitude,

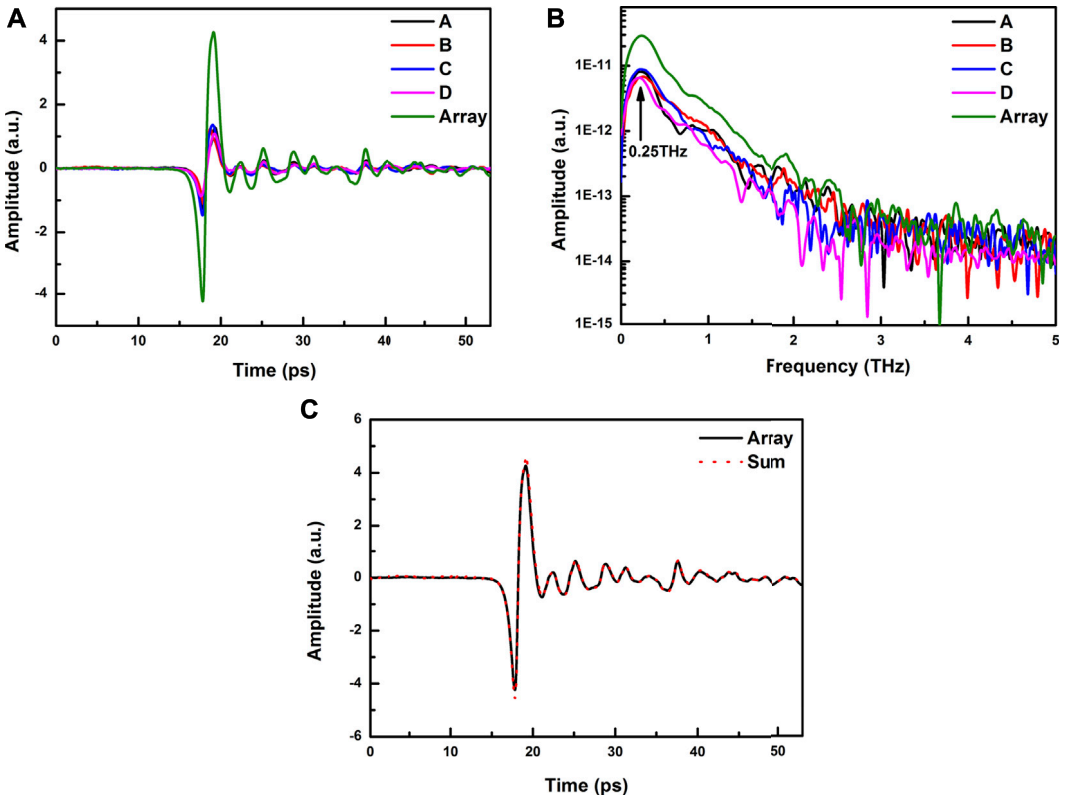

FIGURE 2 | Terahertz wave was detected by photoconductive antenna array: **(A)** Time-domain signals of antenna elements and array; **(B)** Frequency domain signals of antenna elements and array; **(C)** Synthesis efficiency of the antenna array.

indicating that the photo-generated carriers generated in one antenna gap are not limited to movement in this antenna gap. On the contrary, due to the THz electric field, the reverse current can be formed between the adjacent antenna elements, which causes the synthesis efficiency of the PCA array detector decrease. Therefore, the masking process between the array elements for the interdigitated PCA array detector cannot prevent the reverse current between the array elements. In this experiment, we cutting the substrate material of adjacent elements by high power laser, and rearranged the elements with proper distance to eliminate the reverse current between adjacent antenna elements, and the photo-generated carriers generated by the antenna elements were restricted from moving to other antennas. When one antenna element was triggered by laser, the resistance of other antenna elements does not change.

When the PCA array detector was excited by the probe beam with the power of 120 mW, the THz time-domain waveforms of the each antenna element and PCA array detector are shown in **Figure 2A**. The amplitude of THz time domain waveform of the PCA array detector is far greater than that of the antenna elements A, B, C and D when they work alone. Due to the difference of the antenna elements' performance and the uneven irradiation of laser and THz waves, the amplitudes of the time-domain waveforms output from each element antenna are different. At the same time, there is a time difference among the waveforms of antenna elements, and the largest one is about 300 fs between A and D. The reason is caused by the optical path difference between the probe beam and the THz beam received by each antenna element.

In addition, the bandwidth of the PCA array is same as that of the antenna elements. The resonant frequency of the antenna elements is the same as that of the antenna array, and all of them are 0.25 THz, which is marked in **Figure 2B**.

The output photocurrent of the PCA array detector under THz wave excitation can be calculated as,

$$J_i(t) = e\mu \int E_{THz}(t')N_i(t-t')dt'$$

Where, e is the electronic charge, μ is the electron mobility of LT-GaAs, E_{THz} is the incident THz electric field, and $N_i(t)$ is the number of photo-generated carriers on the i^{th} photoconductive antenna element. Due to the low carrier lifetime of LT-GaAs, $J_i(t) \propto E_{THz}$ [10, 11]. Since the PCA array detector is a parallel structure, the theoretical output current is:

$$J_{Array}(t) = \sum_{i=1}^{n} J_i(t)$$

Where n is the number of element antennas, $J_{Array}(t)$ is the current output by the PCA array detector, $\sum_{i=1}^{n} J_i(t)$ is the synchronous superposition of the output current when that each antenna element works independently, as shown in **Figure 2C**. But in the experiment, $J_{Array}(t)$ is always smaller

TABLE 1 | The amplitude and RMS noise of the time domain signal of the antenna elements and the array detector.

Antenna	Amplitude (A)	RMS noise (A)	SNR
Unit A	2.55624E-10	4.40724E-13	55
Unit B	2.37891E-10	8.67724E-13	49
Unit C	2.8485E-10	9.18471E-13	50
Unit D	1.96796E-10	7.01004E-13	49
Antenna array	8.5384E-10	6.45848E-13	62

than $\sum_{i=1}^{n} J_i(t)$. Since there is no reverse current between adjacent antenna elements, $J_{Array}(t) / \sum_{i=1}^{n} J_i(t)$ is the synthesis efficiency of the antenna array, and its efficiency reaches 93.7% in this paper. Since there is no reverse current between adjacent antenna elements, the time-domain signal output by the PCA array detector is approximately equal to the synchronous superposition of the time-domain signal output by all antenna elements.

Generally, the output noise current of the photoconductive detector mainly comes from Johnson-Nyquist noise and shot noise [12, 13]. The root mean square (RMS) value of the noise current output form the symmetrically pumped PCA array detector is as follows:

$$i = \sqrt{4k_B T \overline{G_p(t)} \Delta f} = \sqrt{\frac{4k_B T}{\frac{h\nu L^2}{\eta_e \left(\tau_n \mu_n + \tau_p \mu_p\right) P_0}} \Delta f}$$

where k_B is the Boltzmann constant, T is operation temperature in kelvin, $h\nu$ is the energy of the probe photons, η_e is the photoconductor external quantum efficiency, τ_n and τ_p are lifetimes of electrons and holes in the semiconductor, μ_n and μ_p are electron and hole mobility, P_0 is the DC component of the envelope surface of the optical probe, and Δf is the detection bandwidth. The data of RMS noise of the antenna elements and PCA array are listed in **Table 1**. The noise of the array antenna is lower than the average noise of the elements, that means the PCA array plays the role in reducing the overall noise.

Figure 3A and **Figure 3B** show the time-domain waveforms and frequency-domain spectra detected by the PCA array detector under different probe power, the signal amplitude increases with the increase of the probe power. When the probe power is only 1 mW, the PCA array detector still shows a good response curve. When the probe power increases from 1mW to 120 mW, the THz linear increases. When the probe power is greater than 120 mW, the amplitude tends to be saturated. This saturation is caused by the screening effect,

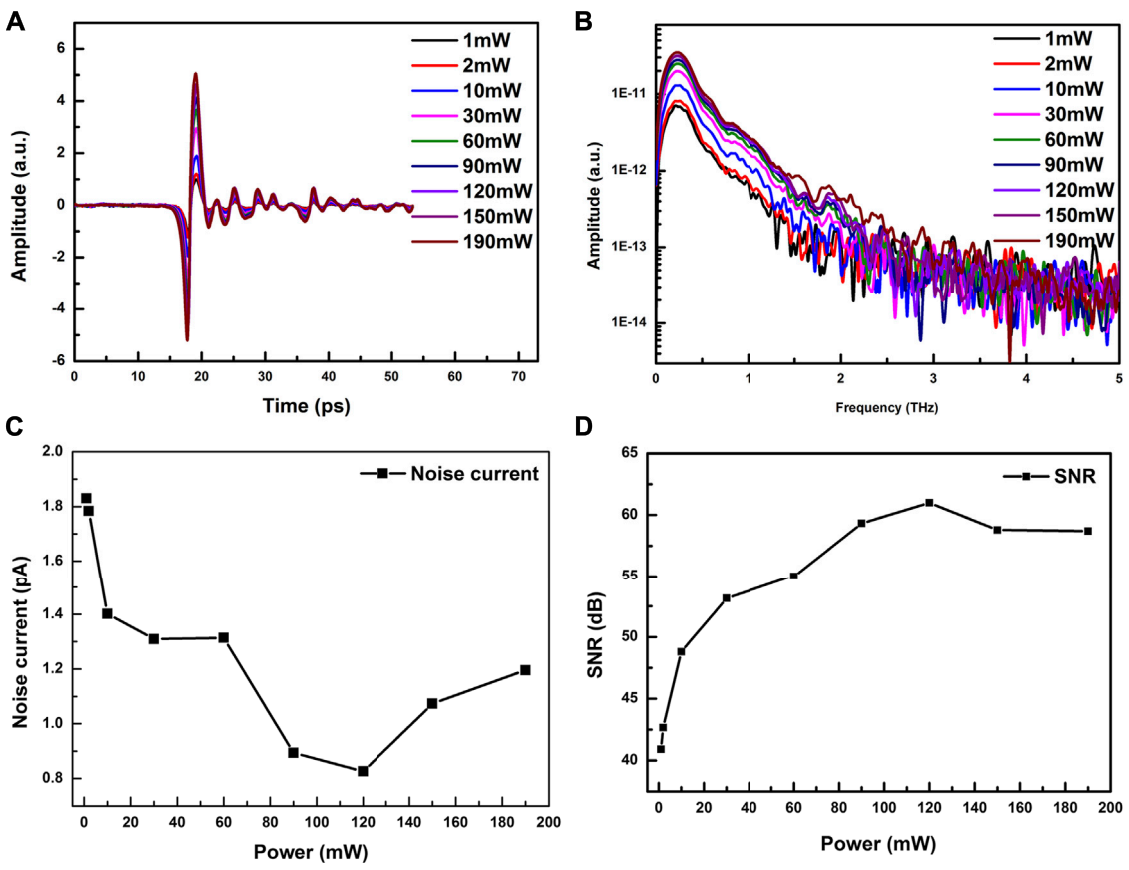

FIGURE 3 | The response of the PCA array detector under different probe power. **(A)** Time-domain spectrum; **(B)** Frequency domain spectrum; **(C)** The noise current of the PCA array detector; **(D)** SNR of the PCA array detector.

which is related to the carrier density generated on the GaAs surface. The influence of the screening effect on the PCA emitter has been reported [14, 15], and its influence on the PCA detector can be expressed as [16].

$$\boldsymbol{E}(\boldsymbol{t}) = \boldsymbol{E}_{\boldsymbol{THz}}(\mathbf{t}) - \frac{\boldsymbol{P}(\mathbf{t})}{\boldsymbol{\alpha\varepsilon}}$$

$E_{THz}(t)$ is the incident THz electric field, ε and α are the dielectric constant and geometric factor of GaAs, respectively. $P(t)$ is the polarization caused by the separation of electron-hole pairs, and it increases as the density of photo-generated carrier increases. The detection bandwidth of the PCA array detector is about 2.5 THz, which is the same as that of a single antenna. At the same time, the noise data of the detector was measured while the terahertz source was working normally. The SNR is proportional to the laser power when the probe power is lower than 120 mW, and the maximum SNR of the detector reaches 62 dB at 120 mW. When the power of probe beam exceeds 120 mW, the noise of the detection current increases and the SNR decreases due to the carrier shielding effect, as is shown in **Figure 3C**and **Figure 3D**.

CONCLUSION

In summary, we proposed a PCA array detector with high synthesis efficiency. According to experimental verification and theoretical analysis, the reverse current between the array elements is eliminated, and the synthesis efficiency of the PCA array detector reaches 93.7%. At the same time, the results show that the detector has a low noise, which is lower than the average noise of the elements. The bandwidth of the PCA array detector is about 2.5 THz. Within the probe power of 0–120 mW, the THz amplitude of detector shows a linear growth trend. When the probe power exceeds 120 mW, the signal amplitude tends to be saturated and the current noise increases due to the carrier shielding effect. The detector has a maximum SNR of 62 dB at the probe power of 120 mW power. The concept of the proposed PCA array detector can be widely used in both large size and small size PCA array detector to improve its detection efficiency.

DATA AVAILABILITY STATEMENT

The raw data supporting the conclusions of this article will be made available by the authors, without undue reservation.

AUTHOR CONTRIBUTIONS

Conceptualization, WS; methodology, LH; formal analysis, ZW; data curation, MW and CL; writing—original draft preparation, ZW; writing—review and editing, WS. All authors have read and agreed to the published version of the manuscript.

FUNDING

This research was funded by the National Key Research and Development Program of China (Grant No. 2017YFA0701005), the National Natural Science Foundation of China (Grant No. 51807161, Grant No. 62075179), the Natural Science Foundation of Shaanxi Province (Grant No. 2019JZ-04), Special Scientific Research Plan of Shaanxi Provincial Education Department, China (Grant No. 19JK0297).

REFERENCES

1. Wu Q, and Zhang X-C. Free-space Electro-Optics Sampling of Mid-infrared Pulses. *Appl Phys Lett* (1997) 71(10):1285–6. doi:10.1063/1.119873
2. Neu J, and Schmuttenmaer CA. Tutorial: An Introduction to Terahertz Time Domain Spectroscopy (THz-TDS). *J Appl Phys* (2018) 124(23):231101. doi:10.1063/1.5047659
3. Han PY, and Zhang X-C. Coherent, Broadband Midinfrared Terahertz Beam Sensors. *Appl Phys Lett* (1998) 73(21):3049–51. doi:10.1063/1.122668
4. Formanek F, Brun M-A, Umetsu T, Omori S, and Yasuda A. Aspheric Silicon Lenses for Terahertz Photoconductive Antennas. *Appl Phys Lett* (2009) 94(2): 021113. doi:10.1063/1.3072357
5. Dreyhaupt A, Winnerl S, Dekorsy T, and Helm M. High-intensity Terahertz Radiation from a Microstructured Large-Area Photoconductor. *Appl Phys Lett* (2005) 86(12):121114–2756. doi:10.1063/1.1891304
6. Dreyhaupt A, Winnerl S, Helm M, and Dekorsy T. Optimum Excitation Conditions for the Generation of High-Electric-Field Terahertz Radiation from an Oscillator-Driven Photoconductive Device. *Opt Lett* (2006) 31(10): 1546. doi:10.1364/OL.31.001546
7. Hattori T, Egawa K, Ookuma SI, and Itatani T. Intense Terahertz Pulses from Large-Aperture Antenna with Interdigitated Electrodes. *Jpn J Appl PhysicsLetters Express Lett* (2006) 45(No. 15):L422–L424. doi:10.1143/jjap.45.l422
8. Yardimci NT, and Jarrahi M. High-performance terahertz detectors based on plasmonic nano-antennas[[Conference presentation]. In: 41st International Conference on Infrared, Millimeter, and Terahertz waves (IRMMW-THz), Copenhagen, September, 2016. (Denmark: IEEE) (2016):1–2. doi:10.1109/irmmw-thz.2016.7758867
9. Pradarutti B, Müller R, Freese W, Matthäus G, Riehemann S, Notni G, et al. Terahertz Line Detection by a Microlens Array Coupled Photoconductive Antenna Array. *Opt Express* (2008) 16(22):18443–50. doi:10.1364/oe.16.018443
10. Shen YC, Upadhya PC, Beere HE, Linfield EH, Davies AG, Gregory IS, et al. Generation and Detection of Ultrabroadband Terahertz Radiation Using Photoconductive Emitters and Receivers. *Appl Phys Lett* (2004) 85(2): 164–6. doi:10.1063/1.1768313
11. Tani M, Sakai K, and Mimura H. Ultrafast Photoconductive Detectors Based on Semi-insulating GaAs and InP. *Jpn J Appl Phys* (1997) 36(Part 2, No. 9A/B): L1175–L1178. doi:10.1143/jjap.36.l1175
12. Wang N, and Jarrahi M. Noise Analysis of Photoconductive Terahertz Detectors. *J Infrared Milli Terahz Waves* (2013) 34(9):519–28. doi:10.1007/s10762-013-9995-1
13. Hou L, and Shi W. An LT-GaAs Terahertz Photoconductive Antenna with High Emission Power, Low Noise, and Good Stability. *IEEE Trans Electron Devices* (2013) 60(5):1619–24. doi:10.1109/ted.2013.2253467
14. Murakami H, Fujiwara S, Kawayama I, and Tonouchi M. Study of Photoexcited-Carrier Dynamics in GaAs Photoconductive Switches Using Dynamic Terahertz Emission Microscopy. *Photon Res* (2016) 4(3):A9–A15. doi:10.1364/prj.4.0000a9
15. Awad M, Nagel M, Kurz H, Herfort J, and Ploog K. Characterization of Low Temperature GaAs Antenna Array Terahertz Emitters. *Appl Phys Lett* (2007) 91(18):181124. doi:10.1063/1.2800885

16. Murakami H, Mizui K, and Tonouchi M. High-sensitivity Photoconductive Detectors with Wide Dipole Electrodes for Low Frequency THz Wave Detection. *J Appl Phys* (2019) 125(15):151610. doi:10.1063/1.5080750

Conflict of Interest: The authors declare that the research was conducted in the absence of any commercial or financial relationships that could be construed as a potential conflict of interest.

Publisher's Note: All claims expressed in this article are solely those of the authors and do not necessarily represent those of their affiliated organizations, or those of the publisher, the editors and the reviewers. Any product that may be evaluated in this article, or claim that may be made by its manufacturer, is not guaranteed or endorsed by the publisher.

frontiers in Physics

ORIGINAL RESEARCH
published: 08 September 2021
doi: 10.3389/fphy.2021.751335

Theoretical Study on Characteristics of Glow Discharged Neon Gas and Its Interaction With Terahertz Waves

Lei Hou, Yaodong Wang, Junnan Wang, Lei Yang and Wei Shi*

The Key Laboratory of Ultrafast Photoelectric Technology and Technology and Terahertz Science in Shaanxi, Xi'an University of Technology, Xi'an, China

Discharge gases have been used to detect terahertz (THz) waves, however, there are few relevant theoretical studies. The neon glow discharge model is established by COMSOL Multiphysics software, the characteristics of glow discharged neon and the interaction of the discharged gas with THz waves were investigated. The results show that with the increase of THz wave's frequency, the transmittance increases, the change of plasma discharge characteristics caused by THz wave can be used for THz wave detection. The results provide a theoretical basis for the development of cheap, room temperature THz wave detector with fast response speed, and high sensitivity.

Keywords: terahertz wave, neon gas, glow discharge, COMSOL multiphysics, theoretical study

OPEN ACCESS

Edited by:
Yingxin Wang,
Tsinghua University, China

Reviewed by:
Yan Peng,
University of Shanghai for Science and Technology, China
Jun Wang,
University of Electronic Science and Technology of China, China

****Correspondence:***
Lei Hou
houleixaut@126.com

Specialty section:
This article was submitted to Optics and Photonics, a section of the journal Frontiers in Physics

Received: *31 July 2021*
Accepted: *24 August 2021*
Published: *08 September 2021*

Citation:
Hou L, Wang Y, Wang J, Yang L and Shi W (2021) Theoretical Study on Characteristics of Glow Discharged Neon Gas and Its Interaction With Terahertz Waves. Front. Phys. 9:751335. doi: 10.3389/fphy.2021.751335

INTRODUCTION

Terahertz (THz) radiation spanning from 0.1 to 10 THz falls between the microwave and infrared spectral ranges [1]. In recent years, THz technology applications have been rapidly expanding in areas including nondestructive material evaluation, imaging, sensing, and wireless communication [2]. In the development of THz technology, how to detect THz radiation efficiently is of great significance to the progress of THz technology.

At present, commercial room temperature THz detectors, including Golay cells, pyroelectric detectors and Schottky diodes, have the disadvantages of slow speed, limited bandwidth or high price, so they are difficult to be widely used in THz community [3]. In 1952, the glow discharge plasma was used to detect microwave radiation [4]. It was later discovered that glow discharge plasma can also be used for detection in THz, infrared and ultraviolet bands ([5, 6]). The glow discharge detectors (GDD) based on commercial neon lamps are potential detectors with high sensitivity. In addition, the use of glow discharge plasma to detect THz radiation has the advantages of low cost, wide dynamic range, wide spectral range, room temperature operation, and simple use [7].

The interaction between gas discharge plasma and electromagnetic waves has been investigated in the infrared and microwave bands [8–13]. These preliminary studies have shown that far infrared radiation with relatively high field amplitudes can be detected by GDDs, and the detection mechanism is attributed to the incident far infrared radiation increasing the energy of the plasma, which increase the discharge current. The detection of THz radiation by GDDs can be explained by the interaction of THz wave and plasma in discharge gases. Since the frequency of the glow discharge plasma in a commercial neon lamp is about a few GHz [7], the plasma is almost transparent to the incident THz radiation. In the neon lamp, the strong electric field of the applied voltage will cause the electrons to move from the cathode to the anode, the incident THz wave is absorbed by free electrons and this process cause the discharge current to slightly changes, the sign of

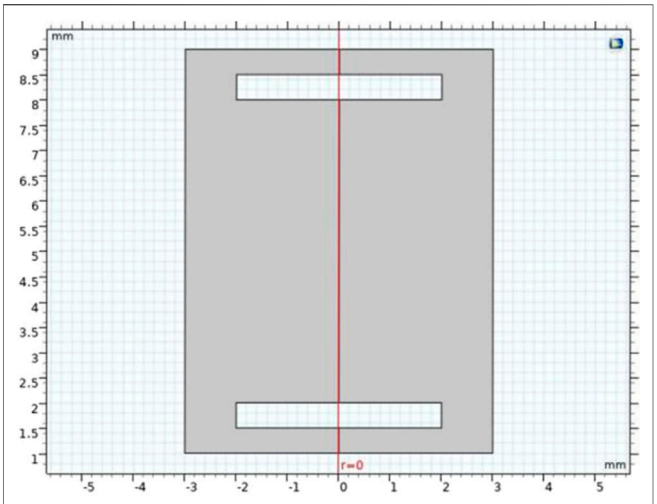

FIGURE 1 | 2D structure of gas discharge model.

the change depends on which of the enhanced ionization and enhanced diffusion mechanisms is dominant in the detection mechanism [14]. Ref. 15 have shown that the main mechanism for detecting THz radiation with GDDs is to enhance cascade ionization, which causes an increase in discharge [15]. The transmission of THz wave decreasing with increasing bias voltage for certain frequencies [16].

TABLE 1 | Reaction formulas and reaction types in discharge process of neon gas.

Reaction formula	Reaction type	Energy loss
$e + Ne \rightarrow e + Ne$	Elastic collision	–
$e + Ne \rightarrow e + Ne^*$	Excitation	16.62
$e + Ne^* \rightarrow e + Ne$	Excitation	–16.62
$e + Ne \rightarrow 2e + Ne^+$	Ionization	21.56
$e + Ne \rightarrow e + Ne^+$	Ionization	4.92
$Ne^* + Ne^* \rightarrow e + Ne + Ne^+$	Surface reaction	–
$Ne^* + Ne \rightarrow Ne + Ne$	Surface reaction	–

In this paper, we provided a theoretical basis for the development of a new type of THz wave detector based on neon glow discharge by investigating the characteristics of neon glow discharge and its interaction with THz waves.

CHARACTERISTICS OF NEON DISCHARGE

2D Neon Discharge Model

In this work, we use the plasma module in COMSOL Multiphysics software to establish the neon discharge model, and obtain the plasma characteristic parameters and electric field distribution parameter diagram, and verify whether the model realizes the glow discharge and the feasibility of the model by comparing with the existing theoretical and experimental results.

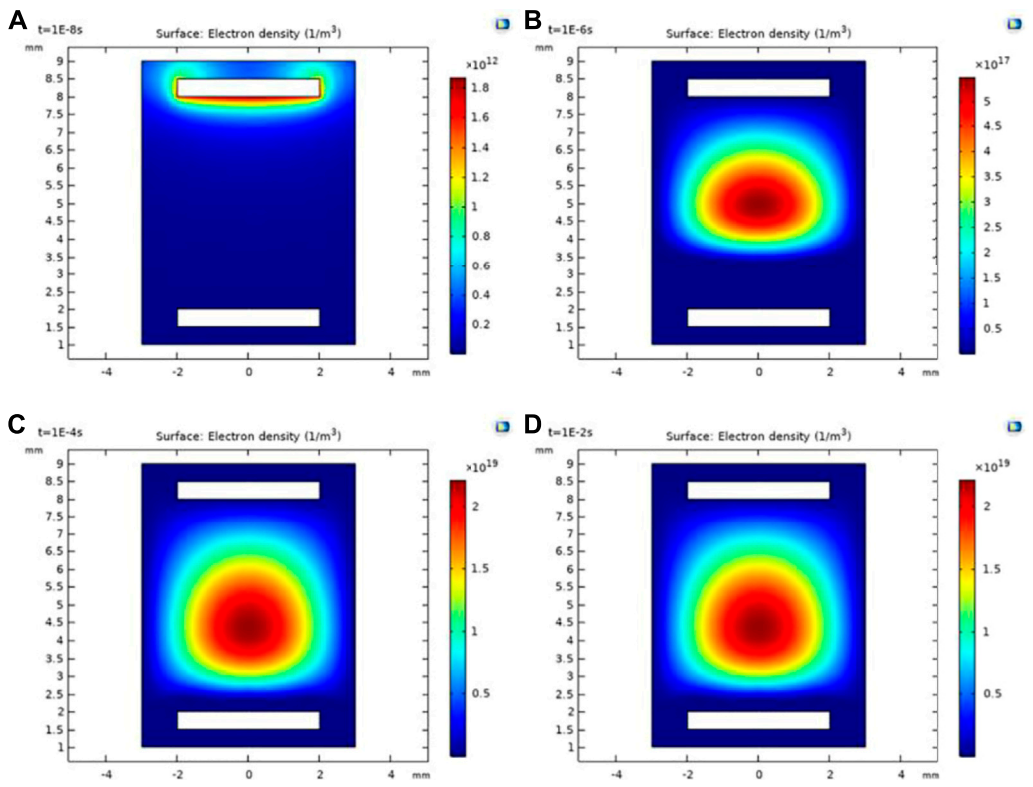

FIGURE 2 | Distributions of electron density at different times. **(A)** $t = 1.0 \times 10^{-8}$s; **(B)** $t = 1.0 \times 10^{-6}$s; **(C)** $t = 1.0 \times 10^{-4}$s; **(D)** $t = 1.0 \times 10^{-2}$s.

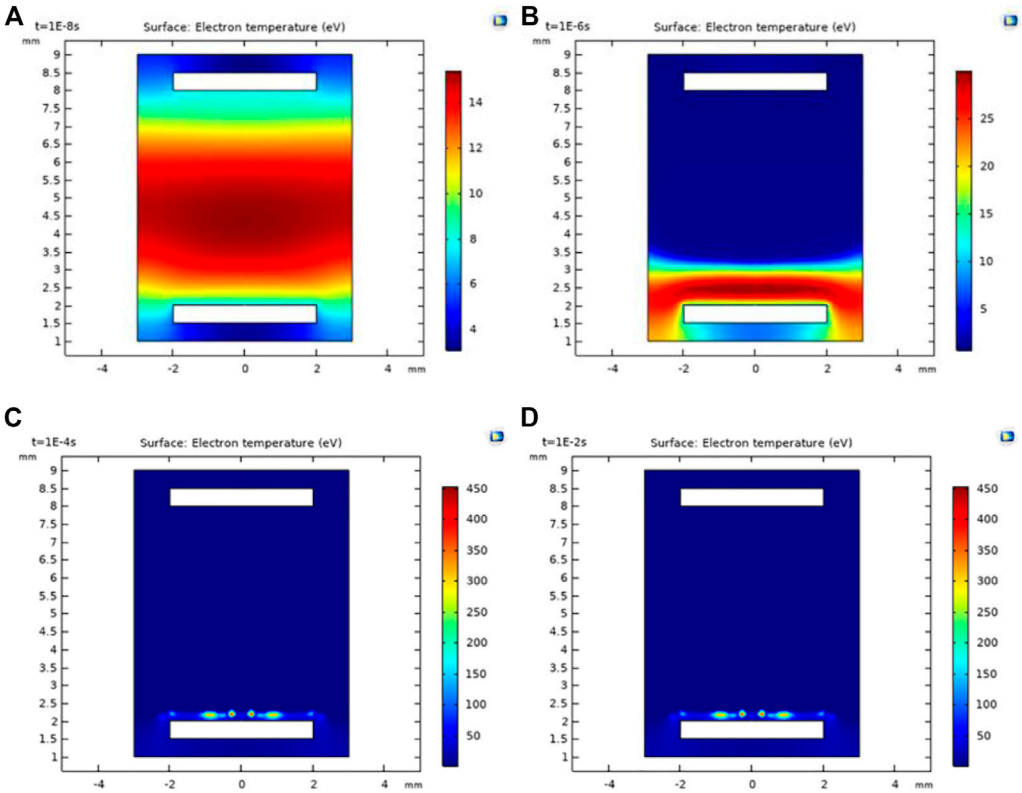

FIGURE 3 | Electron temperature distribution at different times. **(A)** t = 1.0×10^{-8}s; **(B)** t = 1.0×10^{-6}s; **(C)** t = 1.0×10^{-4}s; **(D)** t = 1.0×10^{-2}s.

Assuming that the system is in an ideal plasma environment, the plasma discharge area is filled with pure neon gas. A two-dimensional axisymmetric model was established as shown in **Figure 1**. The outer length of the model is 6mm and the width is 8mm. The white rectangles on the upper and lower sides are electrodes. The length is 4mm, the width is 0.5mm, and the electrode spacing is 6mm. The gray area between two electrodes is neon discharge area, the gas inside the plate is divided into outer region and inner region. Because the fluid does not distinguish between internal and external boundary, errors are easy to occur in calculation if the electrode is set to a metal. Due to this reason the electrodes regions were "hollowed out".

The discharge area includes discharge module, particle drift diffusion module and energy module.

Discharge module: Neon's discharge region includes four kinds of particles, namely electron (e), neon atom (Ne), metastable neon atom (Ne^*) and neon ion (Ne^+). In the calculation of the variation of the dynamic parameters of the gas discharge system, the particle collision of Ne and Ne^+, including elastic collision, excitation and ionization, and the surface reaction on the electrode surface should also be considered. The reaction formulas and reaction types are shown in **Table 1**.

Ion drift diffusion module: it contains the electron drift diffusion equation and the input of model parameters, the setting of gas temperature, gas pressure and reduced electron mobility parameters.

Energy module: it includes insulation surface, initial value, metal contact (anode), grounding (cathode), dielectric contact, wall, as so on. The initial value is the initial electron density and the applied voltage value. Metal contact include the setting of type setting and circuit type setting. The circuit types include RC circuit, ballast resistance, DC isolation resistance and DC isolation capacitor. In this paper, we choose RC circuit.

Simulation Results of Neon Discharge Characteristics

According to the volt-ampere characteristic curve of gas discharge, at first, due to the migration movement of electrons and positive ions, a small current is generated in the discharge tube, and the space charge formed by positive ions is conducive to the movement of electrons towards the anode in the tube. As the electrons slowly gather at the anode, they collide and ionize frequently with the gas atoms near the anode, and a large number of electrons and positive ions generate. The electrons continue to collide with the gas atoms, and the positive ions move to the cathode under the action of the electric field, bombard the cathode and emit secondary electrons, which then collide with the gas particles. And finally the discharge reaches a stable state.

In the 2D Neon discharge model, the electrode spacing is set to 6mm, the discharge voltage is 200V, and the initial plasma density

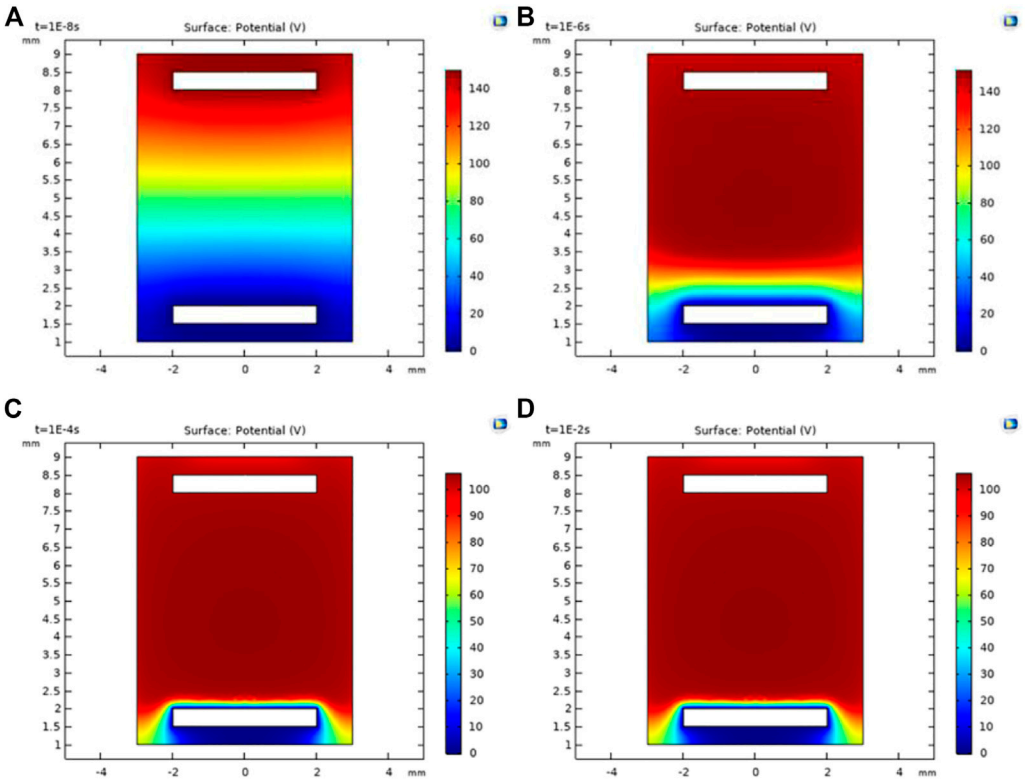

FIGURE 4 | Electric potential distribution at different times. **(A)** t = 1.0×10^{-8}s; **(B)** t = 1.0×10^{-6}s; **(C)** t = 1.0×10^{-4}s; **(D)** t = 1.0×10^{-2}s.

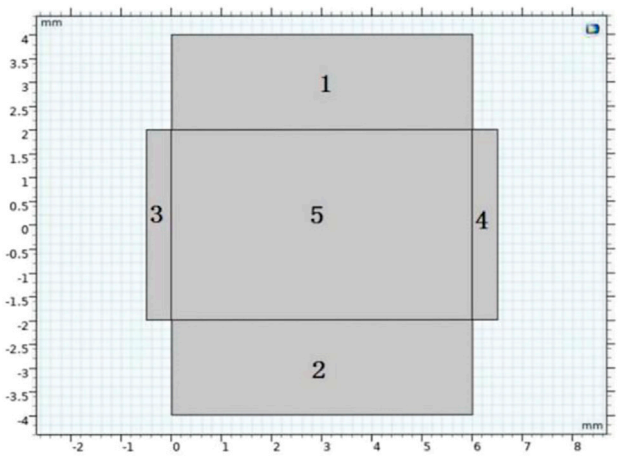

FIGURE 5 | Model of interaction of discharged neon and THz wave.

is 1×10^{13}m^{-3}, and the resulting trend distribution of electron density, electron temperature and electric potential are shown in **Figures 2–4**.

Figure 2 shows the distribution of electron density at different time. In **Figure 2A**, when t = 1.0×10^{-8}s, a large number of electrons and positive ions are generated near the anode due to the collision between electrons and gas atoms, and the electron density is relatively high. In **Figures 2B,C**, from t = 1.0×10^{-6}s to t = 1.0×10^{-4}s, the positive ion moves to the cathode under the action of the electric field, the cathode produces secondary electrons under the bombardment of the positive ion, and the electron density near the cathode is increasing. In **Figures 2C,D**, after when t = 1.0×10^{-4}s, the electron density near the cathode reaches the maximum value, until when t = 1.0×10^{-2}s, the electron density distribution does not change any more, and the discharge reaches a stable state.

Figure 3 shows the distribution of electron temperature at different time. Electron temperature is used to describe the thermal energy of particles. In **Figure 3A**, when t = 1.0×10^{-8}s, electrons continue to move to the anode under the action of the electric field, and the temperature of the electron near the anode is relatively high. In **Figure 3B**, when t = 1.0×10^{-6}s , due to the bombardment of positive ions on the cathode, a large number of electrons are generated near the cathode, which increases the temperature of the electrons near the cathode. The electrons reach the anode from the cathode under the bias electric field. In **Figure 3C**, when t = 1.0×10^{-4}s, the electron' energy decreases due to collision. Until **Figure 3D**, when t = 1.0×10^{-2}s, there is no change in the electron temperature distribution, and finally the discharge reaches a stable state.

Figure 4 shows the distribution of electric potential at different time. In **Figure 4A**, when t = 1.0×10^{-8}s, the discharge has just begun, and the electric potential distribution is linear between the two electrodes. In **Figures 4B,C**, with the increase of secondary

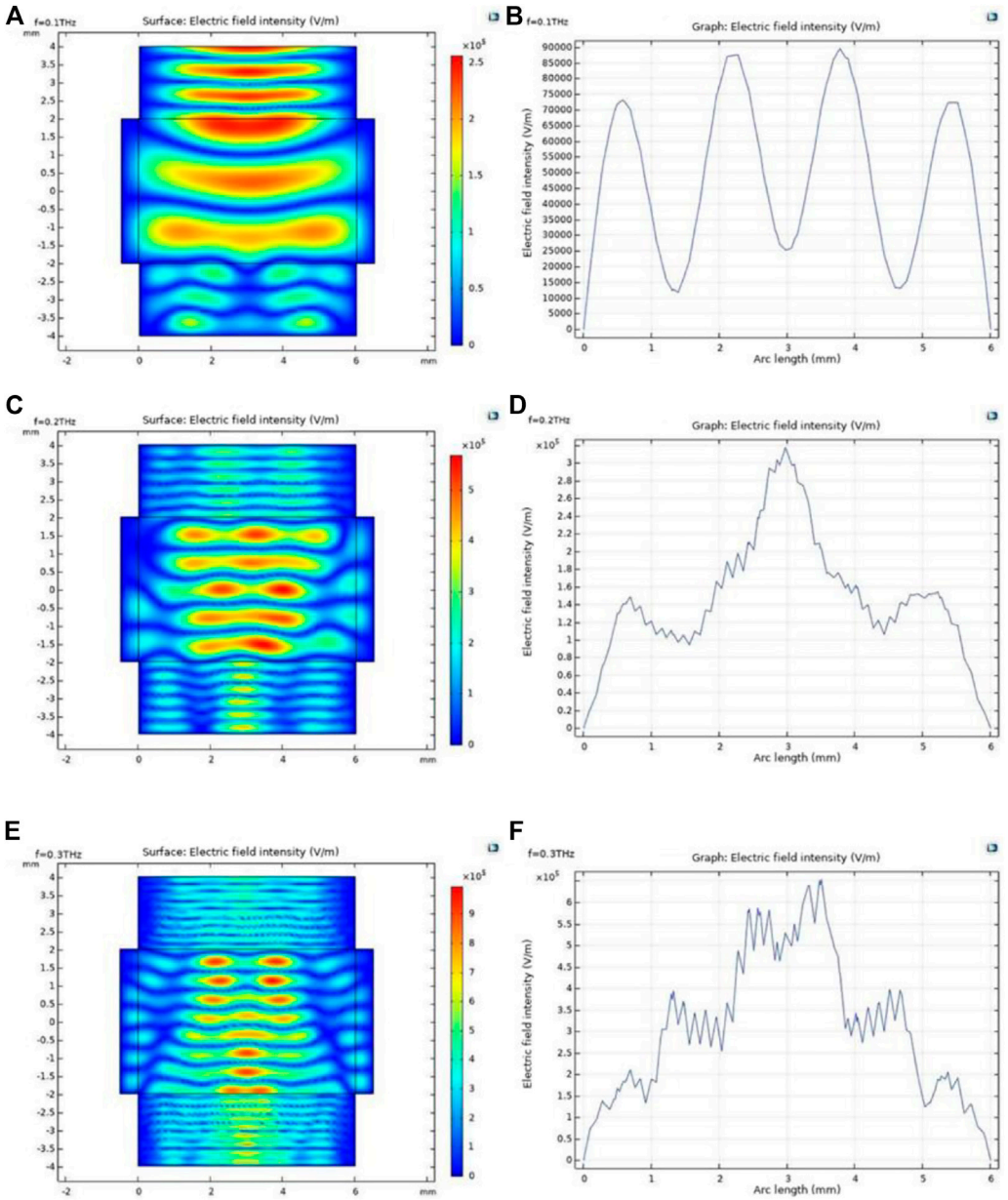

FIGURE 6 | Electric filed intensity distribution of discharge interval **(left column)** and the distribution of THz electric field along the horizontal line of y = −2.5 mm after it passing through the discharge region **(right column)** at different THz frequencies. **(A,B)** f = 0.1THz; **(C,D)** f = 0.2THz; **(E,F)** f = 0.3THz.

electrons emitted by the cathode, the voltage drop gradually approaches the cathode. In **Figure 4D**, when $t = 1.0 \times 10^{-2}$s, there is no change in the electric potential distribution and a stable state is reached.

According to the analysis of simulation results, our model is consistent with the glow discharge theory, so the model can be used to simulate a gas glow discharge. In our simulation, we have simulated the glow discharge respectively when the electrode spacing is 3mm, 4mm, 5mm, 6mm and 7mm, the discharge voltage is 50V, 100V, 150V, 200V and 250V, the initial electron density is 1×10^{11}m^{-3}, 1×10^{13}m^{-3} and 1×10^{15}m^{-3}, respectively. And we found that the neon gas glow discharge is the most stable when the electrode spacing is 6mm, the discharge voltage is 200V, and the initial electron density is 1×10^{13}m^{-3}.

SIMULATION OF INTERACTION OF NEON DISCHARGE AND THZ WAVE

Simulation Model

Based on the results of part 2, we established the interaction model of neon gas and THz wave as shown in **Figure 5**. The

model is divided into five regions. Region one is the incident region; region 2 is the transmission region with a size of 6mm × 2mm; region 3 is the cathode which is grounded; region four is the anode which is connected to the bias voltage, and the size of regions 3 and four is 0.5mm × 4mm; region 5 is a gas discharge area with a size of 6mm × 4mm. THz radiation perpendicularly incident to the discharge area.

The Influence of Frequency of THz Waves on Glow Discharge

We suppose that the electric field is no loss in the incident area. When the THz wave illuminates the discharge area, the part of incident energy is absorbed by the electrons, which will enhance the interaction between the charged particles and the neutral particles in the discharge area. The temperature of the electrons rises to the extent that new electrons can be generated through ionization, and the ionization rate is increased. With the increase of the kinetic energy of electrons, the ionization rate and the number of electrons increases, which increases the frequency of collisions between electrons and neutral particles. The effect of frequency on the interaction between THz wave and plasma was investigated by simulating the electric field distribution of THz wave with different THz frequencies before and after passing through the neon discharge region. The simulated results are shown in **Figures 6A,C,E**.

Take a horizontal line parallel to the discharge section at $y = -2.5$mm in **Figure 5**, and then get the distribution of THz electric field along the line after it passing through the discharge region. The distribution curves of electric field intensity are shown in **Figures 6B,D,F** which illustrates the energy changes of the THz wave after passing through the discharge region.

When the THz wave enters the discharge region, the plasma absorbs the energy of the THz wave to improve its internal energy, collision frequency increases, and a large number of electrons, neon ions and excited neon atoms are constantly produced. After that, high-energy electrons and excited neon atoms are consumed in large quantities, new electrons generated and the electron density in the discharge region increases. The external energy input is difficult to maintain the frequent and violent inelastic collision reaction, and the plasma gradually reaches a new balance. It can be seen from the **Figure 6**, the peak value of the electric field intensity distribution curve is increasing and different peaks appear. The reason is that the interaction of electrons and neutral particles in the plasma is strengthened, which leads to the decrease of energy absorbed by electrons from THz waves with the increase of frequencies. The transmittance of THz wave increases in the discharge region, and the electric field intensity increases in the transmission region. The absorbed THz waves change the plasma density and the potential between the two electrodes also will changes, the THz intensity can be detected according the potential change.

CONCLUSION

In this paper, the discharge characteristics of neon and its interaction with THz wave are simulated. The neon glow discharge model is established by COMSOL Multiphysics software, and the results are consistent with the glow discharge theory. Then, the neon glow discharge model with stable discharge interval is obtained. Finally, based on the neon glow discharge model, the THz electric field intensities of THz wave passing through the discharge region under different terahertz wave frequencies are investigated. The results show that with the increase of THz frequency, the transmittance of terahertz wave is strong and the loss decreases. The results of the paper provide a theoretical basis for the development of cheap, room temperature THz wave detector with fast response speed, and high sensitivity.

DATA AVAILABILITY STATEMENT

The raw data supporting the conclusions of this article will be made available by the authors, without undue reservation.

AUTHOR CONTRIBUTIONS

LH: Conceptualization, Methodology, Writing-Reviewing and Editing; YW: Investigation, Simulation, Writing-Original Draft; JW: Investigation, Results analysis; LY: Methodology; WS: Conceptualization. All authors agree to be accountable for the content of the work.

FUNDING

This work was supported by the National Natural Science Foundation of China (grant numbers 62075179, 61575161); the Natural Science Foundation of Shaanxi Province (grant number 2019JZ-04); the Shaanxi Key Laboratory of Ultrafast Photoelectronic Technology and Terahertz Science (grant number 2018SZS-06); the Xi'an Key Laboratory of Ultrafast Photoelectronic Device Technology (grant number 201805055ZD6CG39).

REFERENCES

1. Siegel PH. Terahertz Technology. *IEEE Trans Microwave Theor Techn* (2002) 50(3):910–28. doi:10.1109/22.989974
2. Jia W, Liu M, Lu Y, Feng X, Wang Q, Zhang X, et al. Broadband Terahertz Wave Generation from an Epsilon-Near-Zero Material. *Light Sci Appl* (2021) 10(1):11. doi:10.1038/s41377-020-00452-y
3. Lewis RA. Terahertz Imaging and Spectroscopy Methods and Instrumentation. *Encyclopedia Spectrosc Spectrom* (2017) 422–6. doi:10.1016/B978-0-12-409547-2.12146-8
4. Burroughs G, and Bronwell A. High-Sensitivity Gas Tube Detector. *Tele-Tech* (1952) 11:62.
5. Severin PJW, and van Nie AG. A Simple and Rugged Wide-Band Gas Discharge Detector for Millimeter Waves. *IEEE Trans Microwave Theor Techn* (1966) 14(9):431–6. doi:10.1109/TMTT.1966.1126292

6. Lei H, and Zhang XC. Broadband Detector Measures IR, Millimeter & THz Waves. In: 2009 34th International Conference on Infrared, Millimeter, and Terahertz Waves IEEE (2009) doi:10.1109/ICIMW.2009.5325580
7. Kopeika NS. Glow Discharge Detection of Long Wavelength Electromagnetic Radiation: Cascade Ionization Process Internal Signal Gain and Temporal and Spectral Response Properties. *IEEE Trans Plasma Sci* (1978) 6(2):139–57. doi:10.1109/TPS.1978.4317104
8. Ferrari RL. Plasma Diagnostic Techniques. Edited by R. H. Huddlestone and S. L. Leonard. Academic Press, 1965, Pp. 627, $19.50. *J Plasma Phys* (1967) 1(01):156. doi:10.1017/s0022377800003160
9. Raizer YP. *Gas Discharge Physics*. Berlin, Germany: Springer (1991).
10. Kopeika NS, and Farhat NH. Video Detection of Millimeter Waves with Glow Discharge Tubes: Part I—Physical Description; Part II—Experimental Results. *IEEE Trans Electron Devices* (1975) 22(8):534–48. doi:10.1109/t-ed.1975.18175
11. Abramovich A, Kopeika NS, Rozban D, and Farber E. Inexpensive Detector for Terahertz Imaging. *Appl Opt* (2007) 46(29):7207–11. doi:10.1364/ao.46.007207
12. Abramovich A, Kopeika NS, and Rozban D. THz Polarization Effects on Detection Responsivity of Glow Discharge Detectors (GDDs). *IEEE Sensors J* (2009) 9(10):1181–4. doi:10.1109/JSEN.2009.2027415
13. Hou L, Park H, and Zhang X-C. Terahertz Wave Imaging System Based on Glow Discharge Detector. *IEEE J Select Top Quan Electron.* (2011) 17(1): 177–82. doi:10.1109/JSTQE.2010.2045640
14. Alasgarzade N, Nebioğlu MA, Takan T, Uzun-Kaymak IU, Sahin AB, and Altan H. Investigating Glow Discharge Detectors as a Millimeter-Wave/ Terahertz Radiation Detection Tool. In: M. Pereira and O. Shulika, editors *THz for CBRN and Explosives Detection ans Diagnosisa. NATO Science for Peace and Security Series B: Physics and Biophysics*. Dordrecht: Springer (2017). doi:10.1007/978-94-024-1093-8_21
15. Rozban D, Kopeika NS, Abramovich A, and Farber E. Terahertz Detection Mechanism of Inexpensive Sensitive Glow Discharge Detectors. *J Appl Phys* (2008) 103(9): 093306–343. doi:10.1063/1.2917386
16. Çınar K, Altan H, and Şahin AB. THz Transmission and Detection through Glow Discharge Detectors. In: Spie Defense, Security, & Sensing (2013). doi:10.1117/12.2017967

Conflict of Interest: The authors declare that the research was conducted in the absence of any commercial or financial relationships that could be construed as a potential conflict of interest.

Publisher's Note: All claims expressed in this article are solely those of the authors and do not necessarily represent those of their affiliated organizations, or those of the publisher, the editors and the reviewers. Any product that may be evaluated in this article, or claim that may be made by its manufacturer, is not guaranteed or endorsed by the publisher.

frontiers in Physics

ORIGINAL RESEARCH
published: 22 September 2021
doi: 10.3389/fphy.2021.744286

Self-Mixing Signal Characteristics of Complex-Coupled Distributed-Feedback Terahertz Quantum-Cascade Lasers

Lei Ge[1], Ning Yang[1], Jian Wang[2], Weidong Chu[1], Suqing Duan[1], Yan Xie[3], Yingxin Wang[3], Lianhe Li[4] and Edmund Linfield[4]*

[1]Institute of Applied Physics and Computational Mathematics, Beijing, China, [2]Department of Physics, Beijing Jiaotong University, Beijing, China, [3]Department of Engineering Physics, Tsinghua University, Beijing, China, [4]School of Electronic and Electrical Engineering, University of Leeds, Leeds, United Kingdom

Self-mixing interference (SMI) in terahertz quantum cascade lasers (THz QCLs) is one of the significant approaches for coherent THz imaging and sensing techniques. Here, the output characteristics of SMI in distributed feedback (DFB) THz QCLs from the index-to the gain-coupling regimes are studied using the coupled wave theory and the multi-mode rate equation method. A mode hopping phenomenon is found to occur when the DFB coupling factor changes from index-coupling to gain-coupling, and the characteristics of the self-mixing signals of DFB-QCLs change greatly with this mode hopping. With the modulus of the coupling factor fixed and its argument varied from 0 to $\pi/2$, an extreme point of the self-mixing frequency and power signals of DFB-QCLs is found at $\pi/9$ due to the mode hopping. For index-coupling dominated DFB-QCLs, both the varying ranges of the self-mixing frequency signals and amplitudes of power signals increase with increasing DFB coupling factor argument. For gain-coupling dominated DFB-QCLs, with increasing argument value, the amplitude of the self-mixing power signal increases, but the varying range of the self-mixing frequency signal decreases. With the argument of the coupling factor fixed, we also found that the varying ranges of the self-mixing frequency signals decrease with increasing modulus for both index-coupling dominated and gain-coupling dominated DFB-QCLs. For index-coupling dominated DFB-QCLs, the amplitudes of the self-mixing power signals decrease with increasing modulus; however, the amplitudes of the self-mixing power signals of gain-coupling dominated DFB-QCLs increase. With the argument of the coupling factor fixed, for index-coupling dominated DFB-QCLs, we found that the varying ranges of the self-mixing frequency signals and amplitudes of power signals decrease with the increasing modulus. For gain-coupling dominated DFB-QCLs, with the coupling factor modulus increasing, the varying ranges of the self-mixing frequency signals decrease, however, the amplitudes of the self-mixing power signals increase. These results may help with the application of DFB-QCLs to self-mixing interferometers.

Keywords: terahertz, quantum cascade lasers, self-mixing interference, distributed feedback, coupled wave theory, multi-mode rate equation method

OPEN ACCESS

Edited by:
Xiaoyong Hu,
Peking University, China

Reviewed by:
Shengfei Feng,
Capital Normal University, China
Yuan Ren,
Purple Mountain Observatory (CAS), China
Xiaoqiong Qi,
The University of Queensland, Australia

****Correspondence:***
Ning Yang
yang_ning@iapcm.ac.cn

Specialty section:
This article was submitted to Optics and Photonics, a section of the journal Frontiers in Physics

Received: *20 July 2021*
Accepted: *06 September 2021*
Published: *22 September 2021*

Citation:
Ge L, Yang N, Wang J, Chu W, Duan S, Xie Y, Wang Y, Li L and Linfield E (2021) Self-Mixing Signal Characteristics of Complex-Coupled Distributed-Feedback Terahertz Quantum-Cascade Lasers. Front. Phys. 9:744286. doi: 10.3389/fphy.2021.744286

1 INTRODUCTION

Terahertz Quantum cascade lasers (THz QCLs) are compact and coherent THz light sources that generate optical transitions between conduction subbands in semiconductor multiple-quantum-well structures [1]. Together with their unipolar nature and wide coherent sensing range, QCLs can meet the increasing needs of applications in materials imaging, THz communication technology, atmospheric science, spectroscopy, and frequency metrology [2].

Self-mixing interference (SMI) (also known as laser feedback interference) is a sensing method that uses measurements of the change in the operating parameters of the laser under optical feedback. In contrast to traditional sensing systems, which employ the laser as a source and an optical interferometer to split and recombine the beam, SMI is based on the interaction of the in-cavity field with the back-scattered field from a target, which induces a modulation in amplitude of the optical emission frequency, power, and terminal voltage [3]. The use of SMI in THz QCLs has been studied in-depth, and it could be a promising solution for THz sensing of displacement, vibration, and velocity, and 2D/3D THz imaging [4]. Under optical feedback, QCLs can maintain a more stable working state than diode lasers because of the absence of relaxation oscillations. This is attributed both to high photon-to-carrier lifetime ratios and a negligible linewidth enhancement factor ($\alpha < 1$) [5, 6].

Typical SMI prefers a stable, single-mode laser with low linewidth, which makes the data processing in a concise way. However, most Fabry–Pérot (FP) QCLs work with a broad emission linewidth in a multi-mode regime. Common candidates are distributed feedback quantum cascade lasers (DFB-QCLs) incorporating a first-order Bragg DFB grating into a standard QCL waveguide, which can provide more strictly single-mode emission with a high side mode suppression ratio (SMSR) [7–9]. Moreover, based on a second- or fourth-order Bragg gratings, some researches achieved high power surface emitting THz QCLs [10]. Rencently, a new model was designed to predict resonant mode characteristics of THz QCLs with a first, second, and third-order DFB-QCLs [11]. And wavelength beam-combining of four terahertz THz DFB-QCLs is demonstrated using low-cost THz components [12]. Base on the self-mixing technique, an experiment has been made to measure the linewidth enhancement factor α [13]. A newest experiment has made an extensive study of the linewidth enhancement factor α of a DFB-QCL, and it used the SMI technique to obtain α factors for current biases up to more than 100% of the threshold current [14]. Typically, the DFB gratings are either purely index coupled, purely gain coupled, or complex coupled, according to adjustments in the etching process based on theory and experience. From this point of view, some early studies investigated the properties of SMI in index-coupled diode lasers using the coupled wave theory, and the results show that the cosine-like self-mixing signal is similar to that from a single-mode FP laser [15, 16]. Furthermore, some studies also have shown that SMI sensors based on gain-coupled DFB lasers exhibit high accuracy [17]. However, a DFB laser with a grating etched into its upper cladding layer has an increased waveguide loss through the top contact layer, and this may in turn decrease its performance [18]. Recently, as a result of their performance, complex-coupled DFB-QCLs have received considerable attention in terms of both theory and experiments; in contrast to FP-QCLs and index-coupled DFB-QCLs, they have a reduced threshold current density and an increased power output via the introduction of built-in longitudinal modulation of the optical gain [19, 20].

A complex-coupled DFB THz QCL has a DFB grating etched into the top surface of the active region across the upper cladding layer; therefore, these devices have mixed index and gain coupling, and they also have a complex coupling factor [18]. Complex-coupled and gain-coupled DFB lasers have shown significant improvements in some studies in terms of reduced spatial hole burning and enhancement of modulation bandwith [18, 21]. In addition, experimental and theoretical works have also reported that complex-coupled and gain-coupled DFB lasers with a very large gain coupling show the potential for lower feedback sensitivity when compared with other DFB lasers [22, 23].

As noted above, complex-coupled and gain-coupled DFB lasers are more appropriate for use in SMI systems, especially in the case of weak optical feedback. However, in experiments, it is difficult to fabricate pure gain-coupled gratings because variations in gain cause variations in carrier density, which in turn cause variations in refractive index. In experiment, the complex coupling of DFB-QCLs has been attainable by chemical wet etching of the top contact layer to a certain depth, with the DFB grating etched close to the active region [24]. Recent studies on complex-coupled DFB-QCLs have reported that they exhibit excellent performance, with high-power continuous-wave, room temperature operation, and single-mode emitting with a high SMSR [25, 26]. However, there have so far been few in-depth studies of the dynamics of complex-coupled DFB-QCLs. In particular, the differences between complex-coupled and index-coupled DFB-QCLs in terms of their response rules for optical feedback are in need of detailed investigation.

The Lang–Kobayashi (L–K) equations are generally employed to study the dynamical behavior of SMI in FP-QCLs. However, the L–K equations cannot be simply applied to DFB-QCLs under optical feedback, despite the fact that several studies have used modified L–K equations to this end [17]. Here, we use the coupled wave theory to describe the mode-coupling phenomenon and calculate the emission power of complex-coupled THz DFB-QCLs under SMI using the multi-mode rate equation method. This model was implemented in our early study on SMI in index-coupled DFB-QCLs with a purely real index-coupling factor [27].

The remainder of this article is organized as follows. In **Section 2**, the coupled wave theory and the multi-mode rate equation method for the simulation of SMI in DFB-QCLs are presented. In **Section 3**, the basic output characteristics of SMI in DFB-QCLs of pure index coupling, complex coupling, and pure gain coupling are discussed. Finally, **Section 4** presents our conclusions.

2 THEORETICAL MODEL OF SMI IN THZ COMPLEX-COUPLED DFB-QCLS

The coupled wave theory is an important method for simulating the longitudinal modes distributed in a DFB structure. **Figure 1**

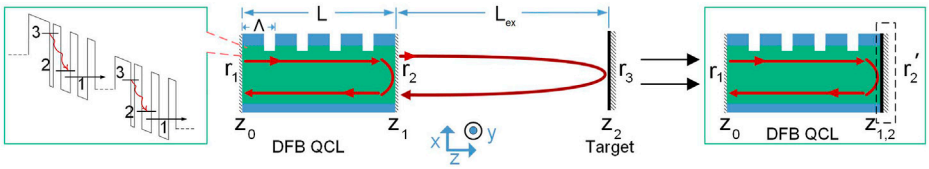

FIGURE 1 | Schematic of a DFB-QCL with an external target and an equivalent reflection coefficient r_2'.

TABLE 1 | Parameters used in the calculations.

Parameter	Symbol	Value
First-order Bragg grating period	Λ	1.59×10^{-3} cm
Laser length	L	0.3 cm
Number of gain stages	Z	100
Initial distance from z_1 to z_2	L_{ex}	47 cm
Linewidth enhancement factor	α	0 [36]
Effective refractive index	n_{eff}	3.63
Peak gain frequency	ν_0	2.6 THz
Confinement factor	Γ	0.5
Spontaneous emission factor	β	5×10^{-4}
Laser waveguide loss	$1/\tau_w$	1/7.57 ps^{-1}
Differential gain coefficient	G	1.41 × 104 s^{-1}
Injection current	I_{in}	300 mA
Scattering lifetime from N_3 to N_2	τ_{32}	2.10 ps [31]
Scattering lifetime from N_3 to N_1	τ_{31}	7.00 ps [31]
Scattering lifetime from N_2 to N_1	τ_{21}	0.26 ps [31]

shows a schematic drawing of a complex-coupled DFB-QCL with a first-order grating, which mainly radiates in the vicinity of Bragg wavevector $\beta_0 = 2\pi/(\Lambda n_{eff})$, where Λ is the grating period, and n_{eff} is the effective refractive index of the medium. Generally, the first-order grating for a QCL is pure real index-coupled grating or complex-coupled one with a small imaginary part that depends on the etching depth. At least in theory, there are also gratings with a pure imaginary coupling factor, i.e., gain-coupled gratings, although they are not common for QCLs.

In accordance with the coupled wave theory, starting from the scalar wave equation and using small-perturbation assumptions, the coupled wave equations are given as [22]:

$$\frac{\partial F(z)}{\partial z} = i(k-\beta_0)F(z) + i\kappa_{FB}B(z), \tag{1}$$

$$-\frac{\partial B(z)}{\partial z} = i(k-\beta_0)B(z) + i\kappa_{BF}F(z), \tag{2}$$

where $F(z)$ is the forward-running envelop wave and $B(z)$ is the backward-running envelop wave. These two counter-running waves grow from the presence of gain, and they feed energy into each other due to Bragg scattering. The parameter k is the wave vector inside the medium of the laser and κ is the coupling factor, which measures the coupling strength between $F(z)$ and $B(z)$. For a complex-coupled DFB-Laser, κ is considered as a complex number satisfying

$$\kappa_{FB} = \kappa_{BF}^{*} = \kappa_{\text{index}} + i\kappa_{\text{gain}} \tag{3}$$

with κ_{index} and κ_{gain} being real numbers measuring the coupling strength of the index and gain coupling of the grating, respectively. The laser modes in the cavity match the boundary conditions

$$F(0) = r_1 B(0) \tag{4}$$

$$B(L) = r_2 F(L), \tag{5}$$

where L is the length of the laser cavity, and r_1 and r_2 are the reflection coefficients of the laser facets. From **Eqs 1–5** we get

$$\frac{(\gamma + r_1)(\gamma + r_2)}{(1 + r_1\gamma)(1 + r_2\gamma)} e^{-2i\sqrt{(k-\beta_0)^2 - \kappa^2}L} = 1, \tag{6}$$

where we adopt the expression of $\kappa = \kappa_{\text{index}} + i\kappa_{\text{gain}}$ from **Eq. 3**, and $\gamma = \kappa / (\sqrt{(k-\beta_0)^2 - \kappa^2} + k - \beta_0)$. From **Eq. 6**, we can solve the complex wave vectors k indicating the modes existing in the laser cavity. In accordance with the expression $k = k_0 n_{\text{eff}} + ig_{\text{th}}$, we can calculate the emitting wave vector k_0 in free space, the effective refractive index n_{eff}, and the threshold gain gth for each mode.

As illustrated in **Figure 1**, when a target with reflection coefficient r_3 reflects part of the light back into the laser cavity, on the consideration of weak optical feedback ($r_2 r_3 \ll 1$), we introduce an equivalent reflection coefficient to the emitting facet of the laser, describing the effect of SMI as [28]

$$r_2' = r_2 + (1 - r_2^2) r_3 e^{-2ik_0 L_{\text{ex}}}, \tag{7}$$

where L_{ex} is the distance from the laser emission facet to the target. In the case of strong optical feedback level, we suggest to refer to the expression of the equivalent reflection coefficient in [29]. From **Eqs 6**, **7**, we can solve the wave vector k_0 and the corresponding threshold gain gth with the influence of self-mixing feedback, and simultaneously solve the corresponding envelop waves $F(z)$ and $B(z)$. We can then obtain the self-mixing frequency signal with the formula

$$\Delta\nu = \nu_l - \nu_{l0} \tag{8}$$

where ν_l is the mode frequency with optical feedback and ν_{l0} is the solitary mode frequency.

In addition to the frequency signal, we use the multi-mode rate equation method to calculate the self-mixing power signal [30, 31]:

$$\frac{dS_l}{dt} = Zg_l S_l - \frac{\Gamma S_l}{\tau_l} + Z\beta\left(\frac{N_3}{\tau_{32}} + \frac{N_3}{\tau_{31}}\right), \tag{9}$$

$$\frac{dN_3}{dt} = \frac{I_{\text{in}}}{q} - \frac{N_3}{\tau_{32}} - \frac{N_3}{\tau_{31}} - \sum_l g_l S_l, \tag{10}$$

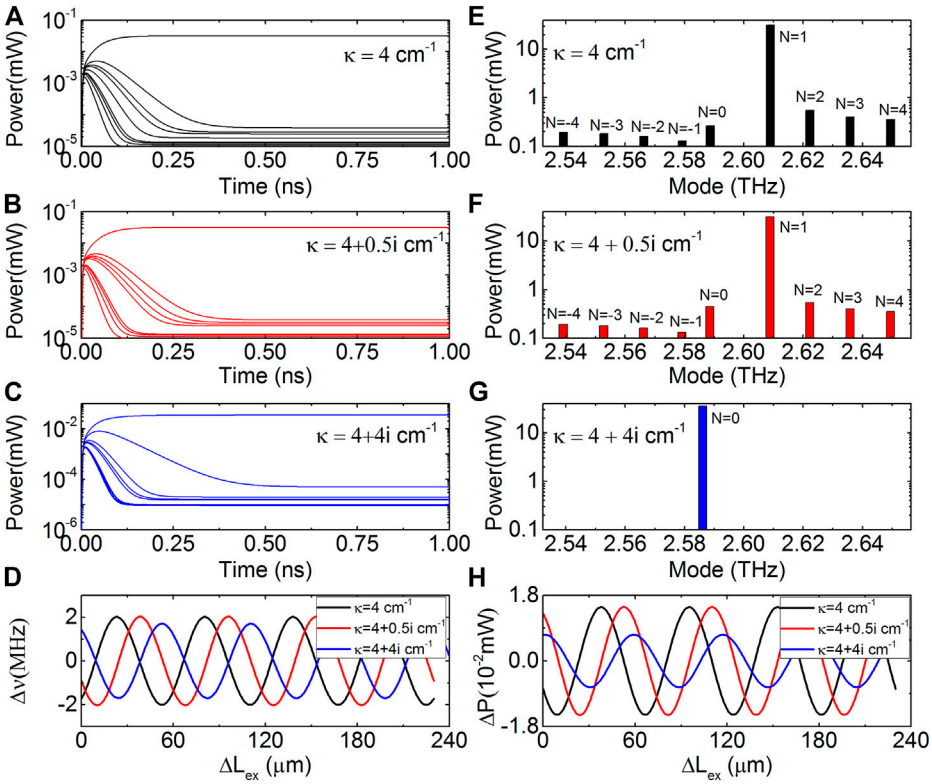

FIGURE 2 | (A–C) Time evolutions of the power of nine modes in THz DFB-QCLs with $r_3 = 0.001$, $L_{ex} = 47$ cm, and $\kappa = 4, 4 + 0.5i, 4 + 4i$ cm^{-1}, respectively, using the multi-mode rate equations. **(E–G)** Self-mixing power spectra corresponding to **(A–C)**. **(D,H)** Self-mixing frequency and power signals of the maximum power modes of DFB-QCLs with the same three values of κ.

$$\frac{dN_2}{dt} = \frac{N_3}{\tau_{32}} - \frac{N_2}{\tau_{21}} + \sum_l g_l S_l, \tag{11}$$

$$\frac{dN_1}{dt} = \frac{N_3}{\tau_{31}} + \frac{N_2}{\tau_{21}} - \frac{N_1}{\tau_{out}}, \tag{12}$$

where: S_l is photon number of mode l; N_3, N_2, and N_1 are the carrier numbers in the upper radiative, lower radiative, and collector levels, respectively; Z is the number of gain stages in the QCL; g_l is the mode gain; Γ is the confinement factor; τ_l is the photon lifetime; β is the spontaneous emission factor; τ_{ij} is the scattering lifetime between levels i and j; I_{in} is the injected current into level 3; q is the electron charge; and τ_{out} is the lifetime from level 1 into the subsequent miniband. The mode gain $g_l = G(N_3 - N_2)$, where G is the differential gain coefficient. In this study, we use the assumption of no carrier losses between the subsequent stages with $N_1/\tau_{out} = I_{in}/q$. In order to gain a better understanding of the mode competition derived from the DFB grating structure with optical feedback, we assume that the value of g_l is the same for the total modes in the laser cavity. The photon lifetime is written as

$$\frac{1}{\tau_l} = \frac{1}{\tau_w} + \frac{1}{\tau_m^l}, \tag{13}$$

where: τ_w is the waveguide loss, which is the same for the total modes; and τ_m^l is the lifetime of a mode within the laser cavity due to mirror loss [30]

$$\tau_m^l(L_{ex}) = \frac{\int_{z_0}^{z_2} < U(z) > dz + \int_{z_0}^{z_1 + L_{ex}} < U(z) > dz}{2\sqrt{\frac{\epsilon_0}{\mu_0}} n_0^2 \left[|B(z_0)|^2 (1 - r_1)^2 + |F(z_2)|^2 (1 - r_2)^2 \right]}, \tag{14}$$

in which the energy density

$$< U(z) > = 2\epsilon_0 n(z)^2 \left[|F(z)|^2 + |B(z)|^2 \right], \tag{15}$$

where ϵ_0, μ_0, and n_0 are the dielectric constant, permeability, and refractive index of a vacuum, and $n(z)$ is the refractive index at coordinate z.

From **Eqs 9–12**, the optical power P_l is obtained as [32]

$$P_l = h\nu_l S_l (1 - R) c / (L \cdot n_{eff}), \tag{16}$$

where $h\nu_l$ is the photon energy and R is the reflectivity of the output facet. We can then obtain the self-mixing power signal by the formula

$$\Delta P = P_l - P_{l0} \tag{17}$$

where P_l and P_{l0} are the optical power with and without optical feedback, respectively. It should be also noted that we assume the linewidth enhancement factor $\alpha = 0$ for THz QCLs [5].

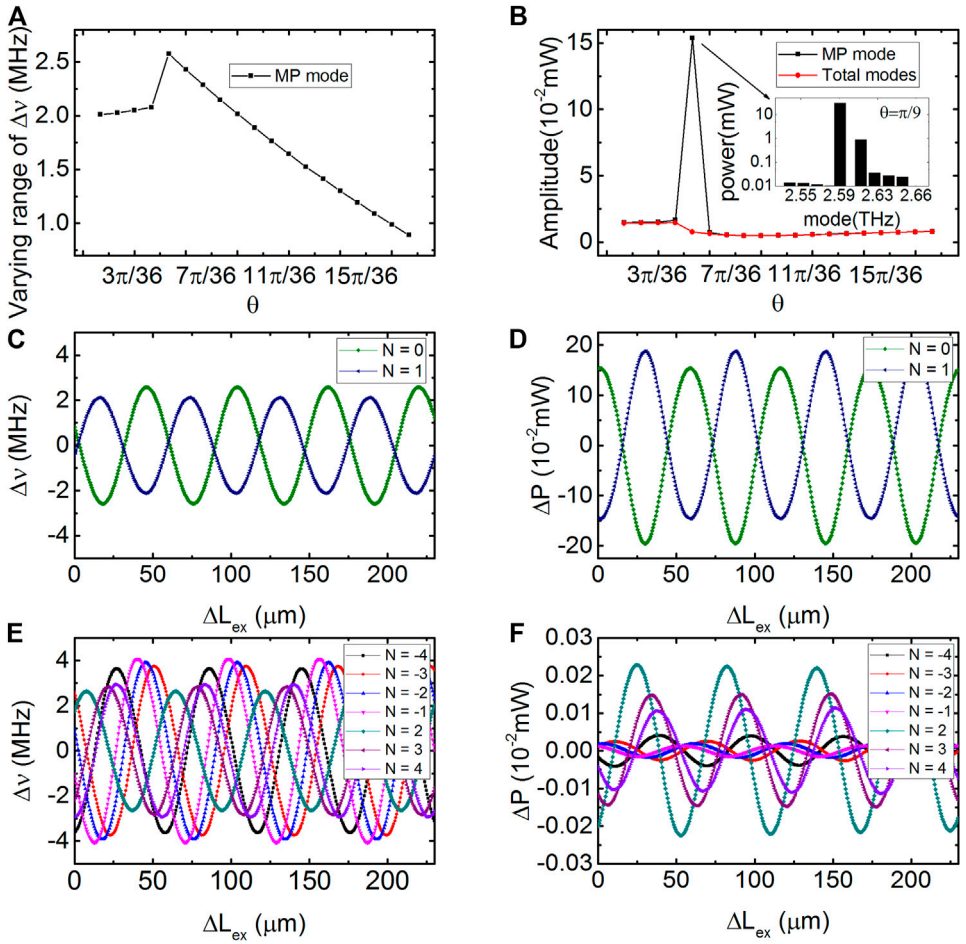

FIGURE 3 | (A,B) Varying range of the self-mixing frequency signals and amplitude of power signals versus argument θ with $\kappa = |\kappa|e^{i\theta}$ and $|\kappa| = 4\ \mathrm{cm}^{-1}$. Inset of **(B)** shows the power spectrum at the extreme point. **(C–F)** Varying range of the self-mixing frequency signals and amplitude of power signals of modes (N = −4–4) as functions of ΔL_{ex}.

3 RESULTS AND DISCUSSION

We assume the facet reflection coefficients to be $r_1 = r_2 = 0.5$ [33] and $r_3 = 0.001$ [3], and the initial distance $L_{ex} = 47$ cm from z_1 to z_2, which is a typical precondition in the application of SMI. In addition, the reflection coefficient of the emitting facet can be changed by the optimized reflectivity facet coatings [9]. Based on the definition of the feedback parameter $C = (1 - r_2^2)r_3L_{ex}/(r_2Ln_{eff})$ in the L-K equations, the above parameters correspond to $C = 0.07$ which is within the weak feedback regime. The feedback parameter C is a typical parameter being chose in the theory and experiment studies of the self-mixing interference [34, 35]. Because of L_{ex}/L being nearly unchanged if the target moves several wavelengths ($\Delta L_{ex} \ll L_{ex}$ and L), we use the reflection coefficient r_3 to describe the optical feedback strength in our investigation. Unless stated otherwise, the parameters used in the calculations are those presented in **Table 1**.

3.1 Mode Hopping From Index Coupling to Gain Coupling

Figures 2A–C illustrate the time evolution results of the DFB-QCLs under self-mixing feedback. Here, we analyze the three cases of DFB coupling factors $\kappa = 4$, $4 + 0.5i$, and $4 + 4i\ \mathrm{cm}^{-1}$, which represent a pure index-coupled DFB-QCL, and a complex-coupled DFB-QCL with a weak gain-coupled part and a strong gain-coupled part, respectively. The time evolution simulations took an average of 0.5 ns to reach a steady state in these three cases. The corresponding output power spectra were obtained, and these are shown in **Figures 2E–G** for nine modes in the vicinity of first-order Bragg frequency. In **Figures 2E–G**, the numbers from −4 to 4 indicate the modes from the Bragg frequency to the side modes. It can be seen that the maximum power mode changes from mode 1 to mode 0 when the value of the imaginary part of the DFB coupling factor is increased from $0.5i$ to $4i$. This mode hopping phenomenon occurs with the DFB-Laser changing from index-coupling dominating to gain-coupling dominating, as demonstrated in an early study [37].

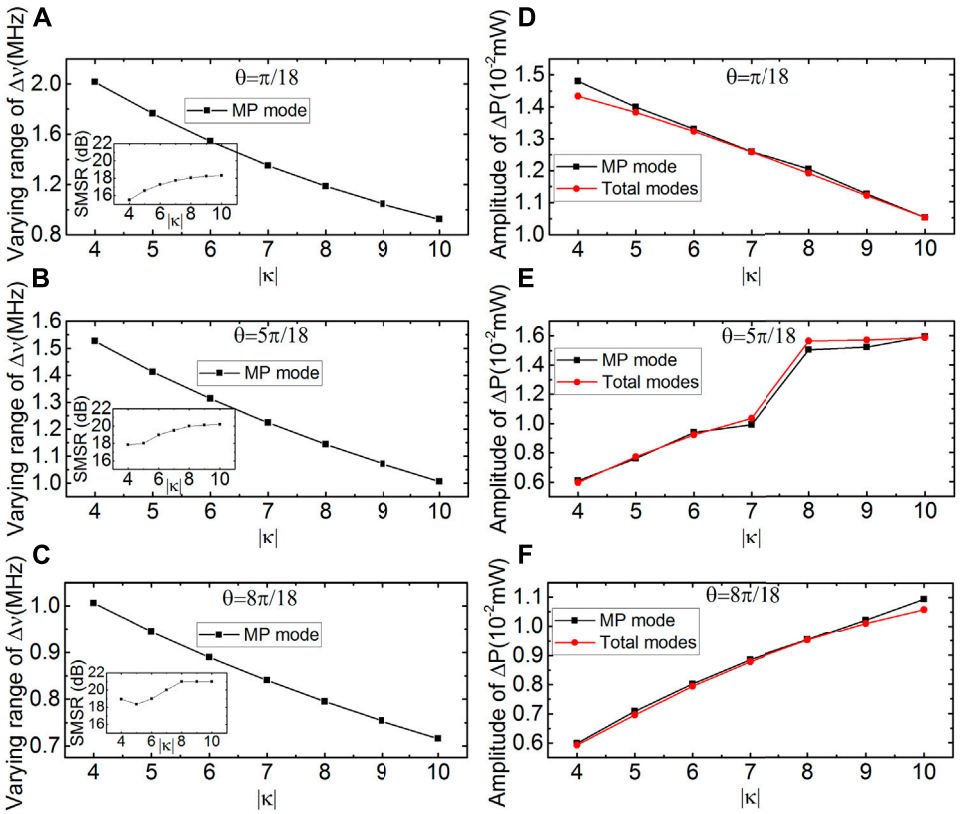

FIGURE 4 | (A–C) Varying range of self-mixing frequency signals of the maximum power mode versus $|\kappa|$ with $\theta = \pi/18$, $5\pi/18$, and $8\pi/18$, respectively. Insets of **(A–C)** shows the SMSR versus $|\kappa|$. **(D–F)** Amplitude of self-mixing power signals of the maximum power mode and the total modes versus $|\kappa|$ with $\theta = \pi/18$, $5\pi/18$, $8\pi/18$, respectively.

Our simulations demonstrate that mode hopping also takes place in DFB-QCLs with SMI. By further examining the SMI signals, it can be seen that the characteristics of the SMI of DFB-QCLs also change with the occurrence of mode hopping.

Figures 2D,H show the self-mixing frequency and power signals of the maximum power (MP) mode of the DFB-QCLs with the three different values of κ. The plots show that the self-mixing signals have cosine-like waveforms. It should be noted here that we only show the self-mixing signals of the MP mode because the power of this mode and the total power of all the modes in the cavity are nearly equal for a stable single mode DFB-QCL. In the next section, we will show both the power signals of the MP mode and total modes in detail. We also found that the initial phase of the self-mixing signal shifts with κ. The variation in the varying range of the self-mixing frequency signals and amplitude of power signals with a complex κ is also discussed in the next section.

3.2 Self-Mixing Signal of Complex-Coupled DFB-QCLs

To explore the mode hopping and its influence on SMI, we firstly set the modulus of the coupling factor $|\kappa| = 4\ \mathrm{cm}^{-1}$ and rewrite the complex coupling factor as $\kappa = |\kappa|e^{i\theta}$. With variation of the argument θ from 0 to π/2, we can obtain a series of self-mixing signals of DFB-QCLs from pure index coupling, complex coupling to pure gain coupling, as shown in **Figure 3**. In **Figures 3A,B**, it can be seen that there is an extreme point at about $\theta = \pi/9$ where the self-mixing frequency and power signals of the MP mode have their maximum amplitudes. The power spectrum at $\theta = \pi/9$ is also shown in the inset of **Figure 3B**. It can be seen that the SMSR at this extreme point decreases to 14 dB, which indicates that the DFB-QCL is not in a stable single-mode working state.

For pure index-coupled DFB-QCLs, our previous work showed that the varying ranges of both the self-mixing frequency and power signals decrease with increasing κ [27]. However, for the index-coupling dominated DFB-QCLs in **Figure 3A**, when θ increases from 0 to the extreme point $\theta = \pi/9$, the varying range of the self-mixing frequency signal increases, and the amplitudes of the self-mixing power signals of both the MP mode and total modes in laser cavity also increase with variation of θ from 0 to $\pi/9$, as shown in **Figure 3B**. When θ continues increasing from the extreme point to $\theta = \pi/2$, mode hopping takes place and the complex-coupled DFB-QCL becomes dominated by gain coupling. For gain-coupling dominated DFB-QCLs with θ increasing from $\pi/9$ to $\pi/2$, **Figure 3A** shows that the varying range of the self-mixing frequency signal decreases, which is similar to the pure index-

coupled DFB-QCL. However, the amplitude of self-mixing power signal increases after mode hopping in **Figure 3B**. It is also found that the varying range of the self-mixing frequency signals and amplitude of power signals of a gain-coupling dominated DFB-QCL are smaller than those of an index-coupling dominated DFB-QCL. These behaviors of the self-mixing signal in a complex-coupled DFB-QCL are obviously different from those of pure index-coupled DFB-QCLs, and the amplitude of the self-mixing signal changes non-monotonically with increasing θ. The self-mixing signal of a DFB-QCL at this extreme point is notably different from that of the index-coupled and gain-coupled DFB-QCLs; hence, this phenomenon of SMI in DFB-QCLs may be of benefit for identifying the type of DFB grating.

Figures 3C–F illustrate the self-mixing frequency and power signals of all the modes in the simulations as functions of L_{ex} at the extreme point $\theta = \pi/9$. From this, we can see that the self-mixing signal of the MP mode is obviously different from the total modes as a result of mode hopping. **Figure 3D** shows that the amplitudes of the self-mixing power signals of mode 0 and mode 1 are of the same order and much larger than those of the other modes existing in the laser cavity as shown in **Figure 3F**. The other self-mixing power signals in **Figure 3F** are in the same level. However, we found that the varying ranges of the self-mixing frequency signals of all modes in the laser cavity are in the same level. And **Figures 3C,E** shows the varying ranges of the self-mixing frequency signal corresponding to the modes in **Figures 3D,F**.

We now examine the characteristics of the self-mixing signal as a function of κ with fixed argument values. **Figures 4A–C** show the varying ranges of the self-mixing frequency signal as functions of $|\kappa|$ values from 4 to 10 cm^{-1} with $\theta = \pi/18$, $5\pi/18$, and $8\pi/18$, respectively. With these values of $|\kappa|$, the DFB-QCLs are in a single-mode working state, and the corresponding SMSR versus $|\kappa|$ are shown in the insets. It is found that no matter the value of θ, the varying ranges of the SMI frequency signals decrease with increasing $|\kappa|$. This response behavior of complex-coupled DFB-QCLs is the same as that of pure index-coupled DFB-QCLs, and this phenomenon can also be found from the L–K equations [27]. **Figures 4D–F** show the amplitudes of the self-mixing power signal versus $|\kappa|$. For the index-coupling dominated DFB-QCLs with $\theta = \pi/18$, **Figure 4D** shows that the amplitude of the self-mixing power signal decreases with increasing $|\kappa|$, and this is also true in the pure index-coupled case. However, for the gain-coupling dominated DFB-QCLs with $\theta = 5\pi/18$ and $8\pi/18$ in **Figures 4E,F**, it can be seen that the amplitudes of the self-mixing power signals increase with $|\kappa|$. This change rule for gain-coupling dominated DFB-QCLs is opposite to that for the index-coupling dominated DFB-QCLs (**Figure 4D**).

4 CONCLUSION

This study explored the output characteristics of self-mixing interference in terahertz distributed feedback quantum cascade lasers in the index-, complex-to gain-coupling regimes. Keeping the modulus of the coupling factor fixed while varying its argument from 0 to $\pi/2$, we found that extreme points occur at $\pi/9$ in the self-mixing frequency and power signals of DFB-QCLs. We also showed that the self-mixing frequency and power signals change with DFB coupling factor before and after a mode hoping phenomenon occurs. In the case of index-coupling dominated DFB-QCLs with a fixed modulus, the amplitudes of the self-mixing frequency and power signals increase while increasing argument. For gain-coupling dominated DFB-QCLs, when the argument of coupling factor is increased, the amplitude of the self-mixing power signal increases; however, the varying range of the self-mixing frequency signal decreases. With a fixed coupling factor argument, for index-coupling dominated DFB-QCLs, the varying ranges of the self-mixing frequency signals decrease with the increasing modulus. For coupling dominated DFB-QCLs, increasing the modulus of coupling factor decreases the varying ranges of the self-mixing frequency signal; however, the amplitude of the self-mixing power signals increase increases with increasing modulus. These findings will be helpful in investigating the nonlinear dynamics of complex-coupled self-mixing interference in THz DFB-QCLs, and this may be valuable for the application to THz DFB-QCLs in self-mixing sensing systems.

DATA AVAILABILITY STATEMENT

The raw data supporting the conclusion of this article will be made available by the authors, without undue reservation.

AUTHOR CONTRIBUTIONS

NY, LG, WC, LL, and EL contributed to conception and design of the study. LG performed the simulation. LG, NY, SD, YX, and YW performed the data analysis. LG wrote the first draft of the manuscript. NY wrote sections of the manuscript. All authors contributed to manuscript revision, read, and approved the submitted version.

FUNDING

The work was financially supported by the National Natural Science Foundation of China Joint Fund (Grant No. U1730246).

REFERENCES

1. Vitiello MS, Scalari G, Williams B, and De Natale P. Quantum cascade Lasers: 20 Years of Challenges. *Opt Express* (2015) 23:5167–82. doi:10.1364/oe.23.005167
2. Williams BS. Terahertz Quantum-cascade Lasers. *Nat Photon* (2007) 1:517–25. doi:10.1038/nphoton.2007.166
3. Donati S. Developing Self-Mixing Interferometry for Instrumentation and Measurements. *Laser Photon Rev* (2012) 6:393–417. doi:10.1002/lpor.201100002
4. Valavanis A, Dean P, Lim YL, Alhathlool R, and Davies G. Self-mixing Interferometry with Terahertz Quantum cascade Lasers. *IEEE Sensors J* (2012) 13:37–43. doi:10.1109/JSEN.2012.2218594
5. Green RP, Xu J-H, Mahler L, Tredicucci A, Beltram F, Giuliani G, et al. Linewidth Enhancement Factor of Terahertz Quantum cascade Lasers. *Appl Phys Lett* (2008) 92:071106. doi:10.1063/1.2883950

6. Grier A, Dean P, Valavanis A, Keeley J, Kundu I, Cooper JD, et al. Origin of Terminal Voltage Variations Due to Self-Mixing in Terahertz Frequency Quantum cascade Lasers. *Opt Express* (2016) 24:21948–56. doi:10.1364/oe.24.021948
7. Faist J, Gmachl C, Capasso F, Sirtori C, Sivco DL, Baillargeon JN, et al. Distributed Feedback Quantum cascade Lasers. *Appl Phys Lett* (1997) 70: 2670–2. doi:10.1063/1.119208
8. Gmachl C, Straub A, Colombelli R, Capasso F, Sivco DL, Sergent AM, et al. Single-mode, Tunable Distributed-Feedback and Multiple-Wavelength Quantum cascade Lasers. *IEEE J Quan Electron* (2002) 38:569–81. doi:10.1109/jqe.2002.1005407
9. Wang DB, Zhang JC, Cheng FM, Zhao Y, Zhuo N, Zhai SQ, et al. Stable Single-Mode Operation of Distributed Feedback Quantum cascade Laser by Optimized Reflectivity Facet Coatings. *Nanoscale Res Lett* (2018) 13:37–7. doi:10.1186/s11671-018-2455-z
10. Jin Y, Gao L, Chen J, Wu C, Reno JL, and Kumar S. High Power Surface Emitting Terahertz Laser with Hybrid Second- and Fourth-Order Bragg Gratings. *Nat Commun* (2018) 9:1407–7. doi:10.1038/s41467-018-03697-9
11. Tang P, Chi X, Chen B, and Wu C. Predictions of Resonant Mode Characteristics for Terahertz Quantum cascade Lasers with Distributed Feedback Utilizing Machine Learning. *Opt Express* (2021) 29:15309–26. doi:10.1364/oe.419526
12. Chen J, Jin Y, Gao L, Reno JL, and Kumar S. Wavelength Beam-Combining of Terahertz Quantum-cascade Laser Arrays. *Opt Lett* (2021) 46:1864–7. doi:10.1364/ol.420398
13. Von Staden J, Gensty T, Elsäßer W, Giuliani G, and Mann C. Measurements of the α Factor of a Distributed-Feedback Quantum cascade Laser by an Optical Feedback Self-Mixing Technique. *Opt Lett* (2006) 31:2574–6. doi:10.1364/ol.31.002574
14. Spitz O, Herdt A, Duan J, Carras M, Elsässer W, and Grillot F. Extensive Study of the Linewidth Enhancement Factor of a Distributed Feedback Quantum cascade Laser at Ultra-low Temperature. *Quan Sensing Nano Elect Photon XVI* (2019) 10926:1092619, 2019. International Society for Optics and Photonics. doi:10.1117/12.2510502
15. Favre F. Theoretical Analysis of External Optical Feedback on DFB Semiconductor Lasers. *IEEE J Quan Electron* (1987) 23:81–8. doi:10.1109/jqe.1987.1073195
16. Zhou J, Wang M, and Han D. Experiment Observation of Self-Mixing Interference in Distributed Feedback Laser. *Opt Express* (2006) 14:5301–6. doi:10.1364/oe.14.005301
17. Zhou J, and Wang M. Effects of Self-Mixing Interference on Gain-Coupled Distributed-Feedback Lasers. *Opt Express* (2005) 13:1848–54. doi:10.1364/opex.13.001848
18. Lowery AJ, and Novak D. Performance Comparison of Gain-Coupled and index-coupled DFB Semiconductor Lasers. *IEEE J Quan Electron* (1994) 30: 2051–63. doi:10.1109/3.309864
19. Gmachl C, Faist J, Bailargeon JN, Capasso F, Sirtori C, Sivco DL, et al. Complex-coupled Quantum cascade Distributed-Feedback Laser. *IEEE Photon Technol Lett* (1997) 9:1090–2. doi:10.1109/68.605510
20. Zhuo N, Zhang J, Liu F, Wang L, Tan S, Yan F, et al. Tunable Distributed Feedback Quantum cascade Lasers by a Sampled Bragg Grating. *IEEE Photon Technol Lett* (2013) 25:1039–42. doi:10.1109/lpt.2013.2257716
21. David K, Morthier G, Vankwikelberge P, Baets RG, Wolf T, and Borchert B. Gain-coupled DFB Lasers versus index-coupled and Phase Shifted DFB Lasers: A Comparison Based on Spatial Hole Burning Corrected Yield. *IEEE J Quan Electron* (1991) 27:1714–23. doi:10.1109/3.89938
22. Hui R, Kavehrad M, and Makino T. External Feedback Sensitivity of Partly Gain-Coupled DFB Semiconductor Lasers. *IEEE Photon Technol Lett* (1994) 6:897–9. doi:10.1109/68.313045
23. Suhara M, Islam S, and Yamada M. Criterion of External Feedback Sensitivity in index-coupled and Gain-Coupled DFB Semiconductor Lasers to Be Free from Excess Intensity Noise. *IEEE J Quan Electron* (1994) 30:3–9. doi:10.1109/3.272053
24. Chen JY, Liu JQ, Liu FQ, Li L, Wang LJ, and Wang ZG. Distributed Feedback Terahertz Quantum cascade Lasers with Complex-Coupled Metallic Gratings. *Electron Lett* (2010) 46:1340–1. doi:10.1049/el.2010.2223
25. Lu QY, Bai Y, Bandyopadhyay N, Slivken S, and Razeghi M. 2.4 W Room Temperature Continuous Wave Operation of Distributed Feedback Quantum cascade Lasers. *Appl Phys Lett* (2011) 98:181106. doi:10.1063/1.3588412
26. Carras M, Maisons G, Simozrag B, Garcia M, Parillaud O, Massies J, et al.Room-temperature Continuous-Wave Metal Grating Distributed Feedback Quantum cascade Lasers. *Appl Phys Lett* (2010) 96:161105. doi:10.1063/1.3399779
27. Ge L, Yang N, Wang J, Li Y, Chu W, Duan S, et al. Properties of Self-Mixing Interference in Terahertz Distributed Feedback Quantum cascade Lasers. *Appl Phys Lett* (2019) 115:261105. doi:10.1063/1.5130447
28. Petermann K. *Laser diode modulation and noise* (1991) 3:251.
29. Coldren LA, Corzine SW, and Mashanovitch ML. *Diode lasers and photonic integrated circuits* (2012) 218:107.
30. Pierce I, Rees P, and Spencer PS. Multimode Dynamics in Laser Diodes with Optical Feedback. *Phys Rev A* (2000) 61:053801. doi:10.1103/physreva.61.053801
31. Petitjean Y, Destic F, Mollier JC, and Sirtori C. Dynamic Modeling of Terahertz Quantum cascade Lasers. *IEEE J Sel Top Quan Electron* (2010) 17:22–9. doi:10.1109/JSTQE.2010.2045476
32. Haldar MK. A Simplified Analysis of Direct Intensity Modulation of Quantum cascade Lasers. *IEEE J Quan Electron.* (2005) 41:1349–55. doi:10.1109/jqe.2005.857062
33. Qi X, Bertling K, Taimre T, Agnew G, Lim YL, Gillespie T, et al. Observation of Optical Feedback Dynamics in Single-Mode Terahertz Quantum cascade Lasers: Transient Instabilities. *Phys Rev A* (2021) 103:033504. doi:10.1103/physreva.103.033504
34. Qi X, Agnew G, Taimre T, Han S, Lim YL, Bertling K, et al.Laser Feedback Interferometry in Multi-Mode Terahertz Quantum cascade Lasers. *Opt Express* (2020) 28:14246–62. doi:10.1364/oe.390433
35. Inoue T, Tsushima K, Mori S, and Kasahara K. Quantum cascade Laser Intensity Noise under External Feedback Conditions Estimated from Self-mixing Method. *Electron Lett* (2013) 49:407–9. doi:10.1049/el.2013.0255
36. Faist J, Capasso F, Sivco DL, Sirtori C, Hutchinson AL, and Cho AY. Quantum cascade Laser. *Science* (1994) 264:553–6. doi:10.1126/science.264.5158.553
37. Kogelnik H, and Shank CV. Coupled-Wave Theory of Distributed Feedback Lasers. *J Appl Phys* (1972) 43:2327–35. doi:10.1063/1.1661499

Conflict of Interest: The authors declare that the research was conducted in the absence of any commercial or financial relationships that could be construed as a potential conflict of interest.

Publisher's Note: All claims expressed in this article are solely those of the authors and do not necessarily represent those of their affiliated organizations, or those of the publisher, the editors and the reviewers. Any product that may be evaluated in this article, or claim that may be made by its manufacturer, is not guaranteed or endorsed by the publisher.

frontiers in Physics

ORIGINAL RESEARCH
published: 20 October 2021
doi: 10.3389/fphy.2021.749501

Properties and Sensing Performance of THz Metasurface Based on Carbon Nanotube and Microfluidic Channel

Yue Wang[1]*, *Xiaoju Zhang*[1,2], *Tao Zhou*[1], *Yongqiang Zhu*[1], *Zijian Cui*[1] and *Kuang Zhang*[3]

[1]Key Laboratory of Ultrafast Photoelectric Technology and Terahertz Science in Shaanxi, Xi'an University of Technology, Xi'an, China, [2]Engineering University of PAP Xi'an, Xi'an, China, [3]Department of Microwave Engineering, School of Electronics and Information Engineering, Harbin Institute of Technology Harbin, Harbin, China

Carbon-based metamaterials are expected to lead to biological and chemical sensing because of their fast electron transfer rate, good biocompatibility, and high absorption ratios. In this work, we integrate carbon nanotubes metasurface (CM) and microfluidic channel (MC) for a composite terahertz (THz) metasurface (CMMC). The absorption properties and sensing performance of the proposed composite metasurface have been studied. It is observed that the absorption is nearly 71.8% at 0.96 THz and 92.4% at 1.65 THz, respectively. The variation of response with refractive index of the analytes for the proposed CMMC is investigated and it is found that the frequency and intensity of the resonance absorption peak at 0.96 THz f_1 decrease obviously with the increase of the refractive index of the analytes. Owing to the coupling of the CM and MC in the microfluidic channel, the interaction between the incident THz wave and analytes has been enhanced, and the frequency and intensity sensitivities has achieved 254 GHz/RIU and 314/RIU, respectively. In addition, the influence of the structural parameters of the proposed CMMC on the absorption characteristics is also studied in detail. The results shown that the absorption properties of the CMMC can be adjusted by changing the structural parameters, which will provide a guideline for design. The proposed CMMC will facilitate the realization of carbon nanotube metamaterials sensing applications, and, when combined with microfluidic channel, will lead to large-area THz biological and chemical sensing.

Keywords: carbon nanotubes, THz, metasurface, microfluidic channel, refractive index sensing

OPEN ACCESS

Edited by:
Yingxin Wang,
Tsinghua University, China

Reviewed by:
Bo Zhang,
Capital Normal University, China
Lin Chen,
University of Shanghai for Science and Technology, China

****Correspondence:***
Yue Wang
wangyue2017@xaut.edu.cn

Specialty section:
This article was submitted to Optics and Photonics, a section of the journal Frontiers in Physics

Received: *29 July 2021*
Accepted: *30 September 2021*
Published: *20 October 2021*

Citation:
Wang Y, Zhang X, Zhou T, Zhu Y, Cui Z and Zhang K (2021) Properties and Sensing Performance of THz Metasurface Based on Carbon Nanotube and Microfluidic Channel. Front. Phys. 9:749501. doi: 10.3389/fphy.2021.749501

INTRODUCTION

Artificial electromagnetic metasurfaces composed of various periodically arranged subwavelength structures have recently generated great interest [1–3]. Owing to the distinguished electromagnetic response which cannot be realized by in nature materials, artificial metasurfaces offer essential information for various applications in imaging, sensing, and other fields [4–8]. With the development of terahertz (THz) spectroscopy and the micro-nanofabrication technology [9], THz spectroscopy technology based on metamaterials has become a potential detection method. On one hand, the resonances of the artificial electromagnetic metasurfaces whose electromagnetic response can be controlled by design [10] are more sensitive to the change of the dielectric environment [11]. On the other hand, THz spectroscopy technology has some unique advantages such as label-free, non-invasive, and non-destructive characteristics

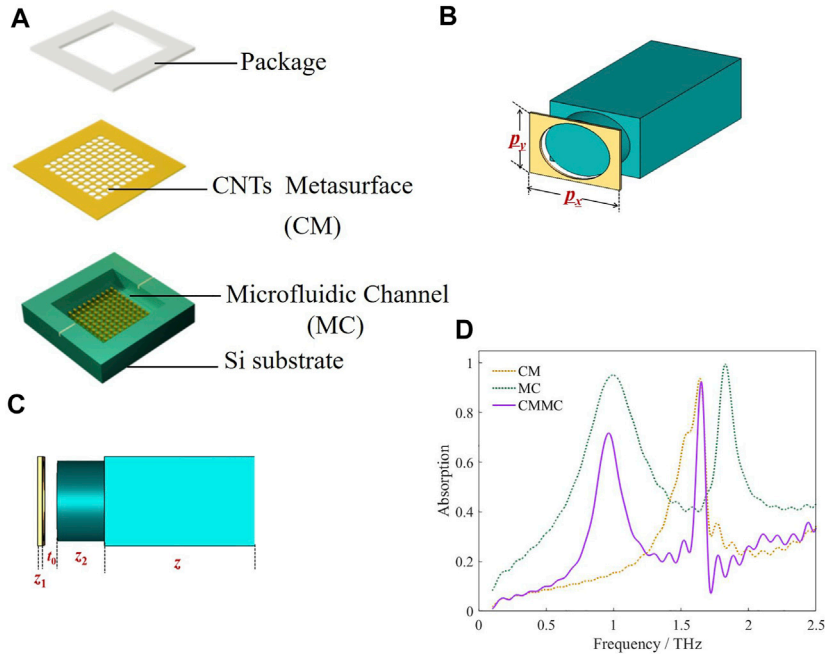

FIGURE 1 | (A) Illustration of the CMMC. **(B)** The unit cell geometry of the CMMC. **(C)** The side view of the unit cell of the CMMC. **(D)** The absorption spectra of the CMMC and other two structures only with CM or MC.

[12]. Therefore, THz metasurface have been utilized for chemical, biological and other sensing applications [13–19].

At present, considerable research efforts have been devoted to metallic metasurface based on metal structural unit cell, but the extended application of the traditional metallic metasurface is limited by the inherent losses, inflexibility, and high processing cost [20, 21]. As a kind of carbon-based material [22, 23], carbon nanotubes (CNTs) film has some merits, such as fast electron transfer rate, good biocompatibility, low-cost, and freely bendable flexibility [24–27]. The metamaterials based on CNTs film are also sensitive to changes in the dielectric environment because of the resonances. All these merits indicate that CNTs-based metamaterials are suitable for THz sensing applications. In addition, the spatial overlap between the analytes and the electric field can enhance the interaction between the analytes and the incident THz wave, which means that it is particularly important to locate the analytes where the concentration of electric field is the largest. Therefore, microfluidic channel maybe provide a new strategy for THz sensing applications [28, 29].

In this paper, we integrate the CNTs metasurface (CM) with periodic elliptical pore structure and the silicon microfluidic channel (MC) with periodic elliptic cylindrical structure at the bottom to form a composite THz metasurface (CMMC). The light-matter interaction between the THz wave and the analytes can be improved by the integration of CM and MC. The absorption spectrum of the designed CMMC is studied, and other two structures only with CM or MC are also investigated for comparison. The CMMC can achieve narrowband absorption, the absorption is nearly 71.8% at 0.96 THz and 92.4% at 1.65 THz, respectively. Because the resonance of the CMMC is sensitive to the changes of the dielectric environment, the refractive index (RI) sensing capabilities of the proposed CMMC are investigated in detail. The study reveals that the resonance peaks shift depends on the change of the refractive index of the analytes. Further calculation results show that the frequency and intensity of f_1 decrease obviously with the increase of refractive index of the analytes. The influence of structural parameters of the CMMC on the absorption properties is also studied and the results can be used as a guideline for design. The proposed CMMC combining the advantages of CM and MC, provides another sensing strategy with tunable resonance characteristics, can be applied for biological and chemical detection [14, 30].

STRUCTURE AND DESIGN

As shown in **Figure 1A**, the proposed CMMC is integrated by CNTs metasurface and microfluidic channel. The CNTs film used in the simulation is treated as composite material, the conductivity is extracted from experimental spectra, which has been reported in our previous work [31]. The microfluidic channel is made of high doped N-type silicon (Si) substrate with doping concentration $b = 2.91 \times 10^{18}\,\mathrm{cm}^{-3}$. A square sample pool with a periodic elliptic cylindrical structure at the bottom was etched on the high doped N-type silicon substrate. The permittivity of the highly doped silicon was descripted by using the Drude dispersion model [32]. It should be noted that the bottom of the sample pool is not smooth and flat, but a metasurface with periodic structure. The high doped N-type

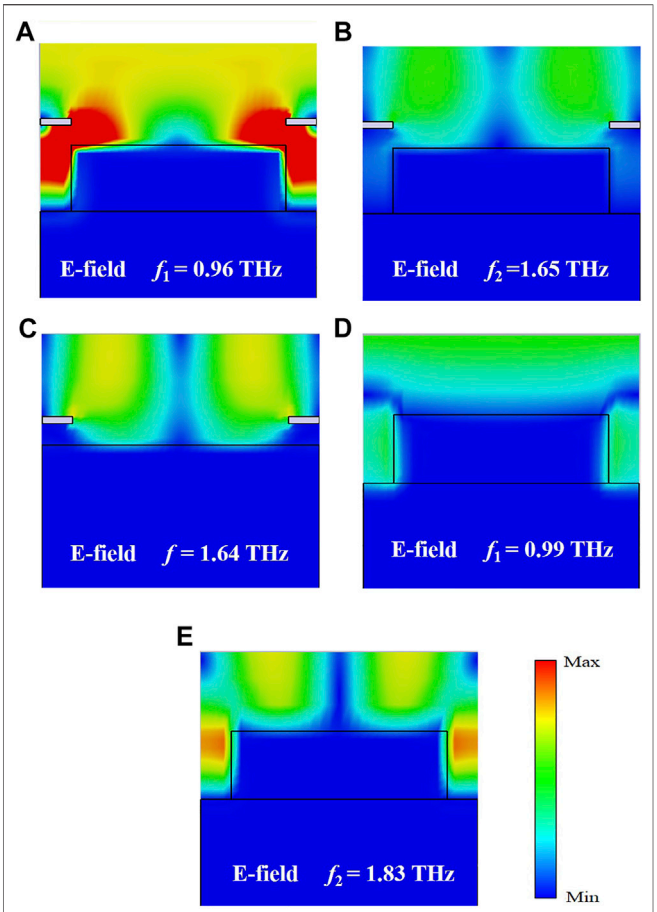

FIGURE 2 | (A,B) Electric field intensity distribution of the proposed CMMC at 0.96 THz and 1.65 THz; **(C)** Electric field intensity distribution of the CM at 1.64 THz. **(D,E)** Electric field distribution of the MC at 0.99 THz and 1.83 THz.

silicon metasurface which can be prepared by lithography shows advantage for simple fabrication. In our design, the square sample pool with a periodic elliptic cylindrical structure at the bottom not only supports the CM as substrate, but also improves the performance of the CMMC. The CNTs film etched periodic elliptical pore is coated on the top of the square sample pool. After that, a microfluidic channel is formed by integrating the CNTs film metasurface and microfluidic channel. Finally, a packaging layer etched with 6 × 6 mm detection window is pressed on the surface of the CM. The unit cell of the CMMC illustrated in **Figures 1B,C**, it is composed of CM and MC. The values of the geometric parameters are set as follows: the repeat period is p_x = 180 μm, and p_y = 110 μm; the thickness of CNTs film is z_1 = 5 μm; the radius of the major and minor axis of the elliptical pore in the CNTs film are R_{x1} = 70 μm and R_{y1} = 50 μm, respectively; the height of the elliptic cylinder is z_2 = 50 μm; the radius of the major and minor axis of the ellipse elliptic cylinder are R_x = 70 μm and R_y = 50 μm, respectively; the thickness of the silicon substrate is z = 350 μm; the etching depth of the sample pool is t_0 = 15 μm. Here, the height of the microfluidic channel is determined by the etching depth of the sample pool.

RESULTS AND DISCUSSION

Absorption Characteristics With Different Structures

Figure 1D shows the simulation absorption spectra of the designed CMMC and other two structures only with CM or MC. As shown in **Figure 1D**, the CMMC exhibits two obvious resonant absorption peaks, f_1 is located at 0.96 THz with absorption of 71.8%, and the resonant peak appears at 1.65 THz f_2 with absorption of 92.4%.

In order to reveal the physical mechanism of the resonance, the electric field distribution of the proposed CMMC, and other two structures only with CM or MC are investigated. **Figures 2A,B** show the electric field distribution of CMMC at the resonant frequency of 0.96 and 1.65 THz. As shown in **Figure 2A**, most of the field intensity is concentrated in the microfluidic channel formed by the integration of CM on the top and MC at the bottom, which will be filled with analytes during sensing detection. It is obvious that the microfluidic channel increases the overlap of space and improves the light-matter interaction between the analytes and the incident THz wave.

From **Figure 2B,** the intensity of the electric field at 1.65 THz is focused on the surface of the CMMC and the resonance is a surface mode. The electric field intensity distribution of the CM at 1.64 THz is shown in **Figure 2C**, the field intensity is mostly located on the surface, which is also surface mode. According to **Figure 2D,E,** the electric field intensity distributions of MC at 0.99 and 1.83 THz are confined on the surface and the gap between adjacent elliptic cylinders along x direction. Although the electric field at 1.83 THz is also concentrated on the surface and the gap between adjacent elliptical cylinders, which is similar to that of 0.99 THz, but the electric field on the surface is not uniformly distributed, which is a surface mode. By comparing the electric field distribution of the three different structures, it is found that the resonant absorption peak at 0.96 THz is related to the coupling of the modes, which increases the interaction between the incident THz wave and the analytes in the microfluidic channel.

Refractive Index Sensing Characteristics of the Proposed THz Metasurface

To study the sensing characteristics of the CMMC, we investigate the absorption spectra of CMMC with different refractive index of analytes n. The height of the microfluidic channel is fixed as 15 μm and the filling thickness of the analytes is t = 45 μm. The range of refractive index from 1.0 to 2.0 covers most bio and chemo specimens, such as DNA, RNA, and amino acids proteins [33, 34].

As shown in **Figure 3A**, it is obvious that the resonant absorption peak at 0.96 THz (f_1) is more sensitive to the change of refractive index than that at 1.64 THz (f_2). In order to gain a further understanding of the different sensitivity of the two peaks to the change of refractive index, we investigate the resonance mechanism in-depth. As shown in **Figure 2A,B,** most of the field intensity is concentrated in the microfluidic channel which will be filled with analytes with different refractive index

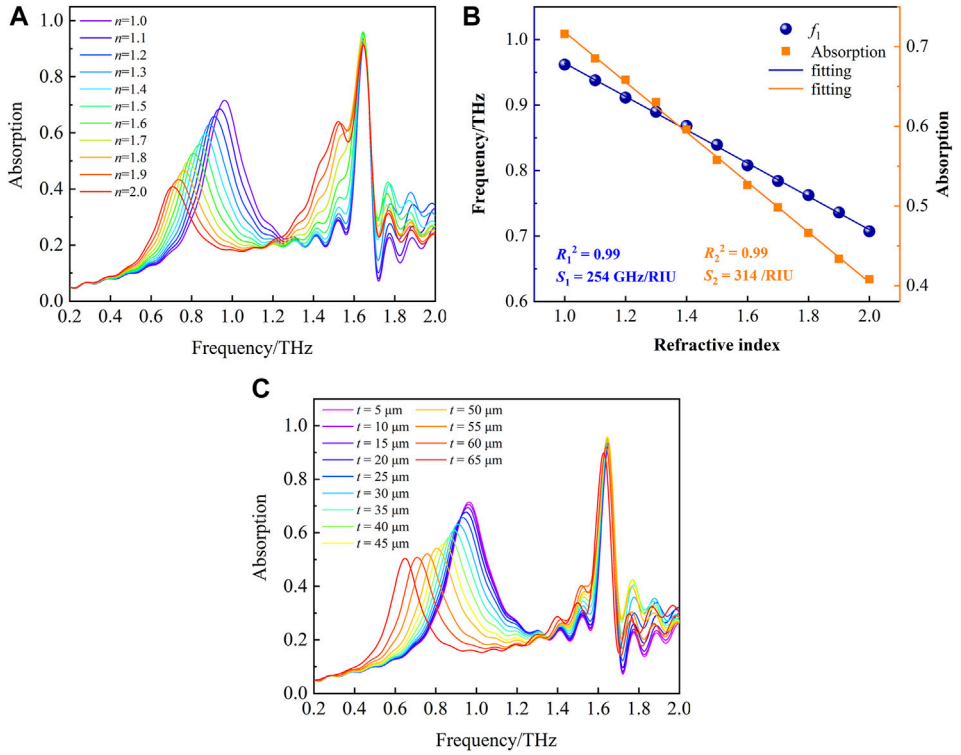

FIGURE 3 | (A) Absorption spectra for the analytes with different refractive indices. **(B)** Regression curves fitted for the refractive indices increases from 1.0 to 2.0, where the filling thickness of the analytes t = 45 μm. **(C)** Absorption spectra of the proposed composite metasurface with different filling thickness, where the refractive index of the analytes is n = 1.5.

during sensing detection and the concentrated electric field resulting from the mode coupling of the CM and MC will improve the light-matter interaction between the analytes and the THz wave. In contrast, the electric field at 1.65 THz is concentrated on the surface, the resonance is an obvious surface mode. Therefore, the resonance peak is not sensitive to changes of the refractive index of the analyte which is located in the microfluidic channel. As shown in **Figure 3A**, the resonant absorption frequency decreases when the refractive index of the analytes in the microfluidic channel increase. Obvious red shift of f_1 is observed, and the total shift is 254 GHz, which indicates that any change in the liquid permittivity will cause the parallel shift of resonance frequency.

In our case, considering the height of the microfluidic channel (t = 15 μm) is far less than the repeat period (p_x = 180 μm, p_y = 110 μm), the gap plasmon model can be used for explaining the physical mechanism [35–37]. In such a model, the resonance at 0.96 THz is caused by the Fabry-Perot resonances in the CNTs/analytes/Si cavity [36].

$$\frac{2\pi\omega n}{\lambda} + \varphi = k\pi \tag{1}$$

where w is the coverage width of the CM ($w = p_x - 2R_{x1}$), n is the effective index of the gap plasmon, λ is the resonance wavelength, φ is reflection phase, and k is the order of resonance. In addition, according to the distribution of electric field in **Figures 2A,D**, the resonance at 0.96 THz is caused not only by the Fabry-Perot resonances in the CNTs/analytes/Si cavity, but also by the Si elliptic cylinder.

It is observed clearly that the resonant frequency decreases as the refractive index of the analytes in the microfluidic channel increases, and f_1 is more sensitive to the change of the refractive index. As shown in **Figure 3B**, the frequency decreases linearly with refractive index increasing, there is a good linear relationships between the position of f_1 and the refractive indices of analytes with the regression coefficients of 0.99 (the blue fitting line). The frequency sensitivity S_1 of the proposed CMMC integrated CNTs film metasurface and the microfluidic channel is defined by frequency shift per refractive index unit, which can be calculated as:

$$S_1 = \frac{\Delta f}{\Delta n} \tag{2}$$

where, S_1 is frequency sensitivity, whose unit is GHz/RIU (RIU = Refractive Index Unit), Δn is the change of the refractive index; Δf is the change of resonant frequency with different n. According to **Eq. 2** and **Figure 3B**, the frequency sensitivity S_1 of the CMMC which equaled to the slope of the blue line in **Figure 3B**, reached 254 GHz/RIU.

In addition, as the refractive index of the analytes increase, the amplitude of f_1 also decreases. The intensity of the resonance decreases linearly with refractive index

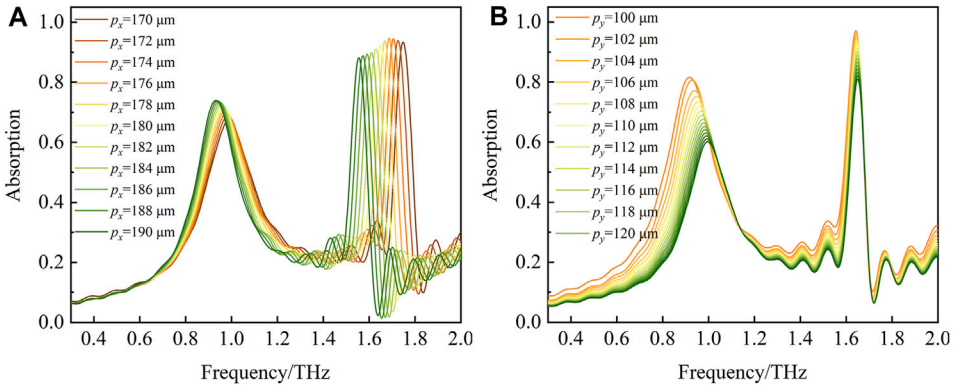

FIGURE 4 | (A) The absorption spectra of the CMMC with p_x increasing from 170 to 190 μm, where the p_y is fixed at 110 μm. **(B)** The absorption spectra of the CMMC with p_y increasing from 100 to 120 μm, where the p_x is fixed at 180 μm.

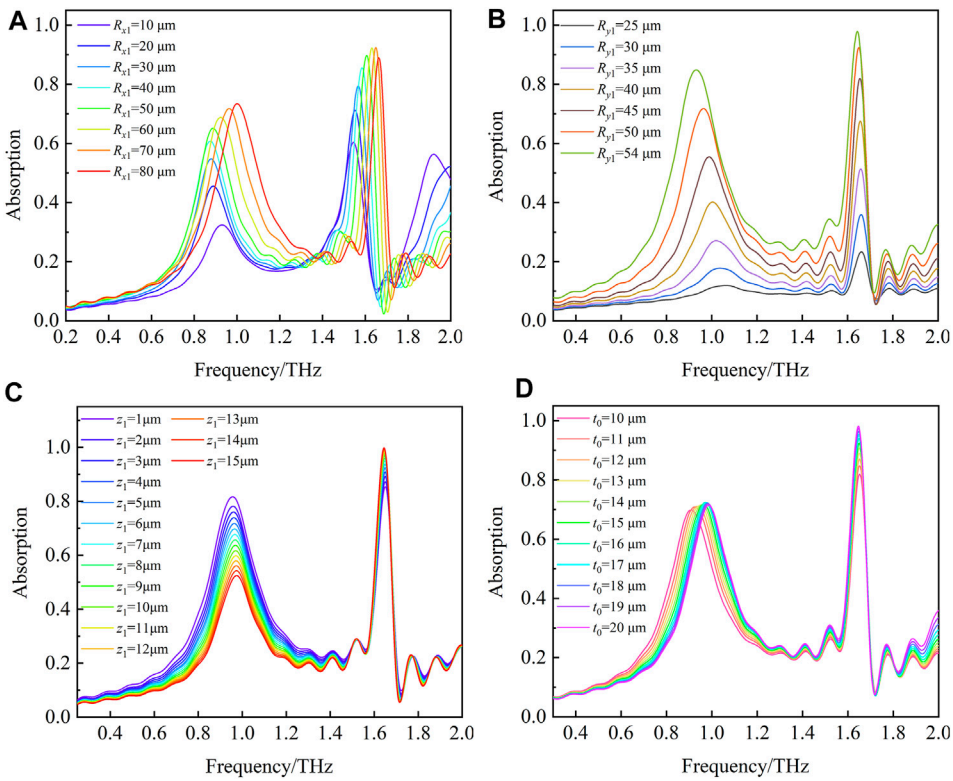

FIGURE 5 | (A) The absorption spectra with the major axis radius of the elliptical pore in the CNTs film R_{x1} increasing from 10 to 70 μm, where R_{y1} is fixed as 50 μm. **(B)** The absorption spectra with the minor axis radius of the elliptical pore in the CNTs film R_{y1} increasing from 25 to 54 μm, where R_{x1} is fixed as 70 μm. **(C)** The absorption spectra with different thickness of the CNTs film z_1. **(D)** The absorption spectra of the CMMC with the height of the microfluidic channel increasing from 10 to 20 μm.

increasing, a good linear relationship between the intensity of resonant peak and the refractive indiex of analytes with the regression coefficients of 0.99 is observed from orange fitting line of **Figure 3B**. Therefore, apart from the sensitivity defined by the frequency shift, the variation of intensity ΔI can also be used for refractive index sensing. The intensity sensitivity S_2 of the proposed CMMC is defined dip the variation of intensity ΔI per refractive index unit, which could be characterized as:

$$S_2 = \frac{\Delta I}{\Delta n} \tag{3}$$

where, the unit of S_2 is/RIU, ΔI is the variation of the intensity of resonance absorption peak with different n. The intensity

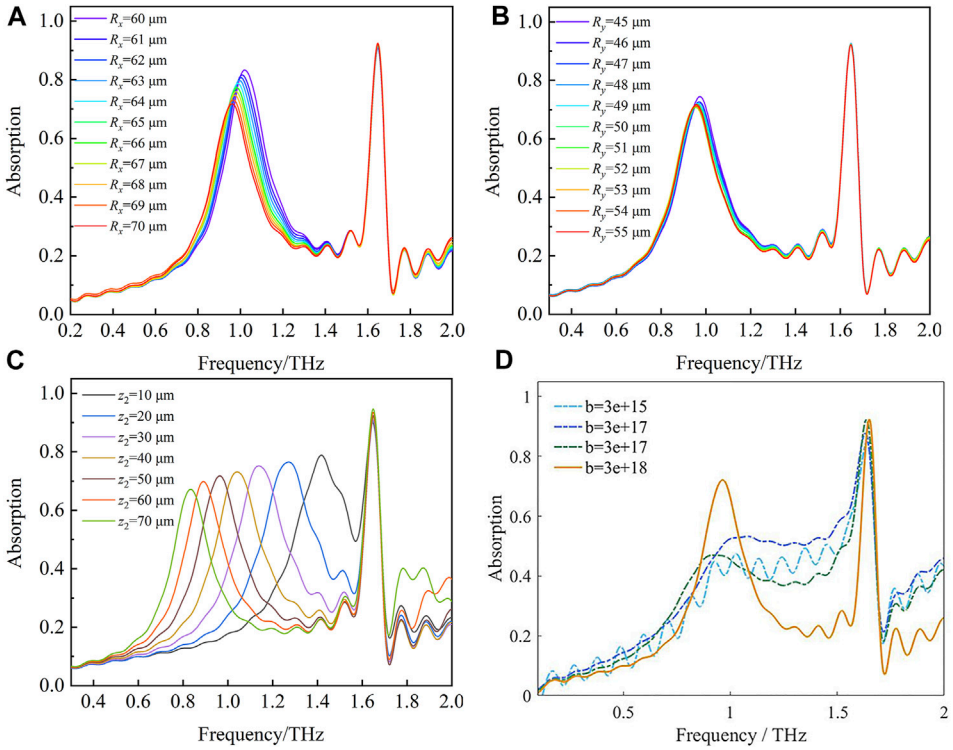

FIGURE 6 | (A) The absorption spectra with the major axis radius of the Si elliptic cylinder R_x increasing from 60 to 70 μm, where R_y is fixed as 50 μm. **(B)** The absorption spectra with the minor axis radius of the Si elliptic cylinder R_y increasing from 45 to 55 μm, where R_x is fixed as 70 μm. **(C)** The absorption spectra with different height of the elliptic cylinder z_2. **(D)** The absorption spectra with different doping concentration of silicon.

sensitivity S_2 of CMMC, (i.e. the slope of the orange fitting lines in **Figure 3B**), reached 314/RIU. That means that both the variation of frequency shift Δf and intensity ΔI can be used for refractive index sensing. **Figure 3C** shows the influence of thickness of the analytes on the absorption spectrum, assuming the RI of the analytes is 1.5. As the thickness of the analytes t increases from 5 to 65 μm, both the frequency and intensity of f_1 decrease, which indicates that the CMMC is also sensitive to the thickness of the analytes. Due to the increase of the filling thickness, the analytes is gradually closer to the region with the largest field intensity, and the interaction between the THz wave and analytes is further enhanced, leading to a more obvious frequency shift, which indicates that the filling thickness of the analytes has an effect on the sensing performance of the CMMC.

The Influence of the Structural Parameters on Absorption Characteristics of the THz Metasurface

In order to guide the structural design of the CMMC, the absorption characteristics with different structural parameters are investigated. **Figure 4A** shows the influence of the period in the x-direction p_x on the absorption. As p_x increases, f_2 shows an obvious red shift, while f_1 has a relatively weak red shift. On the contrary, as shown in **Figure 4B**, with the period in the y-direction p_y increasing, the resonance frequency of f_1 blue shifts while the amplitude gradually decreases. However, the resonance frequency of f_2 is almost unchanged, but the amplitude is significantly reduced. It is obvious that the variations of the period in x-direction or the y-direction have different effects on the two resonance peaks, implying that the resonance mechanisms of the two peaks are different, which is consistent with the analysis of the electric field distribution in **Figures 2A,B**.

Due to the importance of CM in the proposed CMMC, we studied the effect of the structural parameters of CM on the absorption characteristics. As shown in **Figure 5A**, as the major axis radius of the elliptical pore on the CNTs film R_{x1} increases from 10 to 80 μm, the amplitude of f_1 gradually increases, which is resulted from the enlarged aperture and enhanced resonance. With R_{x1} increasing from 10 to 40 μm, the resonance frequency of f_1 decreases. However, the resonance frequency of f_1 increases when R_{x1} increases from 50 to 80 μm. The difference of the shift law might be contribute to the fact that the minor axis radius of the elliptical pore R_{y1} is fixed as 50 μm in this case, when R_{x1} is less than 50 μm (i.e. $R_{x1} < R_{y1}$), it means that the major axis of the elliptical pore is along the y direction; when R_{x1} is greater than 50 μm (i.e. $R_{x1} > R_{y1}$), the major axis is along the x direction. Therefore, the asymmetry of the elliptical structure in the x and y directions results in the difference of shift law of the resonance frequency. **Figure 5B** shows the effect of the change of R_{y1} on the absorption when R_{x1} is fixed at 70 μm ($R_{x1} > R_{y1}$). With the

increase of R_{y1}, f_1 has a slight red shift and the absorption intensity increases significantly. Owing to $R_{x1} > R_{y1}$, the major axis of the ellipse is in the x direction, and there is no critical point in the variation law of frequency. In this case, the increase of R_y1 has a significant effect on the absorption intensity, indicating that the absorption intensity strongly depends on R_y1.

The absorption spectra with different thickness of the CNTs film is shown in **Figure 5C**. As z_1 increases, the intensity of f_1 decreases linearly, but the position of the resonance peak is almost unchanged, which means that the shape and size of the periodic elliptical pore of the CNTs film metasurface affect the position of the peak, and the thickness of the CNTs film only affects the absorption intensity.

The height of the microfluidic channel of the CMMC t_0 is an important parameter for sensing application, the influence of the height of the microfluidic channel on the absorption spectrum is investigated. As shown in **Figure 5D**, as t_0 increasing from 10 to 20 μm, f_1 has a slight blue shift, but the amplitude is almost unchanged. Therefore, the integrated CMMC with different height of microfluidic channel can be designed for refractive index sensing according to practical application.

We also investigate the influence of the structural parameters of the microfluidic channel on the absorption. As shown in **Figure 6A**, with the major axis radius of the Si elliptic cylinder R_x increasing from 60 to 70 μm, both the amplitude and the resonance frequency of f_1 decrease. However, according to **Figure 6B**, compared with R_x, as the minor axis radius of the Si elliptic cylinder R_y increases from 45 to 55 μm, the changes of the amplitude and the frequency of f_1 are not obvious, which results from the electric field distribution of f_1. As shown in **Figure 2A**, most of the electric field of f_1 is along x direction and the intensity is concentrated in the microfluidic channel formed by CM on the top and MC at the bottom. As a result, the amplitude and the frequency of f_1 are not strongly dependent on R_y. **Figure 6C** shows the absorption spectra with different height of the elliptic cylinder z_2. In particular, as z_2 increases from 10 to 70 μm, the resonance frequency of f_1 decreases significantly, the resonant peak has a significant red shift, which imply that the position of f_1 can be controlled by the height of the elliptic cylinder, which provides an idea for sensing and detection in a wider range. Doping concentration is an important parameter affecting the dielectric properties of silicon. Therefore, we investigated the influence of doping concentration on the absorption properties of the proposed CMMC. In **Figure 6D**, as the doping concentration increases, the resonance absorption is significantly enhanced. As discussed above, it is worth noting that the change of structural parameters of silicon microfluidic channel has little effect on f_2, which further indicates that f_2 is a surface mode mainly determined by CM. The results is agree with the electric field distribution in **Figures 2B,C**.

CONCLUSION

To summarize, we proposed a composite THz metasurface CMMC for sensing, which integrates the CNTs metasurface with periodic elliptical pore structure and the microfluidic channel with periodic elliptic cylindrical structure at the bottom. The properties and sensing performance of the CMMC have been investigated. The study reveals that both the resonant frequency and the intensity of f_1 have a linear response with increase in refractive index of the analytes in the microfluidic channel and the sensitivities can achieve 254 GHz/RIU and 314/RIU, respectively, which is attributed to coupling of the CM and MC and the enhanced interaction between the THz wave and the analytes. The influence of the structural parameters on the absorption characteristics illustrates that the absorption performance of the proposed CMMC can be adjusted by changing the structural parameters, which will provide a guideline for the CMMC design. The demonstrated CMMC will facilitate the realization of carbon nanotube metamaterials sensing applications, and, when combined with microfluidic channel, will provide another sensing strategy with tunable resonance characteristics, and lead to large-area THz biological and chemical sensing.

DATA AVAILABILITY STATEMENT

The raw data supporting the conclusion of this article will be made available by the authors, without undue reservation.

AUTHOR CONTRIBUTIONS

YW conceived the idea and led the design; KZ modified the frame. ZC finished the Figure preparation, TZ and YZ collected the references. YW and XZ finished the whole manuscript writing and the manuscript modification, TZ and XZ contributed to the proofreading, and all authors listed approved it for publication.

FUNDING

This work was supported in part by the National Natural Science Foundational of China under Grant 61975163, and in part by the Natural Science Foundation of Shaanxi Province under Grant 2020JZ-48, and in part by the Youth Innovation Team of Shaanxi Universities under Grant 21JP084, and in part by Open Project of Key Laboratory of Engineering Dielectrics and Its Applications, Ministry of Education under Grant KEY1805.

REFERENCES

1. Glybovski S. B., Tretyakov S. A., Belov P. A., Kivshar Y. S., and Simovski C. R.. Metasurfaces: From Microwaves to Visible. *Phys Rep* (2016) 634:1–72. doi:10.1016/j.physrep.04.004
2. Cojocari M. V., Schegoleva K. I., and Basharin A. A.. Blueshift and Phase Tunability in Planar THz Metamaterials: the Role of Losses and Toroidal Dipole Contribution. *Opt Lett* (2017) 42:1700–3. doi:10.1364/ol.42.001700
3. Wang S., Zhao X., Wang S., Li Q., Zhu J., and Han L.. The Investigation of the Electromagnetic Coupling Effect in Terahertz Toroidal Metasurfaces and

Metamaterials. *J Mater Res Tech* (2020) 9:3935–42. doi:10.1016/j.jmrt.2020.02.019
4. Padilla W. J., Taylor A. J., Highstrete C., Lee M., and Averitt R. D.. Dynamical Electric and Magnetic Metamaterial Response at Terahertz Frequencies. *Phys Rev Lett* (2006) 96:107401. doi:10.1103/PhysRevLett.96.107401
5. Qian Q., Fan L., Zhao L., and Wang C.. Non-metallic and Angular-Insensitive Metasurface Transmissive Long-Pass Filter in the Visible and Near-Infrared Regions. *Opt Lett* (2020) 45:359–62. doi:10.1364/OL.384358
6. Wang Z., Liu J., Ding X., Zhao W., Zhang K., Li H., et al. Three-Dimensional Microwave Holography Based on Broadband Huygens' Metasurface. *Phys Rev Appl* (2020) 13:7. doi:10.1103/PhysRevApplied.13.014033
7. Chen M., Wang Y. X., and Zhao Z. R.. Localized Electromagnetic Resonance Enabled THz Photo Thermo Electric Detection in Graphene. *Front Phys* (2020) 8:8. doi:10.3389/fphy.2020.00216
8. Liu W., Yang Q., Xu Q., Jiang X., Wu T., Wang K., et al. Multifunctional All-Dielectric Metasurfaces for Terahertz Multiplexing. *Adv Opt Mater.* (2021) 9:2100506. doi:10.1002/adom.202100506
9. Zhang Z., Zhu Z., Yuan M., Minghui Li M. H., You G., Chen L., et al. Predict Sample's Line Positions of Absorption Peaks in Terahertz Band with the Forced Radiation Intensity of Molecular Electric Dipoles. *Opt Commun* (2020) 458:124848. doi:10.1016/j.optcom.2019.124848
10. Beruete M., and Jáuregui-López I.. Terahertz Sensing Based on Metasurfaces. *Adv Opt Mater.* (2020) 8:1900721. doi:10.1002/adom.201900721
11. Zhang K., Yuan Y., Ding X., Ratni B., Burokur S. N., and Wu Q.. High-Efficiency Metalenses with Switchable Functionalities in Microwave Region. *ACS Appl Mater Inter* (2019) 11:28423–30. doi:10.1021/acsami.9b07102
12. Lu Y., Wang X.-K., Sun W.-F., Feng S.-F., Ye J.-S., Han P., et al. Reflective Single-Pixel Terahertz Imaging Based on Compressed Sensing. *IEEE Trans Thz Sci Technol* (2020) 10:495–501. doi:10.1109/TTHZ.2020.2982350
13. Wang Y., Cui Z., Zhang X., Zhang X., Zhu Y., Chen S., et al. Excitation of Surface Plasmon Resonance on Multiwalled Carbon Nanotube Metasurfaces for Pesticide Sensors. *ACS Appl Mater Inter* (2020) 12:52082–8. doi:10.1021/acsami.0c10943
14. Geng Z., Zhang X., Fan Z., Lv X., and Chen H.. A Route to Terahertz Metamaterial Biosensor Integrated with Microfluidics for Liver Cancer Biomarker Testing in Early Stage. *Sci Rep* (2017) 7:11. doi:10.1038/s41598-017-16762-y
15. Wang Y., Zhu D., Cui Z., Yue L., Zhang X., Hou L., et al. Properties and Sensing Performance of All-Dielectric Metasurface THz Absorbers. *IEEE Trans Thz Sci Technol* (2020) 10:599–605. doi:10.1109/tthz.2020.3010164
16. Lin S., Xu X., Hu F., Chen Z., Wang Y., Zhang L., et al. Using Antibody Modified Terahertz Metamaterial Biosensor to Detect Concentration of Carcinoembryonic Antigen. *IEEE J Select Top Quan Electron.* (2021) 27:1–7. doi:10.1109/jstqe.2020.3038308
17. Yang X., Zhao X., Yang K., Liu Y., Liu Y., Fu W., et al. Biomedical Applications of Terahertz Spectroscopy and Imaging. *Trends Biotechnol* (2016) 34:810–24. doi:10.1016/j.tibtech.2016.04.008
18. Xu W., Xie L., and Ying Y.. Mechanisms and Applications of Terahertz Metamaterial Sensing: a Review. *Nanoscale* (2017) 9:13864–78. doi:10.1039/C7NR03824K
19. Wang Y. X., Wu W. D., and Zhao Z. R.. Recent Progress and Remaining Challenges of 2D Material-Based Terahertz Detectors. *Infrared Phys Technol* (2019) 102:14. doi:10.1016/j.infrared.2019.103024
20. Kabashin A. V., Evans P., Pastkovsky S., Hendren W., Wurtz G. A., Atkinson R., et al. Plasmonic Nanorod Metamaterials for Biosensing. *Nat Mater* (2009) 8:867–71. doi:10.1038/nmat2546
21. Boltasseva A., and Atwater H. A.. Low-Loss Plasmonic Metamaterials. *Science* (2011) 331:290–1. doi:10.1126/science.1198258
22. Tepliakov N. V., Kundelev E. V., Khavlyuk P. D., Xiong Y., Leonov M. Y., Zhu W., et al. sp2-sp3-Hybridized Atomic Domains Determine Optical Features of Carbon Dots. *ACS Nano* (2019) 13:10737–44. doi:10.1021/acsnano.9b05444
23. Liu B., Zhu W., Gunapala S. D., Stockman M. I., and Premaratne M.. Open Resonator Electric Spaser. *Acs Nano* (2017) 11:12573–82. doi:10.1021/acsnano.7b06735
24. Liu K., Sun Y., Chen L., Feng C., Feng X., Jiang K., et al. Controlled Growth of Super-aligned Carbon Nanotube Arrays for Spinning Continuous Unidirectional Sheets with Tunable Physical Properties. *Nano Lett* (2008) 8:700–5. doi:10.1021/nl0723073
25. Nikolaenko A. E., De Angelis F., Boden S. A., Papasimakis N., Ashburn P., Di Fabrizio E., et al. Carbon Nanotubes in a Photonic Metamaterial. *Phys Rev Lett* (2010) 104:4. doi:10.1103/PhysRevLett.104.153902
26. Zhao J., Zhang W., Sherrell P. Razal J. M., Huang X.-F., Minett A. I., et al. Carbon Nanotube Nanoweb-Bioelectrode for Highly Selective Dopamine Sensing. *ACS Appl Mater Inter* (2012) 4:44–8. doi:10.1021/am201508d
27. Liu S. F., Petty A. R., Sazama G. T., and Swager T. M.. Single-Walled Carbon Nanotube/Metalloporphyrin Composites for the Chemiresistive Detection of Amines and Meat Spoilage. *Angew Chem Int Ed* (2015) 54:6554–7. doi:10.1002/anie.201501434
28. Xu J., Liao D., Gupta M., Zhu Y., Zhuang S., Singh R., et al. Terahertz Microfluidic Sensing with Dual-Torus Toroidal Metasurfaces. *Adv Opt Mater.* (2021) 9:2100024. doi:10.1002/adom.202100024
29. Chen L., Yin H, Chen L., and Zhu Y.. Ultra-sensitive Fluid Fill Height Sensing Based on Spoof Surface Plasmon Polaritons. *J Electromagn Waves Appl* (2017) 32:471–82. doi:10.1080/09205071.2017.1395367
30. Keshavarz A., and Vafapour Z. Sensing Avian Influenza Viruses Using Terahertz Metamaterial Reflector. *IEEE Sensors J* (2019) 19:5161–6. doi:10.1109/jsen.2019.2903731
31. Wang Y., Cui Z., Zhu D., Zhang X., and Qian L.. Tailoring Terahertz Surface Plasmon Wave through Free-Standing Multi-Walled Carbon Nanotubes Metasurface. *Opt Express* (2018) 26:15343–52. doi:10.1364/OE.26.015343
32. Enkrich C., Wegener M., Linden S., Burger S., Zschiedrich L., Schmidt F., et al. Magnetic Metamaterials at Telecommunication and Visible Frequencies. *Phys Rev Lett* (2005) 95:203901. doi:10.1103/physrevlett.95.203901
33. Zhang Y., Li T., Zeng B., Zhang H., Lv H., Huang X., et al. A Graphene Based Tunable Terahertz Sensor with Double Fano Resonances. *Nanoscale* (2015) 7:12682–8. doi:10.1039/c5nr03044g
34. Mcmeekin T. L., Groves M. L., and Hipp N. J.. *Refractive Indices of Amino Acids, Proteins, and Related Substances*. Washington, DC, USA: ACS Publications (1964) p. 54–66. doi:10.1021/ba-1964-0044.ch004
35. Nielsen M. G., Gramotnev D. K., Pors A., Albrektsen O., and Bozhevolnyi S. I.. Continuous Layer gap Plasmon Resonators. *Opt Express* (2011) 19:19310–22. doi:10.1364/OE.19.019310
36. Park J., Kang J.-H., Liu X., and Brongersma M. L.. Electrically Tunable Epsilon-Near-Zero (ENZ) Metafilm Absorbers. *Sci Rep* (2015) 5:9. doi:10.1038/srep15754
37. Li Z.-Y., Xu D.-X., Mckinnon W. R., Janz S., Schmid J. H., Cheben P., et al. Silicon Waveguide Modulator Based on Carrier Depletion in Periodically Interleaved PN Junctions. *Opt Express* (2009) 17:15947–58. doi:10.1364/OE.17.015947

Conflict of Interest: The authors declare that the research was conducted in the absence of any commercial or financial relationships that could be construed as a potential conflict of interest.

Publisher's Note: All claims expressed in this article are solely those of the authors and do not necessarily represent those of their affiliated organizations, or those of the publisher, the editors and the reviewers. Any product that may be evaluated in this article, or claim that may be made by its manufacturer, is not guaranteed or endorsed by the publisher.

frontiers in Physics

ORIGINAL RESEARCH
published: 27 October 2021
doi: 10.3389/fphy.2021.764122

Ultrafast Terahertz Complex Conductivity Dynamics of Layered MoS_2 Crystal Probed by Time-Resolved Terahertz Spectroscopy

Yong Yang[1], Chuan He[1], Yuanyuan Huang[1], Lipeng Zhu[2], Yixuan Zhou[1]* and Xinlong Xu[1]**

[1]Shaanxi Joint Lab of Graphene, State Key Laboratory of Photon-Technology in Western China Energy, International Collaborative Center on Photoelectric Technology and Nano Functional Materials, School of Physics, Institute of Photonics and Photon-Technology, Northwest University, Xi'an, China, [2]School of Electronic Engineering, Xi'an University of Posts and Telecommunications, Xi'an, China

OPEN ACCESS

Edited by:
Xinke Wang,
Capital Normal University, China

Reviewed by:
Bo Zhang,
Capital Normal University, China
Maixia Fu,
Henan University of Technology, China

***Correspondence:**
Yuanyuan Huang
yyhuang@nwu.edu.cn
Yixuan Zhou
yxzhou@nwu.edu.cn
Xinlong Xu
xlxuphy@nwu.edu.cn

Specialty section:
This article was submitted to Optics and Photonics, a section of the journal Frontiers in Physics

Received: 25 August 2021
Accepted: 07 October 2021
Published: 27 October 2021

Citation:
Yang Y, He C, Huang Y, Zhu L, Zhou Y and Xu X (2021) Ultrafast Terahertz Complex Conductivity Dynamics of Layered MoS_2 Crystal Probed by Time-Resolved Terahertz Spectroscopy. Front. Phys. 9:764122. doi: 10.3389/fphy.2021.764122

Ultrafast carrier dynamics, including the carrier photoexcitation and relaxation processes, plays an essential role in improving the performance of molybdenum disulfide (MoS_2)-based optoelectronic devices. Herein, we investigate the photo-generated carrier dynamics in layered MoS_2 crystal using a time-resolved terahertz (THz) spectroscopy. We have analyzed the ultrafast changes of the THz complex photoconductivity deduced from the peak and zero-crossing of THz waveforms. The decay time of the real part of the THz photoconductivity in layered MoS_2 crystal is independent with the pump power, while the imaginary part increases with the pump power. We attribute the decay time of the real part to the carrier recombination process via phonon-assistance and the decay time of the imaginary part to the defect-assisted exciton recombination. The peak values of the complex photoconductivity show a trend of saturation with the increase of the pump power because of the many-body effect at high carrier concentration. This work deepens the understanding of the basic ultrafast physical process in MoS_2 crystal, which is enlightening for the design of novel optoelectronic devices.

Keywords: layered MoS_2 crystal, time-resolved terahertz spectroscopy, ultrafast carrier dynamics, exciton dynamics, terahertz photoconductivity

INTRODUCTION

Transition metal dichalcogenides (TMDs) are burgeoning layered semiconductors with a chemical formula of MX_2 (M represents transition metal elements, including Ti, V, Ta, Mo, W, and Re; X represents chalcogenide atoms, such as S, Se, and Te), in which the van der Waals force connects atomic sheets. Because of the superior properties such as high carrier mobility [1], strong optical nonlinearity [2], and high mechanical strength [3], TMDs materials are advancing the development of many optoelectronic devices, including photodetectors [4], light-emitting diodes [5], field-effect transistors [6], solar cells [7], etc. As one of the most typical and important TMDs, molybdenum disulfide (MoS_2) has been reported to have some unique properties. For example, MoS_2 has an indirect-to-direct bandgap transition when vary the layer number from bulk to monolayer [8]; MoS_2 transistor has a high on/off ratio up to 10^8; MoS_2 has a strong spin-orbit coupling [9].

Therefore, many novel optical and electrical applications [2, 10, 11] are expected to be realized by MoS_2.

Clarifying the carrier dynamics mechanisms of MoS_2 is of key significance for developing MoS_2-based optoelectronic devices. Compared with the detection techniques that investigate the photoexcited carrier properties in a static state, such as photocurrent spectroscopy [12], photoluminescence spectroscopy [13], and electroluminescence spectroscopy [14], transient absorption spectroscopy based on the optical pump-probe technology is indispensable for studying the ultrafast carrier dynamics mechanisms [15]. Specifically, many valuable conclusions have been achieved on the ultrafast dynamic properties of MoS_2. For example, Wang *et al.* have reported the intervalley transfer, energy relaxation, and recombination of carriers in bulk MoS_2 crystal by resolving the dynamic process [16]. Huang *et al.* demonstrated that the exciton dynamics of monolayer and few-layer MoS_2 are remarkably different due to the quantum confinement effect and the surface defect effect [17]. Wang *et al.* proposed that the defect-assisted Auger relaxation of electron–hole recombination in MoS_2 is related to the strong Coulomb interaction and the electron-hole correlation in two-dimensional MoS_2 [18].

Compared with the optical pump-probe technology, optical pump-terahertz probe (OPTP) spectroscopy as another important method to probe the ultrafast process, is sensitive to terahertz (THz) conductivity instead of the static conductivity of materials. The sub-picosecond time resolution of OPTP is suitable to study the ultrafast dynamics of carrier, exciton, and phonon. Sood *et al.* have studied the dynamics of photoexcited carriers in a few-layered MoS_2 using OPTP spectroscopy [19]. They find that the fast relaxation time occurs due to the capture of electrons and holes by defects, and the slow relaxation time is related to bounded excitons which prevent the defect-assisted Auger recombination. For comparison, MoS_2 bulk crystal is an indirect bandgap semiconductor, which indicates that the position of electrons in the momentum space will change before and after the transition. In order to satisfy the conservation of momentum, there would be a large number of phonons and bounded excitons involved in the ultrafast process. Additionally, the exciton effect has been reported to be significant in TMDs [20, 21]. Therefore, understanding the exciton dynamics in MoS_2 crystals is of key importance for the application development.

In this work, we use the OPTP technique to explore the dynamics of photo-induced carriers in layered MoS_2 crystal. The complex photoconductivity is calculated from the pump-induced THz amplitude and phase changes. The real and imaginary parts of the photoconductivity is fitted by the exponential model. The real part-related time constant τ_1 of ~80 ps is independent of the pump power, while the imaginary part-related time constant τ_2 increases from 110 to 260 ps as the pump power increases. The former is explained by the phonon-assisted carrier recombination process and the latter is induced by the defect-assisted exciton recombination. Additionally, with the increase of pump power, the peak values of the real and imaginary parts of the complex conductivity exhibit a trend of saturation, which is attributed to the many-body effect. These results deepen the understanding of carrier dynamics in MoS_2 crystals.

EXPERIMENTAL SECTION

The freestanding layered MoS_2 crystal sample (SPI Supplies) is 90 μm in thickness, and its size is approximately 8 × 8 mm. This crystal sample is hexagonal 2H polytype with good crystalline quality as proved from the X-ray diffraction measurement in our previous work [20]. The Raman spectrum (SmartRaman confocal-micro-Raman module) is used to investigate the phonon characteristics of samples. The light source for the OPTP experiment is a Ti:sapphire femtosecond laser, which has a repetition rate of 1 kHz, a central wavelength of 800 nm, and a pulse width of 35 fs. The beam generated by the femtosecond laser is divided into three parts for the THz wave generation, THz wave detection, and optical pump functions [21]. 1) The THz radiation is generated from the air plasma by a two-color method under 800 and 400 nm laser excitation. The generated THz wave was focused onto the sample by a pair of off-axis parabolic mirrors in a transmission configuration. 2) The THz wave is probed by an electro-optic sampling method using a zinc telluride (ZnTe) (110) crystal as the THz detector. A delay line is used to measure the time domain signal of THz electric field E(t). 3) The pump beam is focused onto the MoS_2 sample in a transmission geometry. A pump delay line is used to change the delay time (t_{pump}) between the pump and probe pulses. The sample is measured in a normal incident angle for both the THz wave and the pump laser. All experiments were measured in a nitrogen environment to avoid THz absorption by atmospheric water vapor.

RESULTS AND DISCUSSION

The Raman spectrum of layered MoS_2 crystal under 532 nm excitation is shown in **Figure 1A**. The peaks E^1_{2g} and A_{1g} are two Raman modes, indicating in-plane and out-of-plane vibrations. The frequencies of these two modes are at around 379.2 and 403.8 m^{-1}, which are consistent with the characteristic peak positions of MoS_2 crystal according to previous report [22]. Since there is a close relationship between the photoexcitation process and the band structure of materials, first-principles calculation is performed to study the band structure of MoS_2 crystal (The calculation software is Quantum Espresso. The Perdew-Burke-Ernzerh of generalized gradient approximation is used for the exchange-correlation potential. We use the ultrasoft pseudopotential to describe the electron–ion interactions and the ultrasoft pseudopotential incorporate the electron orbital of Mo 4s5s4p5p4d and O 2s2p. The in-plane lattice constants are set as a = 3.166 Å and c = 18.41 Å. Monkhorst–Pack k-mesh of 15 × 15 × 15 is set for sampling the Brillouin zone. The kinetic energy cutoffs of the plane waves for charge density and basis function are set to 25 and 300 Ry. The van der Waals corrections are described by the vdW-DF method). As shown in **Figure 1B**, the valence band maximum is at the Γ

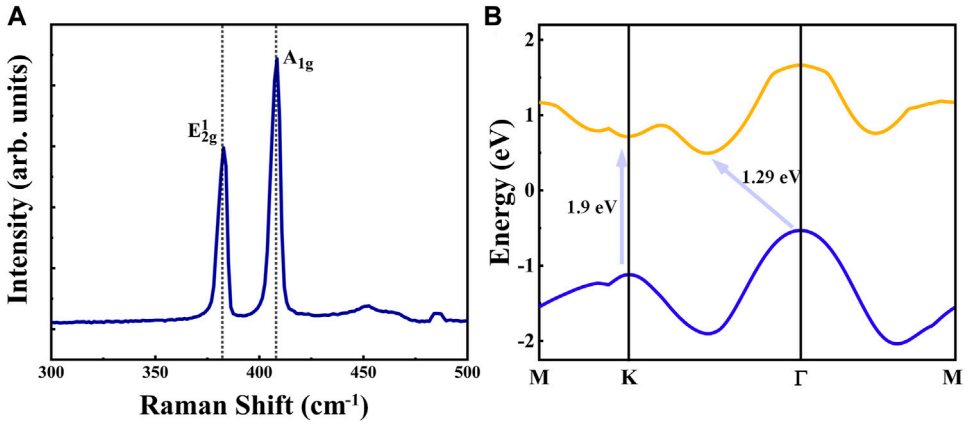

FIGURE 1 | (A) Raman spectrum for layered MoS_2 crystal with 532 nm laser excitation. **(B)** Simplified energy band diagram based on first-principles calculation. The two arrows represent the direct and indirect transition from the valence band maximum to the conduction band minimum.

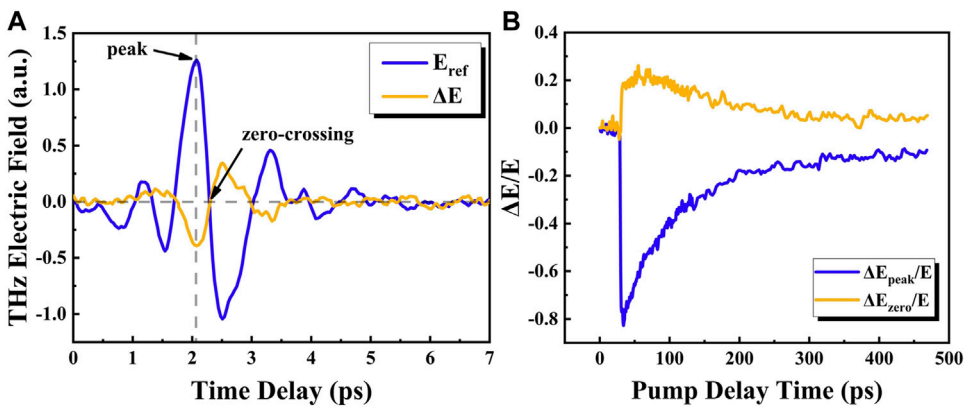

FIGURE 2 | (A) Transmitted THz electric field E(t) (blue line) and photo-induced change of the THz waveform at pump delay time ΔE (t_{pump} = 20 ps) (yellow line) with the pump power of 20 mW for the MoS_2 crystal. **(B)** Pump-induced changes of the THz amplitude and phase of layered MoS_2 crystal at the peak and zero-crossing positions of the THz waveforms.

point, and the conduction band minimum lies at the symmetry point between K and Γ. The transition from valence band maximum to conduction band minimum is indirect [8]. Thus, MoS_2 crystal is an indirect semiconductor with a bandgap energy of 1.29 eV. Additionally, there is a direct transition with bandgap energy of 1.9 eV from valence band K point to conduction band K point, which cannot be realized under the 800 nm (1.55 eV) laser excitation.

We will discuss the ultrafast THz complex conductivity dynamics of MoS_2 by using the OPTP technique in the following parts. The pump laser power is 20 mW. As shown in **Figure 2A**, the THz electric-field transmission waveform through the unexcited layered MoS_2 crystal E_{ref} is labeled as the blue curve, and the photo-induced THz waveform change ΔE at pump delay time t_{pump} = 20 ps is labeled as the yellow curve. The peak and zero-crossing values of the THz waveform are sensitive to absorption and phase change, respectively [23]. The former represents the real component of the complex conductivity and the latter represents the imaginary component of the complex conductivity. Specifically, the THz waveform changes at the peak and zero-crossing positions as a function of pump-probe delay time depict the photoexcitation dynamics of MoS_2 crystal, as shown in **Figure 2B**. Because the photon energy of the incident light is larger than the bandgap of MoS_2 crystal, real carriers will generate after excitation. We can see the THz waveform at both the peak and zero-crossing positions exhibit ultrafast optical response, indicating photo-induced carrier generation and recombination processes.

According to the peak and zero-crossing changes of the THz waveform, the photoconductivity can be calculated by the formula [24]:

$$\Delta\sigma\left(t_{pump}\right) = -\frac{n_{air} + n_{THz}}{Z_0 d} \frac{\Delta E\left(t, t_{pump}\right)}{E\left(t_{\max}\right)}, \tag{1}$$

where n_{air} = 1 is the THz refractive index of air, n_{THz} = 2.95 is the THz refractive index of the MoS_2 crystal [22], Z_0 = 377 Ω is the

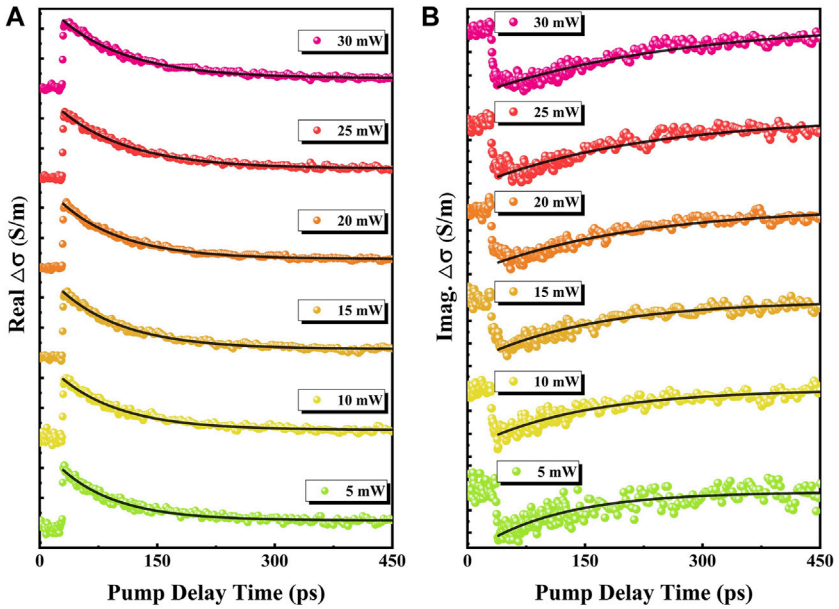

FIGURE 3 | Transient photoinduced real **(A)** and imaginary **(B)** parts of the THz conductivity with different pump power. The dots are experimental data, and the solid lines are the exponential fitting.

free space impedance, and $d = 90$ μm is the thickness of the MoS_2 crystal. Using **Eq. 1**, the photoconductivity of MoS_2 with different pump power from 5 to 30 mW can be obtained. The real and imaginary parts of the photoconductivity are shown in **Figures 3A,B**, respectively. The sub-picosecond abrupt changes observed at ~32 ps in **Figures 3A,B** are related to the process that the photo-induced carriers are excited from the valence band to the conduction band. Subsequently, the slow changes in **Figure 3** correspond to the relaxation processes of photoconductivity. The real and imaginary parts of the complex conductivity reflect the absorption and chromatic dispersion properties of materials, respectively. According to previous reports, the THz absorption properties of MoS_2 are mainly decided by the photo-generated carriers [20], and the THz chromatic dispersion properties of MoS_2 could be contributed from the polarization effects of bound charges such as excitons [25, 26]. Here, the binding energy of exciton in MoS_2 crystals is approximately 0.1 eV [27], which is larger than the thermal energy (≈25 meV) at room temperature. Due to the strong Coulomb interactions among carriers, extraordinary exciton effects have been observed in TMDs such as MoS_2 [17], WSe_2 [21], and WS_2 [20]. Therefore, the exciton effect could be important for the imaginary part of photoconductivity of MoS_2 crystal due to the polarization effect.

Next, the time constants deduced from the pump delay time dependent complex conductivity are analyzed to reveal the relaxation dynamics of the photoexcited carriers and excitons in MoS_2 crystal. The experimental data in **Figure 3** are exponentially fitted by $\Delta\sigma_{RE/IM} = \mathrm{Exp}((t - t_0)/\tau_{1,2})$, where τ_1 (τ_2) is the time constant of the real (imaginary) part of the photoconductivity. The obtained τ_1 and τ_2 with different pump power are shown in **Figure 4A** as depicted by blue and yellow dots, respectively. The time constant τ_1 is approximately 80 ps, independent of the pump power. In comparison, the time constant τ_2 increases linearly from 110 to 260 ps with the increase of the pump power. In MoS_2 crystal, there are many possible relaxation processes. For the fast relaxation processes with a duration of sub-picosecond or several picoseconds, there are carrier-carrier scattering, carrier-phonon scattering, and exciton-exciton scattering in TMD materials [17, 28]. However, these fast processes cannot be identified from our experiment because of the limited time resolution. The time constant τ_1 and τ_2 can mainly be attributed to the slow relaxation processes. For the time constant τ_1, it has been reported that the phonon-mediated recombination time of free carriers is independent on the pump power in layered WSe_2 crystal, monolayer MoS_2, and suspended graphene [17, 21, 29]. Hence, the decay time τ_1 could be attributed to the phonon-assisted free carrier recombination. For the time constant τ_2, it has been reported that defect-assisted exciton recombination can result in an increase of decay time with pump power [20, 21]. The Auger processes for exciton capture by defects are believed to be important in most bulk semiconductors with high carrier densities [18]. Therefore, the time constant τ_2 could be governed by the exciton recombination via defect-assisted Auger process.

Additionally, the peak value of photoconductivity related to the carrier quantity has been discussed. **Figure 4B** shows the pump power dependence of the maximum (minimum) of the real (imaginary) part of photoconductivity. Both the real and imaginary parts exhibit enhanced absolute values with the increase of the pump power, and then present a saturable trend at the high pump power region. Because the photoconductivity is associated with the free carriers and

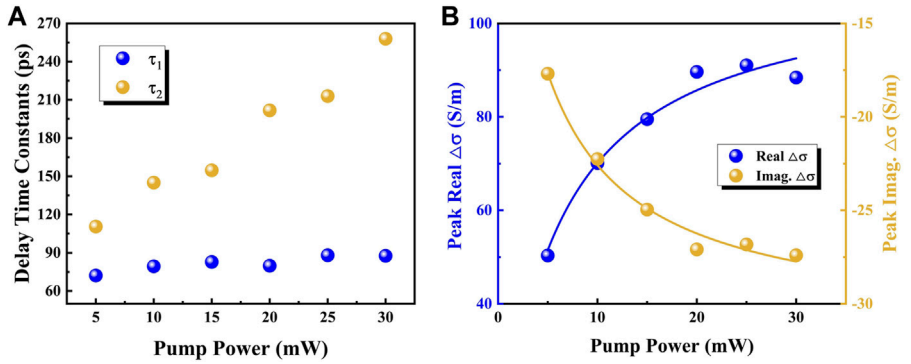

FIGURE 4 | (A) Time constants extracted from the exponential fittings for the real and imaginary parts of the complex conductivity. **(B)** Real (imaginary) part of the complex conductivity at maximum (minimum) points as a function of pump power.

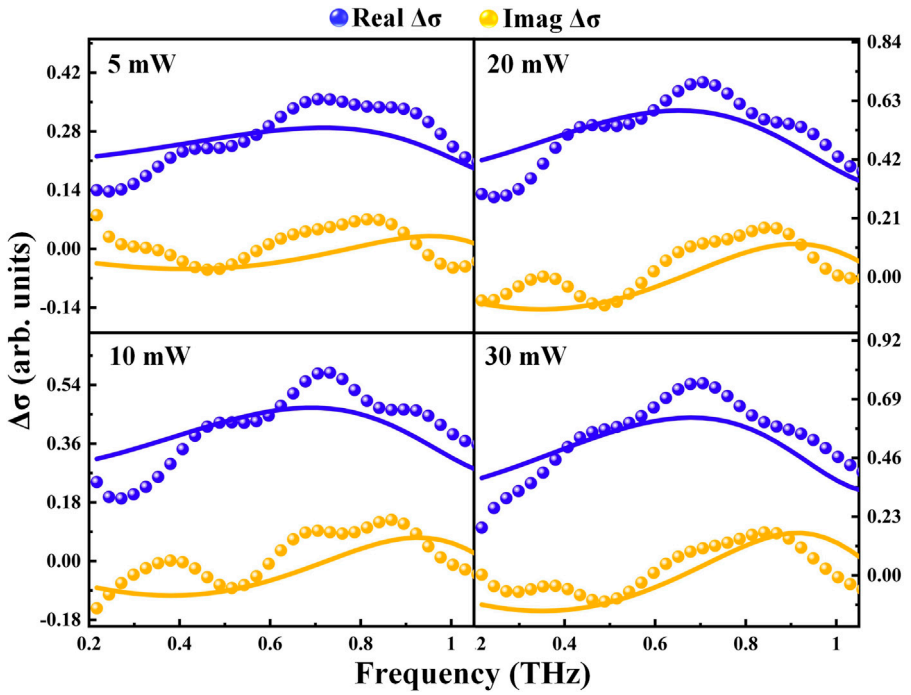

FIGURE 5 | Frequency-dependent transient real and imaginary parts of the photoconductivity measured at the delay time of 5 ps with various pump power of 5, 10, 20, and 30 mW. The blue and yellow solid lines represent the fitting results of the real and imaginary parts of photoconductivity by Drude–Smith-Lorentz model, respectively.

excitons, the enhancement of the peak values indicates that the quantity of photo-induced carriers and excitons increase with the pump power. Then, equation $\Delta\sigma \propto P/(P + P_s)$ (P is the pump power and P_s is the saturation pump power) [21] is used to fit the experimental data. The saturation pump power P_s of the real and imaginary photoconductivity are 3.6 and 5.7 mW, respectively. These results suggest that both photo-induced carriers and excitons are generated before the pump power of 3.6 mW; then, the photo-induced carriers are saturated and excitons are continuously generated before 5.7 mW; at last, both the carriers and excitons become saturated due to the possible many-body effect at high carrier concentration [30, 31]. The carrier density is calculated as [16]:

$$N_0 = \left[1 - \frac{(n_0 - 1)^2 + \kappa_0^2}{(n_0 + 1)^2 + \kappa_0^2}\right] \alpha_0 F_0 / \hbar\omega, \tag{2}$$

where $n_0 = 4.83$ is the real part of the refraction index, $\kappa_0 = 0.78$ is the imaginary part of the refraction index, and $\alpha_0 = 1.23\times10^7$ m^{-1} is the absorption coefficient [22, 32]. The F_0 is the peak energy fluence of the pump pulse, which can be calculated by

TABLE 1 | Fitting parameters used in **Figure 5**.

Pump power [mW]	τ [fs]	C	ω_0 [THz]
5	499	−0.81	1.21
10	612	−0.84	1.17
20	627	−0.85	1.13
30	740	−0.83	1.11

$F_0 = 4\ln(2)P/(\pi f w^2)$, where P is average pump power, $f = 1$ kHz is the repetition rate of the laser, and $w = 2.5$ mm is the radius of focus pump spot. According to **Eq. 2**, the numbers of photo-induced carriers are calculated to be 1.95×10^{25}, 3.9×10^{25}, 5.85×10^{25}, 7.8×10^{25}, 9.75×10^{25}, 11.7×10^{25} m^{-3}, with 5, 10, 15, 20, 25, and 30 mW pump power, respectively.

Finally, the frequency-dependent photoconductivity is obtained by the fast Fourier transform of the time-domain signals. The real and imaginary parts of the photoconductivity are measured at the delay time of 5 ps with a variable pump power of 5, 10, 20, and 30 mW as shown in **Figure 5**. The Drude model can be used to describe the free carrier motion and the Smith term includes the carrier backscattering. In addition, the exciton effect in relaxation process can be described by the Lorentz model. Therefore, we use the Drude–Smith model (free charge species) combined with the Lorentz model (exciton species) to describe the photo-induced complex conductivity. The fitting formula of the Drude-Smith-Lorentz model is described as follows [21]:

$$\sigma_{D-S-L} = \frac{D_0\tau}{1-i\omega\tau}\left(1+\frac{C}{1-i\omega\tau}\right)+\frac{S\omega}{i\left(\omega_0^2-\omega^2\right)+\omega\gamma}, \quad (3)$$

where D_0 is the Drude weight, τ is the free carrier relaxation time, ω is the angular frequency, C ranging from -1 to 0 is related to the degree of carrier scattering, S is the oscillator strength, ω_0 is the resonant frequency, and γ is the damping coefficient. From **Figure 5**, the curves calculated with **Eq. 3** fit well with the dot-denoted experimental data. The fitting coefficients are given in **Table 1**. The relaxation time τ increases with the increase of pump power. The constant C has no pump power dependence, suggesting that the carrier backscattering is not affected by the pump power. In addition, the frequency ω_0 of the oscillator response has no obvious change with the increase of pump power.

CONCLUSION

We have studied the ultrafast photoconductivity response in MoS_2 crystal by OPTP spectroscopy. The time constant of the real part of the photoconductivity, which is independent of the pump power, demonstrates the photo-induced free carrier recombination via phonon-assistance of ~80 ps. The time constant of the imaginary part of the photoconductivity increases with the pump power, revealing the excitons annihilated by a defect-assisted process of ~110–260 ps. The peak values of both the real and imaginary parts of photoconductivity tend to saturate with the increase of pump power due to the many-body effect. This work unveils the relaxation processes of photo-generated carriers and excitons, which could be helpful for developing novel optoelectronic devices based on MoS_2.

DATA AVAILABILITY STATEMENT

The original contributions presented in the study are included in the article/Supplementary Material, further inquiries can be directed to the corresponding authors.

AUTHOR CONTRIBUTIONS

XX, CH, YZ, and YY contributed to conception and design of the study. CH, LZ, and YH designed and built the optics system. YH organized the database. YY wrote the first draft of the article. YY, CH, YZ, and XX wrote sections of the article. All authors contributed to article revision, read, and approved the submitted version.

FUNDING

This work was supported by National Natural Science Foundation of China (No. 12074311, 12004310, 11974279, and 11774288), Natural Science Foundation of Shaanxi Province (2019JC-25, 2020JQ-567).

REFERENCES

1. Strait JH, Nene P, and Rana F. High Intrinsic Mobility and Ultrafast Carrier Dynamics in Multilayer Metal-dichalcogenide MoS_2. *Phys Rev B* (2014) 90(24), 245402. doi:10.1103/PhysRevB.90.245402
2. Huang Y, Zhu L, Yao Z, Zhang L, He C, Zhao Q, et al. Terahertz Surface Emission from Layered MoS_2 Crystal: Competition between Surface Optical Rectification and Surface Photocurrent Surge. *J Phys Chem C* (2017) 122(1): 481–8. doi:10.1021/acs.jpcc.7b09723
3. Mak KF, Lee C, Hone J, Shan J, and Heinz TF. Atomically Thin MoS_2: A New Direct-Gap Semiconductor. *Phys Rev Lett* (2010) 105(13):136805. doi:10.1103/PhysRevLett.105.136805
4. Koppens FHL, Mueller T, Avouris P, Ferrari AC, Vitiello MS, and Polini M. Photodetectors Based on Graphene, Other Two-Dimensional Materials and Hybrid Systems. *Nat Nanotech* (2014) 9(10):780–93. doi:10.1038/nnano.2014.215
5. Sherson JF, Krauter H, Olsson RK, Julsgaard B, Hammerer K, Cirac I, et al. Quantum Teleportation between Light and Matter. *Nature* (2006) 443(7111): 557–60. doi:10.1038/nature05136
6. Radisavljevic B, Radenovic A, Brivio J, Giacometti V, and Kis A. Single-layer MoS_2 Transistors. *Nat Nanotech* (2011) 6(3):147–50. doi:10.1038/nnano.2010.279
7. Singh E, Kim KS, Yeom GY, and Nalwa HS. Two-dimensional Transition Metal Dichalcogenide-Based Counter Electrodes for Dye-Sensitized Solar Cells. *RSC Adv* (2017) 7(45):28234–90. doi:10.1039/c7ra03599c
8. Cheng Y, and Schwingenschlögl U. MoS_2: A First-Principles Perspective. In: ZM Wang, editor. *MoS_2: Materials, Physics, and Devices*. Cham: Springer International Publishing (2014). p. 103–28. doi:10.1007/978-3-319-02850-7_5
9. Huang Y, Yartsev A, Guan S, Zhu L, Zhao Q, Yao Z, et al. Hidden Spin Polarization in the Centrosymmetric MoS_2 crystal Revealed via Elliptically Polarized Terahertz Emission. *Phys Rev B* (2020) 102(8):085205. doi:10.1103/PhysRevB.102.085205

10. Radisavljevic B, and Kis A. Mobility Engineering and a Metal-Insulator Transition in Monolayer MoS_2. *Nat Mater* (2013) 12(9):815–20. doi:10.1038/nmat3687
11. Roy K, Padmanabhan M, Goswami S, Sai TP, Ramalingam G, Raghavan S, et al. Graphene-MoS_2 Hybrid Structures for Multifunctional Photoresponsive Memory Devices. *Nat Nanotech* (2013) 8(11):826–30. doi:10.1038/nnano.2013.206
12. Klots AR, Newaz AKM, Wang B, Prasai D, Krzyzanowska H, Lin J, et al. Probing Excitonic States in Suspended Two-Dimensional Semiconductors by Photocurrent Spectroscopy. *Sci Rep* (2014) 4:6608. doi:10.1038/srep06608
13. Tonndorf P, Schmidt R, Böttger P, Zhang X, Börner J, Liebig A, et al. Photoluminescence Emission and Raman Response of Monolayer MoS_2, MoSe_2, and WSe_2. *Opt Express* (2013) 21(4):4908–16. doi:10.1364/OE.21.004908
14. Cheng R, Li D, Zhou H, Wang C, Yin A, Jiang S, et al. Electroluminescence and Photocurrent Generation from Atomically Sharp WSe2/MoS2 Heterojunction P-N Diodes. *Nano Lett* (2014) 14(10):5590–7. doi:10.1021/nl502075n
15. Wang Q, Ge S, Li X, Qiu J, Ji Y, Feng J, et al. Valley Carrier Dynamics in Monolayer Molybdenum Disulfide from Helicity-Resolved Ultrafast Pump-Probe Spectroscopy. *ACS Nano* (2013) 7(12):11087–93. doi:10.1021/nn405419h
16. Kumar N, He J, He D, Wang Y, and Zhao H. Charge Carrier Dynamics in Bulk MoS_2 crystal Studied by Transient Absorption Microscopy. *J Appl Phys* (2013) 113(13):133702. doi:10.1063/1.4799110
17. Shi H, Yan R, Bertolazzi S, Brivio J, Gao B, Kis A, et al. Exciton Dynamics in Suspended Monolayer and Few-Layer MoS_2 2D Crystals. *ACS Nano* (2013) 7(2):1072–80. doi:10.1021/nn303973r
18. Wang H, Zhang C, and Rana F. Ultrafast Dynamics of Defect-Assisted Electron-Hole Recombination in Monolayer MoS_2. *Nano Lett* (2015) 15(1):339–45. doi:10.1021/nl503636c
19. Kar S, Su Y, Nair RR, and Sood AK. Probing Photoexcited Carriers in a Few-Layer MoS_2 Laminate by Time-Resolved Optical Pump-Terahertz Probe Spectroscopy. *ACS Nano* (2015) 9(12):12004–10. doi:10.1021/acsnano.5b04804
20. Xing X, Zhao L, Zhang Z, Liu X, Zhang K, Yu Y, et al. Role of Photoinduced Exciton in the Transient Terahertz Conductivity of Few-Layer WS_2 Laminate. *J Phys Chem C* (2017) 121(37):20451–7. doi:10.1021/acs.jpcc.7b05345
21. He C, Zhu L, Zhao Q, Huang Y, Yao Z, Du W, et al. Competition between Free Carriers and Excitons Mediated by Defects Observed in Layered WSe_2 Crystal with Time-Resolved Terahertz Spectroscopy. *Adv Opt Mater* (2018) 6(19):1800290. doi:10.1002/adom.201800290
22. Huang Y, Zhu L, Zhao Q, Guo Y, Ren Z, Bai J, et al. Surface Optical Rectification from Layered MoS_2 Crystal by THz Time-Domain Surface Emission Spectroscopy. *ACS Appl Mater Inter* (2017) 9(5):4956–65. doi:10.1021/acsami.6b13961
23. Cunningham PD. Accessing Terahertz Complex Conductivity Dynamics in the Time-Domain. *IEEE Trans THz Sci Technol* (2013) 3(4):494–8. doi:10.1109/tthz.2013.2258193
24. Cunningham PD, Hayden LM, Yip H-L, and Jen AK-Y. Charge Carrier Dynamics in Metalated Polymers Investigated by Optical-Pump Terahertz-Probe Spectroscopy. *J Phys Chem B* (2009) 113(47):15427–32. doi:10.1021/jp906454g
25. Wang F, Shan J, Islam MA, Herman IP, Bonn M, and Heinz TF. Exciton Polarizability in Semiconductor Nanocrystals. *Nat Mater* (2006) 5(11):861–4. doi:10.1038/nmat1739
26. Jensen SA, Ulbricht R, Narita A, Feng X, Müllen K, Hertel T, et al. Ultrafast Photoconductivity of Graphene Nanoribbons and Carbon Nanotubes. *Nano Lett* (2013) 13(12):5925–30. doi:10.1021/nl402978s
27. Komsa H-P, and Krasheninnikov AV. Effects of Confinement and Environment on the Electronic Structure and Exciton Binding Energy of MoS_2 from First Principles. *Phys Rev B* (2012) 86(24), 241201. doi:10.1103/PhysRevB.86.241201
28. Sun D, Rao Y, Reider GA, Chen G, You Y, Brézin L, et al. Observation of Rapid Exciton-Exciton Annihilation in Monolayer Molybdenum Disulfide. *Nano Lett* (2014) 14(10):5625–9. doi:10.1021/nl5021975
29. Gao B, Hartland G, Fang T, Kelly M, Jena D, Xing H, et al. Studies of Intrinsic Hot Phonon Dynamics in Suspended Graphene by Transient Absorption Microscopy. *Nano Lett* (2011) 11(8):3184–9. doi:10.1021/nl201397a
30. Chen K, Ghosh R, Meng X, Roy A, Kim J-S, He F, et al. Experimental Evidence of Exciton Capture by Mid-gap Defects in CVD Grown Monolayer $MoSe_2$. *Npj 2d Mater Appl* (2017) 1(1):15. doi:10.1038/s41699-017-0019-1
31. Mai C, Barrette A, Yu Y, Semenov YG, Kim KW, Cao L, et al. Many-body Effects in Valleytronics: Direct Measurement of valley Lifetimes in Single-Layer MoS_2. *Nano Lett* (2014) 14(1):202–6. doi:10.1021/nl403742j
32. Yan X, Zhu L, Zhou Y, E Y, Wang L, and Xu X. Dielectric Property of MoS_2 crystal in Terahertz and Visible Regions. *Appl Opt* (2015) 54(22):6732. doi:10.1364/ao.54.006732

Conflict of Interest: The authors declare that the research was conducted in the absence of any commercial or financial relationships that could be construed as a potential conflict of interest.

Publisher's Note: All claims expressed in this article are solely those of the authors and do not necessarily represent those of their affiliated organizations, or those of the publisher, the editors and the reviewers. Any product that may be evaluated in this article, or claim that may be made by its manufacturer, is not guaranteed or endorsed by the publisher.

frontiers in Physics

ORIGINAL RESEARCH
published: 28 October 2021
doi: 10.3389/fphy.2021.768186

Spatiotemporal Distribution Characterization for Terahertz Waves Generated From Plasma Induced by Two-Color Pulses

Erli Wang[1,2], Yulong Wang[3,4], Wenfeng Sun[1,2], Xinke Wang[1,2], Shengfei Feng[1,2], Peng Han[1,2], Jiasheng Ye[1,2] and Yan Zhang[1,2]*

[1]Department of Physics, Capital Normal University, Beijing, China, [2]Beijing Key Lab for Metamaterials and Devices, Key Laboratory of Terahertz Optoelectronics Ministry of Education, Beijing, China, [3]Nanophotonics Research Center, Shenzhen Key Laboratory of Micro-Scale Optical Information Technology, Shenzhen University, Shenzhen, China, [4]Songshan Lake Materials Laboratory, Dongguan, China

The spatiotemporal distribution of terahertz (THz) radiation from plasma has been demonstrated with the technology of THz focal-plane imaging. It has been found that the spatiotemporal distribution will vary with the frequency, as well as the length of plasma. A doughnut-shaped distribution appears in the lower frequency range, while the bell-shaped distribution corresponds to the higher frequency range. For plasmas with different lengths, their generated THz images in the time domain are similar, the THz images in the frequency domain as well. The spatiotemporal distributions are simulated with the off-axis-phase matching theory. All the findings will renew the understanding of the THz generation from plasma induced by two-color pulses.

Keywords: THz focal plane imaging, plasma, off-axis-phase matching, spatiotemporal distribution, THz radiation

OPEN ACCESS

Edited by:
Yingxin Wang,
Tsinghua University, China

Reviewed by:
Jiayu Zhao,
University of Shanghai for Science and Technology, China
Dong-Wen Zhang,
National University of Defense Technology, China

****Correspondence:***
Wenfeng Sun
wfsun@cnu.edu.cn

Specialty section:
This article was submitted to Optics and Photonics, a section of the journal Frontiers in Physics

Received: *31 August 2021*
Accepted: *20 September 2021*
Published: *28 October 2021*

Citation:
Wang E, Wang Y, Sun W, Wang X, Feng S, Han P, Ye J and Zhang Y (2021) Spatiotemporal Distribution Characterization for Terahertz Waves Generated From Plasma Induced by Two-Color Pulses. Front. Phys. 9:768186. doi: 10.3389/fphy.2021.768186

INTRODUCTION

Terahertz (THz) wave generated from plasma has been proven to be a valuable tool in the field of nonlinear spectroscopy, imaging, and remote sensing [1–3]. The scheme of THz radiation from plasma induced by two-color laser pulses [4–7] has attracted more attention, and became popular owing to the emitted THz wave with broad spectrum and high intensity, as well as the good quality of polarization. With the widely application of THz radiation from two-color-induced plasma, its spatial characterization is desired. Many efforts have been put on this by using incoherent or coherent methods. The THz spatial distribution was deduced to be the shape of bell [8, 9] by raster scanning with the pyroelectric detectors or doughnut-shape [10] by raster scanning with Michelson interferometer; With a THz camera the transverse intensity of THz wave was captured and 3D-reconstructed to be the dumbbell shape [11]. There is also reported work contributing the conical hollow of THz distribution into the photo-induced carriers in the silicon wafer [12], which was used to filter the THz waves in the experiment. However, all these results seem incomplete for the comprehensive spatial characterization of THz waves. The influence of single-color plasma channel length on an angular THz radiation distribution was studied [13], yet its THz emission mechanism differs significantly from that of the two-color scheme. To fully understand the THz emission from two-color-induced plasma, it is necessary to characterize the spatiotemporal distribution of THz wave generated from plasma induced by two-color pulses.

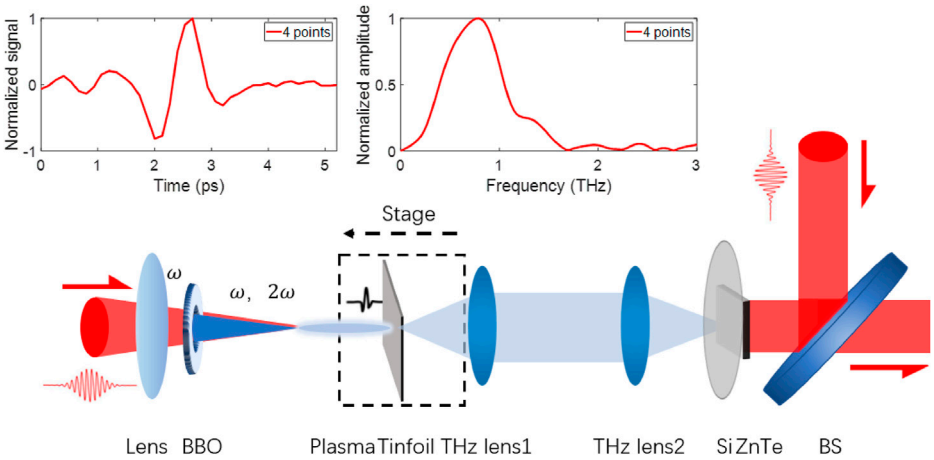

FIGURE 1 | Schematic diagram of experimental setup. BS: Beam Splitter, BBO: Barium Boron Oxide Crystal. The dashed part is used to measure the spatiotemporal distribution of THz waves generated by plasma with different lengths. The insets are the THz time-domain signal and its Fourier-transformed spectrum, obtained by summing the values of four pixels in the center part of the CCD.

In this work, the spatiotemporal distribution of THz wave radiated from plasma has been measured by using the technology of THz focal-plane imaging. For the plasma with unchanged length, THz spatial images in the time domain and frequency domain are presented, as well as their evolution. For plasmas with different lengths, the similarity and difference of the THz spatiotemporal distribution are also demonstrated. The experimental results are in accord with their simulations. These results are helpful in re-understanding the mechanism of the THz generation from plasma.

EXPERIMENTAL AND SIMULATION RESULTS

In the experiment, the technology of THz focal-plane imaging is used to obtain the spatiotemporal distribution of THz waves radiated from plasma induced by two-color pulses. The experimental setup is illustrated in **Figure 1**. A laser amplifier provides laser pulses with the central wavelength of 800 nm, repetition frequency of 1 kHz and pulse width of 35 fs. The femtosecond pulses are divided into two beams by a beam splitter (BS), one is used as the pump pulse and the other one is used as the probe pulse. The average pump and probe power are 700 and 13 mW, respectively. The pump pulse is focused by a lens with the focal length of 200 mm. With this lens, a relative uniform plasma about 7 mm is formed. There is a Barium Boron Oxide (BBO) crystal between the lens and its geometric focus. When the fundamental waves (800 nm) of femtosecond laser pass through the BBO crystal, their second harmonic waves generate. Both the fundamental (ω) and second harmonic (2ω) pulses ionize the air at the focus, which form a filament radiating THz waves. A 4f imaging system consisting of 2 THz lenses with the focal length of 100 mm and diameter of 75.8 mm is introduced in the THz beam. The front focal plane of the 4f imaging system coincides with the focus of the optical lens, while its back focal plane coincides with the ZnTe crystal (<110>, 10 $mm \times 10\ mm \times 1\ mm$). With this 4f

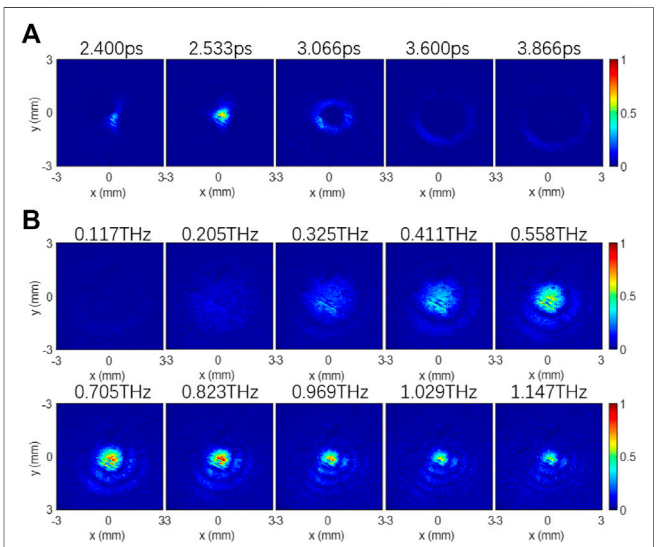

FIGURE 2 | Normalized THz images in the time domain **(A)** and frequency domain **(B)**.

imaging system, THz images delivered from the front focal plane to the detection crystal. A silicon wafer is used to combine the probe pulses and THz waves. The probe pulses are subjected to the refractive index modulation of the crystal by the THz electric field, then they are captured by a CCD. In the measurement, the images of THz waves have been extracted by the technology of dynamic matching and subtraction [14]. For clarity, the THz time-domain signal and its Fourier-transformed spectrum are also shown in the inset of **Figure 1**, which was obtained by summing the values of four pixels in the center part of the CCD.

In the experiment, by selecting proper experimental parameters, such like the crystal axis angle of the BBO crystal and the distance to the geometric focus of the focusing lens, the

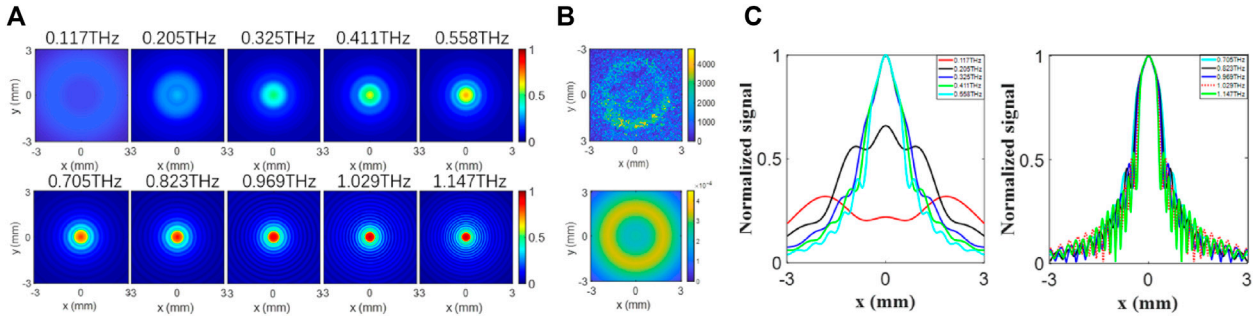

FIGURE 3 | Simulation and experimental results of THz spatial distribution. **(A)** Simulation results by the off-axis phase matching model. **(B)** Unnormalized experimental (up) and simulation (bottom) images at 0.117 THz. **(C)** THz amplitude distributions at lower frequencies (left) and higher frequencies (right).

generated THz signal was optimized. After that, the THz spatiotemporal distribution is measured and shown in **Figure 2A**. At the initial time of the THz pulse $t \leq 2.533$ ps, the spatial intensity distribution obtained by the above system is mainly concentrated near the center of the optical axis, like a solid bright spot. Thereafter, it diffuses when $t \geq 3.066$ ps, and the THz light spot diffuses into a hollow ring with the radius gradually increasing. In the process of diffusion, the amplitude of THz wave in the ring region decreases gradually due to the effect of divergence until the overall signal disappears. These THz temporal images were Fourier-transformed to obtain their field distributions at different frequencies. The results are shown in **Figure 2B**. For clearly, all images are normalized by the maximum value of the THz signal. It is clear that the THz field appears as a weak annular profile in the lower frequency range, while it appears in the region near the optical axis in the higher frequency range. With the frequency increasing, the annular side lobes gradually appear around the solid spot. Compared with that of the central spot the intensity of the annular side lobes becomes more and more obvious. It indicates that the radiation angle is corresponding to the frequency component of the radiated THz wave, which is consistent with the result reported in Ref. [15]. As illustrated in **Figure 2**, it seems that there are some nonuniform intensity distributions in these THz images, which was caused by some defects in the ZnTe crystal.

As shown in **Figure 2B**, with the frequency increasing, the spatial distribution of THz wave changes from the shape of doughnut to bell mixed with dark ring lobes. Currently, there are many theoretical models used to describe THz generation from ionized plasma, including the model of pondermotive, photocurrent, four-wave mixing and off-axis phase matching [7, 16–18]. Considering this experimental system, we adopt an off-axis phase matching model for simulation, in which the parameters similar to that in the experiment was selected. Different from the work in Ref. [16], the near-field profile of THz emission from the plasma has been calculated. For the case of plasma length shorter than the dephasing length, the near-filed integration and their initial phases are also considered in the simulation. The simulation results are shown in **Figure 3A**. In the lower frequency range, $\nu \leq 0.558$ THz, the spatial distribution of THz wave gradually changes from the shape of doughnut to bell, and the ring side lobes begin to appear; In the higher frequency range, $\nu \geq 0.705$ THz, the center spot of THz image becomes smaller and the annular side lobe becomes more obvious. According to the theory of off-axis phase matching, THz waves radiated from each point sources interfere constructively and accumulate continuously in the paraxial region; Away from the axis, THz waves interfere destructively and form alternative dark side ring lobes. For demonstration, we present the unnormalized experimental and simulated images at 0.117 THz, as shown in **Figure 3B**, the upper one is the experimental result, while the lower one is the simulated result. It is obviously that both the experimental and simulated spatial distributions are circular with the similar size, indicating that the theoretical simulation results are in good agreement with the experimental ones. To reveal the dependence of THz spatial distributions at different frequency, we extracted their THz amplitude information along the center line of the simulated images at different frequencies. The values of these curves were normalized by their own maximum, respectively, and plotted in **Figure 3C**. In **Figure 3C**, the left subfigure corresponds the lower frequency range $0.117\ \text{THz} \leq \nu \leq 0.558$ THz, while the right one corresponds the higher frequency range $0.705\ \text{THz} \leq \nu \leq 1.147$ THz. When $0.117\ \text{THz} \leq \nu \leq 0.325$ THz, the simulated distribution transits gradually from the shape of annular to bell with the frequency increasing; When $\nu = 0.411$ THz, the ring side lobe appears. With the frequency increasing, the ring side lobe becomes more obvious, as shown in the right subfigure of **Figure 3C**. Comparing **Figure 3** with **Figure 2B**, one may find that more ring side lobes in the simulation results than that in the experimental ones, it may be caused by an error of optical focus position between the experiment and simulation.

In addition, images of THz radiation from plasma with different lengths are also obtained. As shown in the dashed part of **Figure 1**, a tinfoil is placed slightly away from the end of the plasma. Moving the tinfoil to make it approach the plasma end, until the tinfoil is penetrated by the plasma. Since the diameter of the hole on the tinfoil is similar to that of the plasma, we believe that the THz wave radiated from the plasma at the left side of the foil can be blocked and only the

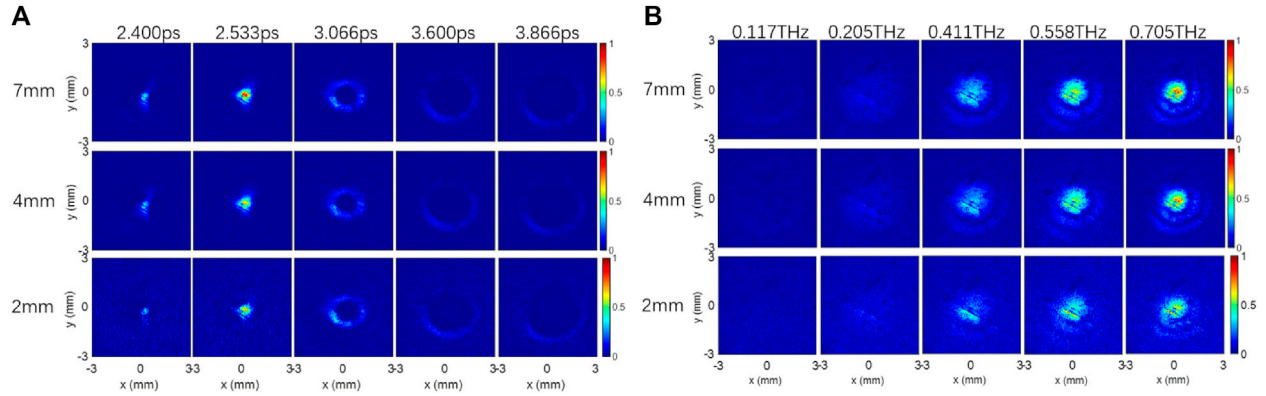

FIGURE 4 | Experimental results of THz waves radiated from plasmas with different lengths. THz images in the time domain **(A)** and frequency domain **(B)**.

THz wave radiated from the plasma on the right side can be detected. By moving the foil to the left, the electric field $E_i\,(i = 1, 2, 3\ldots)$ of THz waves radiated from plasma of different lengths can be obtained. For the case of plasma length comparable with the depth of field of the 4f system, the influence of the fixed front-focus of the 4f system on the experimental results is acceptable. In the experiment, we move the tinfoil across the plasma with the length of 7 mm by the step of 1 mm. The experimental results in the time domain and frequency domain are shown in **Figures 4A,B**, respectively. From **Figure 4A**, it can be found that the patterns of THz radiation from the plasmas with the same length diffuse from solid to hollow ring and then disappear over time. Moreover, the spatial shape and size of THz wave radiated from different lengths of plasma are maintained, but their intensities decrease with the plasma length shortened. Similarly, the images in **Figure 4A** are Fourier-transformed to obtain their frequency-domain images as shown in **Figure 4B**. For the plasmas of the same length, the spatial distribution of THz waves at different frequencies evolves from a doughnut-shape at low frequencies to a bell-shape at high frequencies; For the same frequency, the spatial distribution shape of THz waves radiated from different lengths of plasma is similar, while the intensity decreases with the decrease of plasma length. All these results indicate the accumulation effect of THz waves radiated from plasma.

It is known that the above THz electric fields $E_i\,(i = 1, 2, 3\ldots)$ are generated from plasma fragments with different lengths, and these fragments are obtained by separating from one and the same filament. Thus, it allows us to achieve the THz electric fields at different positions of the plasma by subtracting the electric fields generated from the adjacent plasma fragments,

$$ME_{THzi} = E_i - E_{i-1}\,(i = 1, 2, 3\ldots) \tag{1}$$

E_0 is the THz electric field when the plasma length is 0, i.e., $E_0 = 0$. It is reported that the peak frequency of the THz emission was used in characterizing the plasma density [19], the THz frequency corresponds to the plasma frequency, which can be written as,

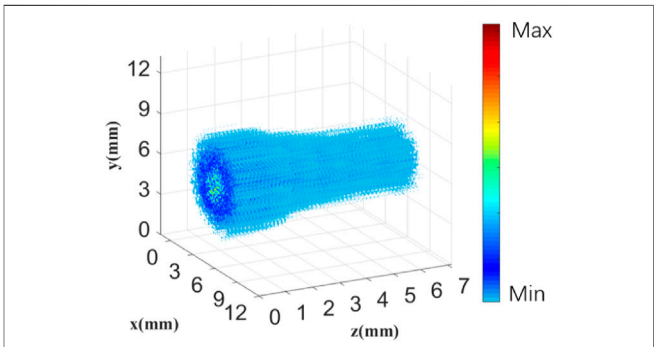

FIGURE 5 | Electron density distributions at different positions of the plasma.

$$\omega_p = \sqrt{4\pi e^2 n_e / m_e}, \tag{2}$$

Where n_e is the electron density and m_e is the electron mass. The electric field E_{THz} is proportional to the oscillation frequency of the plasma under the assumption of the appropriate laser field and gas density [20], meaning that $E_{THz} \propto \sqrt{n_e}$. Therefore, the electron density distributions at different positions of the plasma can be obtained, as shown in **Figure 5**. It can be found that the electron density of the plasma distributes symmetrically in the cross section. Additionally, the electron density is higher in the center of the plasma, and it decreases gradually with the increase of the diameter of the plasma. In the longitudinal direction, the electron density is also not uniform, and its density maximum locates near the beginning of the filament, which is in reasonable agreement with Refs. [19, 21–23].

CONCLUSION

The THz spatiotemporal distribution of THz radiation from plasma has been measured by the technology of THz focal-plane imaging. With the off-axis phase matching model, we obtained their simulation results, and the simulation results are in good agreement with the experimental ones. THz spatial distributions are doughnut-shape at low frequencies and bell-shape at high frequencies. The spatiotemporal distribution characteristics of THz wave from

plasmas with different lengths are similar, but their intensities depend on the length of the plasma seriously. With the THz images radiated from plasmas of different lengths, the electric density inside of the plasma has been revealed.

DATA AVAILABILITY STATEMENT

The original contributions presented in the study are included in the article/Supplementary Material, further inquiries can be directed to the corresponding author.

AUTHOR CONTRIBUTIONS

EW, YW, and WS contributed to experiment and simulation. WS designed the study. XW, SF, PH, JY, and YZ performed the theoretical analysis. All authors contributed to article revision, read, and approved the submitted version.

FUNDING

The National Natural Science Foundation of China (61735002, 11774243, 11774246, 11474206, 11404224); Youth Innovative Re-search Team of Capital Normal University (19530050146, 18530500155, 20530290053); Connotative Development Foundation for Distinguished Young Talents in Capital Normal University (2055105); Capacity Building for Science and Technology Innovation–Fundamental Scientific Research Funds (20530290072, 19530050170,19530050180,18530500186, 025185305000/142, 025185305000/142).

REFERENCE

1. Kampfrath T, Sell A, Klatt G, Pashkin A, Mährlein S, and Dekorsy T. Coherent Terahertz Control of Antiferromagnetic Spin Waves. *Nat Photon* (2011) 5: 31–4. doi:10.1038/nphoton.2010.259
2. Ulbricht R, Hendry E, Shan J, Heinz TF, and Bonn M. Carrier Dynamics in Semiconductors Studied with Time-Resolved Terahertz Spectroscopy. *Rev Mod Phys* (2011) 83:543–86. doi:10.1103/revmodphys.83.543
3. Liu J, Dai J, Chin SL, and Zhang X-C. Broadband Terahertz Wave Remote Sensing Using Coherent Manipulation of Fluorescence from Asymmetrically Ionized Gases. *Nat Photon* (2010) 4:627–31. doi:10.1038/nphoton.2010.165
4. Zhang XC, Shkurinov A, and Zhang Y. Extreme Terahertz Science. *Nat Photon* (2017) 11:16–8. doi:10.1038/nphoton.2016.249
5. Clerici M, Peccianti M, Schmidt BE, Caspani L, Shalaby M, and Giguère M. Wavelength Scaling of Terahertz Generation by Gas Ionization. *Phys Rev Lett* (2013) 110:253901. doi:10.1103/physrevlett.110.253901
6. Siegel PH. Terahertz Technology in Biology and Medicine. *IEEE Trans Microwave Theor Techn.* (2004) 52(10):2438–47. doi:10.1109/tmtt.2004.835916
7. Cook DJ, and Hochstrasser RM. Intense Terahertz Pulses by Four-Wave Rectification in Air. *Opt Lett* (2000) 25(16):1210–2. doi:10.1364/ol.25.001210
8. Akhmedzhanov RA, Ilyakov IE, Mironov VA, Suvorov EV, Fadeev DA, and Shishkin BV. Generation of Terahertz Radiation by the Optical Breakdown Induced by a Bichromatic Laser Pulse. *J Exp Theor Phys* (2009) 109(3):370–8. doi:10.1134/s1063776109090027
9. Zhong H, Karpowicz N, and Zhang X-C. Terahertz Emission Profile from Laser-Induced Air Plasma. *Appl Phys Lett* (2006) 88(26):261103. doi:10.1063/1.2216025
10. Andreeva VA, Kosareva OG, Panov NA, Shipilo DE, Solyankin PM, and Esaulkov MN. Ultrabroad Terahertz Spectrum Generation from an Air-Based Filament Plasma. *Phys Rev Lett* (2016) 116(6):063902–5. doi:10.1103/physrevlett.116.063902
11. Klarskov P, Strikwerda AC, Iwaszczuk K, and Jepsen PU. Experimental Three-Dimensional Beam Profiling and Modeling of a Terahertz Beam Generated from a Two-Color Air Plasma. *New J Phys* (2013) 15(7):075012–3. doi:10.1088/1367-2630/15/7/075012
12. Sørensen C, Guiramand L, Degert J, Tondusson M, Skovsen E, and Freysz E. Conical versus Gaussian Terahertz Emission from Two-Color Laser-Induced Air Plasma Filaments. *Opt Lett* (2020) 7(45):2132–5. doi:10.1364/OL.390112
13. Koribut AV, Rizaev GE, Mokrousova DV, Savinov SA, Reutov AA, and Mityagin YA. Similarity of Angular Distribution for THz Radiation Emitted by Laser Filament Plasma Channels of Different Lengths. *Opt Lett* (2020) 45(45):4009–11. doi:10.1364/OL.394377
14. Wang X, Cui Y, Sun W, Ye J, and Zhang Y. Terahertz Real-Time Imaging with Balanced Electro-Optic Detection. *Opt Commun* (2010) 283(23):4626–32. doi:10.1016/j.optcom.2010.07.010
15. Zhao J, Chu W, Wang Z, Peng Y, Gong C, and Lin L. Strong Spatial Confinement of Terahertz Wave inside Femtosecond Laser Filament. *ACS Photon* (2016) 3(12):2338–43. doi:10.1021/acsphotonics.6b00512
16. You YS, Oh TI, and Kim KY. Off-axis Phase-Matched Terahertz Emission from Two-Color Laser-Induced Plasma Filaments. *Phys Rev Lett* (2012) 109(18):183902–5. doi:10.1103/physrevlett.109.183902
17. Borodin AV, Panov NA, Kosareva OG, Andreeva VA, Esaulkov MN, and Makarov VA. Transformation of Terahertz Spectra Emitted from Dual-Frequency Femtosecond Pulse Interaction in Gases. *Opt Lett* (2013) 38(38): 1906–8. doi:10.1364/OL.38.001906
18. Béjot P, Kasparian J, and Wolf J-P. Dual-color Co-filamentation in Argon. *Opt Express* (2008) 16(18):14115–27. doi:10.1364/oe.16.014115
19. Wang T-J, Ju J, Wei Y, Li R, Xu Z, and Chin SL. Longitudinally Resolved Measurement of Plasma Density along Femtosecond Laser Filament via Terahertz Spectroscopy. *Appl Phys Lett* (2014) 105:051101. doi:10.1063/1.4892424
20. Kim K-Y, Glownia JH, Taylor AJ, and Rodriguez G. Terahertz Emission from Ultrafast Ionizing Air in Symmetry-Broken Laser fields. *Opt Express* (2007) 15(8):4577–84. doi:10.1364/oe.15.004577
21. Gaarde MB, and Couairon A. Intensity Spikes in Laser Filamentation: Diagnostics and Application. *Phys Rev Lett* (2009) 103:043901. doi:10.1103/PhysRevLett.103.043901
22. Chen Y, Théberge F, Kosareva O, Panov N, Kandidov VP, and Chin SL. Evolution and Termination of a Femtosecond Laser Filament in Air. *Opt Lett* (2007) 32(24):3477–9. doi:10.1364/ol.32.003477
23. Sun X, Xu S, Zhao J, Liu W, Cheng Y, and Xu Z. Impressive Laser Intensity Increase at the Trailing Stage of Femtosecond Laser Filamentation in Air. *Opt Express* (2012) 20(4):4790–5. doi:10.1364/oe.20.004790

Conflict of Interest: The authors declare that the research was conducted in the absence of any commercial or financial relationships that could be construed as a potential conflict of interest.

Publisher's Note: All claims expressed in this article are solely those of the authors and do not necessarily represent those of their affiliated organizations, or those of the publisher, the editors and the reviewers. Any product that may be evaluated in this article, or claim that may be made by its manufacturer, is not guaranteed or endorsed by the publisher.

frontiers in Physics

ORIGINAL RESEARCH
published: 03 November 2021
doi: 10.3389/fphy.2021.750588

A Novel Method for the Enhancement of Composite Materials' Terahertz Image Using Unsharp Masking and Guided Filtering Technology

Zhilong Li[1], Jian Zuo[1], Yuanmeng Zhao[1], Zhongde Han[2], Zhihao Xu[2], Yunzhang Zhao[2], Chao Yang[3], Weidong Hu[2] and Cunlin Zhang[1]*

[1]*Beijing Key Laboratory for Terahertz Spectroscopy and Imaging, MOE Key Laboratory of Terahertz Optoelectronics, Department of Physics, Capital Normal University, Beijing, China,* [2]*Beijing Key Laboratory of Millimeter Wave and Terahertz Technology, Beijing Institute of Technology, Beijing, China,* [3]*Kuang-Chi Silver Star Base Technology Room, Shenzhen Kuang-Chi Advanced Technology Co., Ltd, Shenzhen, China*

OPEN ACCESS

Edited by:
Yingxin Wang,
Tsinghua University, China

Reviewed by:
Tao Peng,
Texas A and M University, United States
Ying Liu,
Beijing Normal University, China

***Correspondence:**
Jian Zuo
jian.zuo@cnu.edu.cn

Specialty section:
This article was submitted to Optics and Photonics, a section of the journal Frontiers in Physics

Received: *30 July 2021*
Accepted: *04 October 2021*
Published: *03 November 2021*

Citation:
Li Z, Zuo J, Zhao Y, Han Z, Xu Z, Zhao Y, Yang C, Hu W and Zhang C (2021) A Novel Method for the Enhancement of Composite Materials' Terahertz Image Using Unsharp Masking and Guided Filtering Technology. Front. Phys. 9:750588. doi: 10.3389/fphy.2021.750588

When terahertz imaging technology is used for the nondestructive testing of composite materials, the signal is often affected by the experimental environment and internal noise of the system, as well as the absorption and scattering effect of the tested materials. The obtained image has degradation phenomena such as low contrast, poor resolution of small targets and blurred details. In order to improve the image quality, this paper proposes a novel method for the enhancement of composite materials' terahertz image by using unsharp masking and guided filtering technology. The method includes the processing steps of hard threshold shrinkage denoising based on discrete wavelet transform, amplitude imaging, unsharp masking, guided filtering, contrast stretching, and pseudo-color mapping. In this paper, these steps are reasonably combined and optimized to obtain the final resulting image. To verify the effectiveness of the proposed method, a 150–220 GHz high frequency terahertz frequency modulated radar imaging system was used to image three commonly used sandwich structure composites, and the enhancement processing were carried out. The resulting images with significantly enhanced contrast, detail resolution and edge information were obtained, and the prefabricated defects were all detected; Five objective evaluation indexes including standard deviation, mean gradient, information entropy, energy gradient and local contrast were used to compare and analyze the processing results of different image enhancement methods. The subjective and objective evaluation results showed that the proposed method can effectively suppress the noise in terahertz detection signals, enhance the ability of defect detection and positioning, and improve the accuracy of detection. The proposed method in this paper is expected to play a positive role in improving the practicability of terahertz imaging detection technology and expanding its application fields.

Keywords: terahertz imaging, image enhancement, discrete wavelet, hard threshold shrinkage denoising, guided filtering, unsharp masking

INTRODUCTION

Terahertz imaging detection technology has the advantages of high penetrability. In the detection of composite materials' defect, it is easier to detect the internal defects of composite materials than other traditional detection technologies, and it can be used for imaging without contacting the tested materials [1]. The photon energy of terahertz wave is in the order of millielectron volts, and it will not cause structural damage to the tested material or produce harmful radiation to biological tissue in terahertz imaging detection [2]. However, in the application of this technology, the terahertz wave will be affected by the experimental environment noise (energy level absorption of water vapor and air molecules around the system), the internal noise of the system (photon radiation noise, thermal noise, granular noise, etc.), and the material properties of the sample to be tested (interlaminar multiple reflections caused by the laminated structure and scattering caused by poor surface roughness of the sample) [3, 4], resulting in the degradation of the detection image such as low contrast, low detail resolution and poor sharpness, which affects the application of terahertz imaging detection technology and the accurate judgment of the internal information of the tested material. Thus, the interference properties of terahertz wave in the imaging process are analyzed. Meanwhile, the de-noising technology and image enhancement technology are used to process the detection image, which is expected to obtain the detection image with high contrast and strong detail resolution.

In order to solve the problem of terahertz image degradation, many scholars did a lot of research. Many methods for terahertz image denoising and enhancement were proposed such as mean filtering, Gaussian filtering, nonlocal mean filtering and the edge detection of Laplacian Gaussian operator. Mean filtering has better removal effect on Gaussian noise in the detected image, but the sharpness of the detected image after filtering will be reduced and the image details such as edges will become blurred; Gaussian filtering can effectively filter out speckle noise in the detected image, but it will cause certain damage to the effective information in the detected signal and the edge and texture details of the image; Nonlocal mean filtering can preserve the texture details of the image while filtering out the background noise, but it cannot adaptively select the optimal filtering parameters, resulting in artifacts in the detection image; The edge detection of Laplacian Gaussian operator can effectively enhance the edge and texture details of the detected image, but it will amplify the background noise while enhancing the edge and details of the image, so that the resolution of the detected image cannot be further improved [5–8]. Therefore, it is necessary to develop new terahertz image denoising and enhancement methods. Guided filtering technology was proposed by, after a large number of experiments, which had good performance in image detail enhancement and other aspects [9]. In their research, a guidance image was used to guide the input image, hence the edge of the output image was the same as the input image, and the texture details were similar to the guidance image. It can effectively preserve the edge information while denoising. In addition, Liu et al. and Zhou et al. used the guided filtering technology to enhance the details of infrared images, and achieved good results. However, the direct use of guided filtering technology would cause the problem that the background noise of the detection image is amplified [10, 11]. Wavelet transform has good time-frequency localization analysis ability and multi-resolution analysis characteristics. In this paper, the hard threshold shrinkage denoising method based on discrete wavelet transform is proposed to filter out the high-frequency noise of the original terahertz detection signal, so as to avoid the problem that the noise in the detection image is amplified after the guided filtering. On the other hand, since the unsharp masking method can preserve the smooth region of the image while highlighting the edge and texture details of the image, this paper proposes to use the sharpened image of the unsharp masking as a guidance image to make the details of the output image clearer. After guided filtering, the obtained detail layer and base layer are gained and superimposed to improve the contrast of terahertz detection image and enhance the detail and edge information of the image. In this paper, a 150–220 GHz high frequency terahertz frequency modulated radar imaging system was used to collect terahertz images of samples, and the denoising and enhancement processing were carried out. In the following, the imaging principle, the principle of wavelet-based unsharp masking and guided filtering method, the experimental samples, experimental setup, the experimental results and objective evaluation are described in detail.

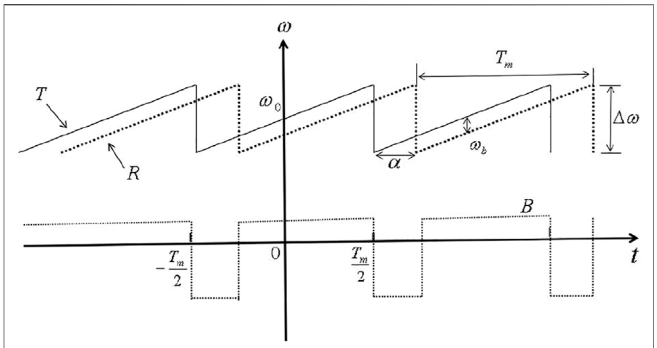

FIGURE 1 | The relationship between angular frequency of the sawtooth wave interference signal and the generated beat frequency signal.

THE PRINCIPLES OF TERAHERTZ FREQUENCY MODULATED RADAR IMAGING SYSTEM

In this paper, a 150–220 GHz high frequency terahertz frequency modulated radar imaging system had been used for imaging experiments [12]. This system uses a sawtooth wave generator to drive a voltage controlled oscillator to produce a linear frequency modulated continuous wave signal in the microwave band. The instantaneous frequency varies linearly with time in the range of 150–220 GHz, and the frequency modulation bandwidth is 70 GHz. The relationship between the angular frequency of the interference signal and the generated beat signal in the sawtooth

wave frequency modulated continuous wave interference is shown in **Figure 1**.

Among them, solid line T represents the modulated signal directly received by the detector, dotted line R represents the sample signal that carries the sample information after the sample reflection, dotted line B represents the beat frequency signal generated by the interference between the modulated signal and the sample signal, $\Delta\omega$ represents the range of the angular frequency of the modulated signal, T_m represents the period of the modulated signal, ω_b represents the frequency difference between the modulated signal and the sample signal, α represents the time delay of the sample signal relative to the modulated signal, and ω_0 represents the central angular frequency and is a constant. According to the principle of frequency modulated continuous wave, the longitudinal resolution of the system is expressed as

$$d = \frac{c}{2 \times \Delta f} \tag{1}$$

Where c is the speed of light, and Δf is the frequency modulation bandwidth of the terahertz source. Therefore, the theoretical longitudinal resolution of the system is 2.1 mm.

When the system is used for terahertz imaging detection of sandwich structure composites with internal defects, the refractive index of defect and non-defect is different, and their reflection coefficient at the interface is different. When the terahertz wave is reflected through the interface, the amplitude of the reflected signal at the defect and non-defect will be different. Therefore, this paper selects the amplitude imaging method that can reflect the specific information of the different interface of the sample to image [13], so as to obtain the internal section information of the sample. The amplitude imaging method is expressed as

$$S_{d_0}(x, y) = S_{Sample}(x, y, d_0), \quad d_0 \in (d_1, d_2) \tag{2}$$

Where $S_{d_0}(x, y)$ is the terahertz signal set at d_0 depth within the sample, and its size is $x \times y$; $S_{sample}(x, y, d_0)$ is the terahertz signal set at different depths, and its size is $x \times y \times (d_2 - d_1)$; d_1, d_2 are distances between the upper surface and the lower surface of the sample and the detector respectively, and d_0 are values according to the actual detection requirements.

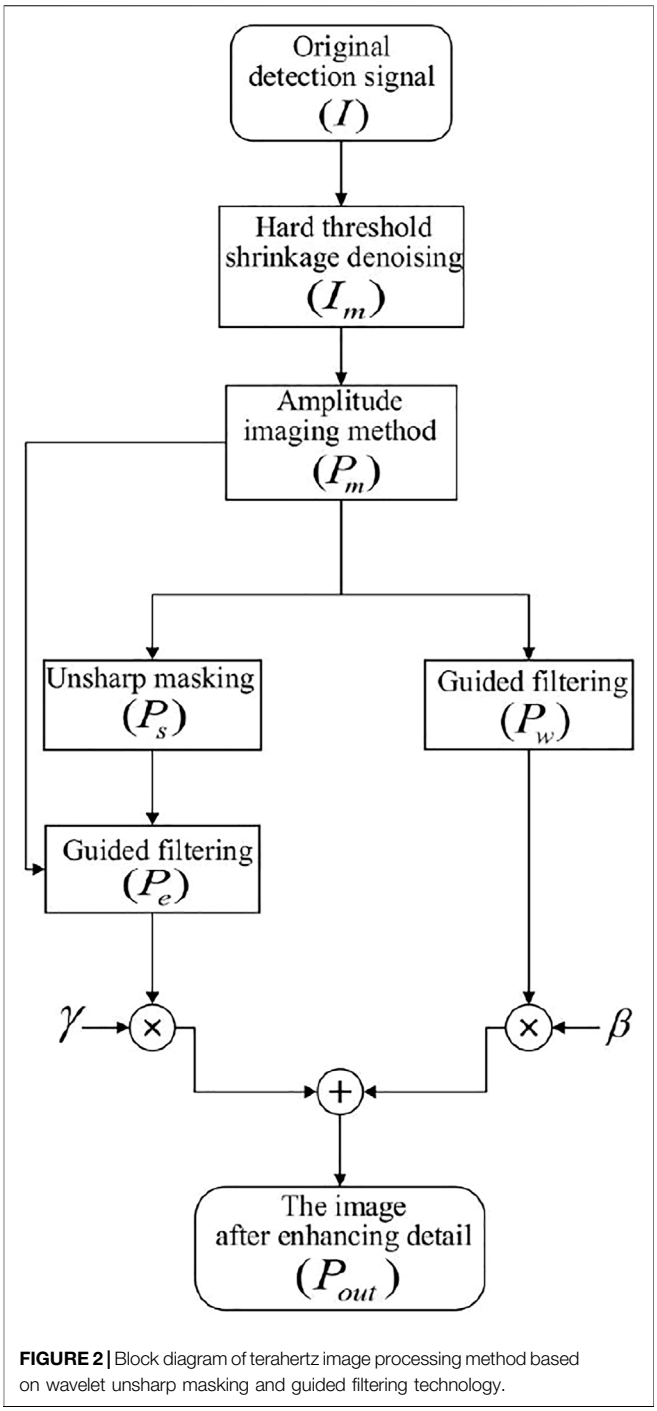

FIGURE 2 | Block diagram of terahertz image processing method based on wavelet unsharp masking and guided filtering technology.

IMAGE DENOISING ENHANCEMENT BASED ON WAVELET UNSHARP MASKING AND GUIDED FILTERING TECHNOLOGY

Wavelet transform is a time-frequency analysis method of signal, which has good time-frequency localization analysis ability and multi-resolution analysis function, and can distinguish the abrupt part of signal and noise in different decomposition layers, so it is suitable for analyzing non-stationary signals and extracting the local characteristics of signals [14]. Terahertz detection signal is a typical non-linear and non-stationary signal, so this paper uses the hard threshold shrinkage denoising method based on discrete wavelet transform to pre-denoise the original terahertz detection signal, and filter out the high-frequency noise in the detection signal. After the first high frequency denoising, the guided filtering technology which can further denoise and keep the edge information of the image well is introduced to filter the image after wavelet denoising. In order to better enhance the texture detail region of the output image, the sharpened image of the unsharpen masking is used as the guidance image to guide and filter the image after wavelet denoising again; Through the gain and superposition of the detail layer and the base layer

obtained after filtering, the purpose of improving the contrast of terahertz detection image and enhancing the resolution of image detail is achieved. The block diagram of the method in this paper is shown in **Figure 2**.

In the first step, the hard threshold shrinkage denoising method based on discrete wavelet transform is used to perform high-frequency denoising preprocessing on the original terahertz detection signal I, and the terahertz detection signal I_m that filters out most of the high-frequency noise is obtained; In the second step, the amplitude imaging method is used to image the detection signal I_m after wavelet denoising, and the preliminary terahertz detection image P_m is obtained; In the third step, the guided filtering technique with the image P_m after wavelet denoising as the guidance image is used to filter its own image to obtain the detail layer P_w; At the same time, the unsharp masking based on mean filtering is applied to the denoised images P_m to get the sharpened image P_s; The fourth step is to use the sharpened image P_s as the guidance image, to repeat the guided filtering operation, and obtain the base layer P_e; In the fifth step, the detail layer P_w and the base layer P_e are gained and superimposed to obtain the terahertz detection image P_{out} with improved contrast and enhanced detail and edge information. In order to further obtain the detection image with better visualization effect, the pseudo-color mapping of image P_{out} is carried out by using the color lookup table method, and the contrast and resolution of the imaging image are enhanced by stretching the contrast and adjusting the scale data range and color scale of the mapping, so as to obtain the final detection resulting image.

Hard Threshold Shrinkage Denoising Enhancement Based on Discrete Wavelet Transform

For a square integrable function $f(t) \in L^2(R)$, $\psi(t)$ is the continuous wavelet generator function, $\psi_{a,b}(t)$ is the continuous wavelet basis function, and the continuous wavelet transform of $f(t)$ is defined as

$$H_f(a,b) = \langle f(t), \psi_{a,b}(t) \rangle = a^{-1/2} \int_{-\infty}^{+\infty} f(t) \overline{\psi(\frac{t-b}{a})} dt \ , \quad a > 0 \tag{3}$$

Where $H_f(a,b)$ is the result of $f(t)$ continuous wavelet transform, a is the scale factor, b is the time shift factor, and $\overline{\psi}(\cdot)$ is the conjugate of the wavelet generating function. Taking $a = a_0^j, b = a_0^j k$ (j is the discretization index, k is the discretization coefficient, $j, k \in Z$), the two are discretized, and the discrete wavelet transform can be defined as

$$H_f(j,k) = \langle f(t), \ \psi_{j,k}(t) \rangle = a_0^{-\frac{j}{2}} \int_{-\infty}^{+\infty} f(t) \overline{\psi(a_0^{\ j} - k)} dt \tag{4}$$

Where $H_f(j,k)$ is the result of discrete wavelet transform of $f(t)$ [15, 16].

In the detection of the sample under test, the detected signal usually contains certain noise, which can be considered as Gaussian white noise. The signal containing noise can be simply expressed as follows

$$y_j = f_j + \delta \cdot z_j \ , \quad j = 1, \ldots, n \tag{5}$$

Where y_j is the signal containing noise, f_j is the ideal noise-free signal, z_j is the doped noise, δ is the noise level, and n is the sampling length. The essence of signal denoising is to use the different characteristics of signal and noise to extract noise $\delta \cdot z_j$ from noise containing signal y_j and restore the ideal signal f_j. For the ideal effective signal, it is continuous in the time domain. Therefore, after the discrete wavelet transform, the energy of the effective signal is mainly concentrated in the low frequency subband, and the modulus of the generated wavelet coefficient would be relatively large. For Gaussian white noise, there is no continuity in the time domain, showing a strong randomness. Meanwhile, after conducting discrete wavelet transform, it also has a strong randomness, thus the energy of noise in wavelet domain is mainly concentrated in the high frequency subband, often still think of the Gaussian white noise, produced by the modulus of wavelet coefficient will be relatively small. Based on the above characteristics, the wavelet coefficients corresponding to noise are still satisfy the Gaussian white noise distribution. According to the definition of standard deviation and variance of random signals, the standard deviation of signals reflects the dispersion degree from each point in the discrete signal to the mean value of signals. Therefore, this paper proposes to take the standard deviation of wavelet coefficients of noise containing signals under the decomposition of each scale of discrete wavelet transform as the threshold to reflect the distribution range of noise wavelet coefficients to a certain extent.

Define the scale function $\varphi(t) \in L^2(R)$ by an integer multiple translation k to get $\varphi_{0,k}(t)$, then

$$\varphi_{0,k}(t) = \varphi(t-k) \ , \ k \in Z \tag{6}$$

If space $V_0 = \overline{\underset{k}{Span}\{\varphi_{0,k}(t)\}}$ is defined by a signal linearly expressed by signal $\varphi_{0,k}(t)$, then V_0 is called a closed signal space of $\varphi_{0,K}(t)$.By translating and stretching the scale function, a new scale function $\varphi_{j,k}(t)$ is obtained, which is expressed as

$$\varphi_{j,k}(t) = 2^{j/2} \varphi(2^j t - k), \ \ j \in Z \ , \ k \in Z \tag{7}$$

Similarly, the newly closed signal space spanned by $\varphi_{j,k}(t)$ is

$$\begin{aligned} \varphi_{j,k}(t) = V_j &= \overline{\underset{k}{Span}\{\varphi_{j,k}(t)\}} \\ &= \overline{\underset{k}{Span}\{2^{j/2}\varphi(2^j t - K\} \ , \ j \in Z \ , \ k \in Z} \end{aligned} \tag{8}$$

After further derivation of the scale function $\varphi_{j,k}(t)$, the multi-resolution analysis equation corresponding to the scale function coefficient is obtained, and the expression is

$$\varphi(t) = \sum_k h_0[k] \cdot \sqrt{2} \varphi(2t-k) \tag{9}$$

The equation shows that different scale functions correspond to different $h_0[k]$ [17, 18]. When the noise containing signal $y_i \in V_{j+1}$, the noise containing signal can be expressed as

$$y_i = \sum_k c_j[k] \cdot \varphi_{j,k}(t) + \sum_k d_j[k] \cdot \psi_{j,k}(t) \tag{10}$$

Among them, there is

$$c_j[k] = \langle y_i, \varphi_{j,k}(t) \rangle, \quad d_j[k] = \langle y_i, \psi_{j,k}(t) \rangle \tag{11}$$

According to the multi-resolution analysis equation $\varphi_t = \sum_k h_0[n] \cdot \sqrt{2}\varphi(2t-n)$ of the scale function, we can obtain

$$\varphi_{j,k}(t) = \sum_n h_0[n-2k] \cdot \varphi_{j+1,n}(t) \tag{12}$$

Then there is

$$\begin{aligned} c_j[k] &= \langle y_i, \varphi_{j,k}(t) \rangle = \sum_n h_0[n-2k] \cdot \langle y_i, \varphi_{j+1,n}(t) \rangle \\ &= \sum_n h_0[n-2k] \cdot c_{j+1}[n] \end{aligned} \tag{13}$$

Similarly, according to $\psi(t) = \sum_n h_1[n] \cdot \sqrt{2}\varphi(2t-n)$, the wavelet coefficient $d_j[k]$ at each scale and each decomposition layer can be obtained as

$$d_j[k] = \sum_n h_1[n-2k] \cdot c_{j+1}[n] \tag{14}$$

Set the standard deviation of the wavelet coefficient $d_j[k]$ as threshold U, and the expression is

$$U = \sqrt{\frac{1}{M-1} \sum_{q=1}^{M} \left\{ \left(\sum_n h_1[n-2k] \cdot c_{j+1}[n] \right)_q - \frac{\sum_{q=1}^{M} \left(\sum_n h_1[n-2k] \cdot c_{j+1}[n] \right)_q}{M} \right\}^2} \tag{15}$$

where M is the number of wavelet coefficients of the noise containing signal under the decomposition of each scale of the discrete wavelet transform.

According to the characteristics of Gaussian distribution, setting the wavelet coefficient within the threshold range to zero can suppress the interference of noise to the maximum extent, namely, the effect of hard threshold function. Therefore, this paper selects the hard threshold function to carry out the hard threshold shrinkage denoising process for the wavelet coefficient of the noise containing signal. When the absolute value of the wavelet coefficient of the noise containing signal is less than the set threshold, it is made to be zero; otherwise, it keeps unchanged. After shrinkage denoising, the wavelet coefficients are reconstructed and restored to the terahertz detection signal, and the amplitude imaging method is used for imaging processing to obtain the preliminary terahertz detection image.

Guided Filtering

Guided filtering [9–11] is a filtering method with good performance in image denoising, defogging and detail enhancement. Its core idea is to guide the input image through a guidance image based on the local linear model, so that the overall contour feature of the output image is similar to that of the input image, and the texture detail region is similar to that of the guidance image. The output image q can be expressed as follows

$$q = f_{guider}(p, I, r, \varepsilon) \tag{16}$$

Where p is the input image, i.e., the image after wavelet denoising, I is the guidance image, r is the size of the filtering window, ε is the regularization parameter, r and ε can be determined by empirical value. In this paper, r is 3 and ε is 0.64. The assumption between output image q and guidance image I is as follows : there is a linear relationship in local window w_v centered on pixel v, and the output expression of a pixel can be expressed as

$$q_i = g_v I_i + o_v \ , \quad \forall i \in w_v \tag{17}$$

Where i corresponds to the pixel index in the local window, g_v and o_v are linear coefficients in the window. By calculating the derivative gradient on both sides of the above equation, $\nabla q = g\nabla I$ can be obtained. It can be seen that when the input guidance image has gradient in a certain region, the output image will also maintain the corresponding gradient. Therefore, the guided filter has good edge preservation performance while smoothing the background. In order to obtain the optimal solution of g_v and o_v, it is necessary to retain the effective information of the input image p as much as possible in the output image q. Even if the difference between the two is the smallest, the method is usually to introduce the minimization cost function and minimize it to solve the optimization problem. $E(g_v, o_v)$ is the minimization cost function, and the expression is as follows

$$E(g_v, o_v) = \sum_{i \in w_v} \left[(g_v I_i + o_v - p_i)^2 + \varepsilon g_v^2 \right] \tag{18}$$

Where εg_v^2 is the penalty term, ε is used to prevent g_v too large regularization parameters. The **Eq. 18** is solved by linear regression model to minimize it, and the optimal solution of g_v and o_v can be obtained as

$$g_v = \frac{\frac{1}{|w|} \sum_{i \in w_v} I_i p_{i-} \mu_v \overline{p_v}}{\sigma_v^2 + \varepsilon} \tag{19}$$

$$o_v = \overline{p_v} - g_v \mu_v \tag{20}$$

Where μ_v and σ_v^2 are the mean value and variance of pixels in local window w_v of the guidance image, $|w|$ is the number of pixels contained in w_v, and $\overline{p_v} = \frac{1}{|w|} \sum_{i \in w_v} p_i$ is the mean value of image p to be filtered in the window. When using **Eq. 19** to calculate the linear coefficient, the g_v and o_v calculated in different window w_v are obviously different, which can be solved by averaging the values obtained from g_v and o_v, so the output image can be expressed as

$$q_i = \frac{1}{|w|} \sum_{i \in w_k} (g_v I_i + o_v) = \overline{g_i} I_i + \overline{o_i} \tag{21}$$

Where $\overline{g_i} = \frac{1}{|w|} \sum_{v \in w_v} g_v$ and $\overline{o_i} = \frac{1}{|w|} \sum_{v \in w_v} o_v$ are the average of linear coefficients of all local windows under the same pixel index.

Guided Filtering Based on Unsharp Masking

Unsharp masking [19, 20] is a common sharpening enhancement technique. Its basic principle is that the high frequency part of the image is obtained by subtracting the original image from the blurred image that is obtained by low-pass filtering, and then the high frequency part of the image is gained and superimposed with the original image to obtain the resulting image with enhanced details and edges. The unsharp masking process can be expressed as follows

$$l(i, j) = f(i, j) + \zeta \times \{f(i, j) - LP[f(i, j)]\} \tag{22}$$

where $f(i, j)$ is the original input image, LP is the low-pass filter, ζ is the gain coefficient of high-frequency details, and $l(i, j)$ is the enhanced output image.

In this paper, the mean filter is selected as the low-pass filter smoothing filter, and the mean filter template with a size of 3×3 is generated to conduct convolution filtering on the image after wavelet denoising, so as to obtain its blurred image. According to the principle of unsharp masking, the difference operation between the original image and the blurred image is used to obtain the mask image, that is, the image reflecting the detail information of the image. After ζ factor multiplication of the mask image, it is superimposed with the original image to obtain the sharpened image with enhanced detail and edge information in the image after wavelet denoising, so as to achieve the effect of image sharpening. Using this linear unsharp masking method to process the terahertz detection image can get better sharpening effect. While the sharpness of the details is improved, the smooth region in the original image is not affected and preserved. Finally, the sharpened image of unsharp masking is used as the guidance image to conduct the guided filtering on the image after wavelet denoising, so that the texture details in the image after wavelet denoising are similar to those in the guidance image.

Image P_m after wavelet denoising is processed by guided filtering technology with its own image P_m and sharpened image P_s as the guidance image, the detail layer P_w reflecting the image detail information and the base layer P_e reflecting the image contour are obtained. The obtained detail layer P_w and the base layer P_e are superposed with the gain of β and γ coefficients respectively, and the terahertz detection resulting image P_{out} with improved contrast, enhanced detail and edge information is obtained. The process can be expressed as follows

$$P_{out} = \beta \times P_w + \gamma \times P_e \tag{23}$$

Where P_{out} is the output terahertz detection resulting image, β and γ are the gain coefficients, P_w is the detail layer, and P_e is the base layer.

IMAGING SAMPLES, EXPERIMENTAL METHODS AND IMAGE PROCESSING

Sample Introduction and Experimental Setup

Polymethacrylimide foam composites are heat-resistant composites with the highest strength and stiffness to weight ratio. As the core material of sandwich structure, polymethacrylimide foam composites are widely used in aerospace, shipbuilding, military and other fields [21]. As one of the three major polymer materials, rubber has high elasticity than metal, high mechanical strength and good bending resistance. Because of its unique properties, rubber is widely used in medical and health, power communication, civil engineering and other fields [22]. Glass fiber reinforced composites are widely used in the bearing and electromagnetic wave transmission structures of unmanned aerial vehicles due to their excellent strength-weight ratio, aerodynamic performance and microwave permeability [23]. With the increasingly wide application of the above composites, the demand for its quality control, nondestructive testing and evaluation is also increasing. In the process of preparation and application, the above composites will be affected by external forces and temperature variations, resulting in internal defects such as cracks, voids and adhesive debonding, affecting the normal use of composite materials, and when the damage reaches a certain level, it will even cause a catastrophe [24], so the accurate detection of composite materials has important practical significance.

Polymethacrylimide Foam Sandwich Structure Composite Material

In this paper, aramid fiber paper honeycomb and polymethacrylimide foam composites were used to combine into sample 1 (the actual photos, defect location and size, structure diagram were shown in **Figure 3**). The sample was composed of thin aramid fiber paper honeycomb with thickness of 4.0 mm, two layers of polymethacrylimide foam with thickness of 4.3 mm and aramid fiber paper honeycomb with thickness of 40.0 mm, which were bonded to each other by epoxy resin adhesive, and two layers of Teflon films with diameters of 10.0 and 6.0 mm and thicknesses of 0.1 mm were used to prefabricate the adhesive debonding defects of different sizes in the sample. The locations of the two adhesive debonding defects were shown in the green mark in **Figure 3**.

Rubber and Glass Fiber Reinforced Composite Sandwich Structure

Sample two rubber and glass fiber reinforced composite sandwich structure (the actual photos, defect location and size, structure diagram were shown in **Figure 4**). The sample consisted of a rubber of 10.0 cm × 10.0 cm in size and 5.0 mm in thickness and a glass fiber reinforced composite of the same size and 13.0 mm in thickness. The two were bonded to each other by epoxy resin adhesive, and three delamination defects with a length of 4.2 cm and a depth of 2.0 mm were prefabricated in the glass fiber reinforced composite. The locations of the defects were shown in the yellow block in **Figure 4**.

Polymethacrylimide Foam and Polyvinyl Chloride Sheet Sandwich Composite Material

Sample 3 polymethacrylimide foam and polyvinyl chloride sheet sandwich composite material (the actual photos, defect location and size, structure diagram were shown in **Figure 5**). The sample was composed of two layers of 4.3 mm in thickness of

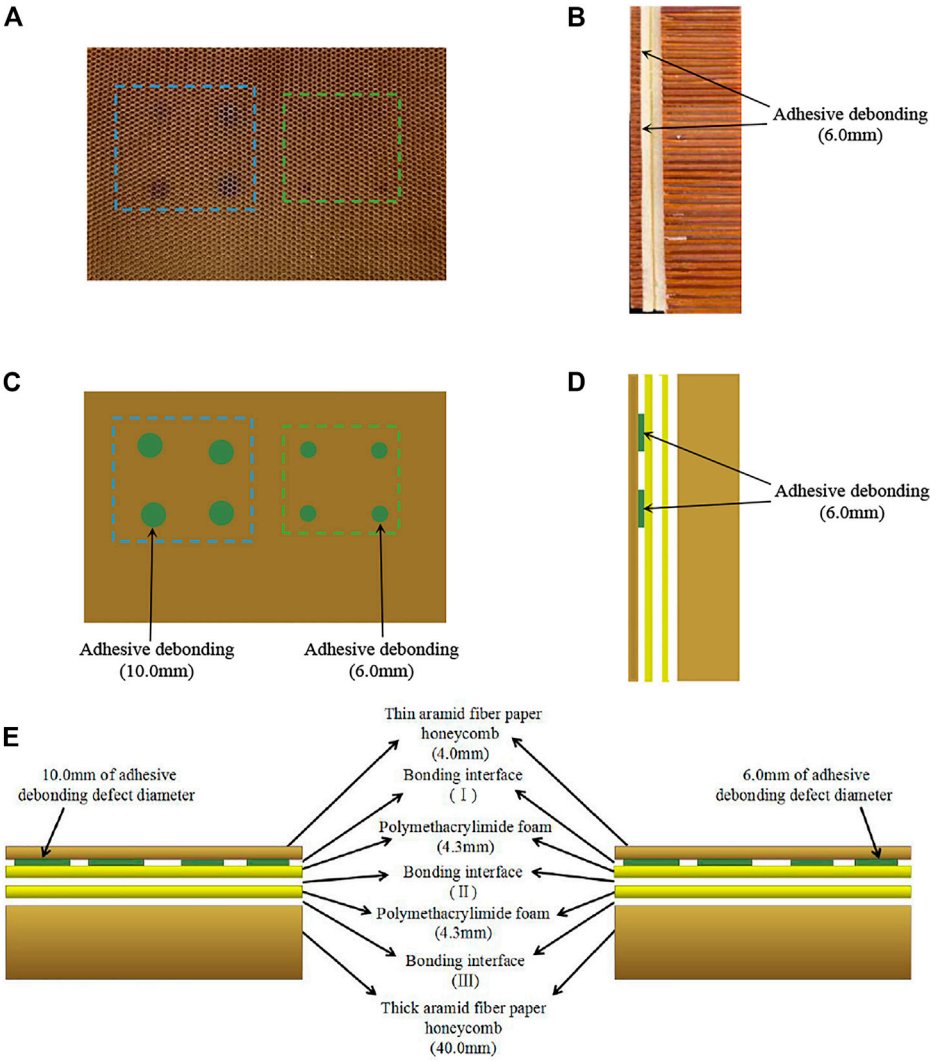

FIGURE 3 | The actual photos, defect location and size, structure diagram of aramid fiber paper honeycomb and polymethacrylimide foam sandwich composite material. **(A)** the actual photo **(top view)**, **(B)** the actual photo (side view), **(C)** the diagram of defect location and size **(top view)**, **(D)** the diagram of defect location and size (side view), **(E)** the structure diagram.

polymethacrylimide foam and a layer of 2.0 mm in thickness of polyvinyl chloride sheet, which were also bonded with epoxy resin adhesive, and Teflon films of 10.0 and 3.0 mm in diameter and 0.1 mm in thickness were respectively used to prefabricate the adhesive debonding defects of different sizes in the sample. The locations of the two adhesive debonding defects were shown in the green mark in **Figure 5**.

Experimental Setup

In this paper, when the 150–220 GHz high frequency terahertz frequency modulated radar imaging system was used for imaging detection of the above composite materials, in order to reduce the system noise and make the detection images clearer, all samples were placed near the focal plane of the detection system and detected by one-way point-by-point scanning. In order to further improve the detection accuracy of the detection system, the minimum detection accuracy of the stepper motor for the adhesive debonding defect in sample 1 with a diameter of 10.0 mm was set as 2.0 mm × 2.0 mm, and the minimum detection accuracy of the stepper motor for the adhesive debonding defect with a diameter of 6.0 mm was set as 1.0 mm × 1.0 mm; The minimum detection accuracy of the stepper motor was set as 1.5 mm × 1.5 mm for the delamination defects in sample two; the minimum detection accuracy of the stepper motor for the adhesive debonding defect in sample 3 with a diameter of 10.0 mm was also set as 1.5 mm × 1.5 mm, and the minimum detection accuracy of the stepper motor for the adhesive debonding defect with a diameter of 3.0 mm was set as 1.0 mm × 1.0 mm.

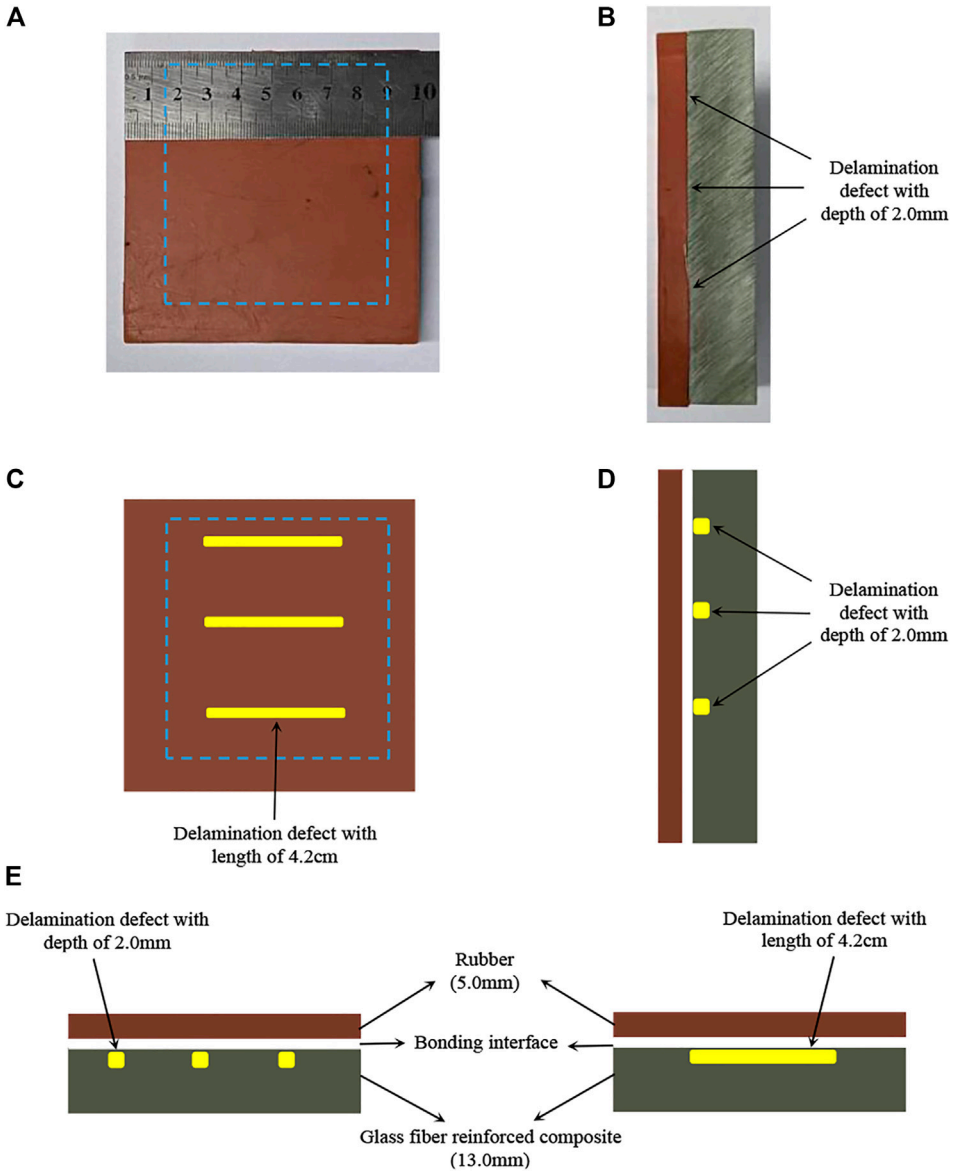

FIGURE 4 | The actual photos, defect location and size, structure diagram of rubber and glass fiber reinforced composite sandwich structure. **(A)** the actual photo **(top view)**, **(B)** the actual photo (side view), **(C)** the diagram of defect location and size **(top view)**, **(D)** the diagram of defect location and size (side view), **(E)** the structure diagram.

Image Processing Results and Analysis

After the imaging detection of the above composite materials, the amplitude imaging method was used to image the obtained terahertz detection signal, and Gaussian filtering and the method proposed in this paper were used to denoise and enhance the terahertz detection image. When the hard threshold shrinkage denoising method based on discrete wavelet transform was used to denoise the original detection signal, for the adhesive debonding defect with a diameter of 10.0 mm in sample 1, "sym4" was selected as the wavelet denoising combination with 3 layers of decomposition layer, and "sym5" was selected as the wavelet denoising combination with four layers of decomposition layer for the adhesive debonding defect with a diameter of 6.0 mm; For the delamination defects in sample 2, "sym5" was selected as the wavelet denoising combination with two layers of decomposition layer; For the adhesive debonding defect with a diameter of 10.0 mm and the adhesive debonding defect with a diameter of 3.0 mm in sample 3, the combination of wavelet denoising with "sym5" as the wavelet basis and the decomposition layer of 3 layers was selected for hard threshold shrinkage denoising.

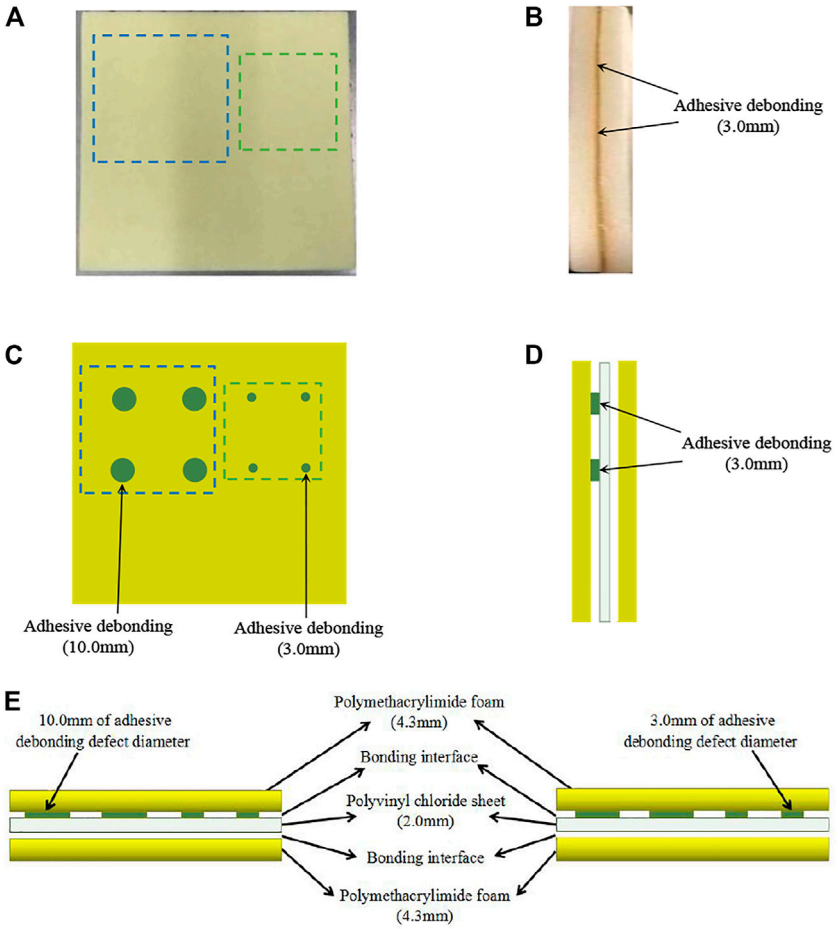

FIGURE 5 | The actual photos, defect location and size, structure diagram of polymethacrylimide foam and polyvinyl chloride sheet sandwich composite material. **(A)** the actual photo **(top view)**, **(B)** the actual photo (side view), **(C)** the diagram of defect location and size **(top view)**, **(D)** the diagram of defect location and size (side view), **(E)** the structure diagram.

Sample1: Imaging Results Analysis

The imaging results of each method for the adhesive debonding defect in sample 1 with a diameter of 10.0 mm are shown in **Figure 6**, and the imaging results of each method for the adhesive debonding defect with a diameter of 6.0 mm are shown in **Figure 7**. Firstly, according to the observation of the original detection images of two different sizes of the adhesive debonding defects, no matter the diameter of 6.0 mm or 10.0 mm, the adhesive debonding defects could not be effectively identified, only part of the defects could be vaguely observed, and the defect edges are blurred, the imaging contrast is not obvious, and the resolution of small targets is poor. Theoretically, the color distribution of the background region of the detection image should be relatively uniform, while there are differences in the color distribution of the background region in the actual detection image, with obvious noise distribution, which affects the quality of the detection image. The main reason for this phenomenon is that the energy loss of terahertz wave propagating in the measured sample is serious, and the effective reflection signal received by the detector is weak, which leads to the effective signal being submerged by noise, thus reducing the signal-noise ratio of the detected signal and reducing the imaging effect. Then observe the results of Gaussian filtering processing, although the use of this method can suppress the background noise of the detection image to some extent and enhance the contrast of the image, but the denoising is not complete, the background region still exists obvious noise distribution, unable to accurately identify the prefabricated adhesive debonding defects. Furthermore, the problem of signal distortion appears after filtering with this method, so that the effective defect information has been damaged. Finally, the results of the method proposed in this paper show that the recognition effect of the prefabricated defect region is significantly better than that of other methods. The prefabricated adhesive debonding defects are all effectively identified, and the details such as the edge of the defect are enhanced, and the contrast with the background region is improved. In addition, the noise in the background region of

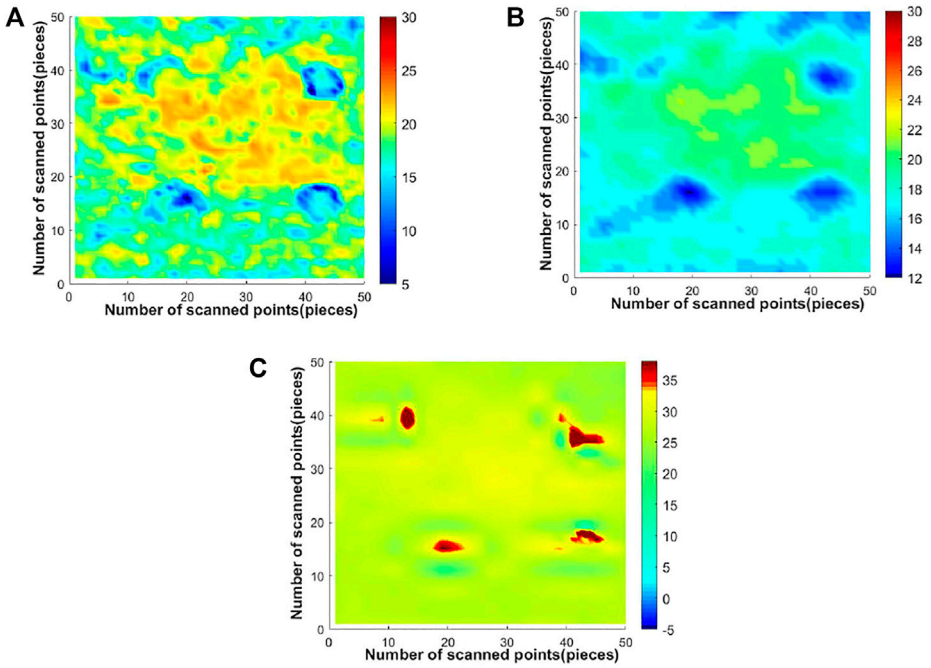

FIGURE 6 | Image of processing results of each method for adhesive debonding with a diameter of 10.0 mm in sample 1. **(A)** image of original detection, **(B)** Gaussian filtering, **(C)** method in this paper.

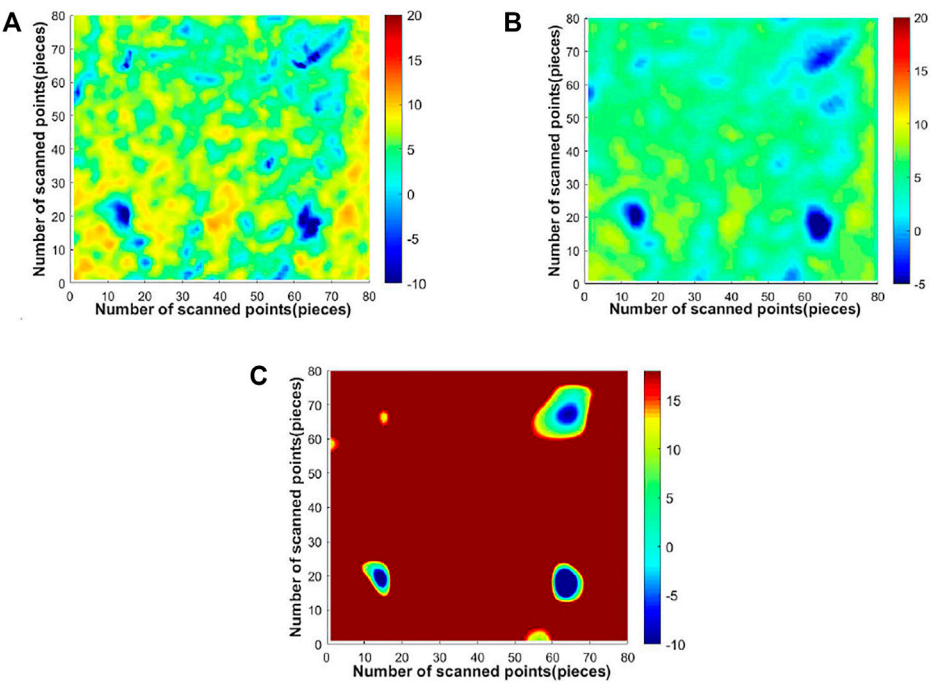

FIGURE 7 | Image of processing results of each method for adhesive debonding with a diameter of 6.0 mm in sample 1. **(A)** image of original detection, **(B)** Gaussian filtering, **(C)** method in this paper.

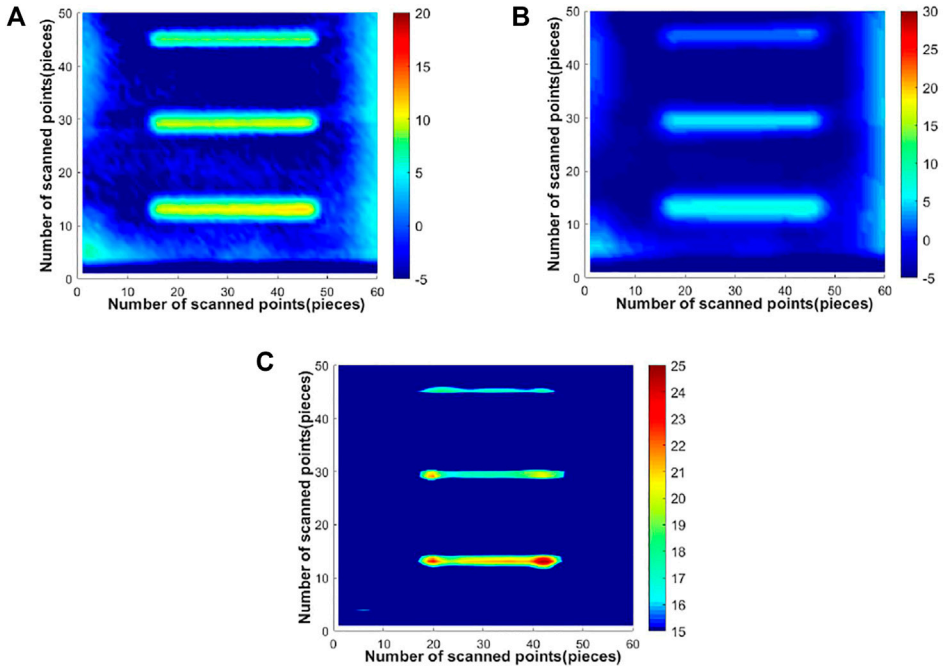

FIGURE 8 | Image of processing results of each method for delamination defects in sample 2. **(A)** image of original detection, **(B)** Gaussian filtering, **(C)** method in this paper.

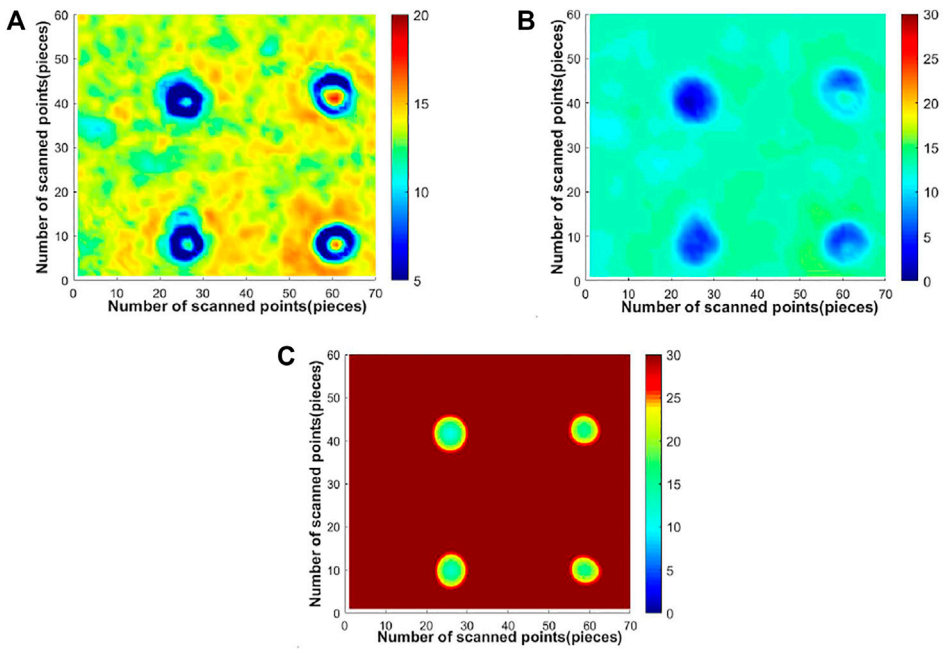

FIGURE 9 | Image of processing results of each method for adhesive debonding with a diameter of 10.0 mm in sample 3. **(A)** image of original detection, **(B)** Gaussian filtering, **(C)** method in this paper.

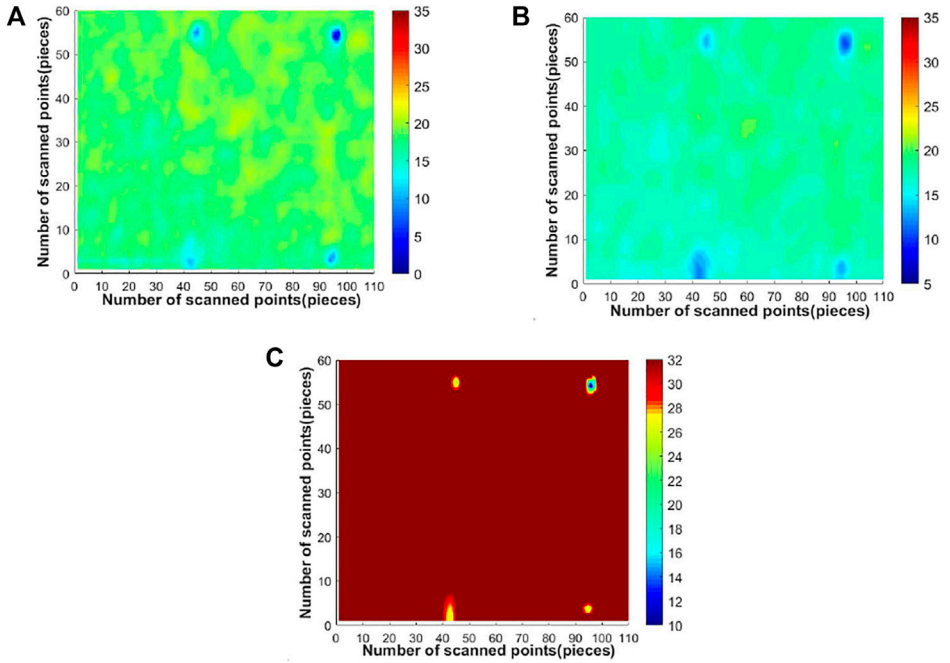

FIGURE 10 | Image of processing results of each method for adhesive debonding with a diameter of 3.0 mm in sample 3. **(A)** image of original detection, **(B)** Gaussian filtering, **(C)** method in this paper.

TABLE 1 | Contrast results of image objective indexes between original image and images with different methods (Bold numbers indicate the optimal value for each set of data).

Detection image	Index	Original image	Gaussian filtering	Method in this paper
Adhesive debonding defect with diameter 10.0 mm (Sample 1)	SD	3.0047	2.7121	**3.6210**
	MG	0.0459	0.0198	**0.0557**
	IE	6.6520	3.1218	**6.7522**
	EG	2.8653e+04	5.3570e+03	**4.2509e+04**
	LC	35.6725	35.0706	**54.6020**
Adhesive debonding defect with diameter 6.0 mm (Sample 1)	SD	2.9775	2.2973	**13.9005**
	MG	0.0264	0.0135	**0.0481**
	IE	6.7008	3.1171	**8.9169**
	EG	2.8306e+04	7.4000e+03	**9.4433e+04**
	LC	9.6327	10.1058	**76.1488**
Delamination defect with depth of 2.0 mm (Sample 2)	SD	6.6101	4.9137	**13.3256**
	MG	0.0618	0.0306	**0.1055**
	IE	7.7592	4.1788	**8.6975**
	EG	6.5960e+04	1.6507e+04	**1.9495e+05**
	LC	2.4933	1.9407	**2.7272**
Adhesive debonding defect with diameter 10.0 mm (Sample 3)	SD	2.4363	2.0684	**8.7838**
	MG	0.0275	0.0130	**0.0308**
	IE	5.6032	2.2544	**7.3732**
	EG	2.5453e+04	5.6940e+03	**3.1882e+04**
	LC	24.6274	23.8015	**98.5350**
Adhesive debonding defect with diameter 3.0 mm (Sample 3)	SD	1.3442	1.6127	**2.6318**
	MG	0.0067	0.0080	**0.0094**
	IE	5.3768	2.0963	**6.2558**
	EG	6.3414e+03	9.2660e+03	**1.2713e+04**
	LC	35.3572	34.4890	**79.1244**

the image is significantly suppressed. Different from the Gaussian filtering method, the effective defect information is retained while filtering out the background noise of the image.

Sample2: Imaging Results Analysis

The imaging results of each method of the delamination defects with depth of 2.0 mm in sample two are shown in **Figure 8**. Firstly,

the original detection image of delamination defects is observed. It can be seen that the prefabricated delamination defects can be identified by the original detection image, but the edge of the defect is blurred, the detail resolution needs to be improved, and the background region also has obvious noise distribution, which affects the quality of the detection image. After observing the results of Gaussian filtering processing, it can be seen that this method has a certain denoising effect, but the denoising effect is not obvious, there is still some residual noise, and the defect edge is still blurred, and the overall sharpness of the detection image is poor. Finally, by observing the results processed by the method in this paper, it can be seen that the overall sharpness of the detection image greatly improved, and the details such as the edge of the prefabricated delamination defects have been significantly enhanced. Moreover, the background noise of the detection image has been effectively suppressed, and the contrast between the defect and the background region has been improved, which is helpful for the accurate identification of internal defects.

Sample3: Imaging Results Analysis

The imaging results of each method for the adhesive debonding defect in sample 3 with a diameter of 10.0 mm are shown in **Figure 9**, and the imaging results of each method for the adhesive debonding defect with a diameter of 3.0 mm are shown in **Figure 10**. Firstly, the original detection images of different sizes of adhesive debonding defect in sample 3 are observed. It is found that the prefabricated adhesive debonding defect with diameters of 10.0 and 3.0 mm could be vaguely identified in the original detection image, but the edge of the defect is blurred and the contrast with the background area is low. In addition, the background region of the image also has obvious noise distribution, which needs further denoising and enhancement to improve the contrast of the detection image and enhance the edge of the defect and other details. By observing the detection image after Gaussian filtering, it can be seen that the prefabricated adhesive debonding defect recognition effect has been improved to some extent, the noise in the background region has been well filtered, and the contrast between the defect and the background region has also been improved to some extent. However, the detection image becomes blurred after Gaussian filtering, and the detail resolution of the small target also needs to be further improved. Finally, through the observation of the results processed by the method in this paper, it can be seen that the detection images of two kinds of adhesive debonding defect have been greatly improved in the overall sharpness, contrast and defect edge details. The prefabricated two kinds of adhesive debonding defect can be well recognized, and the background noise of the detection image has been effectively suppressed. While filtering out the background noise, the defect information is effectively retained. Compared with the original detection image and the image after Gaussian filtering, the image quality is better.

OBJECTIVE EVALUATION OF RESULTING IMAGES

In order to accurately evaluate the image processed by each method, this paper also uses five objective evaluation indexes, namely standard deviation (SD), mean gradient (MG), information entropy (IE), energy gradient (EG) and local contrast (LC), to objectively evaluate the image processing results [25–27].

Standard Deviation

Standard deviation refers to the degree of dispersion of image pixel gray value relative to the mean value. If the standard deviation is larger, it indicates that the gray scale in the image is more dispersed and the image quality is better. Its calculation formula is

$$SD = \sqrt{\frac{1}{GR}\sum_{i=1}^{G}\sum_{j=1}^{R}\left(F(i,j)-u\right)^2} \tag{24}$$

where G and R represent the sizes of the image, $F(i, j)$ represents the gray value of pixel $F(i, j)$ corresponding to image F, and u represents the average gray value of all pixels in the image.

Mean Gradient

The mean gradient represents the ability of image to express details, which is a measure of image sharpness. Usually, the greater the mean gradient is, the more the details of the image are, and the higher the sharpness is. The calculation formula of the mean gradient is as follows

$$MG = \frac{1}{GR}\sum_{i=1}^{G}\sum_{j=1}^{R}\sqrt{\left[\frac{\partial f(x,y)}{\partial x}\right]^2+\left[\frac{\partial f(x,y)}{\partial y}\right]^2} \tag{25}$$

where $\frac{\partial f(x,y)}{\partial x}$ represents the gradient in the horizontal direction, and $\frac{\partial f(x,y)}{\partial y}$ represents the gradient in the vertical direction.

Information Entropy

Information entropy is an effective method to evaluate information content in images. For an image with gray scale in the range of [0,L-1], the expression of information entropy is

$$IE = -\sum_{i=0}^{L-1} p(s_i)\log_2 p(s_i) \tag{26}$$

Where $p(s_i)$ is the probability of gray level s_i, the greater the information entropy indicates that the image contains more details.

Energy Gradient

Image sharpness is an important index to measure the quality of the image, which can better correspond to the subjective feelings of people. The energy gradient can evaluate the image sharpness in real time, and the greater the energy gradient value of the image, the better the image sharpness. The definition of the function is as follows

$$EG = \sum_{x=1}^{G}\sum_{y=1}^{R}\left(\left|f(x+1,y)-f(x,y)\right|^2 + \left|f(x,y+1)-f(x,y)\right|^2\right) \tag{27}$$

Where $f(x, y)$ represents the gray value of image f at the corresponding pixel (x, y).

Local Contrast

The local contrast of the image can reflect the dynamic range of the gray distribution of the image pixels. The larger the dynamic range is, the higher the contrast is. The formula for calculating the local contrast is

$$LC = \frac{1}{GR}\sum_{x=1}^{G}\sum_{y=1}^{R}\frac{I_{x,y}^{\max} - I_{x,y}^{\min}}{I_{x,y}^{\max} + I_{x,y}^{\min} + C} \tag{28}$$

Where $I_{x,y}^{\max}$ and $I_{x,y}^{\min}$ represent the maximum and minimum pixel gray values in a sub-block centered on pixel (x, y), respectively. In this paper, the size of the sub-block is 5×5. In order to avoid the case of denominator 0, C is a smaller constant with a value of 0.1.

The calculation results of objective evaluation indexes of different methods are shown in **Table 1**. It can be seen from the table that the standard deviation, mean gradient, information entropy, energy gradient and local contrast of the five objective evaluation index data are higher than the corresponding values of the original detection image and the detection image after Gaussian filtering. It shows that the method in this paper has obvious advantages in contrast enhancement and level of detail and sharpness improvement.

CONCLUSION

Aiming at the degradation phenomena of terahertz detection images, such as low contrast, poor resolution of small targets and blurred details, this paper proposes a novel method for the enhancement of composite materials' terahertz image using unsharp masking and guided filtering technology. Through the imaging detection of a variety of composite materials, denoise and enhance the imaging by using this novel method, the experimental results and evaluation results show that the proposed method can effectively filter out the noise in the detection signal, improve the image contrast and resolution, and enhance the details of the detection image, which is conducive to the wider application of terahertz technology in the field of nondestructive testing of composite materials. In the future research, the existing methods are further improved to find a new method to achieve the size of the identified defect close to the actual size on the basis of improving the contrast and detail resolution of the terahertz detection image.

DATA AVAILABILITY STATEMENT

The raw data supporting the conclusion of this article will be made available by the authors, without undue reservation.

AUTHOR CONTRIBUTIONS

ZL: Methodology, Experiment, Validation, Investigation, Writing-Original Draft; JZ: Supervision, Investigation; YMZ: Supervision, Methodology, Writing-Reviewing and Editing; ZH: Experiment; ZX: Experiment; YZZ: Experiment; CY: Sample preparation; WH: Experiment, Supervision; CZ: Supervision, Funding acquisition.

FUNDING

This research was supported by the Beijing Advanced Innovation Center for Imaging Theory and Technology Scientific Research Funds (008/19530012003), the Capital Normal University Development Funds by Category–Physics Department–Practice base Projects for Degree Study Program (008-2155089).

REFERENCES

1. Siegel PH. Terahertz Technology. *IEEE Trans Microwave Theor Techn.* (2002) 50(3):910–28. doi:10.1109/22.989974
2. Kawase K, Shibuya T, Hayashi Si., and Suizu K. THz Imaging Techniques for Nondestructive Inspections. *Comptes Rendus Physique* (2010) 11(7-8):510–8. doi:10.1016/j.crhy.2010.04.003
3. Ferguson B, and Abbott D. De-noising Techniques for Terahertz Responses of Biological Samples. *Microelectron J* (2001) 32(12):943–53. doi:10.1016/S0026-2692(01)00093-3
4. Kowalski M, Kastek M, Walczakowski M, Palka N, and Szustakowski M. Passive Imaging of Concealed Objects in Terahertz and Long-Wavelength Infrared. *Appl Opt* (2015) 54(13):3826–33. doi:10.1364/AO.54.003826
5. Hua Zhong H, Yongwei Li YW, and Jiao LC. SAR Image Despeckling Using Bayesian Nonlocal Means Filter with Sigma Preselection. *IEEE Geosci Remote Sens Lett* (2011) 8(4):809–13. doi:10.1109/LGRS.2011.2112331
6. Buades A, Coll B, and Morel JM. A Review of Image Denoising Algorithms, with a New One. *Multiscale Model Simul* (2005) 4(2):490–530. doi:10.1137/040616024
7. Buades A, Coll B, and Morel J-M. A Non-local Algorithm for Image Denoising. In: IEEE Computer Society Conference on Computer Vision and Pattern Recognition (CVPR'05); 2005 Jun 20–25; San Diego, CA, USA. IEEE (2005). doi:10.1109/CVPR.2005.38
8. Shi YX, and Li JS. Based on Double Threshold Canny Equalization Algorithm for Terahertz Image Enhancement. *Spectrosc Spect Anal* (2018) 38(6):1680–3. doi:10.3964/j.issn.1000-0593(2018)06-1680-04
9. He K, Sun J, and Tang X. Guided Image Filtering. *IEEE Trans Pattern Anal Mach Intell* (2013) 35(6):1397–409. doi:10.1109/TPAMI.2012.213
10. Liu N, and Zhao D. Detail Enhancement for High-Dynamic-Range Infrared Images Based on Guided Image Filter. *Infrared Phys Technol* (2014) 67:138–47. doi:10.1016/j.infrared.2014.07.013
11. Zhou B, Luo Y, Yang M, Chen B, Wang M, Peng L, et al. An Improved Adaptive Detail Enhancement Algorithm for Infrared Images Based on Guided Image Filter. *J Mod Opt* (2019) 66(1):33–46. doi:10.1080/09500340.2018.1511861
12. Li Y, Hu W, Zhang X, Zhao Y, Ni J, and Ligthart LP. A Non-linear Correction Method for Terahertz LFMCW Radar. *IEEE Access* (2020) 8:102784–94. doi:10.1109/ACCESS.2020.2998602
13. Dong J, Kim B, Locquet A, McKeon P, Declercq N, and Citrin DS. Nondestructive Evaluation of Forced Delamination in Glass Fiber-Reinforced Composites by Terahertz and Ultrasonic Waves. *Composites B: Eng* (2015) 79:667–75. doi:10.1016/j.compositesb.2015.05.028

14. Maraun D, and Kurths J. Cross Wavelet Analysis: Significance Testing and Pitfalls. *Nonlin Process. Geophys* (2004) 11(4):505–14. doi:10.5194/npg-11-505-2004
15. Mallat S, and Hwang WL. Singularity Detection and Processing with Wavelets. *IEEE Trans Inform Theor* (1992) 38(2):617–43. doi:10.1109/18.119727
16. Sappa A, Carvajal J, Aguilera C, Oliveira M, Romero D, and Vintimilla B. Wavelet-Based Visible and Infrared Image Fusion: A Comparative Study. *Sensors* (2016) 16(6):861. doi:10.3390/s16060861
17. Mallat SG. A Theory for Multiresolution Signal Decomposition: the Wavelet Representation. *IEEE Trans Pattern Anal Machine Intell* (1989) 11(7):674–93. doi:10.1109/34.192463
18. González-Audícana M, Otazu X, Fors O, and Seco A. Comparison between Mallat's and the 'à trous' discrete wavelet transform based algorithms for the fusion of multispectral and panchromatic images. *Int J Remote Sens* (2005) 26(3):595–614. doi:10.1080/01431160512331314056
19. Ramponi G. A Cubic Unsharp Masking Technique for Contrast Enhancement. *Signal Process.* (1998) 67(2):211–22. doi:10.1016/S0165-1684(98)00038-3
20. Polesel A, Ramponi G, and Mathews VJ. Image Enhancement via Adaptive Unsharp Masking. *IEEE Trans Image Process* (2000) 9(3): 505–10. doi:10.1109/83.826787
21. Xing L, Cui H-L, Shi C, Zhang Z, Zhang J, Chang T, et al. Nondestructive Examination of Polymethacrylimide Composite Structures with Terahertz Time-Domain Spectroscopy. *Polym Test* (2017) 57:141–8. doi:10.1016/j.polymertesting.2016.11.022
22. Frydrych I, Xu F, Duan Mu QD, Li LJ, Yang D, and Xia B. Nondestructive Evaluation of Rubber Composites Using Terahertz Time Domain Spectroscopy. *Fibres Text East Europe* (2018) 26(1):67–72. doi:10.5604/01.3001.0010.7799
23. Ospald F, Zouaghi W, Beigang R, Matheis C, Jonuscheit J, Recur B, et al. Aeronautics Composite Material Inspection with a Terahertz Time-Domain Spectroscopy System. *Opt Eng* (2013) 53(3):031208. doi:10.1117/1.OE.53.3.031208
24. Walker J, and Richter J. Nondestructive Evaluation of Foam Insulation for the External Tank Return to Flight. In: 42nd AIAA/ASME/SAE/ASEE Joint Propulsion Conference & Exhibit, Sacramento, California (2006). doi:10.2514/6.2006-4601
25. Liu J, Zhou C, Chen P, and Kang C. An Efficient Contrast Enhancement Method for Remote Sensing Images. *IEEE Geosci Remote Sens Lett* (2017) 14(10):1715–9. doi:10.1109/LGRS.2017.2730247
26. Wang Y, and Pan Z. Image Contrast Enhancement Using Adjacent-Blocks-Based Modification for Local Histogram Equalization. *Infrared Phys Technol* (2017) 86:59–65. doi:10.1016/j.infrared.2017.08.005
27. Subbarao M, Choi T, and Nikzad A. Focusing Techniques. *Opt Eng* (1993) 32(11):2824–36. doi:10.1117/12.147706

Conflict of Interest: Author CY is employed by Shenzhen Kuang-Chi Advanced Technology Co., Ltd.

The remaining authors declare that the research was conducted in the absence of any commercial or financial relationships that could be construed as a potential conflict of interest.

Publisher's Note: All claims expressed in this article are solely those of the authors and do not necessarily represent those of their affiliated organizations, or those of the publisher, the editors and the reviewers. Any product that may be evaluated in this article, or claim that may be made by its manufacturer, is not guaranteed or endorsed by the publisher.

frontiers in Physics

ORIGINAL RESEARCH
published: 03 November 2021
doi: 10.3389/fphy.2021.768192

High-Sensitivity RF Choke-Enhanced Dipole Antenna-Coupled Nb_5N_6 THz Detector

Chengtao Jiang[1], *Xuecou Tu*[1,2]*, *Chao Wan*[2], *Lin Kang*[1,2]*, *Xiaoqing Jia*[1,2], *Jian Chen*[1,2] and *Peiheng Wu*[1,2]

[1]Research Institute of Superconductor Electronics (RISE), School of Electronic Science and Engineering, Nanjing University, Nanjing, China, [2]Purple Mountain Laboratories, Nanjing, China

In this study, we demonstrate an Nb_5N_6 terahertz (THz) detector with radio frequency (RF) choke-enhanced dipole antenna structure for 0.3 THz detection. The maximum electric field intensity of 218 V/m is obtained by optimizing the parameters of the dipole antenna with RF choke. Compared to a dipole antenna without RF choke, the electric field intensity of that with RF choke is improved by 2.6 times. The RF choke-enhanced dipole antenna-coupled Nb_5N_6 THz detector is fabricated and characterized. The measured maximum responsivity of the detector is 1100 V/W at 0.308 THz, and the corresponding noise equivalent power (NEP) is 6.4×10^{-12} W/Hz$^{1/2}$. The measured response time of the Nb_5N_6 THz detector is as low as 8.46 μs. Furthermore, the Nb_5N_6 THz detector is applied to a homemade THz transmission imaging system for demonstrating its performance. The THz imaging results of a blade and access card show that the contrast of the blade image is sharp and the components hidden within the access card are clearly visible. This indicates that the Nb_5N_6 THz detector can be used in THz imaging, particularly in THz active imaging, which will have greater application prospects.

Keywords: Nb_5N_6 microbolometer, THz detector, RF choke, antenna, THz imaging

Edited by:
Meng Chen,
Tsinghua University, China

Reviewed by:
Mingyu Zhang,
Harbin Institute of Technology, Shenzhen, China
Jianming Wen,
Kennesaw State University, United States

***Correspondence:**
Xuecou Tu
tuxuecou@nju.edu.cn
Lin Kang
kanglin@nju.edu.cn

Specialty section:
This article was submitted to Optics and Photonics, a section of the journal Frontiers in Physics

Received: *31 August 2021*
Accepted: *27 September 2021*
Published: *03 November 2021*

Citation:
Jiang C, Tu X, Wan C, Kang L, Jia X, Chen J and Wu P (2021) High-Sensitivity RF Choke-Enhanced Dipole Antenna-Coupled Nb_5N_6 THz Detector. Front. Phys. 9:768192. doi: 10.3389/fphy.2021.768192

INTRODUCTION

In recent years, with the development of science and technology, the terahertz (THz) waves have attracted worldwide interest. THz technology is applicable in many fields such as physics, life science, materials science, astronomy, information technology, and national defense security. THz detectors are crucial components in terahertz technology, which have extensive application prospects in spectrum analysis, medical imaging, radio astronomy, security checks, biosensing, etc. [1–6]. At present, the research on uncooled THz detectors involve Golay cells [7], Schottky diodes [8], field-effect transistors (FETs) [9], and bolometers [10–12]. Among them, bolometers have been attracting more and more attention because of easy fabrication, integration with readout circuits, high sensitivity, low-noise equivalent power (NEP), wide response spectrum, and so on. To date, several materials have been used as the bolometers, such as VO_x [13–16], YBCO [17–19], titanium (Ti) [20], niobium (Nb) [10, 21], platinum (Pt) [22], poly-Si [23], poly-Si-Ge alloys [24], etc. Although polycrystalline VO_x exhibits a temperature coefficient of resistance [TCR = (1/R) *(dR/dT)] ~ −2%/K] at room temperature, it undergoes a semiconductor-metal transition at ~ 67°C, which reduces the dynamic range of the bolometer when working in the semiconductor phase [25]. Amorphous YBCO has been demonstrated as an uncooled bolometer, but its stoichiometric composition is difficult to control, and the resistance and TCR are affected by the oxygen

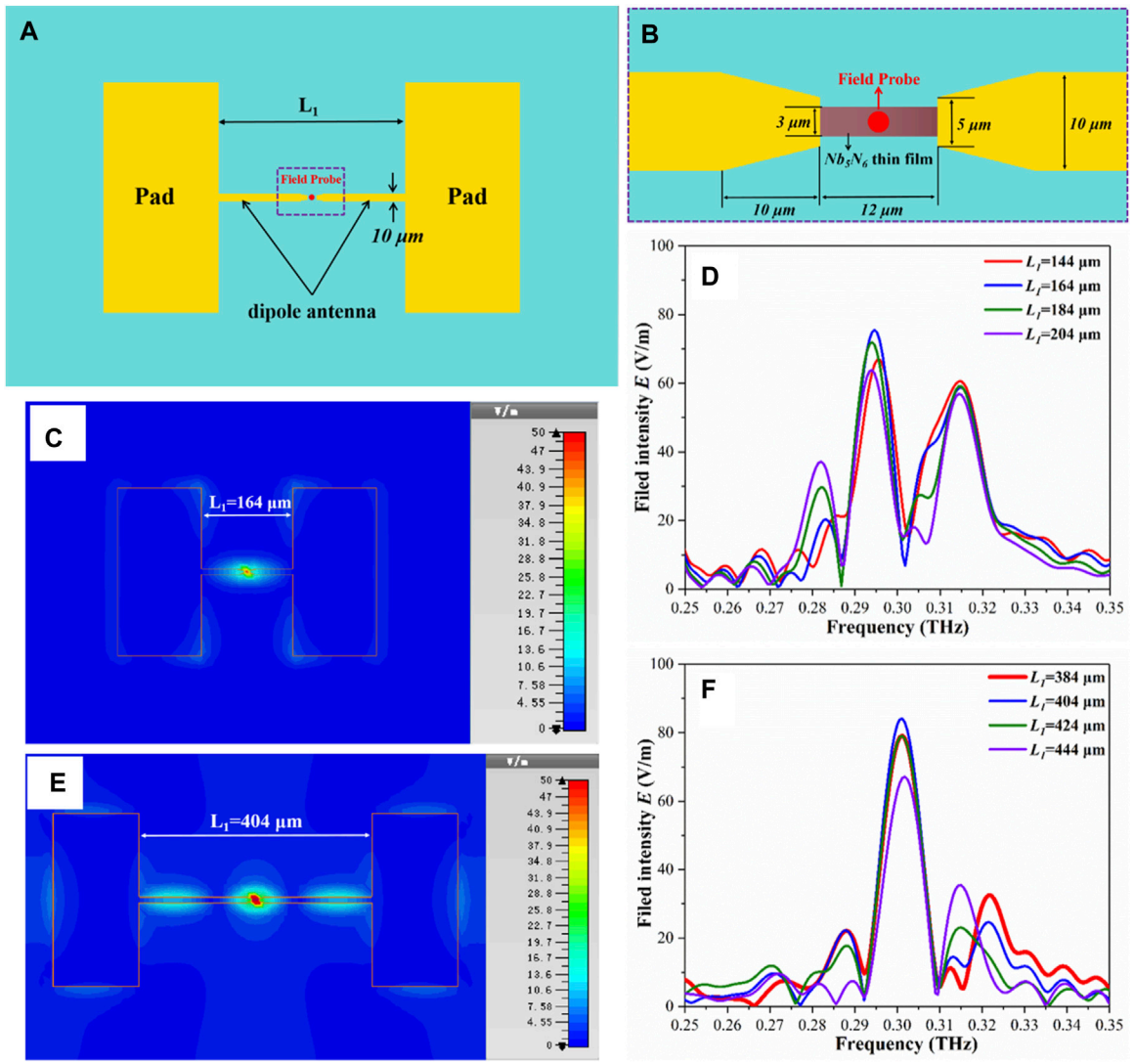

FIGURE 1 | (A) Schematic diagram of the planar dipole antenna on the Si substrate. **(B)** The location and size of the Nb_5N_6 film in the planar dipole antenna. **(C)** The electric field intensity distribution of the half-wave dipole antenna with L_1 = 164 μm at 0.295 THz. **(D)** The electric field intensity varies with L_1 in the half-wave dipole antenna in the range of 0.25–0.35 THz. **(E)** The electric field intensity distribution of the full-wave dipole antenna with L_1 = 404 μm at 0.301 THz. **(F)** The electric field intensity varies with L_1 in the full-wave dipole antenna in the range of 0.25–0.35 THz.

concentration in films [26]. The low TCR value of metallic materials (two orders of the magnitude lower than that of semiconductors) results in low responsivity of detectors. In polycrystalline Si and Si-Ge alloys, the resistivity can be maintained sufficiently low by controlling the doping level, although it limits the TCR to approximately 2.5–3%/K. However, the processing of polycrystalline materials requires temperatures as high as 650°C for achieving the desired crystallinity [23, 24]. Therefore, it is desirable to combine the advantages of both semiconductors (high TCR for high responsivity) and metals (low resistivity) for the development of fast and sensitive THz detectors.

The Nb_5N_6 films made in our laboratory exhibit a high TCR of 0.7%/K, which is higher than that of metals [27–29]. In addition, the resistivity of Nb_5N_6 ($<5 \times 10^{-3}\ \Omega$ cm) is considerably lower than that of the other semiconductors, resulting in reduction of the impedance in comparison with a-Si or VO_x devices of the same dimensions, which is advantageous to impedance matching when integrated with planar antennas. Moreover, the Nb_5N_6 films include other advantages, such as simple fabrication, low cost, large area production, and easy control. Hence, Nb_5N_6 thin films are promising candidate material for THz bolometer detector at room temperature.

Generally, a THz bolometer detector consists of a THz antenna and a thin film microbridge. As the key component of the detector, the antenna plays an important role in coupling THz radiations to the film microbridge; hence, the performance of the detector can be improved by appropriately designing and

optimizing the antenna structure. Radio frequency (RF) choke structures are often used in the antenna design for improving the antenna performance, such as bandwidth enhancement, multiple band operation, gain enhancement, and radiation pattern shaping [30–33]. Their functions are usually to provide direct current (DC) bias and prevent RF signals from leaking to the bias electrodes. Considering the feature of the RF choke, we designed an RF choke-enhanced dipole antenna to improve the performance of the Nb_5N_6 THz detector. Compared to that without RF choke, the electric field intensity of the RF choke-enhanced dipole antenna can be significantly improved. In addition, we applied the Nb_5N_6 THz detector to a THz transmission imaging system and studied the THz imaging of a blade and access card.

Design and Fabrication

We choose 0.3 THz as the center frequency of the dipole antenna for design and optimization, because it is located in the atmospheric transmission window of THz signals, and its loss is small in the atmosphere. To maximize the response of dipole antenna under the 0.3 THz radiation, the antenna length must match the effective wavelength of the surrounding media. The length l of the resonant antenna [34] is given by $l = \lambda/\sqrt{\varepsilon_{eff}}$, where λ is the free-space wavelength and ε_{eff} is the effective dielectric constant; within the effective media approximation, ε_{eff} is the average of the dielectric constants of Si and air, which are 1 and 11.9, respectively. The calculated effective wavelength of the dipole antenna on high resistivity Si is 394 μm for 0.3 THz detection. The geometry of the dipole antenna is depicted in **Figure 1A**. The antenna was placed on a thermally oxidized Si substrate with a period of 800 μm × 800 μm, located in the center of the coordinate system. The thickness of the Si substrate, the SiO_2 on the Si surface, and Au layer were 500, 200, and 200 nm, respectively. A 200 nm thick Au layer was provided on the back of the Si substrate as a Fabry–Perot (F-P) cavity to further enhance the coupling efficiency of the antenna to THz signals. In the simulation model, the X and Y directions were both set as periodic boundary conditions, whereas the ±Z directions were both set as open (add space) boundary conditions. The plane wave excitation was setup to simulate the normal incidence of a uniform plane wave on the antenna and its incidence direction was defined as along the Z-axis. As the wave polarized along the X-axis was of our interest, we defined the plane wave excitation amplitude of 1 V/m on the X-axis, while zero on the Y-axis and Z-axis. An electric field monitor probe was placed in the center of the antenna to detect the changes in electric field intensity of the antenna structure (red point in **Figure 1A**). Therefore, the electric field enhancement performance of the antenna could be obtained by comparing the probe field strength with the plane wave excitation amplitude. The length and width of the dipole antenna were L_1 and 10 μm. To integrate the dipole antenna with the Nb_5N_6 microbolometer THz detector, the Nb_5N_6 film was located in the center place of the antenna indicated by the brown area in **Figure 1B**. The size of the Nb_5N_6 film microbridge was 3 μm × 12 μm, and the length of the transition area between the film microbridge and dipole antenna was 10 μm. The size of the electrodes (pads) used for providing bias current to the THz detector was set to 150 μm × 300 μm. According to microwave antenna theory, the electric field intensity changes with frequency are simulated when the length of the dipole antenna is approximated half wavelength, as shown in **Figure 1D**. In the 0.25–0.35 THz frequency range, the electric field intensity initially increases and then decreases with the increase of L_1. The electric field intensity attains maximum value of 75 V/m at 0.2945 THz when L_1 is 164 μm. **Figure 1C** shows the electric field intensity distribution of the half-wave dipole antenna near the surface of Si substrate at 0.2945 THz when L_1 = 164 μm. The electric field is mainly distributed in the gap area of the half-wave antenna where the Nb_5N_6 film is located. This shows that the Nb_5N_6 film can receive maximum THz energy from the antenna coupling. Additionally, we also simulate the changes in the electric field intensity of the full-wave antenna in the frequency range of 0.25–0.35 THz, as shown in **Figure 1F**. It can be observed that as L_1 increases, the electric field intensity shows a trend of first increasing and then decreasing. When L_1 = 404 μm, the best electric field intensity of the full-wave antenna is 85 V/m at 0.301 THz. The electric field intensity of the full-wave antenna is 10 V/m greater than that of the half-wave antenna. The electric field intensity distribution of the full-wave antenna near surface of Si substrate at 0.301 THz is shown in **Figure 1E**. Compared to the half-wave antenna, the full-wave antenna has a higher local field enhancement. It indicates that the full-wave antenna has higher coupling efficiency to THz radiation signals. However, there is also strong electric field distribution on the dipole antenna and pads.

To further enhance the electric field intensity at the center of the dipole antenna, an RF choke structure was employed to prevent the coupled THz waves from leaking to the bias pads, as depicted in **Figure 2A**. By optimizing the location and the size of the RF choke, a maximum electric field intensity of 218 V/m at the center of the dipole antenna with RF choke is obtained at 0.301 THz, as shown in **Figure 2B**. The optimized parameters of the dipole antenna with RF choke are as follows: L_2 = 66 μm, W_1 = 30 μm, and W_2 = 230 μm. Compared to the dipole antenna without RF choke, the maximum electric field intensity is improved by 2.6 times. The electric field intensity distribution of the antenna with RF choke near the surface of the Si substrate at 0.301 THz is displayed in **Figure 2C**. The antenna gap region has greater local field enhancement due to the suppression effect of RF choke structure. There is almost no electric field distribution on the bias pads, and the electric field is mainly concentrated between RF choke structures, which makes the electric field intensity at the center of the dipole antenna greater. When the RF choke-enhanced dipole antenna is integrated with the Nb_5N_6 microbolometer THz detector, the Nb_5N_6 film can absorb more THz energy, thus improving the sensitivity of the device. **Figure 2D** shows the far-field radiation patterns of the dipole antenna with RF choke in the E plane (Phi = 0°) and H plane (Phi = 0°) at 0.301 THz, with a maximum directivity of 8.34 dBi. This indicates that the dipole antenna with RF choke has a good property of receiving the normal incidence THz waves according to the reciprocity principle.

The fabrication of the RF choke-enhanced dipole antenna-coupled Nb_5N_6 microbolometer THz detector was implemented

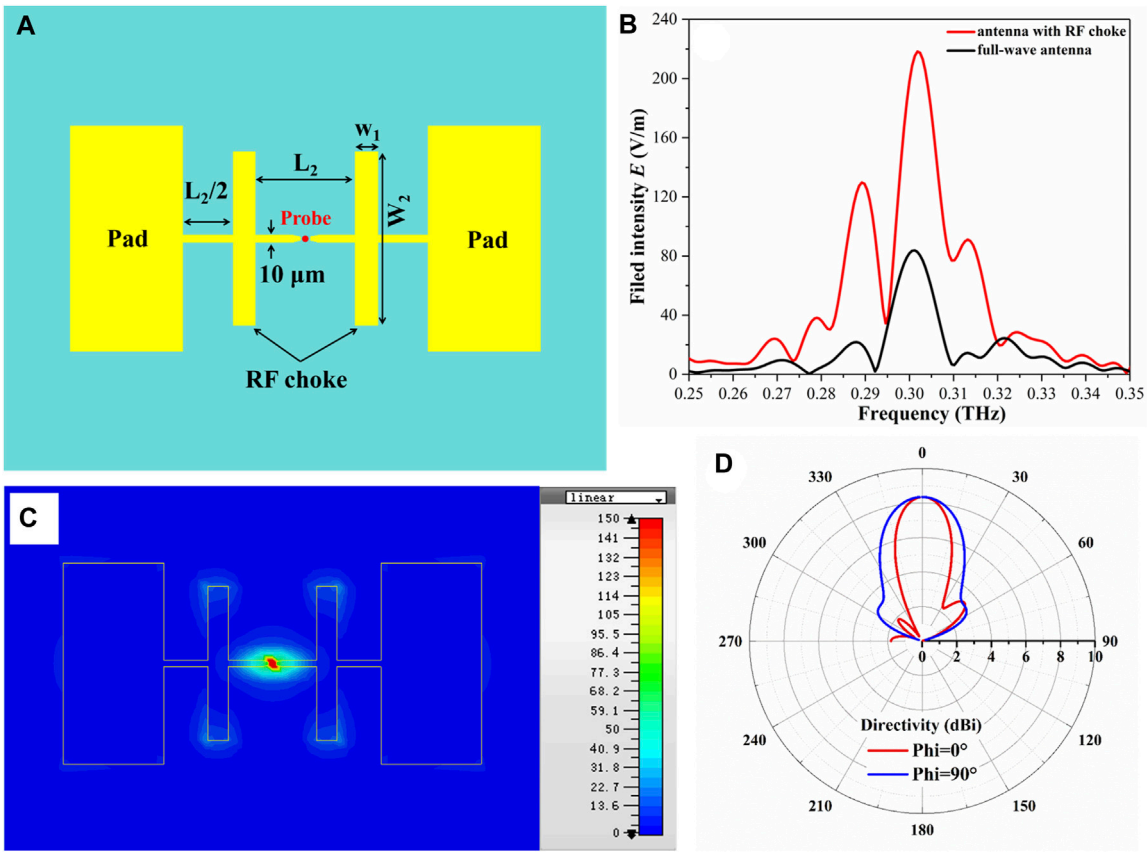

FIGURE 2 | (A) Schematic diagram of the dipole antenna with RF choke on the Si substrate. **(B)** The curve of the electric field intensity varies with the frequency of the dipole antenna with or without RF choke. **(C)** The electric field intensity distribution of the dipole antenna with RF choke near the surface of the Si substrate at 0.301 THz. **(D)** The radiation patterns of the planar dipole antenna with RF choke at 0.301 THz.

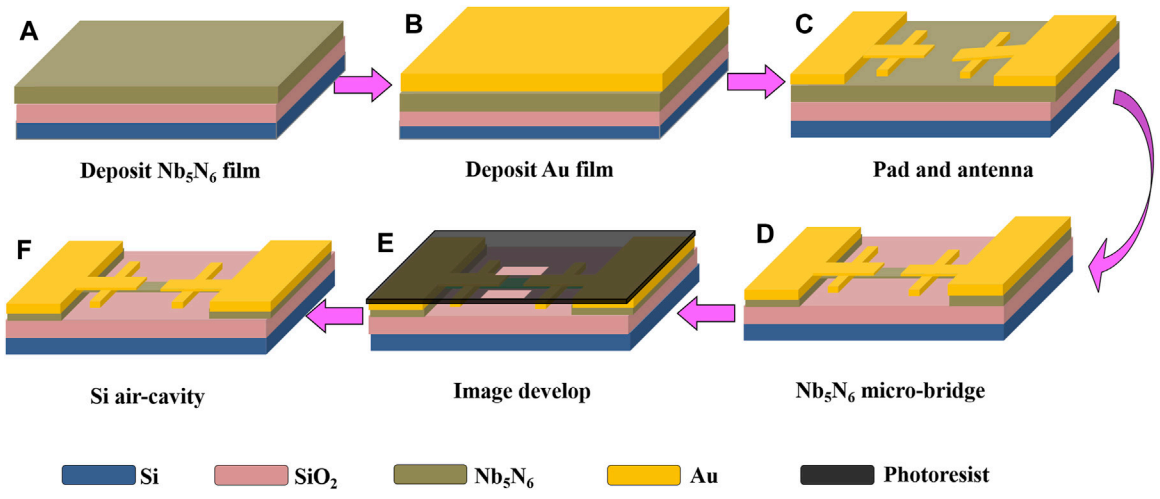

FIGURE 3 | The fabrication process of the Nb_5N_6 THz detector integrated with RF choke-enhanced dipole antenna.

using micromachining technique. The process flow is illustrated in **Figure 3**. The Nb_5N_6 film with a thickness of 120 nm was first deposited on the thermally oxidized Si substrate by using RF magnetron sputtering, as shown in **Figure 3A**. The TCR of the Nb_5N_6 thin film is −0.7% K^{-1} at 300 K. After the required pattern was formed through micro-processing technology, 5 nm thick Ti

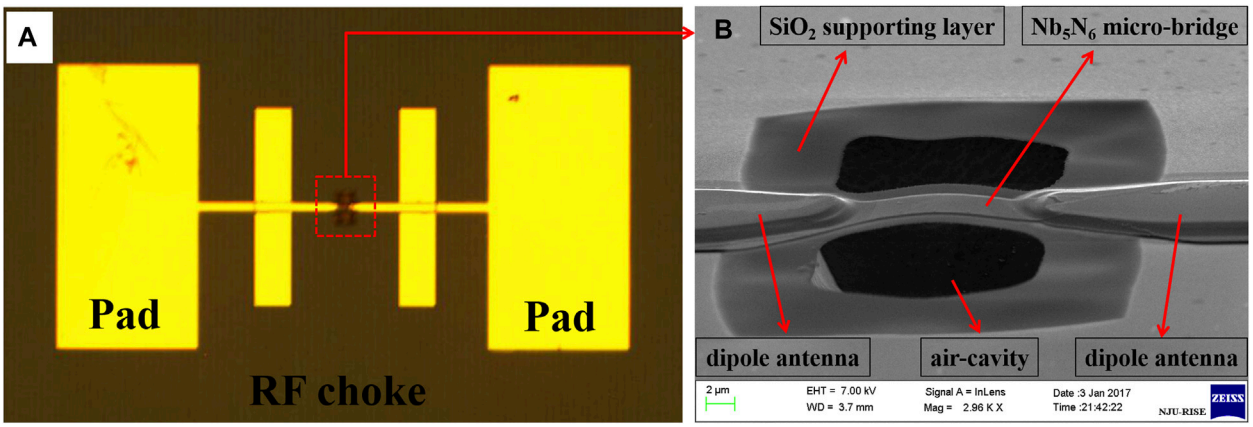

FIGURE 4 | (A) Image of the fabricated antenna-coupled Nb_5N_6 THz detector. **(B)** SEM micrograph of the Nb_5N_6 air-bridge.

membrane and a 200 nm thick Au membrane were deposited on the formed pattern (**Figure 3B**) and the Ti membrane function as an adhesive layer in this process. Further, the Au antenna pattern was formed by using the lift-off technology, as shown in **Figure 3C**. Subsequently, the Nb_5N_6 thin film was patterned into Nb_5N_6 film microbridge using lithography and reactive ion etching (RIE) technique (**Figure 3D**). The resistance of the Nb_5N_6 microbolometer THz detector depends on the dimensions of the Nb_5N_6 film microbridge. Finally, a photoresist protection pattern was generated on the formed pattern using the same lithography technique, with only two open areas on both sides of the Nb_5N_6 film microbridge (**Figure 3E**). After the photoresist pattern was formed, the SiO_2 layer on the surface of the Si substrate was dry-etched through RIE to expose Si pattern only in the two open areas. The RIE was performed in a gas mixture of CF_4 and O_2 at the total pressure of 4 Pa and RF power of 150 W for 3 min. The optimized mixture ratio of CF_4 and O_2 was 30:10. The opening formed on Si was further etched by using RIE to create an air-cavity (**Figure 3F**). The etching conditions are as follows: the flow of SF_6 is 40 sccm, chamber pressure is 8 Pa, and the RF power is 70 W. The air-cavity was formed under the Nb_5N_6 film microbridge with a SiO_2 supporting layer through RIE etching, because the etching rate of Si was much higher than that of SiO_2. In the etching process of the Si air-cavity, we adopted the technology of stepwise etching, etching for 3 min each step, and etching for three steps in total. The advantages of stepwise etching are that, on the one hand, it is conducive to directly observe whether the air-cavity under the Nb_5N_6 film microbridge is formed; on the other hand, when the air-cavity is etched, the photoresistance on the surface of Si substrate will be heated as little as possible to prevent it from solidifying, which is conducive to the removal of photoresistance in the later stage.

The optical image of the fabricated RF choke-enhanced dipole antenna-coupled Nb_5N_6 THz detector and the SEM micrograph of an Nb_5N_6 air-bridge are displayed in **Figure 4**. The fabricated Nb_5N_6 THz detector includes four main parts: a planar dipole antenna, Au bias pads, an Nb_5N_6 film microbridge, and an etched air-cavity. In **Figure 4B**, the Nb_5N_6 film microbridge is thoroughly freestanding from the Si substrate with a 200 nm SiO_2 support layer. The SiO_2 layer mainly plays a role in preventing the Nb_5N_6 film microbridge from fracture or collapse. The air-cavity isolates the heat conduction between the Nb_5N_6 film microbridge and the Si substrate, which further improves the sensitivity of the THz detector. The DC resistance of the fabricated Nb_5N_6 THz detector is 0.76 kΩ.

CHARACTERIZATION OF THE NB_5N_6 THZ DETECTOR

Typical performance parameters of THz detectors are responsivity ($\mathfrak{R}$) and NEP. Responsivity is related to the efficiency of THz detector and is defined as the RF or optical response for a given input power. It can be expressed as follows [35, 36]:

$$\mathfrak{R} = \frac{\Delta U}{P_{in}}, \tag{1}$$

$$P_{in} = \frac{A_{eff}}{S_{beam}} \cdot P_{beam}, \tag{2}$$

where $\triangle U$ is the output voltage of the Nb_5N_6 THz detector, P_{in} is the input power received on the effective area of the Nb_5N_6 THz detector, and S_{beam} and P_{beam} are the spot size and total power of the THz beam at the focus, respectively. The measured total power of the THz beam at the focus is 0.5 mW.

Measuring the power received by the detector is essential to calculate responsivity and NEP, but this power is a function of effective area A_{eff} and impinging of received power density. The effective area A_{eff} is considered as the pixel area that effectively captures the impinging power and it is a function of receiving antenna directivity and signal frequency. Thus, if D is the directivity of receiving antenna, the effective area of the THz detector is given by [37, 38]

$$A_{eff} = \frac{\lambda^2}{4\pi} \cdot D, \tag{3}$$

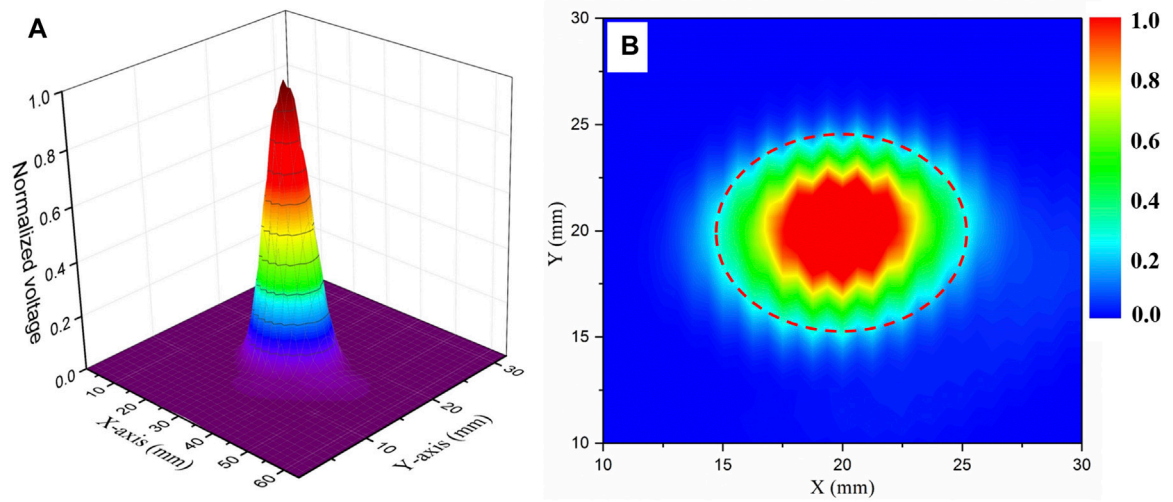

FIGURE 5 | (A) 3-D image of the THz beam scanned by the Nb_5N_6 THz detector at 0.308 THz and **(B)** 2-D image of the THz beam in the focal plane.

where λ is the signal wavelength. For a simulated value of $D = 8.6$ dBi and free-space wavelength $\lambda = 0.97$ mm at 0.301THz, a value of $A_{\text{eff}} = 0.516\ \text{mm}^2$ is obtained.

To calculate the power on the effective receiving area of the Nb_5N_6 THz detector, it is necessary to determine the spot size of the THz beam on the focal plane. The spot distribution of the THz beam at the focus is scanned using the Nb_5N_6 THz detector. At a scan range of 20 mm × 20 mm and the step size of 210 μm, the measured spot distribution of the THz beam at the focus is depicted in **Figure 5**. **Figure 5A** is the three-dimensional distribution of the THz beam scanned by the Nb_5N_6 THz detector. The ordinate denotes the normalized response voltage value, and the X-axis and Y-axis denote the scanning distance of the Nb_5N_6 THz detector, respectively. A scanned image of the THz beam at the focus is displayed in **Figure 5B**. It can be seen that the spot diameter of the THz beam is about 10 mm.

The used THz source is composed of AMC-336 frequency multiplier produced by Virginia Diodes, Inc. (VDI) and Agilent E8251D signal generator. A low-frequency signal provided by the signal generator is amplified by AMC-336 frequency multiplier (WR2.8 VDI horn) to obtain the THz frequency in the range of 0.25–0.35 THz. The modulation signal of the signal generator is 1 kHz, which is input to the lock-in amplifier as a reference signal. The maximum output power of THz source is about 0.5 mW measured by a thermal power sensor (OPHIR, 3A-P-THz). The THz radiation is focused to maximize the electrical signal of the detector by two off-axis parabolic mirrors and the three-dimensional displacement platform. The responses voltage of the detector is read out by a lock-in amplifier (SR830). The responsivity of the Nb5N6 array detector depends on its voltage value and is calculated by **Eqs 1–3**. The measured optical voltage responsivity of the Nb_5N_6 THz detector varies with frequency, as shown in **Figure 6**. The resonant frequency corresponding to the maximum optical responsivity of the Nb_5N_6 THz detector is 0.308 THz, and the best optical responsivity is 1100 V/W. The

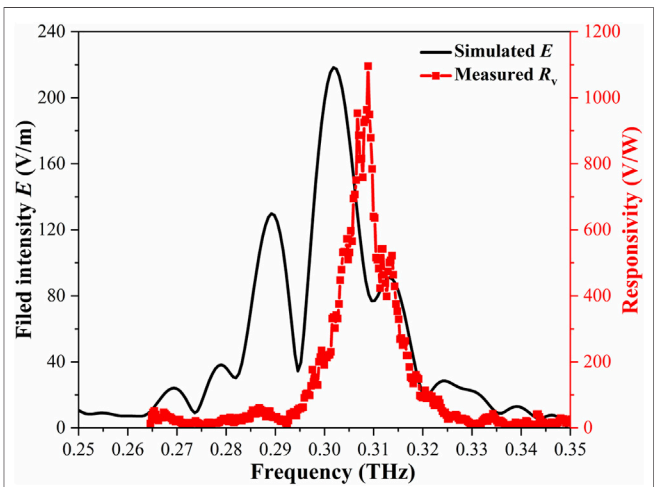

FIGURE 6 | Measured optical responsivity of the Nb_5N_6 THz detector in the frequency range 0.25–0.35 THz.

measured responsivity varying with frequency is the same as the variation trend of simulated electric field intensity with the frequency. A small frequency shift is observed at the resonance frequency. This deviation may be due to the approximate simulation model, in which we neither considered the effect of the air-bridge nor the size deviation in the fabrication process.

Besides the RF responsivity, the NEP is crucial parameter for characterizing the sensitivity of THz detector, which can be expressed as

$$\text{NEP} = \frac{V_{nosie}}{\Re}, \tag{4}$$

where V_{noise} is the voltage noise spectral density and $\Re$ is the optical responsivity of the Nb_5N_6 THz detector.

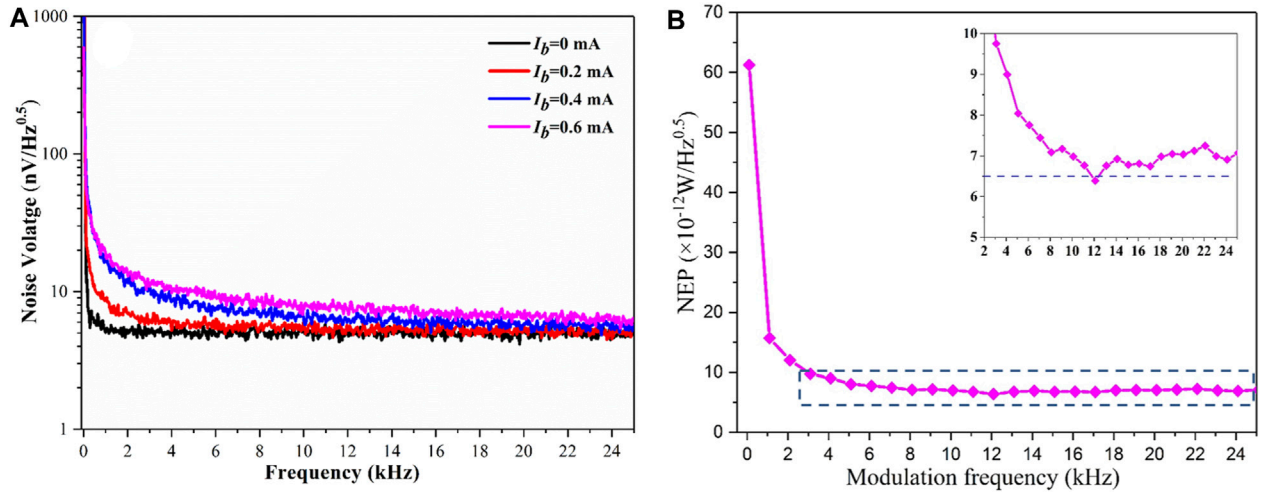

FIGURE 7 | (A) Measured noise voltage under different bias currents and **(B)** the calculated NEP as a function of the modulation frequency for the Nb_5N_6 THz detector.

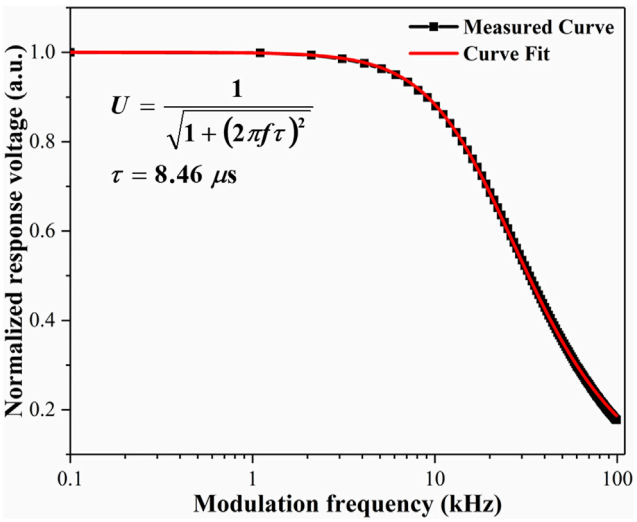

FIGURE 8 | Normalized response voltage of the Nb_5N_6 microbolometer THz detector as a function of modulation frequency for the determination of the thermal time constant.

The voltage noise spectral density of the Nb_5N_6 THz detector was obtained using a spectrum analyzer (Agilent 35670A) and a low-noise amplifier (LNA-SR560) with a voltage gain of 60 dB, as shown in **Figure 7A**. The noise voltage of the Nb_5N_6 THz detector increases with the bias current. Note that the 1/*f* noise cross point also increases with the increase of the bias current. At lower bias current (0 and 0.2 mA) and modulation frequencies greater than 1 and 4 kHz, the noise spectrum tends to be constant and the device is limited by the thermal noise ($\sqrt{4kTR}$), where k is Boltzmann's constant (1.38×10^{-23} J/K), T is the Kelvin temperature, and R is the DC resistance of the device. However, at 0.6 mA bias current, the 1/*f* noise-decay increases to 12 kHz. This indicates that the low-frequency flicker noise (1/*f* noise) is related to the bias current, as explained in [17]. The measured noise voltage of the Nb_5N_6 THz detector with 0.6 mA bias current at 1 kHz is about 17 nV/Hz$^{1/2}$, and the NEP is 1.5×10^{-11} W/Hz$^{1/2}$. As shown in **Figure 8**, the response voltages of the Nb_5N_6 THz detector are a function of modulation frequency of the THz radiation signals. Therefore, the NEP of the Nb_5N_6 THz detector is also related to the modulation frequency of the THz radiation signals. The measured NEP of the Nb_5N_6 THz detector changes with the modulation frequency at the bias current of 0.6 mA, as displayed in **Figure 7B**. It can be observed that the NEP gradually decreases with the increase of the modulation frequency. The NEP which tends to a constant for the modulation frequency is greater than 10 kHz, and the minimum NEP of the Nb_5N_6 THz detector is 6.4×10^{-12} W/Hz$^{1/2}$ at the modulation frequency of 12 kHz. The performance comparison between the proposed Nb_5N_6 THz detector and other published detectors is shown in **Table 1**. The table contains the relevant performance parameters of THz detector published by our research group and other research groups. Compared with other detectors, the Nb_5N_6 THz detectors also have higher sensitivity and will have greater supplication prospects in the THz imaging field. Compared with our previous work [28], the optical responsivity and NEP of the RF choke-enhanced antenna-coupled Nb_5N_6 THz detector are increased by 2 times and 3 times, respectively.

The thermal time constant of the THz detector, which determines the speed of image processing, plays an important role in THz imaging technology. The shorter the response time, the faster the image acquisition speed. The measured normalized response voltage of the Nb_5N_6 THz detector as a function of modulation frequency is depicted in **Figure 8**. The normalized amplitude of the response voltage decreases with the increase of the modulation frequency. The measured data can be well fitted by the formula $1/\sqrt{1+(2\pi f\tau)^2}$, indicating that the detector is well described

TABLE 1 | Performance comparison between the proposed Nb_5N_6 THz detectors and other detectors.

Detector	Antenna types	Detection frequency (THz)	Responsivity (V/W)	NEP (pW/Hz$^{1/2}$)	Reference
$YBa_2Cu_3O_{7-x}$ THz detector	Spiral antenna	0.4	70	50	[17]
Graphene FET THz detector	Bowtie antenna	0.8	535	200	[39]
Graphene FET THz detector	Dipole antenna	0.33	30	51	[40]
GaAs Schottky THz detector	Bowtie antenna	0.22	1,650	3.6	[41]
Nb_5N_6 THz detector	Double-slot antenna	0.65	113	44	[42]
	Dipole antenna	0.28	580	17	[28]
	RF choke-enhanced dipole antenna	0.3	1,100	6.4	This work

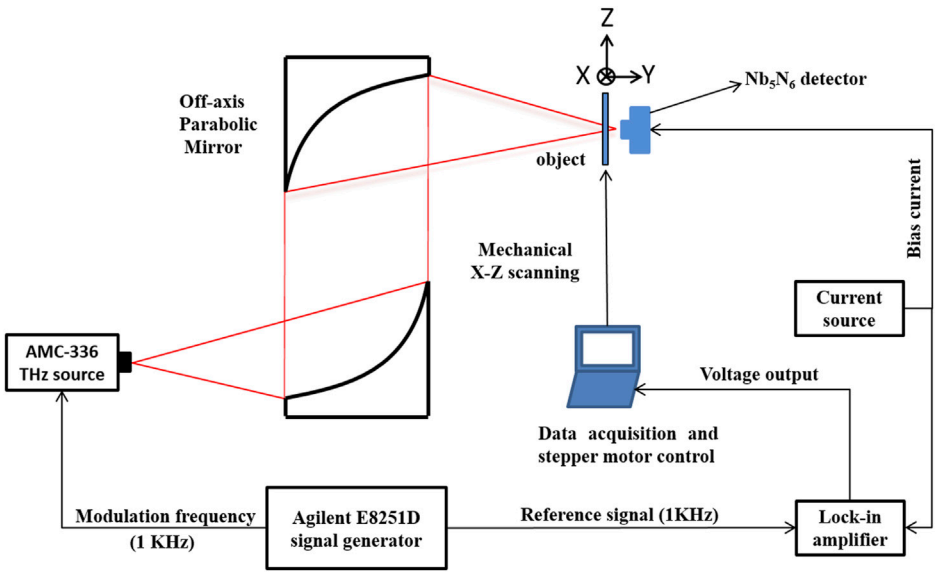

FIGURE 9 | Schematic of the developed imaging system with the Nb_5N_6 THz detector at 0.308 THz.

by the classical thermal model, where the bolometer is represented by an absorber with heat capacity connected to a thermal bath through a small thermal conductance. By fitting the measured response voltage under different modulation frequencies, the thermal time constant of the Nb_5N_6 THz detector was determined to be 8.46 μs.

APPLICATION OF THE NB_5N_6 THZ DETECTOR

To demonstrate the feasibility of the Nb_5N_6 THz detector in practical application, we applied it in a THz transmission imaging system. **Figure 9** shows the schematic diagram of the transmission imaging system. A pair of off-axis parabolic mirrors is used to collimate and focus the modulated THz radiation, a two-dimensional displacement platform is used to move the object to realize the scanning, the THz radiation signals transmitted through the object are detected by the Nb_5N_6 THz detector, the final voltage signals are readout from a lock-in amplifier (SR830) to the computer, and the images of the objects are recovery from these measured raw data without image modification.

Because of the low absorption of THz signals by plastics and the complete reflection of THz signals by metals, THz imaging technology is a very effective way for detecting metal or voids in solid plastic products and other objects containing different THz absorption coefficients. Two objects with different characteristics were used to achieve their images at 0.308 THz with the developed THz imaging system, as shown in **Figure 10**. The first object is a metal blade, and the THz radiation will fully pass through it or not depending on its shape, resulting in that the transmitted THz radiation at different position has nearly the unity intensity. **Figure 10A** shows the image of the blade; the red and the black parts represent the areas where the THz radiation can and not transmit, respectively. Details of the blade imaging, such as the edges and irregular holes, are extremely clear. The second object is an access card, whose components inside are more complicated than the blade, resulting in transmitted THz radiation at different part with different intensities. **Figure 10B** displays the image of the components hidden inside the access card, such as a coil and rectangular chip, which can be observed clearly. These results indicate that the performance of the Nb_5N_6 microbolometer THz detector

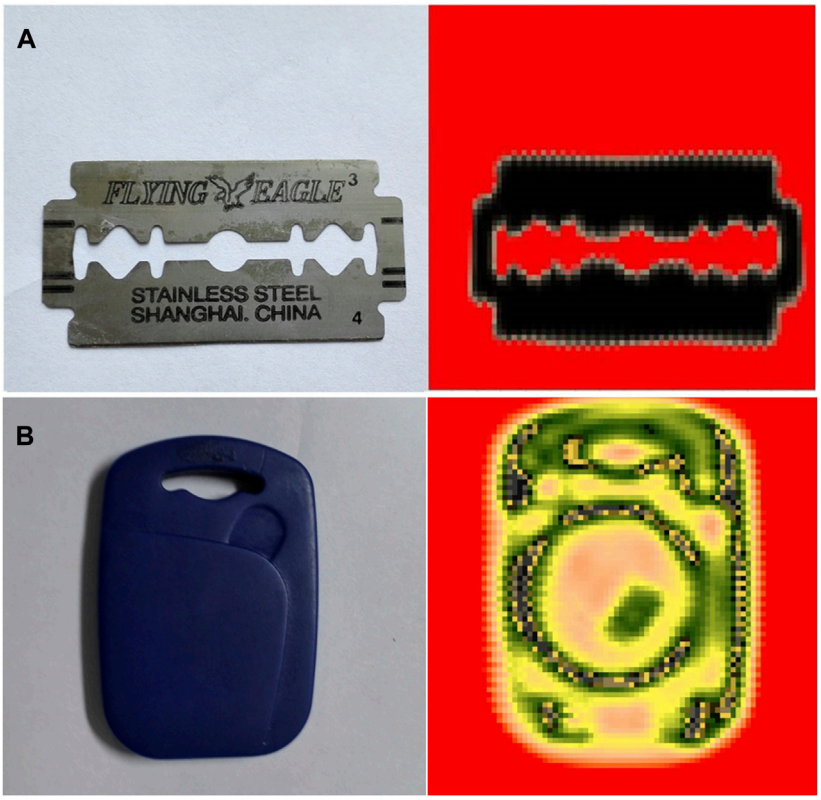

FIGURE 10 | Photographs and THz images of a metal blade **(A)** and access card **(B)**.

integrated with RF choke-enhanced dipole antenna is good from another perspective and it is sufficient for practical applications.

CONCLUSION

The Nb_5N_6 THz detector integrated with RF choke-enhanced dipole antenna was developed and demonstrated for 0.3 THz detection and imaging at room temperature. The simulated electric field intensity of the proposed RF choke-enhanced dipole antenna showed an improvement of 2.6 times compared to that without RF choke. The measured best optical responsivity of the Nb_5N_6 microbolometer THz detector integrated with the proposed antenna was 1100 V/W and the corresponding minimum NEP was 6.4×10^{-12} W/Hz$^{1/2}$ at 0.308 THz with 0.6 mA bias current. The response time of the Nb_5N_6 THz detector was as low as 8.46 μs. The measurement results were in good agreement with the simulation ones. Furthermore, a THz imaging system based on transmission mode was developed using the proposed detector, and the THz imaging of a blade and the access card was investigated. The results show that the obtained THz imaging has high resolution and a clear outline without any image processing. Especially, through the analysis of the transmission image of the access card, its internal structure could be clearly observed. It was demonstrated that the proposed antenna-coupled Nb_5N_6 THz detector had high sensitivity and fast response speed for THz imaging. The development of large-scale detector arrays for terahertz imaging using the proposed detector in this work is on the underway.

DATA AVAILABILITY STATEMENT

The original contributions presented in the study are included in the article/Supplementary Material; further inquiries can be directed to the corresponding authors.

AUTHOR CONTRIBUTIONS

CJ designed and simulated the structure. All authors analyzed and discussed the results. CJ and XT wrote the manuscript. The project was conceived and supervised by XT and LK.

FUNDING

This research was supported by the Key Technologies Research and Development Program (2018YFB1801504); National Natural Science Foundation of China (61521001 and 61801209); Fundamental Research Funds for the Central Universities; and Jiangsu Key Laboratory of Advanced Techniques for Manipulating Electromagnetic Waves.

REFERENCES

1. Chan WL, Deibel J, and Mittleman DM. Imaging with Terahertz Radiation. *Rep Prog Phys* (2007) 70(8):1325–79. doi:10.1088/0034-4885/70/8/R02
2. Siegel PH. Terahertz Technology in Biology and Medicine. *IEEE Trans Microwave Theor Techn.* (2004) 52(10):2438–47. doi:10.1109/TMTT.2004.835916
3. Yu C, Fan S, Sun Y, and Pickwell-Macpherson E. The Potential of Terahertz Imaging for Cancer Diagnosis: A Review of Investigations to Date. *Quant Imaging Med Surg* (2012) 2(1):33–45. doi:10.3978/j.issn.2223-4292.2012.01.04
4. Ferguson B, and Zhang X-C. Materials for Terahertz Science and Technology. *Nat Mater* (2002) 1(1):26–33. doi:10.1038/nmat708
5. Mittleman D. *Sensing with Terahertz Radiation*. Springer Berlin Heidelberg (2003). doi:10.1007/978-3-540-45601-8
6. Sizov F, and Rogalski A. THz Detectors. *Prog Quan Elect* (2010) 34(5): 278–347. doi:10.1016/j.pquantelec.2010.06.002
7. Golay MJE. A Pneumatic Infra-Red Detector. *Rev Scientific Instr* (1947) 18(5): 357–62. doi:10.1063/1.1740949
8. Siegel PH. Terahertz Technology. *IEEE Trans Microwave Theor Techn.* (2002) 50(30):910–28. doi:10.1109/22.989974
9. Knap W, Valusis G, Dyakonov M, Coquillat D, Teppe F, Lusakowski J, et al. Field Effect Transistors for Terahertz Detection: Physics and First Imaging Applications. *J Infrared Millim Terahertz Waves* (2009) 30(12):1319–37. doi:10.1007/s10762-009-9564-9
10. Miller AJ, Luukanen A, and Grossman EN. Micromachined Antenna-Coupled Uncooled Microbolometers for Terahertz Imaging Arrays. *Proc SPIE - Int Soc Opt Eng* (2004) 5411:18–24. doi:10.1117/12.543236
11. Grant J, Escorcia-Carranza I, Li C, McCrindle IJH, Gough J, and Cumming DRS. A Monolithic Resonant Terahertz Sensor Element Comprising a Metamaterial Absorber and Micro-bolometer. *Laser Photon Rev* (2013) 7(6):1043–8. doi:10.1002/lpor.201300087
12. Simoens F, and Meilhan J. Terahertz Real-Time Imaging Uncooled Array Based on Antenna- and Cavity-Coupled Bolometers. *Phil Trans R Soc A* (2014) 372:20130111. doi:10.1098/rsta.2013.0111
13. Lee AWM, Wil BS, Kumar S, Qing Hu fnm, and Reno JL. Real-time Imaging Using a 4.3-THz Quantum cascade Laser and a 320/spl Times/240 Microbolometer Focal-Plane Array. *IEEE Photon Technol Lett* (2006) 18(13):1415–7. doi:10.1109/LPT.2006.877220
14. Chen C, Yi X, Zhang J, and Zhao X. Linear Uncooled Microbolometer Array Based on VOx Thin Films. *Infrared Phys Tech* (2001) 42(2):87–90. doi:10.1016/S1350-4495(01)00058-5
15. Pope T, Savchenko A, Thomas P, and Hornsey R. Nonoptical Characterization Techniques for Uncooled Microbolometer Infrared Sensors. *IEEE Trans Electron Devices* (2000) 47(12):2294–300. doi:10.1109/16.887011
16. Cole BE, Higashi RE, and Wood RA. Monolithic Two-Dimensional Arrays of Micromachined Microstructures for Infrared Applications. *Proc IEEE* (1998) 86(8):1679–86. doi:10.1109/5.704273
17. Bevilacqua S, and Cherednichenko S. Low Noise Nanometer Scale Room-Temperature ${\hbox{YBa}}_{2}{\hbox{Cu}}_{3}{\Hbox{O}}_{7-x}$ Bolometers for THz Direct Detection. *IEEE Trans Thz Sci Technol* (2014) 4(6):653–60. doi:10.1109/TTHZ.2014.2344435
18. Almasri M, Butler DP, and Celik-Butler Z. Self-supporting Uncooled Infrared Microbolometers with Low-thermal Mass. *J Microelectromech Syst* (2001) 10(3):469–76. doi:10.1109/84.946808
19. Shan PC, Çelik-Butler Z, Butler DP, Jahanzeb A, Travers CM, Kula W, et al. Investigation of Semiconducting YBaCuO Thin Films: A New Room Temperature Bolometer. *J Appl Phys* (1996) 80(12):7118–23. doi:10.1063/1.363724
20. Qi L, Minkevičius L, Urbanowicz A, Švigelj A, Grigelionis I, Kašalynas I, et al. Antenna-Coupled Titanium Microbolometers: Application for Precise Control of Radiation Patterns in Terahertz Time-Domain Systems. *Sensors* (2021) 21(10):3510. doi:10.3390/s21103510
21. Monticone E, Boarino L, Lérondel G, Steni R, Amato G, and Lacquaniti V. Properties of Metal Bolometers Fabricated on Porous Silicon. *Appl Surf Sci* (1999) 142(1):267–71. doi:10.1016/S0169-4332(98)00685-0
22. Jin-Shown Shie JS, Yeong-Maw Chen YM, Mang Ou-Yang fnm, and Chou BCS. Characterization and Modeling of Metal-Film Microbolometer. *J Microelectromech Syst* (1996) 5(4):298–306. doi:10.1109/84.546409
23. Sedky S, Fiorini P, Caymax M, Loreti S, Baert K, Hermans L, et al. Structural and Mechanical Properties of Polycrystalline Silicon Germanium for Micromachining Applications. *J Microelectromech Syst* (1998) 7(4):365–72. doi:10.1109/84.735343
24. Sedky S, Fiorini P, Caymax M, Baert C, Hermans L, and Mertens R. Characterization of Bolometers Based on Polycrystalline Silicon Germanium Alloys. *IEEE Electron Device Lett* (1998) 19(10):376–8. doi:10.1109/55.720191
25. Zimmers A, Aigouy L, Mortier M, Sharoni A, Wang S, West KG, et al. Role of Thermal Heating on the Voltage Induced Insulator-Metal Transition inVO2. *Phys Rev Lett* (2013) 110(5):056601. doi:10.1103/PhysRevLett.110.056601
26. Jagtap VS, Dégardin AF, and Kreisler AJ. Low Temperature Amorphous Growth of Semiconducting Y-Ba-Cu-O Oxide Thin Films in View of Infrared Bolometric Detection. *Thin Solid Films* (2012) 520(14):4754–7. doi:10.1016/j.tsf.2011.10.127
27. Lu X, He N, Kang L, Chen J, Jin B, and Wu P. Nb5N6 Thin Film on Silicon and Silicon Oxide: A Good Material for Terahertz Detection. *Chin Sci Bull* (2009) 54(18):3344–6. doi:10.1007/s11434-009-0485-8
28. Tu X-C, Kang L, Liu X-H, Mao Q-K, Wan C, Chen J, et al. Nb5N6microbolometer Arrays for Terahertz Detection. *Chin Phys. B* (2013) 22(4):040701. doi:10.1088/1674-1056/22/4/040701
29. Jiang Z, Men L, Wan C, Xiao P, Jiang C, Tu X, et al. Low-Noise Readout Integrated Circuit for Terahertz Array Detector. *IEEE Trans Thz Sci Technol* (2018) 8(3):350–6. doi:10.1109/TTHZ.2018.2819502
30. Lindberg P, and Ojefors E. A Bandwidth Enhancement Technique for mobile Handset Antennas Using Wavetraps. *IEEE Trans Antennas Propagat* (2006) 54(8):2226–33. doi:10.1109/TAP.2006.879211
31. Wang Y-S, Lu J-C, and Chung S-J. A Miniaturized Ground Edge Current Choke-Design, Measurement, and Applications. *IEEE Trans Antennas Propagat* (2009) 57(5):1360–6. doi:10.1109/TAP.2009.2016709
32. Noghanian S, and Shafai L. Gain Enhancement of Annular Slot Antennas. *IEE Proc Microw Antennas Propag* (2001) 148(2):109–14. doi:10.1049/ip-map:20010331
33. Kishk AA, Shafai L, and Ittipiboon A. Improvement in Radiation Characteristics of Coaxial Feeds Using a Quarter-Wavelength Choke. *Electron Lett* (1984) 20(12):522–3. doi:10.1049/el:19840362
34. Szakmany GP, Orlov AO, Bernstein GH, and Porod W. Response Increase of Antenna-Coupled Nanothermocouples by thermal Insulation. *J Vacuum Sci Tech B* (2018) 36(5):052203. doi:10.1116/1.5044534
35. Coquillat D, Marczewski J, Kopyt P, Dyakonova N, Giffard B, and Knap W. Improvement of Terahertz Field Effect Transistor Detectors by Substrate Thinning and Radiation Losses Reduction. *Opt Express* (2016) 24(1): 272–81. doi:10.1364/OE.24.000272
36. Hosotani T, Kasuya F, Taniguchi H, Watanabe T, Suemitsu T, Otsuji T, and Ishibashi T. Lens-integrated Asymmetric-Dual-Grating-Gate High-Electron-Mobility-Transistor for Plasmonic Terahertz Detection. In: 2017 IEEE MTT-S International Microwave Symposium (IMS); 4-9 June 2017; Honolulu, HI, USA. IEEE (2017). p. 578–81. doi:10.1109/MWSYM.2017.8058632
37. Ali M, Perenzoni M, and Stoppa D. A Measurement Setup for THz Detectors Characterization Validated on FET-Based CMOS Test Structures. In: Conference Record - IEEE Instrumentation and Measurement Technology Conference, 2015; 11-14 May 2015; Pisa, Italy. IEEE (2015). p. 320–4. doi:10.1109/I2MTC.2015.7151287
38. Ojefors E, Pfeiffer UR, Lisauskas A, and Roskos HG. A 0.65 THz Focal-Plane Array in a Quarter-Micron CMOS Process Technology. *IEEE J Solid-state Circuits* (2009) 44(7):1968–76. doi:10.1109/JSSC.2009.2021911
39. G K RM, Deshmukh P, Prabhu SS, and Basu PK. Antenna Coupled Graphene-FET as Ultra-sensitive Room Temperature Broadband THz Detector. *AIP Adv* (2018) 8(12):125122. doi:10.1063/1.5063399
40. Qin H, Sun J, Liang S, Li X, Yang X, He Z, et al. Room-temperature, Low-Impedance and High-Sensitivity Terahertz Direct Detector Based on Bilayer Graphene Field-Effect Transistor. *Carbon* (2017) 116:760–5. doi:10.1016/j.carbon.2017.02.037
41. Qiao HD, Liu H, Mou JC, and Lv X. 220 GHz Focal Plane Imaging Demonstration Using Integrated Terahertz Array Detector. *Microw Opt Technol Lett* (2020) 62(9):2826–9. doi:10.1002/mop.32388

42. Xiao P, Tu X, Jiang C, Li Z, Zhou S, Pan D, et al. Planar Double-Slot Antenna Integrated into a Nb5N6 Microbolometer THz Detector. *Opt Lett* (2020) 45(10):2894–7. doi:10.1364/OL.388771

Conflict of Interest: The authors declare that the research was conducted in the absence of any commercial or financial relationships that could be construed as a potential conflict of interest.

Publisher's Note: All claims expressed in this article are solely those of the authors and do not necessarily represent those of their affiliated organizations, or those of the publisher, the editors, and the reviewers. Any product that may be evaluated in this article, or claim that may be made by its manufacturer, is not guaranteed or endorsed by the publisher.

frontiers in Physics

ORIGINAL RESEARCH
published: 11 November 2021
doi: 10.3389/fphy.2021.774524

Optimization of the Cryogenic Light-Emitting Diodes for High-Performance Broadband Terahertz Upconversion Imaging

Peng Bai[1,2], *Yueheng Zhang*[1]*, *Wenzhong Shen*[1], *Ning Yang*[2] *and Weidong Chu*[2]*

[1]Key Laboratory of Artificial Structures and Quantum Control, School of Physics and Astronomy, Shanghai Jiao Tong University, Shanghai, China, [2]Institute of Applied Physics and Computational Mathematics, Beijing, China

High-performance terahertz (THz) imaging devices have drawn wide attention due to their significant application in a variety of application fields. Recently, the upconversion device based on the integrated homo-junction interfacial workfunction internal photoemission detector and light-emitting diode (HIWIP-LED) has emerged as a promising candidate for broadband THz upconversion pixelless imaging device. In this paper, systematical investigations on the cryogenic-temperature performances of the LED part in HIWIP-LED devices, including electroluminescence (EL) spectra and the EL efficiency, have been carried out by elaborating the radiative recombination mechanism in the quantum well, internal quantum efficiency, and the light extraction efficiency (*LEE*) both experimentally and theoretically. On this basis, we have further studied the operation mode of the HIWIP-LED and concluded that the *LEE* could directly determine the upconversion efficiency. A numerical simulation has been performed to optimize the *LEE*. Numerical results show that the device with a micro-lens geometry structure could significantly improve the *LEE* of the LED thereby increasing the upconversion efficiency. An optimal upconversion efficiency value of 0.12 W/W and a minimum noise equivalent power (NEP) of 14 pW/Hz$^{1/2}$ are achieved using the micro-lens structure together with anti-reflection coating. This work gives a precise description of cryogenic LED performance in the HIWIP-LED device and provides an optimization method for the broadband HIWIP-LED THz upconversion pixelless imaging device.

Keywords: broadband upconversion, THz pixelless imaging, light extraction efficiency (*LEE*), internal photoemission (IPE), light-emitting diode (LED)

OPEN ACCESS

Edited by:
Yingxin Wang,
Tsinghua University, China

Reviewed by:
Xuguang Guo,
University of Shanghai for Science and Technology, China
Tongyi Zhang,
Xian Institute of Optics and Precision Mechanics (CAS), China

***Correspondence:**
Yueheng Zhang
yuehzhang@sjtu.edu.cn
Weidong Chu
chu_weidong@iapcm.ac.cn

Specialty section:
This article was submitted to Optics and Photonics, a section of the journal Frontiers in Physics

Received: *12 September 2021*
Accepted: *12 October 2021*
Published: *11 November 2021*

Citation:
Bai P, Zhang Y, Shen W, Yang N and Chu W (2021) Optimization of the Cryogenic Light-Emitting Diodes for High-Performance Broadband Terahertz Upconversion Imaging. Front. Phys. 9:774524. doi: 10.3389/fphy.2021.774524

INTRODUCTION

Up-converting long-wavelength infrared (IR) light to shorter-wavelength radiation has attracted more attention and has been intensively explored in the last two decades thanks to its tremendous potential in low-cost and large-format IR/terahertz (THz) imaging, high-efficiency solar cells, and sensitive biological imaging [1–4]. Among many upconversion methods, semiconductor upconversion technology is extremely competitive due to its compactness, high efficiency, flexible and adjustable response frequency, and full compatibility with semiconductor manufacturing processes [4]. This idea was proposed and realized by H. C. Liu in 1995 with an integrated upconversion device comprising a quantum well IR photodetector (QWIP) and a light-emitting diode

(LED) [5]. The IR signal at the range of 8–12 μm was first detected by the QWIP, and then the produced photocurrent was injected into the active region of the LED resulting the extra near infrared (NIR) emission under bias voltage [5, 6]. When used for a large-format imaging device, the integrated device converts the incoming IR image into an outgoing NIR or visible image which then is captured by a Si charge-coupled device (CCD). There is no separate pixel in this imaging scheme, and this pixelless imaging technology could realize large-format two-dimensional IR imaging easily without the need for the Si readout integrated circuits (ROIC) on the chip and without the need for the hybrid bonding process. This imaging method also avoids the thermal mismatch problem between the focal plane array (FPA) chip and Si ROIC in the large-format hybrid QWIP FPAs at cryogenic temperatures [6].

Variable upconversion devices have been realized at the ranges of the NIR, mid-infrared (MIR), and THz based on the concept of integrated photodetector and LED [7–13]. At MIR range, the QWP-LEDs are well developed, and a high-temperature resolution for the n-type QWP-LED of 60 mK was successfully realized [14]. In contrast, the relative backwardness of the THz upconversion pixelless imaging demands great effort and further exploration. Due to the diffraction limit and the limitation of low-temperature operation, the THz FPAs based on photon-type detectors has not made significant progress so far. The pixelless imaging provides a good alternative for photon-type THz imaging. THz QWP-LED prototype device was successfully fabricated to upconvert the 4.2 THz radiation from a quantum cascade laser into an 830 nm NIR emission in 2016 [9]. However, the edge coupled optical coupling geometry adopted in the device to excite the intersubband transition caused a severe distortion of the imaging QCL spot. Therefore, this THz QWP-LED pixelless imaging device is far from an optimization for the thermal imaging. The upconversion device based on the homo-junction interfacial workfunction internal photoemission (HIWIP) detector and LED allows normal incidence excitation and realizes a broadband (4–20 THz) THz to NIR upconversion [15]. However, the current limiting factor for this imaging scheme is the low upconversion efficiency. In fact, the problem of low upconversion efficiency also plagues almost all III-V compound semiconductor based upconversion devices. The upconversion efficiency of the MIR or THz upconverter are all below the level of 0.01 W/W [15–17], which greatly restrains the efficiency and quality of the pixelless imaging. How to improve the upconversion efficiency is an urgent problem for HIWIP-LED pixelless imaging devices. And in the past, people paid more attention to the room temperature performance of LEDs. The performance of LEDs at extremely low temperatures (<20 K) is not particularly clear.

In this paper, we present the experimental results of the LED in the HIWIP-LED device at different temperatures and provide the explanation of the variation of temperature-dependent emission spectra by numerically solving the Schrodinger equation. The internal quantum efficiency and light extraction efficiency (*LEE*) of the LED are determined using a developed rate equation method, which reveals that the low *LEE* is the main reason to cause the low upconversion efficiency of HIWIP-LED. The device structure and operation mode of the HIWIP-LED are investigated systematically to further elaborate the upconversion mechanism, bias voltage distribution, and the primary determinant of the upconversion efficiency. Finally, a numerical simulation is carried out to improve the *LEE* of the LED portion, and the results show that the upconversion efficiency for HIWIP-LED could be enhanced one order of magnitude using the micro-lens structure LED. This work makes us have a clearer understanding of the low-temperature performance of HIWIP-LED and provides theoretical guidance for the experiments to improve upconversion efficiency.

DEVICE AND UPCONVERSION PRINCIPLE

The device structure of HIWIP-LED is shown in **Figure 1A**, which consists of a GaAs-based HIWIP detector and an InGaAs/GaAs/AlGaAs quantum well LED directly grown by molecular beam epitaxy (MBE). The active region of the p-type GaAs HIWIP detector consists of 20 repeats of p-GaAs (doped with Be to 3×10^{18} cm^{-3})/i-GaAs (emitter layer/intrinsic) layers with emitter layer and intrinsic layer thickness of 80 and 15 nm. The quantum well LED structure is 9 nm $In_{0.1}Ga_{0.9}As$ quantum well sandwiched by 40 nm intrinsic GaAs. On either side of the GaAs are 80 nm AlxGa1-xAs barriers in order to enhance the carrier confinement effect and increase the internal quantum efficiency of LED. The top $Al_xGa_{1-x}As$ grading barrier ($x = 0.02 \rightarrow 0.1$) doped with Si to $2.5 \times 10^{18}cm^{-3}$ cladding the active region of the LED. The bottom $Al_xGa_{1-x}As$ barrier is a constant barrier with an aluminum component of 2%. This barrier is also the intrinsic connection layer between the HIWIP and LED to avoid the lateral diffusion of the photo-generated carriers. At the top of the device is 50 nm n-GaAs (doped with Si to $2.5 \times 10^{18}cm^{-3}$) layer covered with narrow ring contact formed by deposition of Pd/Ge/Ti/Pt/Au using electron beam evaporation. The bottom contact is 300 nm p-GaAs layer (doped with Be to $3 \times 10^{18}cm^{-3}$) covered with common p-contact of Ti/Pt/Au. The devices were fabricated using standard photo lithographic techniques. Then the samples were mounted on the 14 pin packages and placed into the cryostat for cryogenic measurements. The upconversion could be realized by applying a bias voltage higher than the turn-on voltage of the LED and with the top contact being grounded. Under such conditions, the THz photons were first detected by the HIWIP part. Then the photocurrent will drive the LED to emit NIR photons which could be detected by the Si CCD.

Figure 1B reveals the micro-mechanism of the upconversion process of the HIWIP-LED. THz absorption occurred in the emitter layers of the HIWIP followed by the transportation of the photo-generated carriers. The photo-excited carriers are injected into the $In_{0.1}Ga_{0.9}As$ quantum well for recombination and emitting NIR photons under the external electric field. The measured cryogenic (3.5 K) emission spectrum of the LED portion and the photocurrent spectrum of the HIWIP portion in the upconversion device are displayed in **Figure 1C**. There are two emission peaks in the LED electroluminescence (EL)

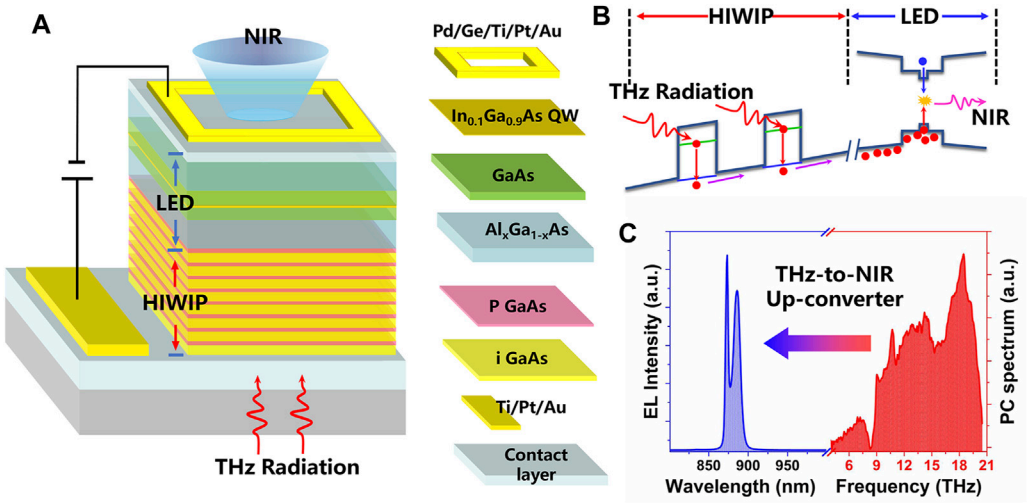

FIGURE 1 | (A) Device structure of HIWIP-LED. **(B)** Micro-mechanism of the upconversion process of the HIWIP-LED: THz absorption occurred in the emitter layers of the HIWIP followed by the transportation of the carriers. The photo-excited carriers are injected into the quantum well for radiative recombination. **(C)** The measured cryogenic emission spectrum of the LED portion and the photocurrent spectrum of the HIWIP portion in the upconversion device at 3.5 K.

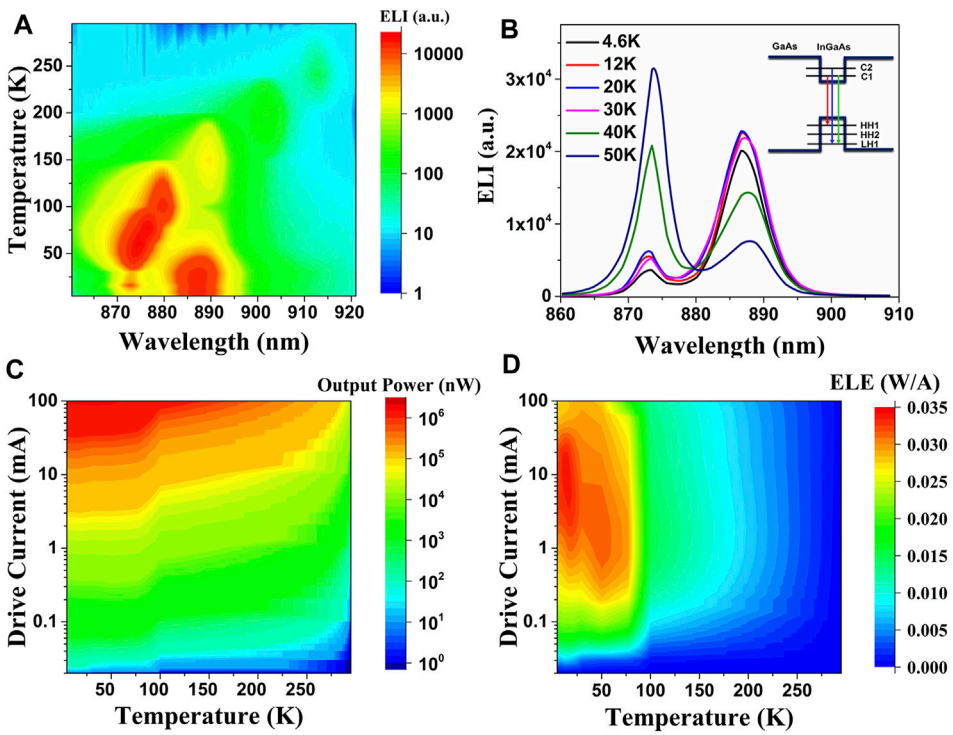

FIGURE 2 | (A) Electroluminescence (EL) spectra with a drive current of 0.5 mA at different temperatures of the LED part. **(B)** EL intensity for the LED part with 0.5 mA drive current at a temperature below 50 K; also shown in the inset is the quantum well structure and interband transition of the LED. **(C)** The experimental variation of the output EL power of the LED with the bias and temperature. **(D)** The mapping result of the EL efficiency (ELE) as a function of drive current and temperature.

spectrum, which is due to the complexity of the valence band in the $In_{0.1}Ga_{0.9}As$ quantum well and will be discussed in detail in the following section. The photocurrent spectrum presents a broadband response range from 4 to 20 THz with a peak response frequency at 18 THz. The deep valley around 8 THz is the Reststrahlen band of GaAs. The small valleys at the range from 9 to 20 THz are associated with the multiple phonon absorption.

PERFORMANCE OF THE LED IN HIWIP-LED

The EL spectra with a drive current of 1 mA at different temperatures of the LED part are presented in **Figure 2A**, which are measured using a fiber spectrometer (Ocean optics QE65PRO) with the same integrated time. There are two luminescence peaks at 873 (peak 1) and 887 nm (peak 2) at the temperature below 50 K. Peak 1 rises with the increasing of the driven current and presents a red-shift effect as the temperature increases. We attribute the red-shift behavior to the energy gap decreases due to the Varshni effect. Peak 2 has no position shift, and the intensity decreases with the temperature increasing. What is more interesting is that there exists a competition between peak1 and peak 2 as is shown in **Figure 2B**. As the temperature increases from 4.6 to 50 K, the intensity of peak 1 increases and peak 2 decreases. The luminescence wavelength of the intrinsic recombination of the GaAs barrier is at about 816 nm (the band gap of the GaAs is 1.519eV at 4.6 K). But the observed EL peaks are all above the wavelength of 816 nm, which indicates they all originate from the InGaAs quantum well. In order to understand the luminescent property of the LED, we calculated the band structure of the $In_{0.1}Ga_{0.9}As/GaAs$ quantum well by solving the Schrodinger equation using the plane wave expansion (PWE) method [18, 19]:

$$\left\{-\frac{\hbar^2}{2}\frac{\partial}{\partial z}\left[\frac{1}{m^*(z)}\frac{\partial}{\partial z}\right]+V_{QW}(z)+V_H(z)+V_{xc}(z)\right\}\varphi(z) = \varepsilon\varphi(z) \quad (1)$$

where $m^\star$ is the electron effective mass, ħ is the reduced Planck constant, V_{QW} is the stepwise potential energy representing the conduction band offset profile, V_H is the Hartree potential energy obtained from Poisson's equation, V_{xc} is the exchange-correlation potential energy which is given by the local density approximation based on the density functional theory, φ is z-direction envelope function, and ε is eigen-energy. The PWE method is used for accurate calculation. The lattice mismatch caused strain, and bias-caused Stark shift is neglected. The band gaps of GaAs and $In_{0.1}Ga_{0.9}As$ are taken as 1.518959 and 1.36495 eV at 4 K, respectively. The ratio of conduction and valence band offsets is set as 6:4. The effective masses of the well (m_w^*) and barrier (m_b^*) are ($m_w^* = 0.05873m_0$, $m_b^* = 0.0916m_0$) for electron, ($m_w^* = 0.5m_0$, $m_b^* = 0.51m_0$) for heavy hole, and ($m_w^* = 0.0764m_0$, $m_b^* = 0.082m_0$) for light hole, respectively, with m_0 the electron mass. Detailed PWE method to self-consistently solve the Schrodinger equation could be found in **Supplementary Materials** and Ref. [18].

According to our calculated results (inset of **Figure 2B**), peak 2 at 887 nm is related to the first conduction subband to the first heavy hole subband transition ($C_1 \rightarrow HH_1$) of the InGaAs quantum well, corresponding to the calculated transition energy of 1.3999 eV (885.7 nm). Peak 1 at 873 nm below 50 K is from the first conduction subband to the first light hole subband transition ($C_1 \rightarrow LH_1$ (876.88nm)) of the InGaAs quantum well [the calculated transition energy is 1.414 eV (876.88 nm)]. At a low temperature, the $C_1 \rightarrow HH_1$ transition dominates, which leads to a relatively stronger signal. As the temperature increases, $C_1 \rightarrow LH_1$ becomes more significant and dominates when the temperature is higher than 40 K. Peak 2 disappears rapidly as the temperature is higher than 77 K. We attribute this behavior to the thermal excited transition between the heavy and light holes, which results in a lower probability of the $C_1 \rightarrow HH_1$ transition. As the temperature further increases, the intensity of peak 2 also decreases significantly. There are two main reasons. First, the high temperature caused a relative lower injection efficiency that the carrier could not be confined in the well due to the serious thermal excitation. The other reason is that as temperature increases, nonradiative recombination lifetime decreases, including that of Auger recombination and Shockley–Read–Hall (SRH) recombination. As a result, the radiative recombination efficiency decreases at high temperatures [20].

The experimental variation of the output EL power of the LED with the bias and temperature is shown in **Figure 2C**. We find that the output power increases with the drive current and decreases with temperature. The electroluminescence efficiency (ELE) is defined as output power divided by the drive current and is proportional to the external quantum efficiency (EQE) of the LED. The mapping result of the ELE as a function of drive current and temperature is presented in **Figure 2D**, which indicates an evident ELE drop when the temperature increases from 4 to 300 K at any drive current. The ELE increases first and then decreases with the drive current at the same temperature. The efficiency drop with larger injection current is mainly caused by the increase of the nonradiative recombination (SRH recombination and Auger recombination) [21, 22]. The peak point of the ELE shifts to lower current as temperature increases because the nonradiative recombination increases sharply with temperature.

A rate equation analysis method developed by Ray et al. can describe the injection current dependence of the LED external efficiency explicitly by numerically solving the following equation (23):

$$\eta_i = 1 - \frac{(\eta_{max})}{2J}\left(1+\frac{\eta_i J}{\eta_{max}J_{max}}\right)\sqrt{\frac{\eta_i J J_{max}}{\eta_{max}}} \quad (2)$$

where η_i is the internal quantum efficiency (*IQE*), *J* is the injection current density, and η_{max} and J_{max} are the maximum value of *IQE* and the corresponding injection current density (see the **Supplementary Materials** for ABC model and rate equation analysis method). **Figure 3A** shows the injection current density-dependent internal efficiency of the LED at 30, 50, and 77 K, respectively. The fitting results from rate equation analysis method indicate the maximum *IQE* of 93%, 95%, and 87.5% at the temperatures of 33, 50, and 77 K, respectively. Using this method, the η_{max} and corresponding J_{max} at different temperatures are given in **Figure 3B**. The η_{max} at low temperatures are relatively lower than that of higher temperature mainly because of the incomplete ionization of the doping acceptor Be. The J_{max} values at low temperature also indicate the need for a larger injection current to realize the η_{max} owing to the incomplete ionization. The inset of **Figure 3B** also presents the measured external efficiency of the LED at different temperatures with the same injection current (500 μA), which agree well with the integrated

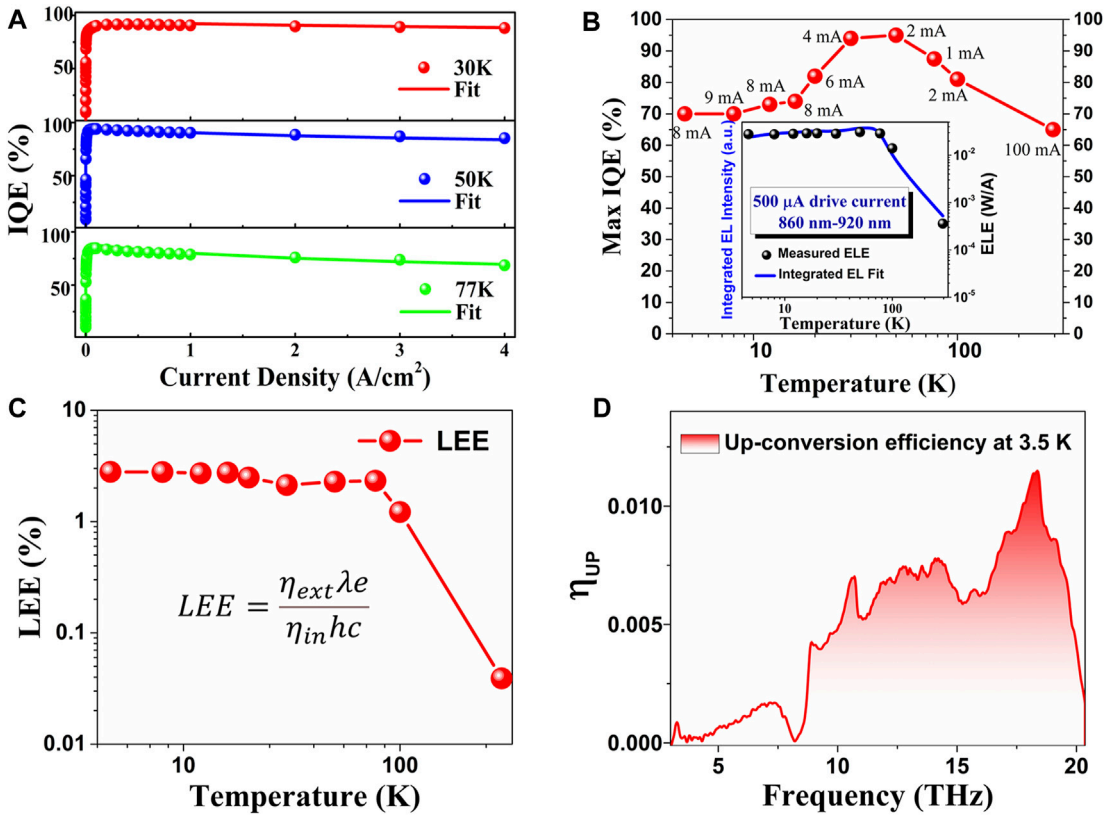

FIGURE 3 | (A) Injection current density-dependent internal efficiencies and the fit results of the LED at 30, 50, and 77 K, respectively. **(B)** η_{max} and corresponding J_{max} at different temperatures, and the inset is the measured external efficiency of the LED at different temperatures with the same injection current (0.5 mA). **(C)** The calculated light extraction efficiency (*LEE*) at different temperatures. **(D)** Calculated upconversion efficiency with a bias voltage of 1.8 V.

EL results. If we neglect the influence of temperature, the *LEE* of the LED is calculated to be about 2.5% at temperature below 100 K (**Figure 3C**) from the relation of $\eta_e = \eta_i \cdot LEE \cdot h\nu/e$, where h is the Planck constant, ν is the frequency of the emitted photon, and e represents the elementary charge. The injection efficiency of the carrier in the rate equation analysis method is assumed to be equal to 100%. When the temperature is higher than 100 K, the calculated *LEE* decreases sharply mainly because of the lower injection efficiency at high temperature. The result of the upconversion efficiency (**Figure 3D**) with a bias voltage of 1.8 V was calculated from the equation $\eta_{up} = \eta_{HIWIP} \cdot \eta_{LED} = R \cdot \eta_i \cdot LEE \cdot h\nu/e$, where R is the responsivity (or detection efficiency) of the HIWIP part. The peak upconversion efficiency is 1.14×10^{-2} at 18 THz.

THEORETICAL OPTIMIZATION OF LED

In order to improve the energy conversion efficiency of the HIWIP-LED, we should have a greater awareness of the operation principle of the HIWIP-LED. **Figure 4A** shows the calculated band diagram across the layer structure of the HIWIP-LED upconversion device under the bias of 0 and 3 V, with the top contact being grounded. The calculation was carried out under the assumption that the band alignment of the heterostructure ($GaAs/Al_xGa_{1-x}As$ or GaAs/InGaAs) follows Anderson's electron affinity rule and the TCAD-based approach is used. We find that the applied bias voltage drops mainly across the LED part, and then the additional bias voltage goes to the HIWIP part. This feature gives rise to a turn-on behavior of the HIWIP-LED device, which is in good agreement with the observed results in the previous experimental measurement [15].

The calculation results of the valence band diagram under different bias voltage are displayed in **Figure 4B**. It is evident that little bias falls across the HIWIP side when the applied bias voltage is lower than 1.5 V, which is equal numerically to the turn-on voltage in the p-i-n structure of the LED. This feature is clear in the larger version of the LED band diagram, which indicates that the applied bias first overcomes the depletion region of the LED and then the other portion of the bias is applied to the HIWIP portion. It should be noted that we did not take the incident radiation into account during the calculation, but the conclusion is still valid when the device is illuminated by the THz radiation. Indeed, the HIWIP is a photoconductor so that the THz excitation of the detector will decrease the resistance of the HIWIP and thereby increase the bias voltage dropped across the LED portion, leading to an increase in the LED emission intensity. Since there is no internal electrical gain

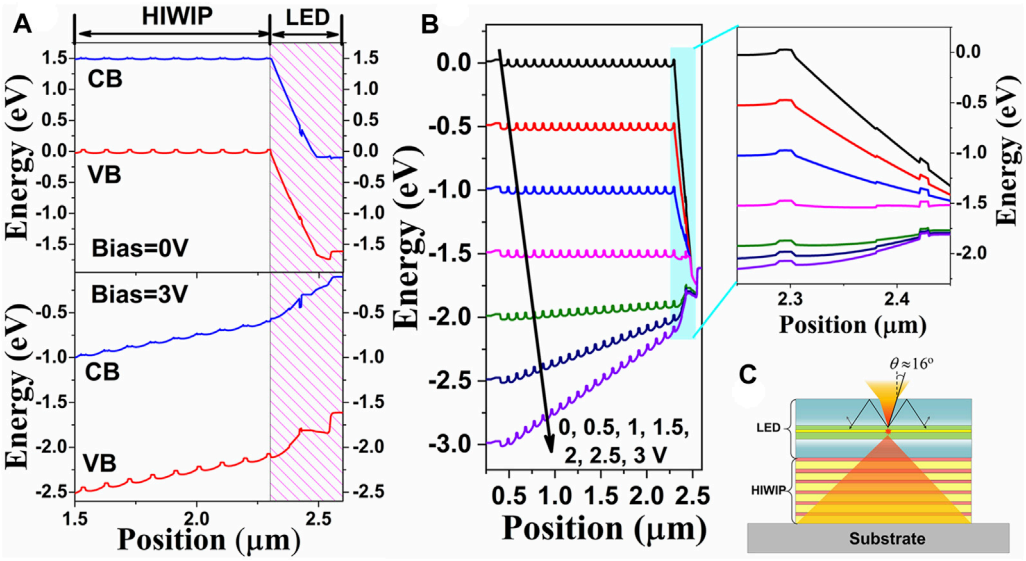

FIGURE 4 | (A) Calculated band diagram across the layer structure of the HIWIP-LED upconversion device under the bias of 0 and 3 V, with the top contact being grounded. **(B)** Calculated results of the valence band diagram under different bias voltage with the larger version of the LED band diagram. **(C)** Schematic diagram of the total internal reflection and critical angle at the air/semiconductor interface.

inside the HIWIP-LED, the upconversion efficiency could be expressed as $\eta = \eta_{HIWIP} \cdot \eta_e$, where η_{HIWIP} is the detection efficiency of the HIWIP and η_e is the external efficiency of the LED. One solution to improve the upconversion efficiency of the HIWIP-LED is to enhance the responsivity of the HIWIP part. However, the resonant cavity enhanced method [24] or bottom mirror enhanced method [25] for the single HIWIP detector is not suitable for the integrated HIWIP-LED device. The resonant cavity or bottom mirror will block the passage of light to the HIWIP part. Most importantly, the photon recycling in the cavity will cause severe distortion of the image. Optimization of the internal structure of the HIWIP may be an alternative approach to improve the detection efficiency [26]. But the thickened active region of the HIWIP may cause lateral diffusion of the carrier thereby inducing serious influence on imaging quality. Another way to improve the upconversion efficiency is to make the LED more efficient. According to the analysis of the preceding context, the internal efficiency of the LED could reach as high as >90%. But the *LEE* of the LED is only about 2.5%, which is mainly caused by the reflection at the semiconductor–air (GaAs/air) interface. As is shown in **Figure 4C**, the critical angle at the air/semiconductor interface is only about 16° corresponding to the escape probability of the emitted photon which is only 1.3% predicted by Snell's law [20]. The difference between the experiment and the calculation is mainly caused by the internal photon recycling. A dramatic increase of the *LEE* could be realized by optimizing the photon recycling process [27, 28], but at the same time the quality of the images will be significantly reduced [15]. In contrast, the most direct and effective method to improve the *LEE* is to change the shape of the semiconductor/air interface and include the use of roughened or textured semiconductor surfaces.

It has been reported that artificial nano- or micro-photonic structures or textured structures on the top of optoelectronic devices can help with light coupling [29, 30]. Wet chemical etching and photoelectrochemical etching can be used to create a substantial amount of surface roughness on III-V semiconductors. These etches are always crystallographic in nature, which makes the textured surface display pyramid-like structures. Both of the nano-pyramid and micro-pyramid have been widely used in photovoltaics, and the pyramid structure is proposed as both the light-trapping and antireflection technique to enhance the solar photon absorption of Si- or GaAs-based solar cells [31]. Conversely, if the textured surface or pyramid structure was used in light-emitting devices, the *LEE* will be significantly improved. Another coupling approach is the micro-lens on the top of the LED, which is also widely used in commercial LEDs as miniaturized extractors. The advantage of the micro-lens is that the critical angle increases from a small value to near 180°, and the influence of the internal total reflection is greatly reduced. Here, we carried out the 3D optical simulations with finite difference time domain (FDTD) method to calculate the *LEE* for devices with different geometries (micro-pyramid arrays and micro-lens arrays). Meanwhile, for the sake of comparison, the planar device structure and the planar structure with SiO_2 anti-reflection optical coating (thickness of the SiO_2 film is set as a quarter of the emitted wavelength) were also modeled (see the **Supplementary Materials** for simulation parameter settings and descriptions). The LED devices with different geometries are shown in **Figures 5A–D**, below which are the cross-sectional electric field intensities (|E|) for the corresponding geometries. The wavelength of the dipole source is set as 870 nm, and the periodic boundary condition is used.

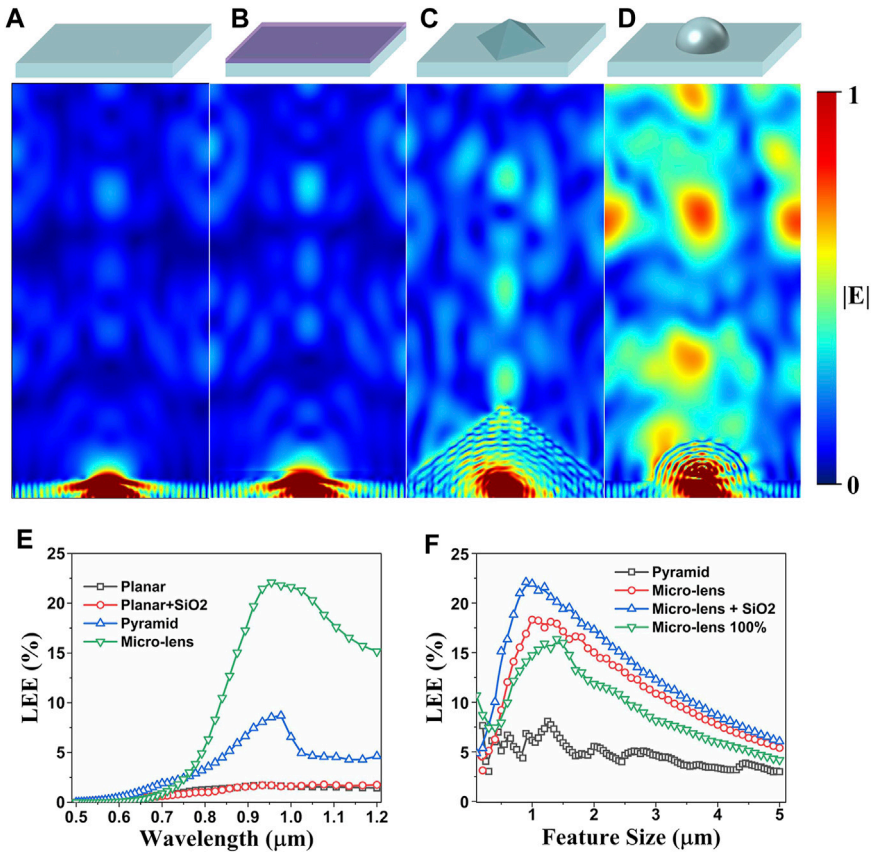

FIGURE 5 | The schematic diagram of the LED device with different geometries, also showing the corresponding optical distribution for the same dipole source with a certain wavelength of 870 nm. **(A)** Planar structure. **(B)** Planar structure with SiO_2 AR coating. **(C)** Micro-pyramid structure. **(D)** Micro-lens structure. **(E)** The calculated *LEE* as a function of the emitting wavelength for the devices with different geometries. **(F)** Optimization results for the pyramid and micro-lens structure. The feature size corresponds to the bottom side length of the pyramid or the radius of the hemi-sphere-like micro-lens.

It is easy to see that most of the light is confined inside the planar device in **Figures 5A, B**, which exhibits the |E| intensity for the device with SiO_2 anti-reflection optical coating, which presents a little enhancement of the *LEE*, although the result is not obvious. **Figure 5C** shows the |E| intensity for the device with the micro-pyramid arrays geometry; apparently the *LEE* of the device is improved, and more photons could escape from the active region of the LED. **Figure 5D** displays the |E| intensity for the device with the micro-lens arrays geometry; the significantly enhanced radiative propagation means that a large number of the photons could be extracted out of the device and the *LEE* is greatly improved. The calculated *LEE* as a function of the emitting wavelength for the devices with different geometries is shown in **Figure 5E**. The simulation periods are set as 4 μm for all the geometries, and the bottom side length of the pyramid and the radius of the hemisphere-like micro-lens are set as 1 μm. The simulation results reveal that the anti-reflective (AR) coating contributes a little to the *LEE*. The maximum *LEE* is improved five times in the micro-pyramid structure at the wavelength of 970 nm. And the micro-lens structure improves the *LEE* by one order of magnitude compared with the planar structure. For a certain emitting wavelength (870 nm), the pyramid and micro-lens structure should be optimized to maximize the *LEE*. **Figure 5F** gives the optimization results for the pyramid and micro-lens structure. The feature size corresponds to the bottom side length of the pyramid or the radius of the hemisphere-like micro-lens. The duty ratio for the pyramid (bottom side length to the period length) and micro-lens (diameter to the period length) are set as 100% and 50%, respectively. The micro-lens 100% represents the duty ratio which is set as 100%. It could be found that the micro-lens with a radius about 1 μm and a 50% duty ratio can effectively enhance the *LEE*, which increases to a factor of 2.5 compared with the pyramid structure. If the AR coating was applied in the micro-lens structure, the *LEE* will be further improved.

On the basis of the above simulation, the upconversion efficiency for the devices with different geometries could be determined. The calculated upconversion efficiencies for the devices with planar structure, micro-pyramid, micro-lens, and micro-lens combined with AR coating are shown in **Figure 6A**. We can find that the upconversion efficiency for the device with the micro-lens structure and SiO_2 AR coating is improved by an order of magnitude compared with the planar structure. The noise equivalent power (NEP) is a figure of merit for photodetectors. **Figure 6B** shows the calculated NEPs under different bias voltages at 3.5 K for the upconversion imaging

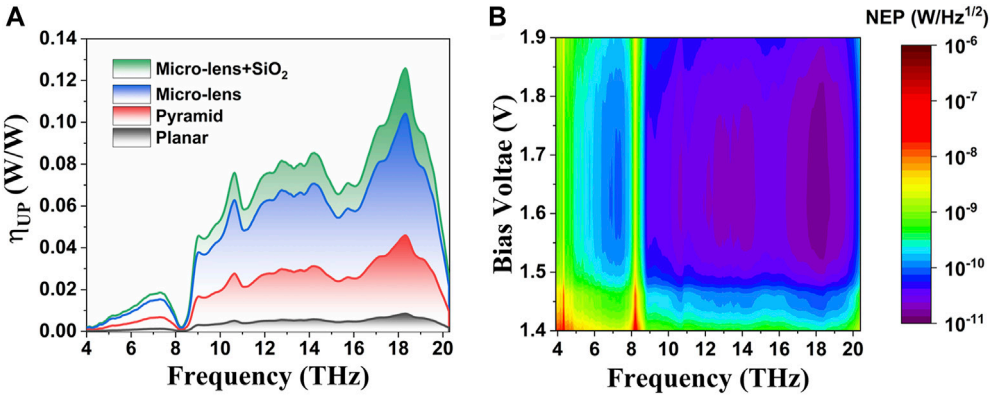

FIGURE 6 | (A) The calculated upconversion efficiencies for the devices with planar structure, micro-pyramid, micro-lens, and micro-lens combined with AR coating. **(B)** The calculated NEP under different bias voltages at 3.5 K for the upconversion imaging system with the optimal micro-lens structure and SiO_2 AR coating.

system with the optimal micro-lens structure and SiO_2 AR coating using **Eq. 3**.

$$NEP = \frac{i_n}{R} = \frac{e\lambda_{out}}{hcR_{HW}}\left[\left(4eg_{HW}i_{bg}\Delta f + 4eg_{HW}i_{dark}\Delta f\right) + \left(2ei_{bg}\Delta f + 2ei_{dark}\Delta f\right) + \frac{2e\Delta f}{\eta_{LED}\eta_{Si}}\left(i_{bg} + i_{dark}\right) + \frac{2ei_{dark,Si}\Delta f}{\left(\eta_{LED}\eta_{Si}\right)^2}\right]^{1/2} \quad (3)$$

where η_{Si} is the quantum efficiency of the Si CCD at the luminescence wavelength of the LED; η_{LED} is the external quantum efficiency of the LED, which is determined by the internal quantum efficiency and the *LEE* simultaneously; e is the elementary charge; g_{HW} is the gain in the HIWIP; i_{bg} is the background photocurrent of the 300 K radiation; i_{dark} is the device dark current; Δf is the system measurement bandwidth; and $i_{dark,Si}$ is the dark current of the Si CCD. The first item of the above equation is mainly determined by the HIWIP detector, the second item is mainly determined by the LED, and the last two items are mainly determined by the Si CCD.

The detailed calculation of the NEP could be found in the **Supplementary Materials** and Refs. [15, 32]. The bias voltage range start from the value of 1.4 V corresponds to the turn-on voltage of HIWIP-LED. We can find that the NEPs for all frequencies are almost below the level of 100 $pWHz^{-1/2}$ and the optimal value is about 14 $pWHz^{-1/2}$ at 18.4 THz in the bias range of 1.5–1.8 V. This value is close to the minimum NEP of the single HIWIP (12.4 $pWHz^{-1/2}$ [15]) and about one-half smaller than that of the HIWIP-LED device with planar structure (about 29 $pWHz^{-1/2}$ [15]).

CONCLUSION AND OUTLOOK

In this paper, we have reported a systematic investigation on the cryogenic-temperature performances of the LED part in HIWIP-LED devices, including EL spectra and the EL efficiency. Numerical calculations have been carried out to elaborate the radiative recombination mechanism in the quantum well and explain the internal quantum efficiency as well as the *LEE*. On this basis, we have further studied the operation mode of the HIWIP-LED and concluded that the *LEE* is the determining factor of the upconversion efficiency. Then, a numerical simulation has been performed to optimize the *LEE*. The calculated results show that a device with the micro-lens geometry structure could significantly improve the *LEE* of the LED thereby increasing the upconversion efficiency. An optimal upconversion efficiency value of 0.12 W/W and minimum NEP of 14 $pW/Hz^{1/2}$ are achieved using the micro-lens structure together with anti-reflection coating. This work not only gives the experimental results and theoretical explanations of LEDs at low temperatures but also clarifies that for a given upconversion device, the most direct way to improve the upconversion efficiency is to increase the *LEE* at the LED portion. The surface micro-lens coupling structure we proposed can increase the upconversion efficiency of HIWIP-LED by an order of magnitude, and the corresponding imaging performance NEP can be reduced to one-half of the previous value, which is a good improvement. Our theoretical work provides guidance for the experimental research of pixelless imaging. In addition, the working mechanism of the upconverter and the method of improving upconversion efficiency clarified in this article are also applicable to other MIR or NIR upconversion devices based on III-V compound semiconductors. This means that the efficiency of MIR and NIR upconversion devices and corresponding pixelless imaging performance will also be further improved, which is important for the development of larger area, higher resolution, and low-cost IR and THz imaging devices.

DATA AVAILABILITY STATEMENT

The raw data supporting the conclusions of this article will be made available by the authors, without undue reservation.

AUTHOR CONTRIBUTIONS

PB performed the research and wrote the paper. YZ and WS proposed the concept. YZ and WC supervised the project. NY contributed to the simulation. All authors discussed the results and co-wrote the article.

FUNDING

This work was supported by the Natural Science Foundation of China (12104061, U1730246, 1207424, and 911834011), Natural Science Foundation of Shanghai (19ZR1427000), Project funded by China Postdoctoral Science Foundation (2020M680458), and Open Project funded by Key Laboratory of Artificial Structures and Quantum Control (2020-03).

SUPPLEMENTARY MATERIAL

The Supplementary Material for this article can be found online at: https://www.frontiersin.org/articles/10.3389/fphy.2021.774524/full#supplementary-material

REFERENCES

1. Chen J, Tao J, Ban D, Helander MG, Wang Z, Qiu J, et al. Hybrid Organic/Inorganic Optical Up-Converter for Pixel-Less Near-Infrared Imaging. *Adv Mater* (2012) 24:3138–42. doi:10.1002/adma.201200587
2. Yang Y, Zhang YH, Shen WZ, Liu HC. Semiconductor Infrared Upconversion Devices. *Prog Quan Electron* (2011) 35:77–108. doi:10.1016/j.pquantelec.2011.05.001
3. Wu DM, García-Etxarri A, Salleo A, Dionne JA. Plasmon-enhanced Upconversion. *J Phys Chem Lett* (2014) 5:4020–31. doi:10.1021/jz5019042
4. Liu Q, Feng W, Yang T, Yi T, Li F. Upconversion Luminescence Imaging of Cells and Small Animals. *Nat Protoc* (2013) 8:2033–44. doi:10.1038/nprot.2013.114
5. Liu HC, Li J, Wasilewski ZR, Buchanan M. Integrated Quantum Well Intersub-Band Photodetector and Light Emitting Diode. *Electron Lett* (1995) 31:832–3. doi:10.1049/el:19950522
6. Liu HC, Allard LB, Buchanan M, Wasilewski ZR. Pixelless Infrared Imaging Device. *Electron Lett* (1997) 33:379–80. doi:10.1049/el:19970242
7. Liu HC, Gao M, Poole PJ. 1.5 [micro Sign]m Upconversion Device. *Electron Lett* (2000) 36:1300–1. doi:10.1049/el:20000915
8. Ban D, Luo H, Liu HC, Wasilewski ZR, Paltiel Y, Raizman A, et al. Midinfrared Optical Upconverter. *Appl Phys Lett* (2005) 86:201103. doi:10.1063/1.1921330
9. Fu ZL, Gu LL, Guo XG, Tan ZY, Wan WJ, Zhou T, et al. Frequency Upconversion Photon-type Terahertz Imager. *Sci Rep* (2016) 6:1–8. doi:10.1038/srep25383
10. Ban D, Luo H, Liu HC, SpringThorpe AJ, Glew R, Wasilewski ZR, et al. 1.5 to 0.87 [micro Sign]m Optical Upconversion Device Fabricated by Wafer Fusion. *Electron Lett* (2003) 39:1145–7. doi:10.1049/el:20030732
11. Luo H, Ban D, Liu HC, SpringThorpe AJ, Wasilewski ZR, Buchanan M, et al. 1.5 μm to 0.87 μm Optical Upconversion Using Wafer Fusion Technology. *J Vac Sci Technol A* (2004) 22(3):788–91. doi:10.1116/1.1689300
12. Ban D, Han S, Lu ZH, Oogarah T, SpringThorpe AJ, Liu HC. Near-infrared to Visible Light Optical Upconversion by Direct Tandem Integration of Organic Light-Emitting Diode and Inorganic Photodetector. *Appl Phys Lett* (2007) 90:093108. doi:10.1063/1.2710003
13. Ban D, Han S, Lu ZH, Oogarah T, SpringThorpe AJ, Liu HC. Organic-Inorganic Hybrid Optical Upconverter. *IEEE Trans Electron Devices* (2007) 54:1645–50. doi:10.1109/TED.2007.898462
14. Dupont E, Byloos M, Oogarah T, Buchanan M, Liu HC. Optimization of Quantum-Well Infrared Detectors Integrated with Light-Emitting Diodes. *Infrared Phys Tech* (2005) 47:132–43. doi:10.1016/j.infrared.2005.02.018
15. Bai P, Zhang Y, Wang T, Fu Z, Shao D, Li Z, et al. Broadband THz to NIR Upconversion for Photon-type THz Imaging. *Nat Commun* (2019) 10:1–9. doi:10.1038/s41467-019-11465-6
16. Allard LB, Liu HC, Buchanan M, Wasilewski ZR. Pixelless Infrared Imaging Utilizing a P-type Quantum Well Infrared Photodetector Integrated with a Light Emitting Diode. *Appl Phys Lett* (1997) 70:2784–6. doi:10.1063/1.119058
17. Dupont E, Byloos M, Gao M, Buchanan M, Song C-Y, Wasilewski ZR, et al. Pixelless thermal Imaging with Integrated Quantum-Well Infrared Photodetector and Light-Emitting Diode. *IEEE Photon Technol Lett* (2002) 14:182–4. doi:10.1109/68.980504
18. Zhang S, Wang TM, Hao MR, Yang Y, Zhang YH, Shen WZ, et al. Terahertz Quantum-Well Photodetectors: Design, Performance, and Improvements. *J Appl Phys* (2013) 114:194507. doi:10.1063/1.4826625
19. Jia JY, Wang TM, Zhang YH, Shen WZ, Schneider H. High-temperature Photon-Noise-Limited Performance Terahertz Quantum-Well Photodetectors. *IEEE Trans Thz Sci Technol* (2015) 5:715–24. doi:10.1109/TTHZ.2015.2453632
20. Ban D, Luo H, Liu HC, Wasilewski ZR, SpringThorpe AJ, Glew R, et al. Optimized GaAs⁄AlGaAs Light-Emitting Diodes and High Efficiency Wafer-Fused Optical Upconversion Devices. *J Appl Phys* (2004) 96:5243–8. doi:10.1063/1.1785867
21. Piprek J. Efficiency Droop in Nitride-Based Light-Emitting Diodes. *Phys Stat Sol (A)* (2010) 207:2217–25. doi:10.1002/pssa.201026149
22. Bai P, Zhang Y, Wang T, Shi Z, Bai X, Zhou C, et al. Cryogenic Characteristics of GaAs-Based Near-Infrared Light Emitting Diodes. *Semicond Sci Technol* (2020) 35:035021. doi:10.1088/1361-6641/ab6dbf
23. Ryu H-Y, Kim H-S, Shim J-I. Rate Equation Analysis of Efficiency Droop in InGaN Light-Emitting Diodes. *Appl Phys Lett* (2009) 95:081114. doi:10.1063/1.3216578
24. Zheng MM, Zhang YH, Shen WZ. Performance Optimization of Resonant Cavity Enhanced N-GaAs Homojunction Far-Infrared Detectors: A Theoretical Study. *J Appl Phys* (2009) 105:084515. doi:10.1063/1.3116726
25. Zhang YH, Luo HT, Shen WZ. Demonstration of Bottom Mirrors for Resonant-Cavity-Enhanced GaAs Homojunction Far-Infrared Detectors. *Appl Phys Lett* (2003) 82:1129–31. doi:10.1063/1.1553992
26. Bai P, Zhang YH, Guo XG, Fu ZL, Cao JC, Shen WZ. Realization of the High-Performance THz GaAs Homojunction Detector below the Frequency of Reststrahlen Band. *Appl Phys Lett* (2018) 113:241102. doi:10.1063/1.5061696
27. Schnitzer I, Yablonovitch E, Caneau C, Gmitter TJ. Ultrahigh Spontaneous Emission Quantum Efficiency, 99.7% Internally and 72% Externally, from AlGaAs/GaAs/AlGaAs Double Heterostructures. *Appl Phys Lett* (1993) 62:131–3. doi:10.1063/1.109348
28. Dupont E, Gao M, Buchanan M, Wasilewski ZR, Liu HC. Optimization of P-Doping in GaAs Photon-Recycling Light-Emitting Diodes Operated at Low Temperature. *Semicond Sci Technol* (2001) 16:L21–L23. doi:10.1088/0268-1242/16/5/101
29. Schubert EF. *Light-emitting Diodes*. New York: Cambridge University Press (2018).
30. Zhmakin AI. Enhancement of Light Extraction from Light Emitting Diodes. *Phys Rep* (2011) 498:189–241. doi:10.1016/j.physrep.2010.11.001
31. Shin S-R, Lee HB, Jin W-Y, Ko K-J, Park S, Yoo S, et al. Improving Light Extraction of Flexible OLEDs Using a Mechanically Robust Ag Mesh/ITO Composite Electrode and Microlens Array. *J Mater Chem C* (2018) 6:5444–52. doi:10.1039/C8TC01415A

32. Bai P, Zhang YH, Shen WZ. Infrared Single Photon Detector Based on Optical Upconversion at 1550 Nm. *Sci Rep* (2017) 7:1–12. doi:10.1038/s41598-017-15613-0

Conflict of Interest: The authors declare that the research was conducted in the absence of any commercial or financial relationships that could be construed as a potential conflict of interest.

Publisher's Note: All claims expressed in this article are solely those of the authors and do not necessarily represent those of their affiliated organizations, or those of the publisher, the editors and the reviewers. Any product that may be evaluated in this article, or claim that may be made by its manufacturer, is not guaranteed or endorsed by the publisher.

frontiers in Physics

REVIEW
published: 15 November 2021
doi: 10.3389/fphy.2021.751018

Research Progress on Terahertz Quantum-Well Photodetector and Its Application

*Dixiang Shao[1], Zhanglong Fu[1], Zhiyong Tan[1,2], Chang Wang[1,2], Fucheng Qiu[1,2], Liangliang Gu[3], Wenjian Wan[1] and Juncheng Cao[1,2]**

[1]Key Laboratory of Terahertz Solid-State Technology Shanghai Institute of Microsystem and Information Technology Chinese Academy of Sciences, Shanghai, China, [2]Center of Materials Science and Optoelectronics Engineering University of Chinese Academy of Sciences, Beijing, China, [3]School of Optical-Electrical and Computer Engineering University of Shanghai for Science and Technology, Shanghai, China

Compared with other typical terahertz (THz) detectors, the quantum-well photodetector (QWP) has the advantages of high detection sensitivity, fast response, mature fabrication, small size, and easy integration. Therefore, it is suitable for high-speed detection and imaging applications at the THz band. Researchers, both domestic and overseas, have systematically studied material design and device performance of the THz QWP. The design of the device is such that the peak frequency error is within 8%, the maximum peak responsibility is 5.5 A/W, the fastest response speed is 6.2 GHz, the best noise equivalent power is ~10^{-13} W/Hz$^{0.5}$, and the spectrum range is 2.5–6.5 THz. In this article, firstly the basic principles and theoretical calculations of the THz QWP are described, and then the research progress of the THz QWP in our research group at imaging and communication is reviewed, which looks forward to its future development.

Keywords: terahertz detection, terahertz imaging, terahertz communication, terahertz, terahertz quantum-well photodetector

OPEN ACCESS

Edited by:
Xinke Wang,
Capital Normal University, China

Reviewed by:
Qiye Wen,
University of Electronic Science and Technology of China, China
Changlong Liu,
University of Chinese Academy of Science, China

****Correspondence:***
Juncheng Cao
jccao@mail.sim.ac.cn

Specialty section:
This article was submitted to Optics and Photonics, a section of the journal Frontiers in Physics

Received: *31 July 2021*
Accepted: *20 September 2021*
Published: *15 November 2021*

Citation:
Shao DX, Fu ZL, Tan ZY, Wang C, Qiu FC, Gu LL, Wan WJ and Cao JC (2021) Research Progress on Terahertz Quantum-Well Photodetector and Its Application. Front. Phys. 9:751018. doi: 10.3389/fphy.2021.751018

INTRODUCTION

1 Terahertz Quantum-Well Photodetector

Terahertz (THz) waves are electromagnetic waves falling between the millimeter and infrared [1, 2] spectrum as shown in **Figure 1**. This region ranges in frequency from about 0.1 to 10 THz (30–1000 μm). It has the advantages of strong dielectric penetration and weak ionization. It has a broad application prospect in material research, environmental monitoring, nondestructive testing, medical diagnosis, wireless communication, and other fields.

1.1 Working Principle

THz detectors have been studied since 1960s [3]. THz quantum-well photodetector (QWP) is the natural expansion of quantum-well infrared detector (QWIP) at the THz band [4–7]. The THz QWP material system is GaAs/AlGaAs, which is usually composed of many quantum wells. When THz wave radiation is incident on the THz QWP, the electrons in the bound state of the quantum well absorb THz photons and transit to the continuous state, forming a photocurrent under the external bias voltage, so as to complete the detection of the THz waves [8]. Compared with the QWIP, the energy between the bound and the continuous state in the THz QWP is just 20 meV, and the doping in the quantum well is lower, which directly leads to the decreasing absorption efficiency and the responsibility. In 2004, H.C. Liu and coworkers [9] developed a quantum-well detector working in the THz band by reducing the barrier height and doping in the quantum well. Reference 40 used the THz QWP to demonstrate THz communication. Professor Hu

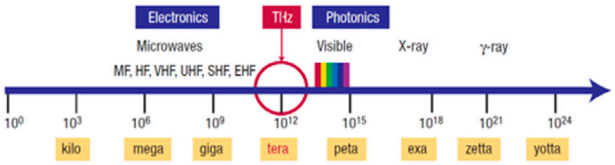

FIGURE 1 | The spectrum of THz wave [2].

Qing, an authoritative expert in the THz field at the Massachusetts Institute of Technology, believes that THz QWP may improve the speed and sensitivity of THz imaging. The main problem of the THz QWP [10, 11] is that the energy difference between the first bound sub-band in the quantum well and the quasi-continuous state is less than 30 meV. The signal-to-noise ratio (SNR) of the device needs to be improved by limiting the thermally excited electrons, such that the device needs to work at a low temperature (<20 K). According to the differences in the active structure, internal charge distribution, and carrier transport mode of the detector, the QWP is divided into photoconductive detector and photovoltaic detector. The active region and conduction band structure of the photoconductive THz QWP are shown in **Figure 2**.

1.2 Theoretical Design

Due to the high degree of freedom of the multiparticle system, the many-body effect can only be approximated [12, 13]. Considering the interaction between electrons, we established on the basis of density functional theory, combined with the local density approximation (LDA), meanwhile considering including exchange self-energies effect, depolarization-shift effect, and excitonic effect, between the depolarization and exciton interaction contributes to the optical many-body effect. The many-body effect is an electronic collective effect. When the wavelength is extended to the THz region because of the small carrier transition energy involved in the detection process, the influence of the many-body effect cannot be ignored, which needs to be considered during device design.

The THz QWP design needs to satisfy the following **Equation (9)** [14], [15]:

1) The Schrodinger equation is as follows:

$$-\frac{\hbar^2}{2}\frac{d}{dz}\frac{1}{m^*(z)}\frac{d}{dz}\psi(z)+V(z)\psi(z)=E\psi(z), \quad (1)$$

$$V(z)=V_0(z)+V_{ex}(z)+V_H(z), \quad (2)$$

where, $V_0(z)$ is the original potential distribution without extra electric field and doping:

$$V_0(z)=\begin{cases}V_w=0\\ V_B=0.67\times 1.247x=0.12532eV\end{cases}, \quad (3)$$

$V_{ex}(z)$ in **Equation 2** is the potential distribution caused by the extra electric field.

$$V_{ex}(z)=|e|F(L_P-z)=|e|\times\frac{0.064}{L_p}\times(L_P-z) \quad (4)$$

where, F is the extra field intensity, e is the electron charge, and $L_p=52.4nm$ is the whole-period width. $V_H(z)=-|e|\varphi(z)$, $\varphi(z)$ is the field potential caused by the doped impurities.

The Poisson equation is as follows:

$$\frac{d}{dz}\left[\varepsilon(z)\frac{d}{dz}\right]\varphi(z)=-|e|\left[N_D(z)-N_A(z)+p(z)-n(z)\right], \quad (5)$$

where, ε(z) is the dielectric constant of the material,

$$\begin{cases}\varepsilon_w=12.9\varepsilon_0\\ \varepsilon_B=(12.9-2.84x)\varepsilon_0=12.474\varepsilon_0\end{cases} \quad (6)$$

where, ε_0 is the dielectric constant of the material. n(z) and p(z) are, respectively, the concentrations of electrons and holes. For the type N-doped quantum-well structure, where N_D(z) and N_A(z) are respectively the concentrations of donor impurities and acceptor impurities; n(z) and p(z) are respectively the concentrations of electrons and holes; concentration effect can be ignored:

$$\frac{d}{dz}\left[\varepsilon(z)\frac{d}{dz}\right]\phi(z)=-|e|\left[N_D(z)-n(z)\right] \quad (7)$$

2) For the THz QWP (consider many-body), the Hamilton function is as follows:

$$H=p\frac{1}{2m^*(z)}p+V_{QW}(z)+V_H(z)+V_{XC}(z) \quad (8)$$

where, p is the momentum, V_{QW} is the limited potential of the well, V_H is the Hartley potential, and V_{xc} is the exchange correlation potential; m^* is the effective quality of the electrons. The expression of V_{xc} is as follows:

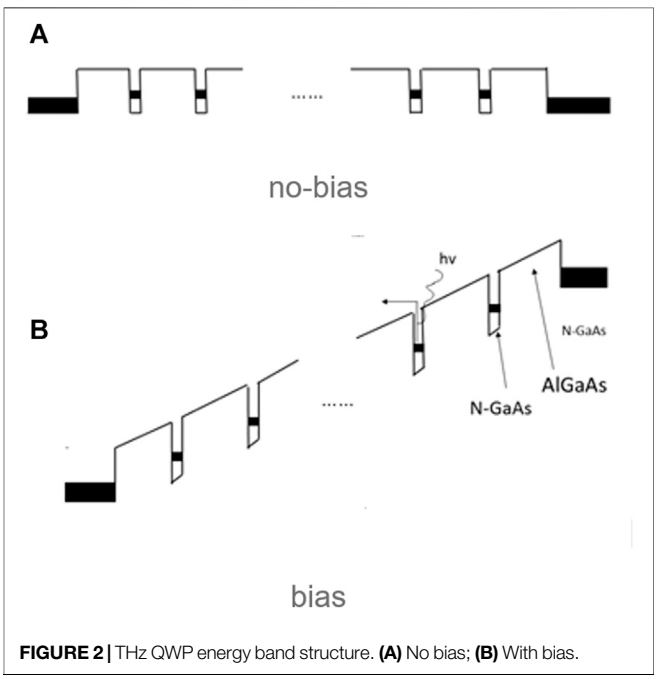

FIGURE 2 | THz QWP energy band structure. **(A)** No bias; **(B)** With bias.

$$V_{xc}(z) = \frac{e^2}{4\pi^2 \epsilon a_B r_s(z)} \sqrt[3]{\frac{9}{4}}\pi \times \left\{1 + 0.0545 r_s(z) In\left[1 + \frac{11.4}{r_s(z)}\right]\right\} \tag{9}$$

Considering the condition of the Schrodinger equation,

$$\left\{-\frac{h^2}{2}\frac{\partial}{\partial_z}\left[\frac{1}{m^*(z)}\frac{\partial}{\partial_z}\right] + V_{QW}(z) + V_H(z) + V_{xc}(z)\right\}\varphi_{l,k_z}(z) = \varepsilon_{l,k_z}\varphi_{l,k_z}(z) \tag{10}$$

Electronic charge is $E_{k,l} = \frac{h^2 k_H^2}{2m^*} + \epsilon_{k_z,l}$,
Electronic density is $\rho_e(z) = |e|\sum_{k,l} f(E_{k,l}, \varepsilon_F, T)|\varphi_{l,k_z}(z)|^2$, where, e is the electron, f is the Fermi distribution function, and T is the temperature.

When the electron density is known, the Hartley potential can be obtained by solving the Poisson equation $\frac{\partial^2}{\partial_{Z^2}} V_H(z) = \frac{\rho_e(z) - \rho_d(z)}{\varepsilon}$

In this study, researches were carried out based on the density functional theory. When the energy dispersion relations and wave functions can be obtained by Fermi's golden rule, the relationship between them is as follows:

$$\begin{aligned}\eta(w) &= \frac{\pi e^2}{\varepsilon_0 c n_0 \omega m^{*2}} \sum_j \int \frac{dk}{(2\pi)^3} |< j|p_z|0 >|^2 \left[f(E_{k,0}, \varepsilon_F, T) - f\left(E_{k,j}, \varepsilon_F, T\right)\right]\delta\left(\Delta\tilde{E}_{kl,0} - h\omega\right)\Delta\tilde{E}^2_{k,1,0} \\ &= \Delta E^2_{k,l,0}\left(1 + \alpha_{k,l,0} - \beta_{k,l,0}\right), \alpha_{k,l,0} \\ &= \frac{2e^2\rho_{2D}}{\varepsilon \Delta E_{k,l,0}} \int dz \left[\int_{-\infty}^{z} dz' \varphi_{k_z,l}(z')\varphi_{k_z,0}(z')\right]^2, \beta_{k,l,0} \\ &= -\frac{2\rho_{2D}}{\Delta E_{k,l,0}} \int dz \varphi_{k_z,l}(z)^2 \varphi_{k_z,0}(z)^2 \frac{\partial V_{xc}[\rho(z)]}{\partial \rho(z)}.\end{aligned} \tag{11}$$

2 TERAHERTZ QUANTUM-WELL PHOTODETECTOR IMAGING TECHNOLOGY

Compared with electromagnetic waves in other bands, the THz waves have many excellent characteristics, such as good penetrability to nonpolar substances, characteristic spectrum of biological macromolecules, and non-damage to human body [15–21]. THz waves have been used for imaging applications since 1990. The principle of THz imaging [22–26] is to obtain a THz image of the sample by collecting the amplitude, phase, and polarization information reflected or transmitted at different positions of the sample, and transforming the collected THz information into parameters that can reflect the physical and chemical properties of the sample, then corresponding to the spatial position parameters of the sample, combining with image restoration technology. THz imaging has many classification methods. According to the different ways of acting on the sample, it can be divided into transmission imaging and reflection imaging. According to the different working modes of the THz light source, it can be divided into continuous- wave imaging and pulse imaging. According to the imaging speed, it can be divided into scanning imaging and real-time imaging. According to whether the hidden wave effect is considered, it can be divided into far-field imaging and near-field imaging.

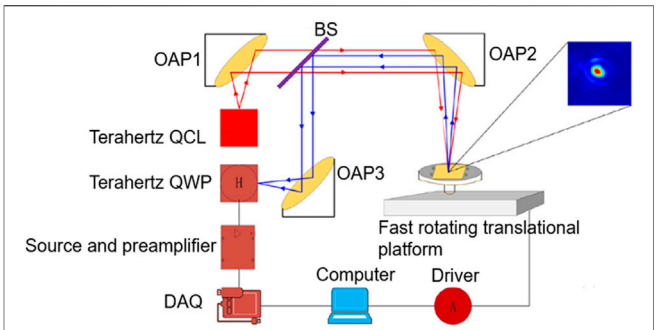

FIGURE 3 | The fast scanning imaging system [27].

2.1 Imaging Modes

2.1.1 Scanning Imaging

Tan Zhiyong et al. from the Shanghai Institute of Microsystem and Information Technology (SIMIT) developed the fast scanning imaging system based on THz quantum devices [27]. The system used 4.3 THz quantum cascade laser (QCL) as the THz light source and a high-speed THz QWP with matching frequency. A rotating scanning platform was used to realize rapid scanning of the sample (**Figure 3**), so as to improve the imaging speed of the system. The system used a new pulse signal acquisition method and a practical image restoration program to obtain THz images of blades and shaving blades under different shelters within 5 s. In addition, the system also used an image processing algorithm to deal with the noise problem during practical application, which improves the quality of the THz images.

2.1.2 Reflection Imaging

Wang Chang from SIMIT set up a reflective THz fast confocal imaging system [28](**Figure 4**). The THz light source used was 4.3 THz QCL, with a THz QWP and fast-rotating translation platform to complete the fast scanning imaging of the sample. The imaging optical path adopts confocal microscopy. Two 200-μm pinholes were placed at the two conjugate focuses to filter out the scattered light of the system and improve the spatial resolution of the imaging system. Finally, lateral resolution better than 110 μm and axial resolution about 320 μm were achieved. The two-dimensional THz imaging of common metal samples and toothpicks was carried out by using the rapid confocal microscopy imaging system, and a high-contrast image of the samples was obtained within 5 s. Finally, using the high axial resolution of the system, three-dimensional slice imaging of the sample was carried out. The imaging results are clearly visible, and the thickness of the sample could be measured.

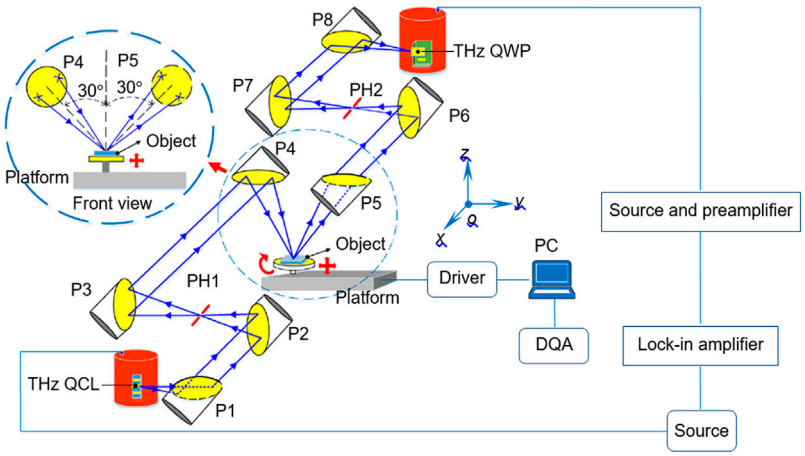

FIGURE 4 | The fast THz confocal microscopic imaging system [28].

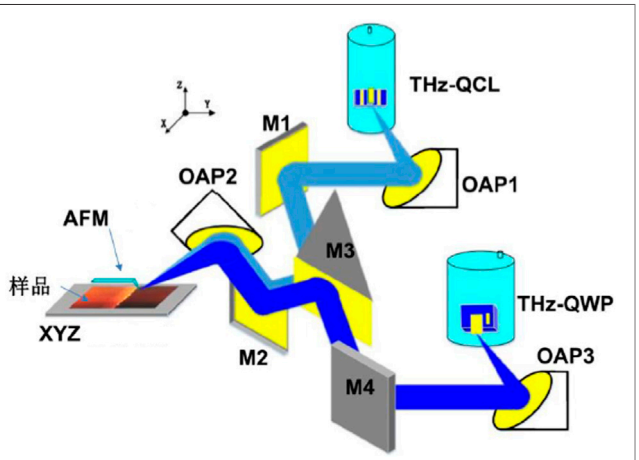

FIGURE 5 | The THz scanning near-field optical microscopic imaging system [30].

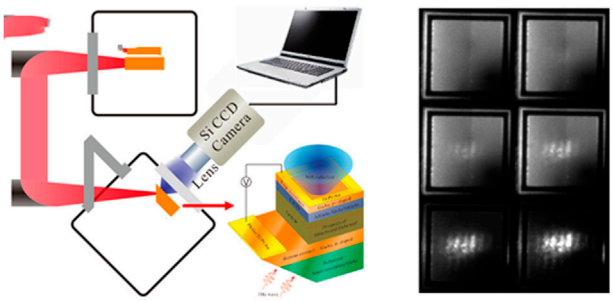

FIGURE 6 | (A) Set-up for THz pixel-less imaging system; **(B)** The focal laser spots of THz QCL imaged by using THz QWP-LED [31].

2.1.3 Near-Field Imaging

Qiu Fucheng [30] established a scattering-type scanning near-field optical microscopy system based on the THz QCL and THz QWP. Using the self-developed THz QCL and THz QWP, the low-bias continuous-wave THz QCL laser source module and THz QWP high-sensitivity detection module were developed for near-field microscopic imaging, and the scattering-type scanning near-field optical microscopic imaging system was built. The demodulation of the THz near-field signal was completed by using signal high-order demodulation technology. The THz imaging system with THz scattering-type scanning near-field optical microscopy was used to image pure gold samples with scratches. The minimum resolution of the system was calculated to be about 200 nm (**Figure 5**).

2.1.4 Pixel-less Imaging

In 2016, Z.L. Fu et al. from SIMIT fabricated the THz frequency up-conversion device (THz QWP-LED) formed by stacking THz QWPs and the light-emitting diode (LED) and using this device for pixel-less imaging. The 45-degree coupled THz QWP-LED imaging system is shown in **Figure 6A** The peak frequency is 5.2 THz, the peak responsibility is 0.22 A/W, the noise equivalent power is 5.2×10^{-12} W/Hz$^{0.5}$, and the operating temperature is 3.5 K. The frequency point of THz QCL RF is 4.3 THz. **Figure 6B** shows the imaging results of THz QWP-LED for THz QCL with different laser powers. The imaging resolution is better than 0.05 mm; the SNR is better than 10,000; and the imaging time is 1 s. At present, the one-dimensional and two-dimensional metal grating coupling devices with normal incidence have achieved real-time imaging. The two-dimensional metal grating coupling device can rapidly image the THz QCL laser spot within 10 μs. The energy of the imaging spot is Gaussian distribution, which is basically consistent with the results of long imaging time. This experiment shows that the frequency up-conversion device based on THz QWP has high-resolution and high-speed imaging ability.

2.2 Imaging Applications

Terahertz is used in various imaging scenes, such as in intelligence, security, crime detection, biology, and medicine

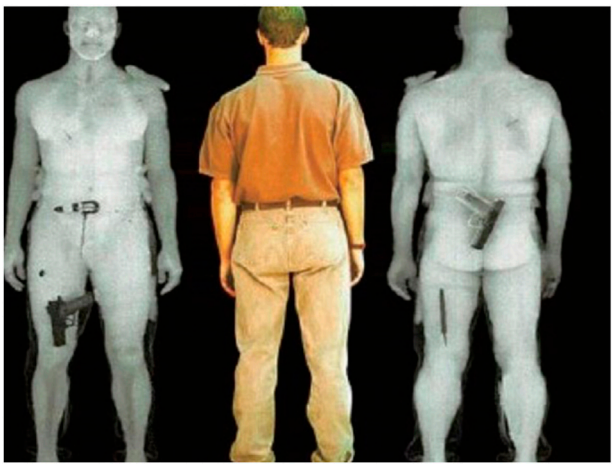

FIGURE 7 | L3 security and detection systems [32].

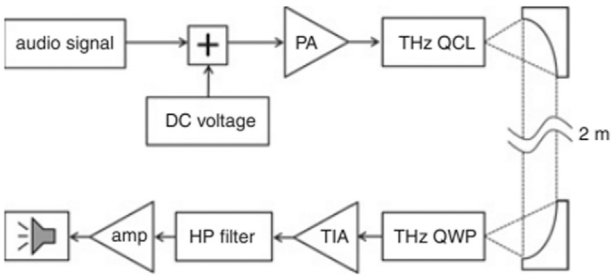

FIGURE 8 | THz audio communication system [36, 37].

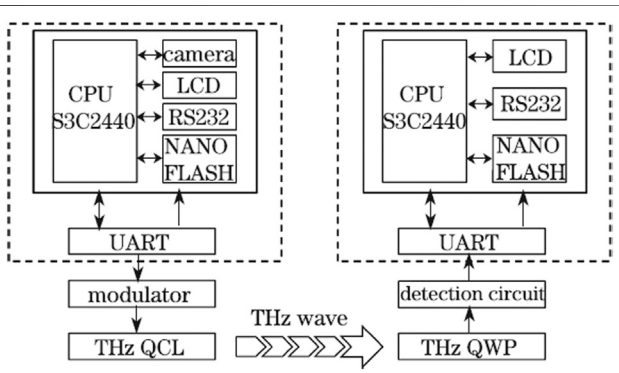

FIGURE 9 | THz communication experiment demonstration system [38].

[32–35]. At present, some THz passive imaging security products have been released, such as the ThruVision series released by Digital Barriers. It works at 0.25 THz; the detection distance is 4–10 m; and the imaging speed can reach 6 frames/s. The device can effectively compensate for the limitations of slightly poor light transmittance, macromolecules that cannot penetrate, imaging contrast, and so on when visible light and X-rays are used for imaging. The application of THz imaging can supplement these disadvantages. THz waves have no ionization characteristics, and they can safely and nondestructively detect the human body through clothing. Therefore, these can be used for human security and the security of some prohibited items (**Figure 7**), and also for the identification of ancient cultural relics. The most popular is THz tomography (THz CT), which can scan molecules such as materials and samples.

In the field of medicine, THz radiation is used for low-energy, nondestructive detection and minimizes radiation damage to the human body. Compared with X-rays, THz waves do little damage to cells and objects and can be applied for organ identification and in gene research. They can also be used in dental treatment, examination of skin cancer and other diseases, real-time imaging in surgery, medical diagnosis, biomedical engineering, and other medical fields.

In terms of environmental monitoring, THz waves can analyze and characterize the chemical components of solid, liquid, gas, and other states. It can also be used for pollutant detection, such as compound leakage, problems caused by microorganisms, food quality problems, and the detection of harmful substances in decoration materials.

3 TERAHERTZ QUANTUM-WELL PHOTODETECTOR COMMUNICATION

Terahertz waves have great potential in high spectrum bandwidth, more information can be carried, low photon energy, and high security, which has the significant advantage of the future communication to achieve ultra-wideband and high rate [35]. Compared with microwave frequency communication, terahertz for high-speed communications application has a very rich frequency resource, has a workable bandwidth as high as dozens of GHz, and is the sixth generation of carrier wave communication technology.

In 2009, H.C. Liu group of the Institute of Microstructure Science of the National Research Institute of Canada built a THz communication system based on THz QCL and THz QWP and realized audio signal transmission at 3.8 THz frequency points. Other researchers also actively follow up the wireless communication project research based on THz QCL and THz QWP and carry out the demonstration experiment of using THz carrier to transmit analog audio signals with THz QCL as the transmitting source and THz QWP as the receiver. The frequency point of THz waves is 4.1 THz. The communication system using THz QCL and THz QWP as transmitter and detector, respectively, has great development potential.

Tan Zhiyong from SIMIT demonstrated a wireless transmission system of THz waves with a transmission distance of 2 m (**Figure 8**) and detailed the circuit design of the transmitter and receiver. The system uses THz QCL working in continuous-wave mode as the transmitter and THz QWP as the detector. By means of intensity modulation/direct detection, we use this system to transmit analog signals such as sine wave,

FIGURE 10 | Video display at transmitter and receiver [39].

triangle wave, and audio signal. The system is capable of transmitting signals at a −3 dB cutoff frequency of about 750 kHz. Theoretically, both THz QCL and THz QWP have modulation and detection bandwidths of tens of GHz if the circuit design and packaging of the devices are optimized. But in our experiment, the modulation bandwidth is mainly limited by the external modulation circuit and a detection circuit.

Gu Li et al. from SIMIT used THz QCL and THz QWP working in continuous mode to build the THz communication system, as shown in **Figure 9**. In this system, the digital signal to be transmitted from the signal generator is sent to the drive circuit to drive THz QCL, and the radiated THz light is transmitted through the optical path and is detected at the receiving end of the THz QWP. The THz QWP converts the received THz light into photocurrent of corresponding intensity, and the receiving end circuit amplifies the photocurrent and converts it into voltage signal, which is output in the oscilloscope.

The framework of the THz wave wireless communication system with transmission distance of 2.2 and 6 m, using THz QCL as transmitter and THz QWP as a detector, is presented in **Figure 10**. The experimental results show that the rate of the 2.2-m communication system is less than 16 Mbps and the bit error rate is 0. The rate is less than 22 Mbps, and the error rate is less than 10^{-3}. The rate of the 6-m communication system is less than 8 Mbps, and the bit error rate of the transmission system is 0. The maximum transmission rate can reach 14 Mbps. Meanwhile, the OOK modulation real-time digital video transmission is realized by using the 2.2-m THz wireless communication link platform. The transmission rate is 5 Mbps, and the video signal transmission is stable. The video picture can be played smoothly on the display screen of both the transmitter and the receiver.

4 CONCLUSION

THz technology is a very important cross-cutting frontier, showing enormous potential application and practical value in astrophysics, plasma physics, spectroscopy, biology, medical imaging, environmental science, and other fields. In this article, the new terahertz detector, THz QWP, is reviewed. The development history, design principle, imaging application, and communication application of the detector are introduced. The THz QWP imaging system indicators are resolution, area, speed, and SNR. In the future, we can study the influence of off-axis parabolic mirrors with different parameters and sub-millimeter holes of different sizes on the spatial resolution of the system, so that the spatial resolution of the imaging system can break through the diffraction limit. In the mechanical scanning module, the accuracy of mechanical scanning can be optimized and the scanning range of mechanical scanning can be improved by controlling image distortion and improving the size of the imaging area. The imaging speed can be further improved by increasing the scanning speed and data acquisition speed. The SNR of imaging is mainly limited by the stability of the light path, stability of light source power, power of the light source, and sensitivity of the detector. Developing high-performance THz devices (lasers and detectors) to solve THz signal modulation and signal processing is the key to THz communication research. In the future, through the efforts of researchers, THz QWPs will become the mainstream detector of THz just as the corresponding band of QIWP and promote the development of THz technology and application.

AUTHOR CONTRIBUTIONS

DS proposed and wrote this manuscript; ZF, ZT, CW modified this manuscript; FQ, LG, WW performed the experiment; JC helped perform the analysis with constructive discussions.

FUNDING

This work was supported by the National Key R&D Program of China (2017YFF0106302, 2017YFA0701005, and 2018YFB1801502), the National Natural Science Foundation of China (Grant Nos. 61927813, 61975225, 61775229, 61704181, and 61875220), and the Fundamental Frontier Scientific Research Program of the Chinese Academy of Sciences (ZDBS-LY-JSC009).

REFERENCES

1. Lee YS. Principles of Terahertz Science and Technology. *Masayoshi Tonouchi, 2007 Nat Photon* 1 (2009): 97. doi:10.1007/978-0-387-09540-0
2. Ferguson B, and Zhang X-C. Materials for Terahertz Science and Technology. *Nat Mater* (2002) 1(1):26–33. doi:10.1038/nmat708
3. Schneider H, and Liu HC. *Quantum Well Infrared Photodetectors: Physics and Applications*. Berlin: Springer (2006).
4. Cao JC. *Semiconductor Terahertz Source Detector and Application*. Beijing: Science Press (2012). p. 1.
5. Fu Z, Li R, Li H, Shao D, and Cao J. Progress in Biomedical Imaging Based on Terahertz Quantum Cascade Lasers. *China laser* (2020) 47(2):0207014. doi:10.3788/cjl202047.0207014

6. Zhiyong T, and Juncheng C. Photoelectric Characterization Technique Based on Terahertz Semiconductor Quantum-Well Devices and its Applications. *China laser* (2019) 46(6):0614004. doi:10.3788/cjl201946.0614004
7. Levine BF. Quantum-well Infrared Photodetectors. *J Appl Phys* (1993) 74: R1–R81. doi:10.1063/1.354252
8. Liu HC, Buchanan M, and Wasilewski ZR. How Good Is the Polarization Selection Rule for Intersubband Transitions. *Appl Phys Lett* (1998) 72(14): 1682–4. doi:10.1063/1.121151
9. Liu HC, Song CY, SpringThorpe AJ, and Cao JC. Terahertz Quantum-Well Photodetector. *Appl Phys Lett* (2004) 84(20):4068–70. doi:10.1063/1.1751620
10. Cao JC. Terahertz Semiconductor Detectors (In Chinese). *Physics* (2006) 35(11):953–956. doi:10.3321/j.issn:0379-4148.2006.11.013
11. Liu HC, Luo H, Song Cy., Wasilewski ZR, SpringThorpe AJ, and Cao JC. Terahertz Quantum Well Photodetectors. *IEEE J Select Top Quan Electron.* (2008) 14(2):374–7. doi:10.1109/jstqe.2007.910710
12. Shao D, Guo X, Zhang R, Wang F, Fu Z, Wang H, et al. Influence of Many-Body Effect on Terahertz Quantum Well Photodetectors. *Acta Opt* (2017) 37(10):1004001. doi:10.3788/aos201737.1004001
13. Guo XG, Tan ZY, Cao JC, and Liu HC. Many-body Effects on Terahertz Quantum Well Detectors. *Appl Phys Lett* (2009) 94(20):201101. doi:10.1063/1.3134485
14. Zhang R, Fu ZL, Gu LL, Guo XG, and Cao JC. Terahertz Quantum Well Photodetectors with Reflection-Grating Couplers. *Appl Phys Lett* (2014) 105(23):231123. doi:10.1063/1.4904221
15. Zhang R, Shao DX, Fu ZL, Wang HX, Zhou T, Tan ZY, et al. Terahertz Quantum Well Photodetectors with Metal-Grating Couplers. *IEEE J Select Top Quan Electron.* (2017) 23(4):1–7. doi:10.1109/jstqe.2016.2608618
16. Abbott D, and Zhang XC. Special Issue on T-Ray Imaging, Sensing, and Retection. *Proc IEEE* (2007) 95(8):1509–13. doi:10.1109/jproc.2007.900894
17. Hu BB, and Nuss MC. Imaging with Terahertz Waves. *Opt Lett* (1995) 20(16): 1716–8. doi:10.1364/ol.20.001716
18. Shi SC, Paine S, Yao QJ, Lin ZH, Li XX, Duan WY, et al. Terahertz and Far-Infrared Windows Opened at Dome A in Antarctica[J]. *Nat Astron* (2016) 1: 0001. doi:10.1038/s41550-016-0001
19. Luukanen A, Appleby R, Kemp M, and Salmon N. Millimeter-wave and Terahertz Imaging in Security Applications. In: KE Peiponen, A Zeitler, and GM Kuwata, editors. *Terahertz Spectroscopy and Imaging*. Berlin, Heidelberg: Springer (2012). p. 491–520. doi:10.1007/978-3-642-29564-5_19
20. Liu HC, Buchanan M, and Wasilewski ZR. How Good Is the Polarization Selection Rule for Intersubband Transitions. *Appl Phys Lett* (1998) 72(14): 1682–4. doi:10.1063/1.121151
21. Planken PCM, and Bakker HJ. Towards Time-Resolved THz Imaging. *Appl Phys A: Mater Sci Process* (2004) 78:465–9. doi:10.1007/s00339-003-2405-0
22. Dean P, Valavanis A, Keeley J, Bertling K, Lim YL, Alhathlool R, et al. Terahertz Imaging Using Quantum cascade Lasers-A Review of Systems and Applications. *J Phys D: Appl Phys* (2014) 47(37):374008. doi:10.1088/0022-3727/47/37/374008
23. Chan WL, Deibel J, and Mittleman DM. Imaging with Terahertz Radiation. *Rep Prog Phys* (2007) 70:1325–79. doi:10.1088/0034-4885/70/8/r02
24. Watanabe Y, Kawase K, Ikari T, Ito H, Ishikawa Y, and Minamide H. Component Spatial Pattern Analysis of Chemicals Using Terahertz Spectroscopic Imaging. *Appl Phys Lett* (2003) 83:800–2. doi:10.1063/1.1595132
25. Dobroiu A, Yamashita M, Ohshima YN, Morita Y, Otani C, and Kawase K. Terahertz Imaging System Based on a Backward-Wave Oscillator. *Appl Opt* (2004) 43:5637–46. doi:10.1364/ao.43.005637
26. Tan Z, Li H, Wan W, Fu Z, Wang C, and Cao J. Direct Detection of a Fast Modulated Terahertz Light with a Spectrally Matched Quantum-well Photodetector. *Electron Lett* (2017) 53(2):91–3. doi:10.1049/el.2016.3099
27. Qiu F, Tan Z, Fu Z, Wan W, Li M, Wang C, et al. Reflective Scanning Imaging Based on a Fast Terahertz Photodetector. *Opt Commun* (2018) 427:170–4. doi:10.1016/j.optcom.2018.06.030
28. Qiu FC, Fu YZ, Wang C, Tan ZY, Fu ZL, Wan WJ, et al. Fast Terahertz Reflective Confocal Scanning Imaging with a Quantum cascade Laser and a Photodetector. *Appl Phys B* (2019) 125(5):86. doi:10.1007/s00340-019-7198-8
30. Qiu FC. *Fast Microscope Research Based on Terahertz Quantum Devices [D]*. University of Chinese Academy of Sciences (2020).
31. Fu ZL, Gu LL, Guo XG, Tan ZY, Wan WJ, Zhou T, et al. Frequency Up-Conversion Photon-type Terahertz Imager. *Sci Rep* (2016) 6:25383. doi:10.1038/srep25383
32. Hou D, Li X, Cai J, Ma Y, Kang X, Huang P, et al. Terahertz Spectroscopic Investigation of Human Gastric normal and Tumor Tissues. *Phys Med Biol* (2014) 59(18):5423–40. doi:10.1088/0031-9155/59/18/5423
33. Shiraga K, Ogawa Y, Suzuki T, and Naoshi K. Characterization of Dielectric Responses of Human Cancer Cells in the Terahertz Region. *J Infrared, Millimeter, Terahertz Waves* (2014) 35(5):493–502. doi:10.1007/s10762-014-0067-y
34. Wallace VP, Fitzgerald AJ, Pickwell E, and Richard J. Pulsed Spectroscopy of Human Basal Cell Carcinoma. *Appl Spectrosc* (2006) 60(10):1127–33. doi:10.1366/000370206778664635
35. Kleine-Ostmann T, and Nagatsuma T. A Review on Terahertz Communications Research. *J Infrared Milli Terahz Waves* (2011) 32(2): 143–71. doi:10.1007/s10762-010-9758-1
36. Chen Z, Tan ZY, Han YJ, Zhang R, Guo XG, Li H, et al. Wireless Communication Demonstration at 4.1 THz Using Quantum cascade Laser and Quantum Well Photodetector. *Electron Lett* (2011) 47:1002. doi:10.1049/el.2011.1407
37. Chen Z, and Cao J-C. Channel Characterization at 120 GHz for Future Indoor Communication Systems. *Chin Phys. B* (2013) 22:059201. doi:10.1088/1674-1056/22/5/059201
38. Zhen Chen ZC, Li Gu LG, Zhiyong Tan ZT, Chang Wang CW, and Juncheng Cao JC. Real-time Video Signal Transmission over a Terahertz Communication Link. *Chin Opt Lett* (2013) 11:112001–3. doi:10.3788/col201311.112001
39. Gu L, Tan ZY, Wu QZ, Wang C, and Cao JC. Twenty Mbit/s Wireless Communication-Demonstration Using Terahertz Quantum Devices. *Chin Opt Lett* (2014) 12:120401. doi:10.3788/col201513.081402
40. Grant P. D., Laframboise S. R., Dudek R., Graf M., Bezinger A., Liu H. C., et al. (2021). Terahertz Free Space Communications Demonstration with Quantum Cascade Laser and Quantum Well Photodetector. *Electron. Lett.* 45(18), 952–954.

Conflict of Interest: The authors declare that the research was conducted in the absence of any commercial or financial relationships that could be construed as a potential conflict of interest.

Publisher's Note: All claims expressed in this article are solely those of the authors and do not necessarily represent those of their affiliated organizations, or those of the publisher, the editors, and the reviewers. Any product that may be evaluated in this article, or claim that may be made by its manufacturer, is not guaranteed or endorsed by the publisher.

Advantages of publishing in Frontiers

OPEN ACCESS
Articles are free to read for greatest visibility and readership

FAST PUBLICATION
Around 90 days from submission to decision

HIGH QUALITY PEER-REVIEW
Rigorous, collaborative, and constructive peer-review

TRANSPARENT PEER-REVIEW
Editors and reviewers acknowledged by name on published articles

Frontiers
Avenue du Tribunal-Fédéral 34
1005 Lausanne | Switzerland

Visit us: www.frontiersin.org
Contact us: frontiersin.org/about/contact

REPRODUCIBILITY OF RESEARCH
Support open data and methods to enhance research reproducibility

DIGITAL PUBLISHING
Articles designed for optimal readership across devices

FOLLOW US
@frontiersin

IMPACT METRICS
Advanced article metrics track visibility across digital media

EXTENSIVE PROMOTION
Marketing and promotion of impactful research

LOOP RESEARCH NETWORK
Our network increases your article's readership